

Light Hadron Spectroscopy in Quenched QCD

Paul Anthony Rowland



Doctor of Philosophy
The University of Edinburgh
1997



To my family and friends.

Abstract

This thesis presents an *ab initio* calculation of masses of light hadrons composed of up, down and strange quarks in lattice QCD.

The results are obtained from a series of simulations performed in the quenched approximation to lattice QCD, at different lattice spacings and lattice sizes, which enables us to extrapolate to zero lattice spacing (i.e. the continuum), and to estimate any finite-size effects. Our simulations employ the Wilson gauge field action, the Sheikholeslami-Wohlert $O(a)$ -improved Wilson fermion action with two choices for the clover coefficient, and two lattice volumes. Comparisons are made where possible, with simulations from other groups using unimproved Wilson fermions to investigate the effects of improvement and to compare continuum results. Systematic errors in the calculation are investigated in detail. Finally a comparison is made between our results and experiment to estimate the effects of the quenched approximation.

Declaration

This thesis has been wholly composed by me. It contains work I have carried out as a member of the UKQCD collaboration.

The computer programs used to generate the gauge configurations and propagators described in chapter 3 were written by members of the UKQCD collaboration, with recent improvements in solver code by Nicholas Hazel and Stephen Pickles. The correlation functions were computed from code that was developed by Peter Boyle, Stephen Pickles and myself. The gauge configurations were generated by members of the UKQCD collaboration, with the exception of the gauge configurations on the large volume at $\beta = 6.0$ which was generated by myself. The running of the code in production for the data at $\beta = 5.7$ was carried out by Hugh Shanahan. The tadpole data at $\beta = 6.0$ and $\beta = 6.2$ was produced by Peter Boyle, David Richards and myself. All the non-perturbative data were produced by myself. All results were analysed by myself alone. The code used in the analysis were developed from basic routines for statistical analysis written by Nicholas Hazel, David Henty, Henning Hoerber, and Hugh Shanahan.

The results of these calculations have been published in

- Improvement and the quenched light hadron spectrum and matrix elements by Paul Rowland Talk Presented at Lattice '97

Other work to which I have co-authored includes:

- Hybrid and Orbitally Excited Mesons in Quenched QCD, P. Lacock et al. Contributed to Lattice 97
- Hybrid Mesons from Quenched QCD P. Lacock et al, Phys.Lett **B401** (1997) 308-312
- Orbitally Excited and Hybrid Mesons from the Lattice, P. Lacock et al, Phys.Rev **D54** (1996) 6997-7009

- Light-meson decay constants using an improved fermionic action, P.A. Rowland (UKQCD Collaboration), Nucl. Phys. **B (Proc. Suppl.)** 53 (1997) 309
- The effect of tree-level and mean-field improvement on the light-hadron spectrum in quenched QCD, Phys.Rev. **D55** (1997) 1548-1558

Acknowledgements

I would first like to thank my family for all their help and encouragement through my studies.

On finishing my undergraduate studies I had considered entering the “real world”, but preferred to stay on and study for a PhD, so I would like to thank Ken Bowler for finding me a studentship at short notice and PPARC for supplying the funding.

I would like to thank David Richards and Richard Kenway for their careful reading of this thesis and their encouragement through my research. I would like to thank the other members of EDQCD and the UKQCD collaboration for their helpful discussions. A big shout goes out to Douglas and Zbigniew my office mates for putting up with me whilst I was writing up, and especially Zbigniew for making lots of coffee.

Throughout my time in Edinburgh I have made a number of friends from inside and outside the Physics Department, which have made it enjoyable and memorable experience. I have enjoyed playing for the Department postgrad football team and E=MCC the Department cricket team, and would like to say cheers to the members of both teams. I would like to say a special thanks to my flatmates and friends Al, Tom, Jon, Tim, John, Maz and Gail for been such good fun.

Contents

1	Introduction	1
1.1	QCD in the continuum	3
1.2	Euclidean Field Theory	5
1.3	Lattice Field Theory	7
1.4	Lattice Gauge Theory	7
1.4.1	Pure Gauge Action	9
1.5	Lattice Fermions	10
1.5.1	Naive Fermions	10
1.5.2	Wilson Fermions	12
1.6	Lattice Simulations	15
1.6.1	Monte Carlo Techniques	16
1.6.2	The lattice Quark Propagator	18
1.7	From Lattice QCD to Continuum QCD	19
1.8	Errors: Systematic and Statistical	22
1.8.1	Systematic Errors	23
1.8.2	Statistical Errors	24
1.9	Improvement	27
1.9.1	Tree-level $O(a)$ improvement	28
1.9.2	The Tadpole-Improved SW Action	30
1.9.3	Full $O(a)$ Improvement	32
2	Correlation Functions and Smearing	38
2.1	Correlation Functions	38
2.1.1	Interpolating Operators	38
2.1.2	Meson Two-Point Functions	40
2.1.3	Meson Masses	41
2.1.4	Fitting Meson Two-Point Functions	43
2.1.5	Baryons	44
2.1.6	Fitting Baryon Two-point Functions	50
2.1.7	Monte Carlo Measurements: Signal vs. Noise	51

2.2	Smearing	52
2.2.1	Source and Sink Smearing	54
2.2.2	The Jacobi Smearing Algorithm	58
2.2.3	Fuzzing	67
3	Simulation Details and Fitting Hadron Masses	77
3.1	Simulation Details	77
3.2	Fitting Hadron Masses	92
3.2.1	The Multi-Exponential Fitting Procedure	92
3.2.2	Some comments on the other hadronic states measured	113
4	The Light Hadron Spectrum	116
4.1	Finite Volume Effects	116
4.2	Chiral Extrapolations	117
4.2.1	Pion Chiral Extrapolations	117
4.2.2	Vector Meson Chiral Extrapolations	127
4.2.3	Spin- $\frac{1}{2}$ Octet Baryons Chiral Extrapolations	131
4.2.4	Spin- $\frac{3}{2}$ Baryons Chiral Extrapolations	138
4.3	A Brief Investigation of Scaling	141
4.4	Determination of the Light Quark Masses	144
4.4.1	The Normal Quark Mass	144
4.4.2	The Strange Quark Mass	145
4.5	Scaling Behaviour	145
4.5.1	How to set the mass scale	146
4.5.2	The String Tension	146
4.6	Light Hadron Masses and Continuum Extrapolations	147
4.6.1	The ρ mass in the continuum	147
4.6.2	Conventions used in future continuum extrapolations	153
4.6.3	Strange Meson Masses	154
4.6.4	The J parameter	159
4.6.5	The Hyperfine Splitting	162
4.7	Light Baryons Masses	167

4.7.1	Spin- $\frac{1}{2}$ Octet Baryons	167
4.7.2	Spin- $\frac{3}{2}$ Decuplet Baryons	170
5	Summary and Conclusions	172
5.1	Improvement and the continuum limit	172
5.2	Can we see the effects of the Quenched Approximation?	173
5.3	What have we achieved?	178
A	Appendix – Fitted Lattice Hadron Masses	180
B	Appendix – Light Hadron Spectrum Results	203
	References	211

Chapter 1

Introduction

In particle theory today there is a highly successful model of particle interactions called the Standard Model (SM). In the SM the fundamental particles of nature are fermions interacting with each other via exchange of virtual gauge bosons. To understand the interaction requires gauge invariance and the SM demands invariance under $SU(3) \otimes SU(2) \otimes U(1)$ rotations. The unbroken, non-Abelian group $SU(3)$ describes Quantum Chromodynamics (QCD) the strong interaction of coloured quarks and gluons. $SU(2) \otimes U(1)$ is the electroweak force describing the interaction between the leptons and the W and Z particles with spontaneous symmetry breaking at low energies to the $U(1)$ of electromagnetism and the weak interaction.

Traditionally to calculate quantities of physical interest, such as scattering amplitudes and matrix elements, requires the use of perturbation theory where a power series in the coupling constant between the appropriate fermion and gauge boson is used. Higher terms in the series represent more complex possibilities for exchange of virtual gauge bosons between fermions. Collectively these differing processes are called Feynman diagrams. For Quantum Electrodynamics (QED) the characteristic coupling constant $\alpha_e \approx \frac{1}{137}$ and the series is asymptotic making QED relatively simple to solve. QCD has the property of asymptotic freedom, as a consequence of the non-Abelian structure of the gauge group [1, 2, 3, 4], where the typical coupling constant increases as the momentum scale at which one wants to solve QCD decreases. The opposite is true for QED. One probable consequence of asymptotic freedom is that the quarks are confined into bound states called hadrons. The coupling constant increases as the separation of the quarks increases

and the typical momentum exchange between such quarks decreases ($\Delta p \Delta x \approx 1$). Perturbation theory accurately describes QCD processes at short distance, i.e. high energy physics. However, the correct theory of the strong interaction, must also describe the low energy, mass spectrum of particles and matrix elements between particles states, which are observed experimentally. At the length scales relevant to observable quantities the coupling constant is $\alpha_s \approx O(1)$ and perturbation theory becomes unreliable, making a non-perturbative formalism of QCD essential.

To date, Lattice QCD [5, 6, 7, 8] is the most successful non-perturbative theory of the strong interaction. Formulating QCD on a lattice provides a theory in which *ab initio* calculations of physical observables can be made, to an accuracy limited only by the available computational resources.

This thesis is concerned with a determination of the light hadron spectrum (hadrons made from u, d and s quarks). This is a central goal of Lattice QCD: such a successful calculation would be both a validation of QCD, as the theory of the strong interaction and of Lattice QCD as a computational tool. The first calculation of the light hadron spectrum was reported in 1981, where the calculations were done on computers capable of sustaining about 1 Megaflop [9]. Today, computers exist that can achieve over one million times that speed, but progress appears to be slow in achieving this goal, as a large amount of effort is required in controlling the systematic errors arising in the calculation of physical observables.

In this chapter, a brief overview of Lattice QCD is given, focusing on discretising the continuum theory to the lattice, on the calculation of observables and the associated systematic and statistical errors and finally how to relate quantities calculated on a lattice to the continuum. The approximations that are made can be systematically improved. This improvement can occur not only because of increases in computer power, which allows larger lattices to be used in the simulation, but also due to analytical advances, e.g “improving the action” so that we can work with larger lattice spacings without increasing the errors due

to discretisation. The improvement of the Lattice QCD action will be another subject discussed in this chapter.

1.1 QCD in the continuum

The strong interaction of quarks and gluons is described by the QCD Lagrangian

$$\mathcal{L} = \sum_{\psi=u,d,s,c,b,t} \bar{\psi}_i (i \not{D}_{ij} - m_q \delta_{jk}) \psi_k - \frac{1}{4} F_{\mu\nu}^a F^{\mu\nu a}, \quad (1.1)$$

where ψ are the quark fields and $i, j = 1, 2, 3$, is the quark-colour index (the Dirac index is dropped for clarity), and $a = 1, \dots, 8$ is the gluon colour index. Repeated colour indices are summed over.

The covariant derivative which makes the action invariant under local gauge transformations is given by

$$D_\mu = \partial_\mu - igA_\mu \text{ and } \not{D} = \gamma^\mu D_\mu. \quad (1.2)$$

The gauge fields, A_μ are elements of the $su(3)$ the Lie Algebra of $SU(3)$ and are collected in a matrix

$$A_\mu = A_\mu^a \frac{\lambda^a}{2} \quad a = 1, \dots, 8, \quad (1.3)$$

where the λ^a are the Gell-Mann traceless, hermitian matrices which are the generators of the $SU(3)$ symmetry and which satisfy

$$[\lambda^a, \lambda^b] = if^{abc} \lambda^c \text{ and } Tr(\lambda^a \lambda^b) = 2\delta_{ab}. \quad (1.4)$$

The f^{abc} are the structure constants. The gauge part of the action is described by the field strength tensor

$$F_{\mu\nu} = F_{\mu\nu}^a T^a = \frac{i}{g} [D_\mu, D_\nu] = \partial_\mu A_\nu - \partial_\nu A_\mu - ig[A_\mu, A_\nu], \quad (1.5)$$

where the last term arises from the non-Abelian nature of the theory, in which gluons, like quarks, carry colour charge.

The Lagrangian in equation (1.1) is invariant under local gauge transformations,

$\Lambda(x) \in SU(3)$, in which the quark and gluon fields transform in the following way,

$$\psi(x) \longrightarrow \Lambda(x)\psi(x), \quad (1.6)$$

$$\bar{\psi}(x) \longrightarrow \bar{\psi}(x)\Lambda^{-1}(x), \quad (1.7)$$

$$A_\mu(x) \longrightarrow \Lambda(x)A_\mu(x)\Lambda^{-1}(x) - \frac{1}{ig}(\partial_\mu\Lambda(x))\Lambda^{-1}(x), \quad (1.8)$$

$$F_{\mu\nu}(x) \longrightarrow \Lambda(x)F_{\mu\nu}(x)\Lambda^{-1}(x), \quad (1.9)$$

$$D_\mu\psi(x) \longrightarrow \Lambda(x)D_\mu\psi(x). \quad (1.10)$$

The gauge fields, $A_\mu(x)$ have the same function as the Christoffel symbols (connections) in general relativity. To compare two infinitesimally separated quark fields $\psi(x)$ and $\psi(x+dx)$ they must be considered at the same point in space-time using parallel transport. An $SU(N)$ matrix associated with a path in spacetime, which parallel transports the field $\psi(x)$ along a curve, \mathcal{C} to the field $\psi(x+dx)$ is defined by

$$\mathcal{U}(\mathcal{C}) \equiv I - igA_\mu(x)dx^\mu. \quad (1.11)$$

The effect of many parallel transports can be generalised from the above, to describe how a finite path is traversed, as [10],

$$\mathcal{U}(\mathcal{C}) = \mathcal{P}e^{ig\int_{\mathcal{C}} A_\mu dx^\mu}. \quad (1.12)$$

\mathcal{P} is a path ordering similar to the time-ordering operator in ordinary quantum mechanics, acting on matrices, $A_\mu(x)$ such that $A_\mu(x_1)$ is placed to the right of $A_\mu(x_2)$ if the curve \mathcal{C} reaches x_1 before x_2 . The parallel transport is a useful geometric concept¹, inherent in any gauge theory. The parallel transport over a finite interval

$$P(x', x) = \mathcal{P}\exp\left\{ig\int_x^{x'} A_\mu(y)dy^\mu\right\} \in SU(3), \quad (1.13)$$

where the line integral is ordered along the path joining x and x' . Under parallel transport $\psi(x)$ picks up a path-dependent phase factor. Thus, for every path

¹The relationship between QCD and geometry is explained in detail in [11]

there is a corresponding group element. From equations (1.6) and (1.7) the parallel transport operator transforms as follows:

$$P(x, x') \rightarrow P'(x', x) = \Lambda(x')P(x', x)\Lambda^{-1}(x). \quad (1.14)$$

The quantity $\psi(x')P(x', x)\psi(x)$ is clearly gauge invariant. Another important geometrical concept is the “curvature tensor” on the group space. A space has non-zero curvature if a vector experiences a change under parallel transport around a closed path. This change is proportional to the vector itself, to the area bounded by the path, and to the curvature tensor. By considering parallel transport around an infinitesimal rectangle

$$P_{\square} = P(x, y; x, y + dy)P(x, y + dy; x + dx, y + dy) \times \\ P(x + dx, y + dy; x + dx, y)P(x + dx, y, x, y), \quad (1.15)$$

and using the following matrix identity

$$e^{\lambda A}e^{\lambda B} = e^{\lambda(A+B)} + e^{\frac{\lambda^2}{2}[A,B]} + O(\lambda^3), \quad (1.16)$$

it can be shown that

$$P_{\square} = \exp\left\{igF_{\mu\nu}dx^{\mu}dy^{\nu}\right\}, \quad (1.17)$$

which suggests identifying $F_{\mu\nu}$ as the curvature tensor in group space. From equation (1.9) it is clear that parallel transport around any closed path is a gauge invariant operation.

1.2 Euclidean Field Theory

Lattice calculations are performed in Euclidean space which is related to Minkowski space through the Wick rotation

$$t \rightarrow \tau = it, \quad (1.18)$$

which is accomplished by continuing the signature of the space-time metric from $(1, -1, -1, -1)$ to $(1, 1, 1, 1)$. The gamma matrices of the theory are defined to satisfy the algebra,

$$\{\gamma_\mu^E, \gamma_\nu^E\} = 2\delta_{\mu\nu}, \quad (1.19)$$

$$\gamma_\mu^{E\dagger} = \gamma_\mu^E, \quad (1.20)$$

for the Hermitian choice

$$\gamma_0 = \gamma_4^E, \quad -i\gamma_i = \gamma_i^E \text{ and } \gamma_5 = \gamma_5^E. \quad (1.21)$$

With this choice the Euclidean, continuum QCD action is

$$S = \int d^4x \left[\frac{1}{4} F_{\mu\nu} F^{\mu\nu} + \bar{\psi}(x) (\not{D} + m) \psi(x) \right]. \quad (1.22)$$

The move from Minkowski to Euclidean space has two advantages. Firstly, the integrand in a Minkowski path integral $\exp(iS_M)$, is complex. In contrast, the Euclidean integrand is, real and positive, the Euclidean action, $S_E = iS_M$. Thus in the Minkowski integral there are large cancellations between different regions of configuration space, and these make it hard to simulate all but very small systems. This is an algorithmic, not a fundamental, issue. Secondly, the generating function in Euclidean space

$$Z_E = \int_{\text{field configurations}} e^{-S_E}, \quad (1.23)$$

where sources are suppressed, looks like the partition function of statistical mechanics. This analogy between Euclidean Quantum Field Theory and classical statistical mechanics is exploited to use Monte Carlo techniques to calculate expectation values of operators in terms of classical fields:

$$\langle \mathcal{O}(\bar{\psi}, \psi, A) \rangle = \frac{1}{Z_E} \int \mathcal{D}\bar{\psi} \int \mathcal{D}\psi \int \mathcal{D}A \mathcal{O}(\bar{\psi}, \psi, A) \exp[-S_E(\bar{\psi}, \psi, A)]. \quad (1.24)$$

The Feynman path integral is written in terms of the variables of Lattice QCD, the quark fields $\bar{\psi}$ and ψ , and the gauge fields A_μ .

1.3 Lattice Field Theory

To perform numerical simulations a discrete four-dimensional hypercubic lattice of space-time points separated by the lattice spacing a is introduced. The elements of this lattice are the sites and connections between the sites called links. The variables of the Lattice Field Theory are defined on the elements of the lattice; quark fields on the sites and gauge fields on the links. The integral over space-time in equation (1.23) is approximated by

$$\int d^4x \rightarrow a^4 \sum_x, \quad (1.25)$$

where the sum is over all lattices sites, labelled by a four-vector $x = (n_x, n_y, n_z, n_t)$. On a finite lattice, field theory has a finite number of degrees of freedom and is thus amenable to computer simulation.

The discretisation of space-time provides a natural ultraviolet cut-off on momenta which are restricted to a domain bounded by π/a ; wavelengths less than twice the lattice spacings have no lattice representation. Furthermore, the introduction of periodic boundary conditions quantises the allowed values of three-momenta:

$$\vec{p} = \frac{2\pi}{aN_s}(n_x, n_y, n_z), \quad (1.26)$$

where n_x , n_y and n_z are integers, and N_s is the spatial dimension of the lattice. As with any cut-off prescription, there is considerable freedom in the lattice formulation. This allows the regulation of unwanted lattice artifacts by the addition of non-continuum terms to the lattice which vanish in the continuum limit.

Lattice QCD is defined as a theory which has as its limit the continuum theory of QCD, when the lattice spacing a is taken to 0 and the volume of the lattice is taken to infinity in a prescribed way. This will be discussed further below.

1.4 Lattice Gauge Theory

Discretising a gauge theory by replacing the continuum gauge fields, $A^\mu(x)$, by gauge variables at the sites of the lattice, breaks gauge symmetry. This would necessitate establishing its restoration in the continuum limit. Wilson [12] introduced the following formulation in which the gauge fields are represented by elements of the $SU(3)$ gauge group.

Recall from section 1.1, a field $\psi(x)$ picks up the following path-dependent phase factor under parallel transport from x to x'

$$U(x', x) = \mathcal{P} \exp \left\{ ig \int_x^{x'} A_\mu(y) dy^\mu \right\}, \quad (1.27)$$

and that every path can be associated with an $SU(3)$ group element. On the lattice, Wilson introduced the link variable defined as:

$$U_\mu(x + \hat{\mu}) \equiv U_\mu^\dagger(x) \in SU(3), \quad (1.28)$$

which represents parallel transport between nearest-neighbour sites, from x to $x + \hat{\mu}$, where $\hat{\mu}$ is a lattice unit vector (length a), pointing in the μ direction. The gauge transformation properties of the link variables

$$U_\mu(x) = V(x) U_\mu(x) V(x + \hat{\mu}), \quad (1.29)$$

where the $V(x) \in SU(3)$ are gauge transformation matrices which live on the sites. The relation between these link variables and the gauge fields, $A^\mu(x)$, is given by

$$U_\mu(x) = \mathbb{I} + iga A_\mu(x + \frac{1}{2}\hat{\mu}) + O(a^2), \quad (1.30)$$

where the mid-point rule is used to approximate the line integral in equation (1.27). The phase factor associated with parallel transport across the lattice is the path-ordered product of link variables traversed.

There are two types of gauge-invariant objects which can be constructed from the link variables on the lattice:

a string terminated by a fermion at one end and an antifermion at the other,

$$\bar{\psi}(x)U_\mu(x)\dots\dots U_\nu(y-\hat{\nu})\psi(y); \quad (1.31)$$

the trace of the path-ordered integral around any closed path, a closed string, these are called Wilson loops, the simplest of which is the plaquette,

$$P_{\mu\nu} = \text{Tr}[U_{\mu\nu}^\square(x)], \quad (1.32)$$

$$\text{with } U_{\mu\nu}^\square(x) = U_\mu(x)U_\nu(x+\hat{\mu})U_\mu^\dagger(x+\hat{\nu})U_\nu^\dagger(x). \quad (1.33)$$

1.4.1 Pure Gauge Action

We shall now be concerned with the discretising the pure Yang-Mills part of the continuum QCD action. Using these gauge invariant definitions and recalling from section 1.1, parallel transport around an infinitesimal closed path is proportional to the field strength tensor, $F_{\mu\nu}$, lead Wilson to suggest the following pure gauge action:

$$S_G = -\frac{1}{g^2} \sum_x \sum_{\mu>\nu} \text{Tr}[U_{\mu\nu}^\square(x) + U_{\mu\nu}^{\square\dagger}(x)], \quad (1.34)$$

where $U_{\mu\nu}^\square(x)$ is the Wilson loop in equation (1.33) and the sum $\sum_{\mu>\nu}$ is for $1 \leq \nu < \mu$. The bare coupling is related to the strong coupling constant as $g^2 = 4\pi\alpha_s$.

Wilson showed that equation (1.34) gives

$$S_G = \int d^4x \left\{ \frac{1}{4} F_{\mu\nu} F^{\mu\nu} + O(a^2) \right\}, \quad (1.35)$$

which corresponds to the continuum action with a discretisation error of $O(a^2)$. The Wilson pure gauge action is usually written in the following parameterisation

$$S_G = \beta \sum_x \sum_{\mu>\nu} \left[1 - \frac{1}{N_c} \text{ReTr}U_{\mu\nu}^\square(x) \right], \quad (1.36)$$

with

$$\beta = \frac{2N_c}{g^2}, \quad (1.37)$$

where N_c is the dimension of the $SU(N_c)$ gauge group.

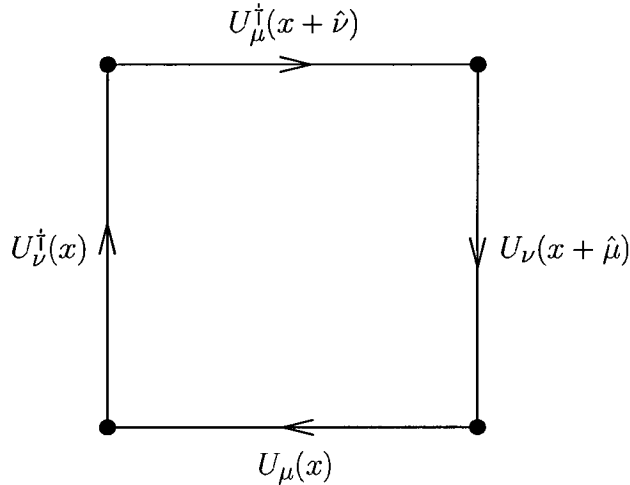


Figure 1.1: An elementary plaquette.

1.5 Lattice Fermions

1.5.1 Naive Fermions

Naively discretising the fermionic part of the action:

$$S_F = \int d^4x \bar{\psi}(x)(\not{D} + m)\psi(x), \quad (1.38)$$

by replacing continuum derivatives with a central difference approximation gives

$$S_{NF} = \sum_x \left\{ \frac{a^3}{2} \sum_{\mu=1}^d \bar{\psi}(x) \gamma_\mu [U_\mu(x) \psi(x + \hat{\mu}) - U_\mu^\dagger(x - \hat{\mu}) \psi(x - \hat{\mu})] \right\} + a^4 \sum_x \{m \bar{\psi}(x) \psi(x)\}. \quad (1.39)$$

If the naive lattice Lagrangian is Taylor expanded in the lattice spacing, the

following continuum result is obtained:

$$\mathcal{L}_{NF} = \bar{\psi}(x)(\not{D} + m)\psi(x) + O(a^2). \quad (1.40)$$

The naive lattice fermion action is equal to the continuum Dirac action, up to $O(a^2)$ corrections. The harmless looking action of equation (1.39) gives rise to an infamous problem: in d dimensions, it represents 2^d degenerate Dirac fermions, rather than one. This sixteenfold replication in 4 dimensions is referred to as the “fermion doubling problem”. Consider the naive lattice fermion propagator in momentum space

$$G(p) = \frac{1}{i\gamma_\mu \sin(p_\mu) + m} = \frac{-i\gamma_\mu \sin(p_\mu) + m}{\sum_\mu \sin^2(p_\mu) + m^2}. \quad (1.41)$$

It is useful to reinstate factors of a , so that $m = am_{\text{phys}}$ and $p = ap_{\text{phys}}$. In the continuum limit, for fixed physical quark mass, $m \rightarrow 0$. There is thus a pole near $p = 0$, and we can expand $\sin(p_\mu) = ap_{\mu,\text{phys}}(1 + O(a^2))$, yielding

$$aG(p) = \frac{-i\gamma_\mu \sum_\mu p_{\mu,\text{phys}} + m_{\text{phys}}}{p_{\text{phys}}^2 + m_{\text{phys}}^2}. \quad (1.42)$$

This has a pole at $p_{\text{phys}}^2 = -m_{\text{phys}}^2$, representing the fermion that we expected to find. The lattice momentum function $\sin(p_\mu a)$ vanishes at $p_\mu = \pi$ as well as $p_\mu = 0$. In the neighbourhood of the momentum $(\pi, 0, 0, 0)$, if we define new variables $p'_1 = \pi - p_1$, $p'_i = p_i$, $i = 2 - 4$, then

$$G(p') \approx \frac{-i \sum_\mu p'_\mu \gamma'_\mu + m}{p'^2 + m^2}. \quad (1.43)$$

To bring the propagator into the standard continuum form, we have introduced new gamma-matrices, $\gamma'_1 = -\gamma_1$, $\gamma'_i = \gamma_i$, $i = 2 - 4$, unitarily equivalent to the standard set. Equation (1.43) shows that there is a second pole, at $p'^2 = -m^2$, which also represents a continuum fermion. This is our first “doubler”.

The saga continues in an obvious way: $\sin(p_\mu)$ vanishes if each of the four components of k_μ equals 0 or π . There is a pole near each of these 16 possible positions.

Our single lattice fermion turns out to represent 16 degenerate states.

A theorem by Nielsen and Ninomiya [13] (the "No-Go" theorem) says that such doubling is a feature of any reasonable, lattice regularisation scheme. The theorem states that for a local lattice action that is bilinear, translationally invariant, Hermitean and with chiral symmetry, the continuum limit will contain multiple fermion species in opposite chirality pairs.

The naive lattice fermion action equation (1.39) satisfies the criteria of the "No-Go" theorem. Can this be fixed up? There are various ways to circumvent these problems each with their own problems:

- explicitly break chiral symmetry right from the start, and aim to recover it only in the continuum limit, which is akin to rotations and translations. For fermions in vector representations this is the approach originally taken by Wilson [15], which will be discussed in more detail next, and is the approach which we shall take;
- keep the extra doublers and divide their effects out by hand. This is the approach taken by "staggered" or Kogut-Susskind fermions [16]. In this formulation one reduces the number of fermion flavours by using one component staggered fermion fields rather than four component Dirac spinors. The Dirac spinors are constructed by combining staggered fields on different lattice sites.

1.5.2 Wilson Fermions

The formulation of Lattice QCD used in this study is based on the Wilson action. Recall from section 1.3, there is freedom in the lattice formulation which allows terms to be added to the action which vanish in the continuum limit. Wilson [15], exploited this ambiguity by adding irrelevant operators, ones which vanish in the classical continuum limit, to reduce the fermion content of the lattice theory to one fermion.

Wilson's choice was to add a second derivative term to the naive action,

$$S_{WF} = S_{NF} + S_W, \quad (1.44)$$

where the Wilson term is,

$$S_W = -\frac{ar}{2} \sum_x \bar{\psi}(x) \Delta \psi(x), \quad (1.45)$$

with the Wilson coefficient, r , and Δ is the lattice discretisation of the second derivative,

$$\Delta \psi(x) = \sum_{\mu} \frac{1}{a^2} \left(U_{\mu}(x) \psi(x + \hat{\mu}) - 2\psi(x) + U_{\mu}^{\dagger}(x) \psi(x - \hat{\mu}) \right). \quad (1.46)$$

The Wilson fermion action is

$$S_{WF} = \sum_x \frac{a^3}{2} \left\{ - \sum_{\mu=1}^4 \bar{\psi}(x) \left[(r - \gamma_{\mu}) U_{\mu}(x) \psi(x + \hat{\mu}) + (r + \gamma_{\mu}) U_{\mu}^{\dagger}(x) \psi(x - \hat{\mu}) \right] + (2ma + 8r) \bar{\psi}(x) \psi(x) \right\}. \quad (1.47)$$

For computational purposes, S_{WF} can be rewritten in matrix form as

$$S_{WF} = \bar{\psi}(x) M_{WF}(x, y) \psi(y), \quad (1.48)$$

where we have redefined the quark fields, $\psi \rightarrow \sqrt{2\kappa} \psi$. The Wilson fermion matrix $M_{WF}(x, y)$ is defined as

$$M_{WF}(x, y) = \delta(x, y) - \kappa \mathcal{D}(x, y), \quad (1.49)$$

where $\delta(x, y)$ is the Kronecker delta,

$$\mathcal{D}(x, y) \equiv \sum_{\mu} \left((r - \gamma_{\mu}) U_{\mu}(x) \delta(x + \hat{\mu}, y) + (r + \gamma_{\mu}) U_{\mu}^{\dagger}(x) \delta(x - \hat{\mu}, y) \right), \quad (1.50)$$

and κ is the ‘‘hopping parameter’’, which measures the strength of nearest neighbour interactions in the lattice theory. In practical lattice calculations, this is

the input parameter which controls the bare quark mass and will be referred to frequently in the following. For free fermions,

$$\kappa = \frac{1}{2m + 8r} \Rightarrow m = \frac{1}{2} \left(\frac{1}{\kappa} - 8r \right), \quad (1.51)$$

in the presence of gauge interactions the bare quark mass is given by

$$m_q = \frac{1}{2} \left(\frac{1}{\kappa} - \frac{1}{\kappa_c} \right). \quad (1.52)$$

The Wilson term explicitly breaks chiral symmetry. This has the consequence that the zero bare quark mass limit is not respected by interactions; the quark mass is additively renormalised. The value of κ_c , is not known a priori before beginning a simulation; it must be computed. In general, this is that the pion mass vanish in the critical limit.

The effect of adding this irrelevant operator is to introduce an explicit mass term which breaks the degeneracy of the doublers. In terms of the free quark propagator, the naive continuum limit is modified to

$$G(p) = \frac{-i\gamma_\mu \sin(p_\mu) + m - r \sum_\mu (\cos(p_\mu) - 1)}{\sum_\mu \sin^2(p_\mu) + (m - r \sum_\mu (\cos(p_\mu) - 1))^2}, \quad (1.53)$$

with only a single pole (at $p_\mu = 0$) in the continuum limit. On the lattice, the extra fermion species acquire masses of $O(r/a)$, which are infinite in the continuum limit and thus decouple from the low energy behaviour.

If the action in equation (1.47) is Taylor expanded in the lattice spacing, the following continuum action is obtained

$$S_{WF} = \int d^4x \bar{\psi}(x) \left(\not{D} + m - \frac{arD^2}{2} \right) \psi(x) + O(a^2). \quad (1.54)$$

From the continuum action, it can be seen that a price is paid for the removal of the species doublers, the addition of an $O(a)$ correction to the action.

The Lattice QCD action can now be written

$$S_{QCD} = S_G + S_{WF}. \quad (1.55)$$

The Wilson r parameter is set to 1 throughout the rest of this thesis.

1.6 Lattice Simulations

Having formally defined the Lattice QCD action, a practical means of numerically simulating the theory must be developed. The generating functional for Lattice QCD is

$$Z = \int \mathcal{D}\bar{\psi}\mathcal{D}\psi\mathcal{D}U \exp\left\{-S_G(U) - \bar{\psi}M(x, y : U)\psi\right\}, \quad (1.56)$$

where $M(x, y; U)$ is the fermion matrix. $\mathcal{D}U$ is constructed from the Haar measure, so the measure in the functional integral is:

$$\mathcal{D}U = \prod_{x, \mu} \mathcal{D}U_\mu(x), \quad (1.57)$$

The Haar measure has the following property:

$$\begin{aligned} \int dU f(U) &= \int D(UV) f(U) = \int d(U) f(UV^{-1}) \\ &= \int D(VU) f(U) = \int d(U) f(V^{-1}U), \end{aligned} \quad (1.58)$$

required to make the functional integral gauge invariant. $\mathcal{D}\bar{\psi}\mathcal{D}\psi$ is defined over the Grassmann variables at every site, given by

$$\mathcal{D}\bar{\psi}\mathcal{D}\psi = \prod_x d\bar{\psi}(x) d\psi(x). \quad (1.59)$$

In the functional integral of equation (1.56), the Grassmann-valued quark fields $\psi(x)$ and $\bar{\psi}(x)$, cannot be evaluated in a stochastic process and must be integrated out before any numerical simulations can be attempted. This creates an effective

action, which depends only on the gauge fields, so the path-integral is

$$Z = \int \mathcal{D}U \det M e^{-S_G(U)}. \quad (1.60)$$

The vacuum expectation value of an observable is expressed as

$$\langle \mathcal{O}(\bar{\phi}, \phi, U) \rangle = \frac{1}{Z} \int \mathcal{D}U \det M e^{-S_G(U)} \mathcal{O}(\bar{\phi}, \phi, U). \quad (1.61)$$

Since the action has been rotated to Euclidean time a Monte Carlo algorithm can be used to determine vacuum expectation, using techniques developed for statistical mechanics.

1.6.1 Monte Carlo Techniques

A “generic” Monte Carlo simulation in QCD breaks up naturally into two parts. In the “configuration generation” phase one constructs an ensemble of states with the appropriate Boltzmann weighting: we compute observables by averaging N measurements using the field variables $\phi^{(i)}$ appropriate to the sample

$$\langle \Gamma \rangle \simeq \bar{\Gamma} \equiv \frac{1}{N} \sum_{i=1}^N \Gamma[\phi^{(i)}]. \quad (1.62)$$

As the number of measurements N becomes large the quantity $\bar{\Gamma}$ will become a Gaussian distribution about a mean value. Its standard deviation from [17] is

$$\sigma_{\Gamma}^2 = \frac{1}{N} \left(\frac{1}{N} \sum_{i=1}^N |\Gamma[\phi^{(i)}]|^2 - \bar{\Gamma}^2 \right). \quad (1.63)$$

The idea of essentially all simulation algorithms is that one constructs a new configuration of field variables from an old one. One begins with some field configuration and monitors observables while the algorithm steps along. After some number of steps, the value of observables will appear to become independent of the starting configuration. At this point the system is said to be “in equilibrium” and equation (1.62) can be used to make measurements.

The simplest method for generating configurations is called the Metropolis algorithm, [18]. It works as follows: from the old configuration $\{\phi\}$ with action S , transform the variables, in some reversible way, to a new trial configuration $\{\phi\}'$ and compute the new action S' . Then, if $S' < S$ make the change and update all the variables; if not, make the change with probability $\exp(-(S' - S))$. How does this generate the right probability distribution? In equilibrium, the rate at which configurations i turn into configurations j is the same as the rate for the back reaction $j \rightarrow i$, this is the additional constraint which the algorithm must satisfy known as “detailed balance”. The rate of change is (number of configurations) \times (probability of change). Assume for the sake of argument that $S_i < S_j$. Then the rate $i \rightarrow j$ is $N_i P(i \rightarrow j)$ with $P(i \rightarrow j) = \exp(-(S_j - S_i))$ and the rate $j \rightarrow i$ is $N_j P(j \rightarrow i)$ with $P(j \rightarrow i) = 1$. Thus $N_i/N_j = \exp(-(S_i - S_j))$.

Let us now consider the generation of configurations for the Lattice QCD partition function in equation (1.60), $P \propto \mathcal{D}U \det M e^{-S_G(U)}$. The determinant² introduces a non-local interaction among the U 's, whereas the variation of the gauge action involves only a local calculation, i.e. one involving links close to that being changed. The present algorithm of choice for simulating QCD is the “hybrid Monte Carlo” algorithm [19]. We can estimate that the time it takes to generate an independent configuration is roughly

$$\text{cost} \propto \left(\frac{N_s}{a}\right)^4 \left(\frac{1}{a}\right) \left(\frac{1}{am_\pi^2}\right), \quad (1.64)$$

where the first factor is just the number of lattice sites in the grid, and the remaining factors account for “critical slowing down” of the algorithms used in the numerical integration [20]. As the quark mass decreases, so does the pion mass, $m_\pi^2 \propto m_q$. Naively, it is necessary for the lattice length to exceed the pion Compton by a factor of a few, so $N_s \propto 1/m_\pi$. Using this, one finds $CPU \propto m_q^{-3}$. The cost of generating dynamical gauge configurations at light

²To obtain a positive measure one can either simulate degenerate pairs of quarks, in which case the measure contains the square of the single quark determinant or simulate with $\det M = \det(M^\dagger M)^{0.5}$.

quark masses is computationally expensive, even with today's computers. To make progress an approximation must be made, and this is what know as the "quenched" approximation,³ this amounts to

$$\det M = \text{constant} \equiv 1, \quad (1.65)$$

so that equation (1.60) becomes

$$Z = \int \mathcal{D}U e^{-S_G(U)}. \quad (1.66)$$

This corresponds to throwing away internal quark loops, while keeping the valence quarks, which now propagate through a modified distribution of gauge configurations. Quenching reduces the CPU requirement by a factor of $\sim 10^2 - 10^3$ at current parameter values. Furthermore the time to generate new gauge configurations only grows as $\text{CPU} \propto N_s^5 \propto m_q^{-2.25}$, so that it is easier to go to smaller quark masses. The quenched approximation will be used in the remainder of this thesis.

1.6.2 The lattice Quark Propagator

On the lattice, particle masses and matrix elements are extracted from correlation functions.⁴ These correlation functions are constructed from quark propagators computed for a fixed number of gauge configurations. The quark propagator is the basic building block in Lattice QCD.

In QFT the quark propagator is defined as follows:

$$G_{\alpha\beta}^{ab}(x, y) \equiv \langle 0 | \mathcal{T} \psi_{\alpha}^a(x) \bar{\psi}_{\beta}^b(y) | 0 \rangle, \quad (1.67)$$

where the Greek and Latin indices denote the spin and colour components of the quark fields respectively, and \mathcal{T} is the time ordering operator. In Euclidean

³Many of the artifacts of the quenched approximation can be absorbed through a shift of the coupling. This is explained in more detail later on in the chapter.

⁴Correlation functions are discussed in detail in the next chapter.

space, using the Feynman path integral formalism equation (1.67) is given by

$$\begin{aligned}
\langle 0|\psi(x)\bar{\psi}(y)|0\rangle &= \frac{1}{Z} \int \mathcal{D}U \mathcal{D}\bar{\psi} \mathcal{D}\psi \psi(x)\bar{\psi}(y) e^{-\bar{\psi}M\psi + S_G(U)} \\
&= \frac{1}{Z} \int \mathcal{D}U G(x, y; U) e^{-S_G(U)} \\
&= \frac{1}{Z} \int \mathcal{D}U M^{-1}(x, y; U) e^{-S_G(U)}, \tag{1.68}
\end{aligned}$$

where $G(x, y; U)$ is the quark propagator in a given configuration U , and is computed from the inverse of the fermion matrix $M^{-1}(x, y; U)$.

The Monte Carlo estimate of equation (1.68) is given by

$$G(x, y) = \langle 0|\mathcal{T}\psi(x)\bar{\psi}(y)|0\rangle \simeq \frac{1}{N} \sum_{i=1}^N M^{-1}(x, y; U_i), \tag{1.69}$$

where U_i is a statistically independent sample of N gauge configurations generated with the following probability distribution

$$\frac{1}{Z} \mathcal{D}U e^{-S_G(U)}. \tag{1.70}$$

In subsequent chapters and sections if a lattice quark propagator is used to calculate a correlation function the summation of gauge configurations is assumed, to reduce the notation.

The local (point) source quark propagator is computed using iterative methods to solve the linear equations of the form

$$M_{\alpha\beta}^{ab}(x, y, U) G_{\beta\gamma}^{bc}(y, 0; U) = \delta_{\alpha\gamma} \delta^{ac} \delta(x, 0). \tag{1.71}$$

In practice, $G_{\beta\gamma}^{bc}(y, 0; U)$ is computed for all twelve spin-colour combinations of point source, which describes the propagator of a quark from a fixed origin. The source function can be non-local to produce a smeared propagator and shall be discussed in the next chapter.

1.7 From Lattice QCD to Continuum QCD

Lattice QCD is a theory with the following free parameters.

- The bare lattice coupling g .
- The hopping parameters κ_f , $f = 1, \dots, n_f$, where n_f is the number of flavours.

Clearly with so few free parameters, the predictive power of such a theory is high, however an experimental measurement is needed to fix each parameter.

By formulating a field theory on a finite lattice, a regulator is introduced limiting the range of momentum values, the ultraviolet cutoff being $\Lambda \sim 1/a$, where a is the lattice spacing and all the coupling constants in the action are the bare couplings defined with respect to it. When we take a to zero we must also specify how $g(a)$ behaves. The proper continuum limit comes when we take a to zero holding dimensionless ratios of physical quantities fixed, not when we take a to zero holding the couplings fixed.

If we compute on the lattice, masses of physical particles at several values of the lattice spacing. Ratios of these masses will depend on the lattice cutoff. The typical behaviour will look like

$$(am_1(a))/(am_2(a)) = m_1(0)/m_2(0) + O(m_1a) + O((m_1a)^2) + \dots \quad (1.72)$$

The leading term does not depend on the value of the UV cutoff, while the other terms do. The goal of a lattice calculation is to discover the value of some physical observable as $a \rightarrow 0$, so the physics is in the first term. Everything else is an artifact of the calculation. We say that a calculation “scales” if the a -dependent terms in equation (1.72) are zero or small enough that one can extrapolate to $a = 0$, and generically refer to all the a -dependent terms as “scale violations.”

Lets now consider QCD at zero quark mass, where there is only a single parameter the bare coupling. We can express each dimensionless combination $am(a)$ as some

function of the bare coupling $\{g(a)\}$, $am = f(\{g(a)\})$. As $a \rightarrow 0$ we must tune the set of couplings $\{g(a)\}$ so

$$\lim_{a \rightarrow 0} \frac{1}{a} f(\{g(a)\}) \rightarrow \text{constant}. \quad (1.73)$$

From the point of view of the lattice theory, we must tune $\{g\}$ so that correlation lengths $1/ma$ diverge. This will occur only at the locations of second (or higher) order phase transitions in the lattice theory.

The Callan-Symanzik β -function is defined by

$$\beta(g) = a \frac{dg(a)}{da} = \frac{dg(a)}{d \ln(1/\Lambda_{LAT} a)}, \quad (1.74)$$

where Λ_{LAT} is a cutoff independent, renormalisation-group-invariant mass parameter describing the strength of the strong interaction. At a critical point $\beta(g_c) = 0$. Thus the continuum limit is the limit

$$\lim_{a \rightarrow 0} \{g(a)\} \rightarrow \{g_c\}. \quad (1.75)$$

In QCD the fixed point is $g_c = 0$ so we must tune the coupling to vanish as a goes to zero.

The two-loop β -function is prescription independent,

$$\beta(g) = -\beta_0 g^3 + \beta_1 g^5 + O(g^7), \quad (1.76)$$

where⁵

$$\beta_0 = \frac{11 - \frac{2}{3}n_f}{16\pi^2} \quad \text{and} \quad \beta_1 = \frac{1}{(16\pi^2)^2} \left(102 - \frac{38}{3}n_f \right), \quad (1.77)$$

At small enough coupling so that the two-loop beta function is approximately correct, if the lattice theory is reproducing the continuum, we might want to observe perturbative scaling, or ‘‘asymptotic scaling’’, m/Λ_{LAT} fixed, or a varying

⁵Note that when working in the quenched approximation the number of flavours, n_f is zero.

with g as

$$a\Lambda_{LAT} = (\beta_0 g^2(a))^{-\frac{\beta_1}{2\beta_0^2}} e^{-\frac{1}{2\beta_0 g^2(a)}} (1 + O(g^2)). \quad (1.78)$$

Asymptotic scaling is not scaling. Scaling means that dimensionless ratios of physical observables do not depend on the cutoff. Asymptotic scaling involves perturbation theory and the definition of coupling constants. One can have scaling without asymptotic scaling.

In practice, one proceeds as follows:

- at a given value of the lattice spacing, data are generated at different quark masses (different κ). This is done at unphysically heavy quark masses which must be extrapolated to the critical quark mass at κ_c .
- The value of κ_c is determined non-perturbatively. To first approximation using the PCAC relation, the square of the pion mass is proportional to the mass of the light quark, $m_\pi^2 \propto m_q$, and the criterion that $m_\pi^2 = 0$ at the critical point, κ_c is extracted.
- The ρ mass at the critical point is then found by extrapolating to its value at κ_c . The number is compared with its experimental counterpart to set the scale for this particular lattice calculation. In principle any dimensionful quantity can be used to set the scale and clearly it is best to find a choice which is most insensitive to the lattice mass.
- Scaling has to be verified by calculating the same physical quantity at different values of the lattice spacing $a(g)$. If scaling violations are seen, an extrapolation to $a \rightarrow 0$ has to be performed.

1.8 Errors: Systematic and Statistical

In a reliable calculation of hadronic masses ratios and other physical observables from lattice data, it is essential to understand the possible sources of systematic and statistical errors.

1.8.1 Systematic Errors

The Quenched Approximation

The quenched approximation sets the fermion determinant $\det M$ in equation (1.61), equal to a constant, i.e. $\det M = 1$, as discussed in section 1.6 and this represents a significant saving in computer time. This amounts to throwing away internal quark loops, while keeping the valence quarks, which now propagate through a modified distribution of gauge configurations. It is *a priori* not possible to determine the effect of quenching on the theory since it does not constitute a systematic approach: different quantities will be affected differently. Most importantly one hopes that the main features of full QCD, confinement and asymptotic freedom, remain intact in the quenched theory.

One of the unphysical effects of quenched QCD is that resonances in QCD, e.g. the ρ meson, become stable states in quenched QCD. This is because internal quark loops are necessary to obtain the on-shell intermediate states (e.g. $\pi\pi$ in the case of the ρ) which give rise to the imaginary parts of the propagators, and thus to the width of the resonances. However discarding these intermediate states affects not only the imaginary part, but also the real part of the propagator. In other words, not only is the width of the state changed to zero, but the mass is shifted. The most naive estimate is that $\delta m \sim \delta\Gamma = \Gamma$, the width of the ρ meson at 151.5 ± 1.2 MeV indicates its coupling to pions and correspondingly these dynamics must have significant influence on the ρ -meson mass. This mass shift will not be uniform in sign or magnitude, since it depends on the available thresholds, and possible cancellations. The change in the ρ mass may in fact be small [21].

In the quenched approximation the gauge coupling runs differently to that of the full theory. Lattice calculations adjust the quenched gauge coupling at the scale of the cutoff $\frac{1}{a}$ to agree with a coupling at the scale of physics, say for example at the mass of the ρ meson. One of the drawbacks of this procedure, called “setting the scale”, is that different quantities used in this procedure lead to different spacings. This will be discussed further in chapter 4.

Finite Volume Effects and Chiral Extrapolations

It is not possible to calculate the quark propagators at the physical values of the masses of the u- and d-quarks. In this limit the system of linear equations for the quark propagators becomes more and more singular. The physical reason for this effect can be seen as follows: the size of the light particles is given approximately by $\frac{1}{\Lambda_{\text{QCD}}} \approx 0.8\text{fm}$ whereas the spatial length of the lattices used here $\approx 1.8\text{fm}$. However, due to periodic boundary conditions there will be many copies of the hadron and volume would have to be very large for them not to interact with each other. The range of such interactions is of the order $O(\frac{1}{m_\pi})$ the pion Compton wavelength, which is the lightest particle of the system. The most important consideration for light hadron spectroscopy is that the lattice size at which simulations are done is bigger than the pion. To avoid these interactions one works with unphysically high masses of the light quarks. Correlators are calculated at several value of the hopping parameter κ and extrapolates in κ according to chiral perturbation theory to the physical quark masses. Therefore this procedure has introduced a systematic error. However, the chiral behaviour is modified due to quenching effects and this procedure is not as straightforward as it first seems and this too is discussed in chapter 4. The systematic error due to finite volume effects can be quantified by doing calculations at the same value of the lattice spacing but different physical volumes and comparing the results and this is explained in more detail in chapter 4.

Discretisation Errors due to Non-zero Lattice Spacing

This will be discussed in detail in a later section. Simulating with the Wilson gauge action and fermion action introduces discretisation errors of $O(a)$. Thus simulating at a finite lattice spacing has introduced a systematic error. There are two possible approaches to this problem. The first is to do the lattice simulations at different values of the lattice spacing and then extrapolate the results to the $a \rightarrow 0$, continuum limit. The second is to work with an improved action which reduces the discretisation errors, see section 1.9

1.8.2 Statistical Errors

With the chosen discretised action, the functional integral is evaluated using Monte Carlo techniques outlined in section 1.6. Expectation values are calculated on a finite sample of N gauge configurations. For N statistically independent configurations the statistical error falls off only as $\frac{1}{\sqrt{N}}$. A large set of gauge configurations however is computationally very expensive. To save computer time, propagators at different values of the hopping parameter κ are calculated on the same set of gauge configurations. Clearly different physical quantities will be highly correlated. This is also true of data for the same quantity but on different timeslices. We shall therefore briefly describe how the correlation of the data is taken into account in the fitting of the data.

Fitting Correlated Data

The covariance matrix is estimated from the data by

$$\sigma(t_i, t_j) = \frac{1}{N(N-1)} \sum_{k=1}^N (x_k(t_i) - \bar{x}(t_i))(x_k(t_j) - \bar{x}(t_j)), \quad (1.79)$$

where $x_k(t)$ are values of some lattice quantity calculated on a sample of $k = 1, \dots, N$ configurations and on timeslice t_i , $i = 1, \dots, N_t$. The quantity $\bar{x}(t_i)$ is the configuration average of $x_k(t_i)$. It is often more convenient to work with the *data correlation matrix*, defined as

$$\rho(t_i, t_j) = \frac{\sigma(t_i, t_j)}{\sqrt{\sigma(t_i, t_i)}\sqrt{\sigma(t_j, t_j)}}, \quad (1.80)$$

because the elements of this matrix are normalised in such a way that $\rho(t_i, t_i) = 1$ and $\rho(t_i, t_j) \in [-1, 1]$ so that it is easy to read off how strongly correlated the data on different timeslices is. For uncorrelated data, equation (1.80) reduces to the identity. In practice, equation (1.80) is computed because the correlation matrix is easier to invert numerically.

To fit the data to an analytical model function, $f(t; \vec{a})$, parameterised by m parameters, $a_i = a_1, a_2, \dots, a_m$, to the data $x_k(t)$, the fit is performed by minimising

the following chi-squared function with respect to the model parameters, \vec{a} :

$$\chi^2 = \sum_{t_i, t_j} [f(t_i; \vec{a}) - \bar{x}(t_i)] \times \sigma^{-1}(t_i, t_j) \times [f(t_j; \vec{a}) - \bar{x}(t_j)], \quad (1.81)$$

where the sum is over all timeslices t the fit is performed on. The goodness of a fit is estimated by the ratio $\chi^2/\text{d.o.f.}$ where d.o.f. denotes the number of degrees of freedom, in this case $d.o.f. = t - m$. A usual indication that the best fit to the data has been found is a

$$\chi^2/\text{d.o.f.} \sim 1. \quad (1.82)$$

Bootstrap Resampling

To estimate the error on a fitted parameter, the simulation should be repeated (many times) for different gauge configuration samples. In practice, this is prohibitive since both gauge configurations and quark propagators are computationally expensive. The error on a fit parameter can instead be estimated using Bootstrap methods [22]. Assume the complete simulation has been performed many times with different sets of N configurations. Performing a chi-squared minimisation procedure on each of these hypothetical simulations would yield a distribution for each parameter a_i which could be used to estimate the error in selecting the one particular configuration. To mimic this setup using the Bootstrap method one can proceed as follows. The N configurations are resampled randomly, allowing for repetitions, to generate a large number, typically 1000, of new simulated ensembles. For each bootstrap ensemble the covariance matrix is recomputed using equation (1.79) and the chi-squared minimisation procedure is performed. The bootstrap ensembles yield a distribution of fitted parameters a_i . The quoted error corresponds to the 68% confidence limit of the bootstrap distribution.

1.9 Improvement

For the Lattice QCD action $S_{QCD} = S_G + S_{WF}$, as discussed above, the discretisation errors of the gluonic part of the action are $O(a^2)$, whereas those of the fermionic part of the action are $O(a)$, so the residual cut off effects are $O(a)$. To simulate at fixed physical volume the computation cost of generating gauge configurations in full QCD, ⁶, equation (1.64) rise as:

$$\text{cost} \propto \frac{1}{a^6}. \quad (1.83)$$

Therefore the computational overhead can be reduced if we work at a coarser lattice spacing, but at the cost of increasing the discretisation errors in the measurements of physical observables. The aim of the improvement program is to reduce the cutoff effects of the Lattice QCD action, make the action more continuum like. The benefits of such an exercise are enormous, especially for simulations in full QCD where the computational overhead is much greater than in quenched QCD. There are two types of improved actions.

- Fixed point actions; the aim is to find the “perfect action”, a trajectory in coupling constant space where there are no corrections at all. The method relies on the renormalisation group and blocking along a renormalised trajectory to a fixed point, see [23].
- An improvement scheme proposed by Symanzik [24, 25] uses the non-uniqueness of the lattice action (and composite fields) to remove cutoff effects systematically order by order through the addition of local higher-dimensional irrelevant counter-terms to the lattice action and the composite fields of interest. He has shown that the approach of Green’s functions to their continuum limit can be accelerated using an improved action and improved composite fields.

⁶Full QCD is that which corresponds to the continuum QCD, i.e. fermion loops are included.

In this thesis improved actions and improved composite fields constructed under the Symanzik program to remove the leading $O(a)$ cutoff effects shall be investigated. A considerable simplification is achieved if the improved continuum approach is only required for on-shell quantities such as particles masses and matrix elements of improved fields between physical states [26, 27, 28]. The structure of the counter-terms is governed by the symmetries,⁷ their coefficients have to be fixed by improvement conditions. Although they can be estimated in perturbation theory, a non-perturbative determination of the improvement coefficients through Monte Carlo simulations is clearly preferable.

1.9.1 Tree-level $O(a)$ improvement

Two-link Action

Hamber and Wu [29] suggested adding the following “two-link” term:

$$\begin{aligned} \Delta S^{II} = a^4 \sum_{x,\mu} \left\{ \frac{\kappa}{4a} \left[\bar{\psi}(x) U_\mu(x) U_\mu(x + \hat{\mu}) \psi(x + 2\hat{\mu}) \right. \right. \\ \left. \left. + \bar{\psi}(x + 2\hat{\mu}) U_\mu^\dagger(x + \hat{\mu}) U_\mu^\dagger(x) \right) \psi(x) \right\}, \end{aligned} \quad (1.84)$$

which cancels the $O(a)$ term in the Wilson action. The Two-Link action is

$$S_{QCD}^{II} = S_G + S_{WF} + \Delta S^{II}, \quad (1.85)$$

which differs from the continuum action by terms of $O(a^2)$ at tree-level. Heatlie *et al.* have argued [30] that correlation functions computed with the Two-Link action have no discretisation errors of $O(a)$ or $O((g^2)^n a \log^n a)$, to all orders in perturbation theory, since in the asymptotic scaling limit $g^2 \sim 1/\log a$. Unfortunately, the Two-link term is difficult to implement on a parallel machine because it requires next-to-nearest-neighbour communications.

⁷The counter-terms are invariant under gauge parity-and charge-conjugation transformations and discrete rotations.

Sheikholeslami-Wohlert Action

Sheikholeslami and Wohlert proposed the following nearest-neighbour action:

$$S_{QCD}^{SW} = S_G + S_{WF} + \Delta S^{SW}, \quad (1.86)$$

where ΔS^{SW} is a Pauli-interaction term:

$$\Delta S^{SW} = a^4 \sum_{x, \mu\nu} \left[-ig\kappa \frac{a}{2} \bar{\psi}(x) \sigma_{\mu\nu} \hat{F}_{\mu\nu} \psi(x) \right]. \quad (1.87)$$

$\hat{F}_{\mu\nu}$ is an appropriate lattice definition of the field strength tensor, $F_{\mu\nu}$, for example the one given by the average over the four plaquettes lying in the plane (μ, ν) and stemming from the point x [31], shown in figure 1.2 and is defined as

$$\hat{F}_{\mu\nu} = \frac{1}{4} \sum_{\square=1}^4 \frac{1}{2iga^2} \left[U_{\mu\nu}^{\square} + U_{\mu\nu}^{\square\dagger} \right]. \quad (1.88)$$

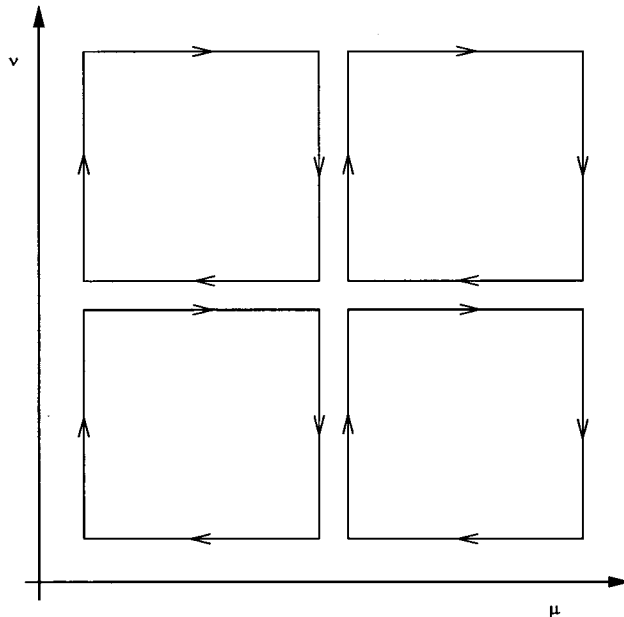


Figure 1.2: Graphical representation of the products of gauge field variables contributing to the lattice field strength tensor in equation (1.88).

The key observation made by [28, 30] is that the Sheikholeslami-Wohlert Action is related to the Two-Link action by the following rotation of the quark fields

$$\psi \rightarrow \psi' = \left[1 - \frac{a}{4} (\vec{\mathcal{D}} - m) \right] \psi + O(a^2), \quad (1.89)$$

$$\bar{\psi} \rightarrow \bar{\psi}' = \bar{\psi} \left[1 + \frac{a}{4} (\overleftarrow{\mathcal{D}} + m) \right] \psi + O(a^2), \quad (1.90)$$

where the forward and backward lattice derivatives are defined as

$$\vec{\mathcal{D}} \psi = \frac{1}{2} \left\{ U_\mu(x) \psi(x + \hat{\mu}) - U_\mu^\dagger(x - \hat{\mu}) \psi(x - \hat{\mu}) \right\}, \quad (1.91)$$

$$\overleftarrow{\mathcal{D}} \bar{\psi} = \frac{1}{2} \left\{ \bar{\psi}(x + \hat{\mu}) U_\mu^\dagger(x) - \bar{\psi}(x - \hat{\mu}) U_\mu(x - \hat{\mu}) \right\}. \quad (1.92)$$

These rotations simply constitute a change of variable in the functional integral; and thus results concerning the discretisation errors for the Two-Link action also hold for the SW action. The advantage of using the SW action it is nearest-neighbour and can be implemented efficiently on a parallel machine.

The improved QCD action, called the Sheikholeslami-Wohlert (SW) action is

$$S_{QCD}^{SW} = S_G + S_{WF} - \sum_{x, \mu\nu} C a^5 \frac{i\kappa}{2} \bar{\psi}(x) \sigma_{\mu\nu} \hat{F}_{\mu\nu} \psi(x). \quad (1.93)$$

The coefficient of the clover term, C is a function of the bare coupling, g , with tree-level value $C = 1$. An initial study of the effect of the clover term in the action, using the tree-level value, on hadronic observables and matrix elements was done in [32] and substantial improvement was found. The residual cut-off effects in the tree-level $O(a)$ -improved SW action are $O(g^2 a)$ in perturbation theory.

1.9.2 The Tadpole-Improved SW Action

One can use perturbative ideas to motivate non-perturbative improvement schemes. Perturbative expansions in terms of the bare coupling are useless for most quantities, because of large contributions from tadpole graphs. If these tadpole con-

tributions are treated non-perturbatively, e.g by writing $U_\mu = u_0[1 + iagaA_\mu + \dots]$ with $u_0 = (\frac{1}{3}(\text{Tr}U^\square))^{1/4}$ from the simulations, and the perturbative expressions are adjusted to remove the one-loop contribution from u_0 , then the perturbative estimates are more reliable [33]. The mean-field, or tadpole, prescription for the action is to replace

$$U_\mu(x) \rightarrow \frac{U_\mu(x)}{u_0}, \quad (1.94)$$

everywhere, and then to use perturbation theory (excluding the perturbative contributions from u_0) for the coefficients. Applying this prescription to the SW action in equation (1.93) we obtain the coefficients,

$$g^2 = \tilde{g}^2 u_0^4, \quad (1.95)$$

$$\kappa = \frac{\tilde{\kappa}}{u_0}, \quad (1.96)$$

$$C = \frac{\tilde{C}}{u_0^3}, \quad (1.97)$$

then $\tilde{\kappa}_c$ and \tilde{c} should be close to their perturbative values of 1/8 and 1, respectively. In other words,

$$C = \frac{1}{u_0^3}, \quad (1.98)$$

which is tadpole-improved value of the clover coefficient.

The $O(a)$ tree-level improvement of matrix elements for the tadpole improved action requires the rotation of the quark fields ψ and $\bar{\psi}$, as follows

$$\psi \rightarrow \psi' = \left[1 - \frac{a}{4u_0} (\vec{\not{D}} - m) \right] \psi + O(a^2), \quad (1.99)$$

$$\bar{\psi} \rightarrow \bar{\psi}' = \bar{\psi} \left[1 + \frac{a}{4u_0} (\overleftarrow{\not{D}} + m) \right] + O(a^2). \quad (1.100)$$

For an on-shell observable the equation of motion can be used to rewrite the rotated operators, which are bilinear in the quark fields as [30, 34]

$$O_\Gamma^{\text{imp}} = \left(1 + \frac{am}{u_0} (1 - z) \right) \bar{\psi}' (\Gamma + z \frac{a}{2u_0} (\overleftarrow{\not{D}} \Gamma - \Gamma \vec{\not{D}})) \psi, \quad (1.101)$$

with $z \in [0, 1]$. However, for $z \neq 1$ it is not clear what lattice quark mass am to use in equation (1.101). The authors of [35] show that the bare unrenormalised quark mass am_q is a reasonable choice in the case $z = 0$ equation (1.101) becomes

$$O_{\Gamma}^{\text{imp}} = \left(1 + \frac{am_q}{u_0}\right) \bar{\psi} \Gamma \psi, \quad (1.102)$$

the rotation of the operator is an additive renormalisation which vanishes in the chiral limit, and is required to improve matrix elements at non-zero quark mass.

1.9.3 Full $O(a)$ Improvement

In a number of publications [36, 37, 38, 39, 40] the ALPHA collaboration have calculated non-perturbatively the improvement coefficients for the $O(a)$ counter-terms to the action and composite fields to remove all leading cut off effects in the Wilson action, equation (1.55).

The Wilson fermions violate chiral symmetry which is more directly seen by studying the conservation of the isovector axial current A_{μ} . The current and the associated axial density on the lattice are defined through

$$A_{\mu}(x) = \bar{\psi}(x) \gamma_{\mu} \gamma_5 \psi(x), \quad (1.103)$$

$$P(x) = \bar{\psi}(x) \gamma_5 \psi(x). \quad (1.104)$$

The PCAC relation

$$\tilde{\partial}_{\mu} A_{\mu}(x) = 2\tilde{m}P(x) + O(a), \quad (1.105)$$

$$\tilde{\partial}_{\mu} = \frac{1}{2}(\partial_{\mu}^{*} + \partial_{\mu}), \quad (1.106)$$

then includes an error term of order a . Above, ∂_{μ} and ∂_{μ}^{*} denote forward and backward lattice derivatives and \tilde{m} is the unrenormalised current quark mass at scale $1/a$.

The isospin symmetry remains unbroken on the lattice and there exists an associated conserved vector current. However, it is often advantageous to use the

current which is strictly local,

$$V_\mu(x) = \bar{\psi}(x)\gamma_\mu\psi(x). \quad (1.107)$$

The conservation of this current is then also violated by cutoff effects, and a finite renormalisation is required to ensure that the associated charge takes half-integral values.

Symanzik's local effective theory

Near the continuum limit the lattice theory can be described in terms of a local effective theory [25],

$$S_{\text{eff}} = S_0 + aS_1 + a^2S_2 + \dots, \quad (1.108)$$

where S_0 is the action of the continuum theory, defined e.g. on a lattice with spacing $\varepsilon \ll a$. The terms S_k , $k = 1, 2, \dots$, are space-time integrals of Lagrangians $\mathcal{L}_k(x)$. These are given as general linear combinations of local gauge-invariant composite fields which respect the exact symmetries of the lattice theory and have canonical dimension $4 + k$. A possible basis of fields for the Lagrangian $\mathcal{L}_1(x)$ then reads

$$\begin{aligned} \mathcal{O}_1 &= \bar{\psi} \sigma_{\mu\nu} F_{\mu\nu} \psi, \\ \mathcal{O}_2 &= \bar{\psi} \vec{D}_\mu \vec{D}_\mu \psi + \bar{\psi} \overleftarrow{D}_\mu \overleftarrow{D}_\mu \psi, \\ \mathcal{O}_3 &= m \operatorname{tr} \{ F_{\mu\nu} F_{\mu\nu} \}, \\ \mathcal{O}_4 &= m \{ \bar{\psi} \gamma_\mu \vec{D}_\mu \psi - \bar{\psi} \overleftarrow{D}_\mu \gamma_\mu \psi \}, \\ \mathcal{O}_5 &= m^2 \bar{\psi} \psi, \end{aligned} \quad (1.109)$$

where $F_{\mu\nu}$ is the field tensor and $\sigma_{\mu\nu} = \frac{i}{2}[\gamma_\mu, \gamma_\nu]$.

When considering correlation functions of local gauge invariant fields the action is not the only source of cutoff effects. If $\phi(x)$ denotes such a lattice field, one expects the connected n -point function

$$G_n(x_1, \dots, x_n) = (Z_\phi)^n \langle \phi(x_1) \dots \phi(x_n) \rangle_{\text{con}}, \quad (1.110)$$

to have a well-defined continuum limit, provided the renormalisation constant Z_ϕ is correctly tuned and the space-time arguments x_1, \dots, x_n are kept at a physical distance from each other.

In the effective theory the renormalised lattice field $Z_\phi\phi(x)$ is represented by an effective field,

$$\phi_{eff}(x) = \phi_0(x) + a\phi_1(x) + a^2\phi_2(x) + \dots, \quad (1.111)$$

where the $\phi_k(x)$ are linear combinations of composite, local fields with the appropriate dimension and symmetries. For example, in the case of the axial current (1.103), ϕ_1 is given as a linear combination of the terms

$$\begin{aligned} (\mathcal{O}_6)_\mu &= \bar{\psi} \gamma_5 \frac{1}{2} \sigma_{\mu\nu} [\vec{D}_\nu - \overleftarrow{D}_\nu] \psi, \\ (\mathcal{O}_7)_\mu &= \bar{\psi} \frac{1}{2} \gamma_5 [\vec{D}_\mu + \overleftarrow{D}_\mu] \psi, \\ (\mathcal{O}_8)_\mu &= m \bar{\psi} \gamma_\mu \gamma_5 \frac{1}{2} \psi. \end{aligned} \quad (1.112)$$

The convergence of $G_n(x_1, \dots, x_n)$ to its continuum limit can now be studied in the effective theory,

$$\begin{aligned} G_n(x_1, \dots, x_n) &= \langle \phi_0(x_1) \dots \phi_0(x_n) \rangle_{\text{con}} - a \int d^4y \langle \phi_0(x_1) \dots \phi_0(x_n) \mathcal{L}_1(y) \rangle_{\text{con}} \\ &\quad + a \sum_{k=1}^n \langle \phi_0(x_1) \dots \phi_1(x_k) \dots \phi_0(x_n) \rangle_{\text{con}} + \mathcal{O}(a^2), \end{aligned} \quad (1.113)$$

where the expectation values on the right-hand side are to be taken in the continuum theory with action S_0 . Contact terms arise if any of the points x_k and y coincide. Generally we need only consider correlation functions at non-zero physical distances and any contact terms coming from the integration over y can be absorbed in a redefinition of ϕ_1 .

Using the field equations

It is then possible to make use of the classical field equations to reduce first the

number of basis fields in the effective Lagrangian \mathcal{L}_1 and, in a second step, also in the $\mathcal{O}(a)$ counter-term ϕ_1 of the effective composite fields.

We may eliminate two of the terms in equation (1.109). A possible choice is to retain the terms \mathcal{O}_1 , \mathcal{O}_3 and \mathcal{O}_5 , which yields the effective continuum action for on-shell quantities to order a . Having made this choice one may apply the field equations once again to simplify the term ϕ_1 in the effective field as well. In the example of the axial current it is then possible to eliminate the term \mathcal{O}_6 in equation (1.112).

Improved lattice action and fields

The on-shell $\mathcal{O}(a)$ improved lattice action is obtained by adding a counter-term to the unimproved lattice action such that the action S_1 in the effective theory is cancelled in on-shell amplitudes. This can be achieved by adding lattice representations of the terms \mathcal{O}_1 , \mathcal{O}_3 and \mathcal{O}_5 to the unimproved lattice Lagrangian, with coefficients that are functions of the bare coupling g only. Here note that the fields \mathcal{O}_3 and \mathcal{O}_5 already appear in the unimproved theory and thus merely lead to a re-parameterisation of the bare parameters g and m . In the following, we will not consider these terms any further. Their relevance in connection with massless renormalisation schemes is discussed in detail in [37].

Here again we arrive at the Sheikholeslami and Wohlert improved action

$$S_{QCD}^{SW} = S_G + S_{WF} - \sum_{x,\mu\nu} C a^5 \frac{i\kappa}{2} \bar{\psi}(x) \sigma_{\mu\nu} \hat{F}_{\mu\nu} \psi(x). \quad (1.114)$$

With a properly chosen coefficient $C(g)$, this yields the on-shell $\mathcal{O}(a)$ improved lattice action. The perturbative expansion of C reads $C = 1 + C^{(1)}g^2 + \mathcal{O}(g^4)$, with [41] $C^{(1)} = 0.26590(7)$.

The $\mathcal{O}(a)$ improved isospin currents and the axial density can be parametrised⁸

⁸The origin of the 2κ comes from the rescaling of the quark fields

as follows,

$$\begin{aligned} A_\mu^{\text{R}} &= Z_{\text{A}} 2\kappa(1 + b_{\text{A}} am_{\text{q}}) \{A_\mu + ac_{\text{A}} \tilde{\partial}_\mu P\}, \\ V_\mu^{\text{R}} &= Z_{\text{V}} 2\kappa(1 + b_{\text{V}} am_{\text{q}}) \{V_\mu + ac_{\text{V}} \tilde{\partial}_\nu T_{\mu\nu}\}, \\ P^{\text{R}} &= Z_{\text{P}} 2\kappa(1 + b_{\text{P}} am_{\text{q}}) P, \end{aligned} \tag{1.115}$$

where

$$T_{\mu\nu} = i\bar{\psi}\sigma_{\mu\nu}\psi.$$

The normalisation constants $Z_{\text{A},\text{V},\text{P}}$, have to be fixed by appropriate normalisation conditions [42]. Again, the improvement coefficients $b_{\text{A},\text{V},\text{P}}$ and $c_{\text{A},\text{V}}$ are functions of g only. At tree level of perturbation theory, they are given by $b_{\text{A}} = b_{\text{P}} = b_{\text{V}} = 1$ and $c_{\text{A}} = c_{\text{V}} = 0$ [30, 41]. Lüscher, Sint and Weisz have calculated these coefficients to one-loop [41, 43].

Non-perturbative determination of the Improvement Coefficients

The ALPHA collaboration have determined C and c_{A} non-perturbatively [38] by requiring the PCAC relation, equation (1.106), holds irrespective of the states between which it is sandwiched, i.e.,

$$\tilde{\partial}_\mu \langle (A^{\text{R}})_\mu(x_0) \mathcal{O} \rangle = 2\tilde{m}_{\text{R}} \langle (P^{\text{R}})_\mu(x_0) \mathcal{O} \rangle + O(a^2), \tag{1.116}$$

for any product \mathcal{O} of renormalised improved fields, separated from x_0 . The calculational tool employed is the Schrödinger functional [44, 45, 46, 47, 48], where field configurations taking specified values at $x_0 = 0, T$ are considered. The advantages of the Schrödinger functional are as follows.

- For finite lattice size L there are corrections of order a/L , so simulating at large β with fixed L is safe allowing contact to be made with lattice perturbation theory.
- The Schrödinger functional contains a number of “kinematic” variables, including L and T , which should not affect final physical answers: varying

these provides a systematic error check.

- It also has a built in infra red cutoff, allowing zero mass quarks to be simulated.

The renormalised quark mass \tilde{m}_R appearing in equation (1.116) is then given by

$$\tilde{m}_R = \tilde{m} \frac{Z_A(1 + b_A am_q)}{Z_P(1 + b_P am_q)} + O(a^2). \quad (1.117)$$

⁹ At fixed bare parameters, \tilde{m}_R , and hence also the unrenormalised mass \tilde{m} should be independent of the kinematical parameters such as T, L and x_0 . This will be true up to corrections of order a^2 , provided C and c_A have been assigned their proper values.

In the range $0 \leq g^2 \leq 1$, the non-perturbative results for C are well represented by, [38]

$$C = \frac{1 - 0.656 g^2 - 0.152 g^4 - 0.054 g^6}{1 - 0.922 g^2}. \quad (1.118)$$

and

$$c_A = -0.00756 \times g^2 \frac{1 - 0.748 g^2}{1 - 0.977 g^2}. \quad (1.119)$$

⁹To calculate a non-perturbative value for the renormalised quark mass; the renormalisation constants and improvement coefficients need to be determined through a non-perturbative calculation.

Chapter 2

Correlation Functions and Smearing

2.1 Correlation Functions

2.1.1 Interpolating Operators

Correlation functions are constructed from time-ordered products of field operators, chosen such as to possess the desired quantum numbers of the particle of interest. The necessary requirement for these interpolating field operators is that

$$\langle 0|\Phi(0)|H,\vec{p}\rangle \neq 0, \quad (2.1)$$

i.e. $\langle 0|\Phi(0)$ has a non-zero overlap with $|H(\vec{p})\rangle$, or

$$\Phi(0)|H(\vec{p})\rangle = a(0)|0\rangle + a(1)|1\rangle + \dots, \quad (2.2)$$

where $a(0) \neq 0$. The arbitrariness in the field operator Φ can be exploited practically to maximise the overlap with the desired state and minimise this with respect to radial excitations, and is the subject of the next section.

For mesons this suggests that Φ is a colour singlet with the same spin, parity and valence quark content as the particle of interest. The most general form for a meson interpolating field is

$$\Phi_M = \int dydz \bar{\psi}_{1,\alpha}^a(y) \chi^{ab}(x:y,z) \Gamma_{\alpha\beta} \psi_{2,\beta}^b(z), \quad (2.3)$$

where ψ_1 and ψ_2 can be different flavour valence quarks with colour indices a and b , and Γ is one of the 16 Dirac matrices which has the correct spin and parity

properties. The simplest form of the interpolating field Φ_M is of a point operator where χ is given by

$$\chi^{ab}(x : y, z) = \delta(x, y)\delta(x, z)\delta^{ab}, \quad (2.4)$$

and inserting gauge fields to maintain gauge invariance is unnecessary.

Two-point meson correlators

A two-point correlation function describing the propagation of a meson, from a fixed origin, is defined as

$$G_M(x, 0) = \langle 0 | \hat{\mathcal{T}}[\Phi_M(x)\Phi_M^\dagger(0)] | 0 \rangle, \quad (2.5)$$

with a time ordering operator $\hat{\mathcal{T}}$. The operator at the source Φ_M^\dagger creates the meson, and the operator Φ_M annihilates the meson at the sink.

Pseudoscalar Two-point Functions

Taking $\Gamma = \gamma_5$ in equation (2.3) to ensure the operator transforms with parity -1, gives the following pseudoscalar operators

$$\hat{P}(x) = \bar{\psi}_u(x)\gamma_5\psi_d(x) \quad (2.6)$$

$$\hat{P}^\dagger = -\bar{\psi}_d(x)\gamma_5\psi_u(x). \quad (2.7)$$

Substituting these operators into equation (2.5) one obtains the pseudoscalar propagator

$$G_{PP}(x, 0) = \langle 0 | \hat{\mathcal{T}}[\hat{P}(x)\hat{P}^\dagger(0)] | 0 \rangle. \quad (2.8)$$

We can Wick decompose the pseudoscalar propagator in terms of quark and anti-quark propagators

$$\begin{aligned} G_{PP}(x, 0) &= -\langle 0 | \hat{\mathcal{T}}[\bar{\psi}_{u,i}^\alpha(x)\gamma_{\alpha\beta}^5\psi_{d,i}^\beta(x)\bar{\psi}_{d,j}^\gamma(0)\gamma_{\gamma\delta}^5\psi_{u,j}^\delta(0)] | 0 \rangle \\ &= -\frac{1}{Z} \int \mathcal{D}U \mathcal{D}\bar{\psi} \mathcal{D}\psi \bar{\psi}_{u,i}^\alpha(x)\psi_{u,j}^\delta(0)\psi_{d,i}^\beta(x)\bar{\psi}_{d,j}^\gamma(0)\gamma_{\alpha\beta}^5\gamma_{\gamma\delta}^5 e^{-S(U, \bar{\psi}, \psi)} \\ &= \frac{1}{Z} \int \mathcal{D}U G(u; 0, x; U)\gamma^5 G(d; x, 0; U)\gamma^5 e^{-S(U)} \\ &= \text{Tr}(G(x, 0)\gamma^5 G(0, x)\gamma^5) \end{aligned}$$

$$= \text{Tr}(G(x, 0)G^\dagger(x, 0)). \quad (2.9)$$

To condense the notation here we have defined the quark propagator $G(x, y)$ as

$$\begin{aligned} \langle 0 | \mathcal{T} \psi(x) \bar{\psi}(y) | 0 \rangle &= \frac{1}{Z} \int \mathcal{D}U \mathcal{D}\bar{\psi} \mathcal{D}\psi \psi(x) \bar{\psi}(y) e^{-S(U, \bar{\psi}, \psi)} \\ &= \frac{1}{Z} \int \mathcal{D}U G(x, y; U) e^{-S(U)}, \end{aligned} \quad (2.10)$$

where $G(x, y; U)$ is the quark propagator in a given configuration U . In equation (2.9) we have used the hermiticity property of the lattice quark propagator

$$G_{\alpha\beta}^\dagger(x, 0) = \gamma_{\alpha\gamma}^5 G_{\gamma\delta}(0, x) \gamma_{\delta\beta}^5, \quad (2.11)$$

and Tr is the trace over spin and colour indices. We assume exact isospin symmetry in the u and d quarks, therefore after the flavour contractions have been performed, at the quark propagator level, the flavour index can be dropped here, in this case. The problem of calculating meson propagators becomes one of calculating simple quark propagators, tracing the appropriate spin and colour components, and summing over the gauge field U .

2.1.2 Meson Two-Point Functions

On the lattice a generic meson operator is bilinear in the quark fields,

$$\mathcal{O}_1(x) = \bar{\psi}(x) \Gamma_1 \psi(x), \quad (2.12)$$

where Γ_1 is one of the 16 independent Dirac matrices. The Dirac structure of the Γ matrices does not need to be the same at the source and sink, but must have the same J^{PC} quantum numbers, so we take the meson operator at the sink to be

$$\begin{aligned} \mathcal{O}_2^\dagger(x) &= (\bar{\psi}(x) \Gamma_2 \psi(x))^\dagger \\ &= \psi^\dagger(x) \Gamma_2^\dagger \gamma_4^\dagger \psi(x) \\ &= \bar{\psi}(x) \gamma_4 \Gamma_2^\dagger \gamma_4 \psi(x). \end{aligned} \quad (2.13)$$

Thus for a general meson two-point function we can express this in terms of quark propagators following the Wick decomposition in equation (2.9)

$$\begin{aligned}
G_{\mathcal{O}_1\mathcal{O}_2}(x,0) &= \langle 0|\widehat{\mathcal{T}}[\mathcal{O}_1(x)\mathcal{O}_2^\dagger(0)]|0\rangle \\
&= \langle 0|\overline{\psi}_\alpha(x)\Gamma_{1\alpha\beta}\psi_\beta(x)\overline{\psi}_\gamma(0)(\gamma_4\Gamma_2^\dagger\gamma_4)_{\gamma\delta}\psi_\delta|0\rangle \\
&= -G_{\alpha\delta}(0,x)\Gamma_{1\alpha\beta}G_{\beta\delta}(x,0)(\gamma_4\Gamma_2^\dagger\gamma_4)_{\gamma\delta} \\
&= -Tr(G(x,0)(\gamma_4\Gamma_2^\dagger\gamma_4)\gamma_5G^\dagger(x,0)\gamma_5\Gamma_1). \tag{2.14}
\end{aligned}$$

In table 2.1 we list all the meson operators which are used in this thesis.

Channel	J^{PC}	Operator	Lightest state (MeV)
P	0^{-+}	$\overline{\psi}\gamma_5\psi$	π (140)
V	1^{--}	$\overline{\psi}\gamma_i\psi$	ρ (770)
A ₄	0^{-+}	$\overline{\psi}\gamma_4\gamma_5\psi$	π (140)
A	1^{++}	$\overline{\psi}\gamma_i\gamma_5\psi$	b_1 (1235)
S	0^{++}	$\overline{\psi}\psi$	a_0 (980), f_0 (980)
T	1^{+-}	$\overline{\psi}\sigma_{i4}\psi$	a_1 (1260)
	1^{--}	$\overline{\psi}\sigma_{ij}\psi$	ρ (770)

Table 2.1: Summary of the meson operators and their relationship to the lightest particle states.

2.1.3 Meson Masses

Let us consider for example the meson two-point function given in equation (2.5). “Timeslicing” the two-point function to project out momentum¹ \vec{p} by a Fourier transform, one obtains

$$\begin{aligned}
C_M(\vec{p},t) &= \sum_{\vec{x}} G_M(x,0)e^{-i\vec{p}\cdot\vec{x}} \\
&= \sum_{\vec{x}} \langle 0|\Phi_M(x)\Phi_M^\dagger(0)|0\rangle e^{-i\vec{p}\cdot\vec{x}}, \tag{2.15}
\end{aligned}$$

¹Periodic spatial boundary conditions quantise the allowed values of the lattice momentum as $\vec{p} = \frac{2\pi}{N_s}(p_1, p_2, p_3)$ where p_1, p_2 and p_3 are integers and $0 \leq p_i < L$.

inserting a complete set of states gives

$$C_M(\vec{p}, t) = \frac{1}{L^3} \sum_{\vec{x}} \sum_n \sum_{\vec{q}} \frac{e^{-i\vec{p}\cdot\vec{x}}}{2E_n(\vec{p})} \langle 0 | \Phi_M(x) | n, \vec{q} \rangle \langle n, \vec{q} | \Phi_M^\dagger(0) | 0 \rangle, \quad (2.16)$$

with the lattice completeness relation defined as follows,

$$I = \frac{1}{L^3} \sum_n \sum_{\vec{q}} \frac{1}{2E_n(\vec{q})} |n, \vec{q}\rangle \langle n, \vec{q}|, \quad (2.17)$$

where the sum n is over all states.

Using the translational operator invariance in Euclidean space,

$$\mathcal{O}(\vec{x}, t) = e^{\widehat{H}t + i\widehat{p}\cdot\vec{x}} \mathcal{O}(0) e^{-\widehat{H}t - i\widehat{p}\cdot\vec{x}}, \quad (2.18)$$

where \widehat{H} and \widehat{p} are the lattice Hamiltonian and the three momentum operator respectively, together with the lattice relation

$$\sum_{\vec{x}} e^{\frac{2\pi i}{L} \vec{x}(\vec{k} - \vec{k}')} = L^3 \delta(\vec{k} - \vec{k}'), \quad (2.19)$$

yields

$$\begin{aligned} C_M(p, t) &= \sum_n \frac{e^{-E_n(\vec{p})t}}{2E_n(\vec{p})} |\langle 0 | \Phi_M(0) | n, \vec{p} \rangle|^2 \\ &= \sum_n \frac{A_n e^{-E_n(\vec{p})t}}{2E_n(\vec{p})}, \end{aligned} \quad (2.20)$$

$E_n(\vec{p})$ is the energy of the meson state $|n, \vec{p}\rangle$ with momentum \vec{p} . The lowest energy state in the large t limit dominates the sum. For the case of zero three-momentum then $E_n(\vec{0}) = m_n$, we arrive at the key formula for hadron spectroscopy on the lattice

$$\lim_{t \rightarrow \infty} C_M(\vec{0}, t) = \frac{A_1}{2m_1} e^{-m_1 t}, \quad (2.21)$$

the subscript 1 denotes the lightest meson state with the quantum numbers of the operator Φ_M . Thus we have shown that, in the Euclidean space of the lattice,

a correlation function decays exponentially with time with an exponent equal to the energy of the hadronic state in question.

When analysing the timesliced correlator $C_M(t)$ a useful tool in finding the point in time at which all the higher-mass states have decayed away is the effective mass function:

$$m_{eff}(t) = \ln \left(\frac{C_M(t)}{C_M(t+1)} \right). \quad (2.22)$$

As $t \rightarrow \infty$ this function levels out into a plateau at m_1 , enabling one to identify the ground state.

2.1.4 Fitting Meson Two-Point Functions

From its creation point a meson can propagate both forwards and backwards in time. For a meson which is created at $t = 0$, its maximum propagation time is only $T/2$, where T is the temporal size of the lattice, due to the imposition of antiperiodic boundary conditions in time. For an infinite number of gauge configurations the meson correlator is exactly mirrored about the mid-point of the lattice. Prior to fitting, the configuration data is ‘folded’ by averaging² the corresponding timeslices from the two halves of the lattice.

We fit a zero three-momentum meson two-point function to the form

$$\begin{aligned} C_{\mathcal{O}_1\mathcal{O}_2}(t) &= \sum_{\vec{x}} \langle 0 | \mathcal{T} \mathcal{O}_{\Gamma_1}(\vec{x}, t) \mathcal{O}_{\Gamma_2}^\dagger(0) | 0 \rangle \\ &= \sum_n \frac{1}{2m_n} \left[\langle 0 | \mathcal{O}_{\Gamma_1}(0) | n \rangle \langle n | \mathcal{O}_{\Gamma_2}^\dagger(0) | 0 \rangle e^{-m_n t} \right. \\ &\quad \left. + \langle 0 | \mathcal{O}'_{\Gamma_2}(0) | n \rangle \langle n | \mathcal{O}'_{\Gamma_1}^\dagger(0) | 0 \rangle e^{-m_n(T-t)} \right] \\ &= \lim_{T, t \rightarrow \infty} A_{\mathcal{O}_1\mathcal{O}_2} \left[e^{-m_1 t} + \eta_1 \eta_2 e^{-m_1(T-t)} \right], \end{aligned} \quad (2.23)$$

where $\mathcal{O}' = \eta \mathcal{O}$ with $\eta = \pm 1$ being given by $\hat{T} \Gamma \hat{T}^{-1} = \eta \Gamma$, where $\hat{T} = \gamma_4 \gamma_5$ is the time reversal operator. The η factor tells us how \mathcal{O} behaves under time reversal i.e. whether the two-point function is symmetric or anti-symmetric with respect

²This depends on the time reversal symmetries of the operators of the meson.

to $t \rightarrow T - t$. For example we fit the pion correlator to

$$C_{PP}(t) = A_{PP} [e^{-m_1 t} + e^{-m_1(T-t)}], \quad (2.24)$$

which we can write as

$$C_{PP}(t) = 2A_{PP} e^{-Tm_1/2} \cosh \left[m_1 \left(\frac{T}{2} - t \right) \right]. \quad (2.25)$$

2.1.5 Baryons

We begin with the flavour octet which is the more difficult case since it has mixed symmetry. Assume we have three flavours of quarks labelled by u, d and s. To create spin- $\frac{1}{2}$ baryons we can use the interpolating operators

$$\mathcal{O}_{(ij)k,\epsilon}(x) = (\psi_{i,\alpha}^a(x) (C\gamma_5)^{\alpha\beta} \psi_{j,\beta}^b(x)) \psi_{k,\epsilon}^c(x) \epsilon_{abc}, \quad (2.26)$$

where a, b, c label colours, i, j, k label flavours and α, β, ϵ are Dirac indices. C is the charge conjugation matrix. We shall suppress the Dirac indices. $\mathcal{O}_{(ij)k}$ is antisymmetric under the interchange $i \leftrightarrow j$, and creates octet and singlet states. To project against the singlet state we form

$$B_{ijk} = \mathcal{O}_{(ij)k} + \mathcal{O}_{(ik)j}, \quad (2.27)$$

i.e. allows the first two quark indices to be combined into an anti-quark index

$$\mathcal{B}_{ijk}^q \propto \epsilon_{ijk'} B_k^{k'}, \quad (2.28)$$

following the formalism used in [49, 50]. The overall normalisation is arbitrary, while the relative normalisation is fixed by $SU(3)$ symmetry, and we use

$$\mathcal{B}_{ijk} = \frac{1}{\sqrt{6}} (\epsilon_{ijk'} B_k^{k'} + \epsilon_{ikk'} B_j^{k'}). \quad (2.29)$$

The octet baryons are related to the B field as follows

$$\begin{aligned}
p &= b_{12}, & n &= b_{21}, \\
\Sigma^+ &= b_{13}, & \Sigma^0 &= b_{(+)}, & \Sigma^- &= b_{13}, \\
\Xi^0 &= b_{31}, & \Xi^- &= b_{32}, \\
\Lambda^0 &= b_{(-)}.
\end{aligned} \tag{2.30}$$

and we have used the symmetry relations to define

$$b_{ij} \equiv \sqrt{6}\mathcal{B}_{ijj} = \sqrt{6}\mathcal{B}_{iji} = -\sqrt{\frac{3}{2}}\mathcal{B}_{jii} \quad (i \neq j), \tag{2.31}$$

$$b_{(+)} \equiv \sqrt{3}(\mathcal{B}_{123} + \mathcal{B}_{231}) = -\sqrt{3}\mathcal{B}_{312} = \sqrt{3}(\mathcal{B}_{132} + \mathcal{B}_{213}) = -\sqrt{3}\mathcal{B}_{321}, \tag{2.32}$$

$$b_{(-)} \equiv (\mathcal{B}_{123} - \mathcal{B}_{231}) = (\mathcal{B}_{132} - \mathcal{B}_{213}). \tag{2.33}$$

We consider two types of correlators ‘ Σ like’ and ‘ Λ like’, the first can be exemplified by the Σ^0 state which is $S\{UD\} = S\{DU\}$, where this notation means that the wave function of this state is symmetric in flavours up and down. We have now switched from labelling the flavour indices of quarks from 1,2,3 to explicitly giving each quark a flavour u,d,s which reduces the number of indices, but we need to re-introduce the Dirac indices which were suppressed earlier. Following the definitions in equations (2.29) through to (2.32) we obtain

$$\begin{aligned}
G_{\Sigma^0}(x, 0) &= \langle 0 | \Sigma_\epsilon^0(x) \overline{\Sigma_\xi^0(0)} | 0 \rangle \\
&= \langle 0 | B_{sud,\epsilon}(x) \overline{B_{sud,\xi}(0)} | 0 \rangle \\
&= \langle 0 | (\mathcal{O}_{(su)d,\epsilon}(x) + \mathcal{O}_{(sd)u,\epsilon}(x)) (\overline{\mathcal{O}_{(su)d,\xi}(0)} + \overline{\mathcal{O}_{(sd)u,\xi}(0)}) | 0 \rangle \\
&= \langle 0 | \mathcal{O}_{(su)d,\epsilon}(x) \overline{\mathcal{O}_{(su)d,\xi}(0)} | 0 \rangle + \langle 0 | \mathcal{O}_{(su)d,\epsilon}(x) \overline{\mathcal{O}_{(sd)u,\xi}(0)} | 0 \rangle \\
&\quad + \langle 0 | \mathcal{O}_{(sd)u,\epsilon}(x) \overline{\mathcal{O}_{(su)d,\xi}(0)} | 0 \rangle + \langle 0 | \mathcal{O}_{(sd)u,\epsilon}(x) \overline{\mathcal{O}_{(sd)u,\xi}(0)} | 0 \rangle \\
&= \langle 0 | \epsilon_{ijk} \epsilon_{lmn} (s_\alpha^i(x) (C\gamma_5)^{\alpha\beta} u_\beta^j(x)) d_\epsilon^k(x) [\overline{(s_\gamma^l(0) (C\gamma_5)^{\gamma\delta} d_\delta^m(0)) u_\xi^n(0)}] | 0 \rangle \\
&\quad + \langle 0 | \epsilon_{ijk} \epsilon_{lmn} (s_\alpha^i(x) (C\gamma_5)^{\alpha\beta} u_\beta^j(x)) d_\epsilon^k(x) [\overline{(s_\gamma^l(0) (C\gamma_5)^{\gamma\delta} u_\delta^m(0)) d_\xi^n(0)}] | 0 \rangle \\
&\quad + \langle 0 | \epsilon_{ijk} \epsilon_{lmn} (s_\alpha^i(x) (C\gamma_5)^{\alpha\beta} d_\beta^j(x)) u_\epsilon^k(x) [\overline{(s_\gamma^l(0) (C\gamma_5)^{\gamma\delta} d_\delta^m(0)) u_\xi^n(0)}] | 0 \rangle
\end{aligned}$$

$$\begin{aligned}
& + \langle 0 | \epsilon_{ijk} \epsilon_{lmn} (s_\alpha^i(x) (C\gamma_5)^{\alpha\beta} d_\beta^j(x)) u_\epsilon^k(x) [\overline{(s_\gamma^l(0) (C\gamma_5)^{\gamma\delta} u_\delta^m(0)) d_\xi^n(0)}] | 0 \rangle \\
= & \langle 0 | -\epsilon_{ijk} \epsilon_{lmn} s_\alpha^i(x) (C\gamma_5)^{\alpha\beta} u_\beta^j(x) d_\epsilon^k(x) \overline{u_\xi^l(0) d_\delta^m(0)} (\overline{C\gamma_5})^{\gamma\delta} \overline{s_\gamma^n(0)} | 0 \rangle \\
& \langle 0 | -\epsilon_{ijk} \epsilon_{lmn} s_\alpha^i(x) (C\gamma_5)^{\alpha\beta} u_\beta^j(x) d_\epsilon^k(x) \overline{d_\xi^l(0) u_\delta^m(0)} (\overline{C\gamma_5})^{\gamma\delta} \overline{s_\gamma^n(0)} | 0 \rangle \\
& \langle 0 | -\epsilon_{ijk} \epsilon_{lmn} s_\alpha^i(x) (C\gamma_5)^{\alpha\beta} d_\beta^j(x) u_\epsilon^k(x) \overline{u_\xi^l(0) d_\delta^m(0)} (\overline{C\gamma_5})^{\gamma\delta} \overline{s_\gamma^n(0)} | 0 \rangle \\
& \langle 0 | -\epsilon_{ijk} \epsilon_{lmn} s_\alpha^i(x) (C\gamma_5)^{\alpha\beta} d_\beta^j(x) u_\epsilon^k(x) \overline{d_\xi^l(0) u_\delta^m(0)} (\overline{C\gamma_5})^{\gamma\delta} \overline{s_\gamma^n(0)} | 0 \rangle \\
= & \epsilon_{ijk} \epsilon_{lmn} (C\gamma_5)^{\alpha\beta} (\overline{C\gamma_5})^{\gamma\delta} \times \\
& \{ -\langle 0 | s_\alpha^i(x) \overline{s_\gamma^n(0)} u_\beta^j(x) \overline{u_\delta^m(0)} d_\epsilon^k(x) \overline{d_\xi^l(0)} | 0 \rangle \\
& + \langle 0 | s_\alpha^i(x) \overline{s_\gamma^n(0)} u_\beta^j(x) \overline{u_\xi^l(0)} d_\epsilon^k(x) \overline{d_\delta^m(0)} | 0 \rangle \\
& + \langle 0 | s_\alpha^i(x) \overline{s_\gamma^n(0)} d_\beta^j(x) \overline{d_\delta^m(0)} u_\epsilon^k(x) \overline{u_\xi^l(0)} | 0 \rangle \\
& - \langle 0 | s_\alpha^i(x) \overline{s_\gamma^n(0)} d_\beta^j(x) \overline{d_\xi^l(0)} u_\epsilon^k(x) \overline{u_\delta^m(0)} \} | 0 \rangle \\
= & \epsilon_{ijk} \epsilon_{lmn} (C\gamma_5)^{\alpha\beta} (\overline{C\gamma_5})^{\gamma\delta} \times \\
& \{ -G_{\alpha\gamma}^{in}(s, x, 0) G_{\beta\delta}^{jm}(u, x, 0) G_{\epsilon\xi}^{kl}(d, x, 0) \\
& + G_{\alpha\gamma}^{il}(s, x, 0) G_{\beta\xi}^{jm}(u, x, 0) G_{\epsilon\delta}^{kn}(d, x, 0) \\
& + G_{\alpha\gamma}^{in}(s, x, 0) G_{\beta\delta}^{jm}(d, x, 0) G_{\epsilon\xi}^{kl}(u, x, 0) \\
& - G_{\alpha\gamma}^{il}(s, x, 0) G_{\beta\xi}^{jm}(d, x, 0) G_{\epsilon\delta}^{kn}(u, x, 0) \} \\
= & \langle us \rangle d + \langle usd \rangle + \langle dsu \rangle + \langle ds \rangle u. \tag{2.34}
\end{aligned}$$

The bar over a quantity, $\overline{\Sigma^0}$, is the usual Dirac notation for $\Sigma^{0\dagger} \gamma_4$, following the rules in Minkowski space

$$\overline{\mathcal{O}_{(su)d,\xi}(0)} = -\epsilon_{lmn} \overline{u_\xi^l(0) d_\delta^m(0)} \overline{C\gamma_5} \overline{s_\gamma^n(0)}, \tag{2.35}$$

where $\overline{C\gamma_5} = (C\gamma_5)^\dagger \gamma_4$. The correlation function $G_{\Sigma^0}(x, 0)$ can be express in terms of two basic types of contractions. The first type $\langle ud \rangle s = \langle du \rangle s$ using the notation in [51], corresponds to quarks of flavours u and d contracted into a closed loop, while the propagator for s carries the spin quantum numbers of the baryon. The notation $\langle dus \rangle$ corresponds to an ordered contraction of three quarks. On calculating the correlation function for this state, the other ‘ Σ like’ states, the proton, neutron, Σ^+ , Σ^- , Ξ^0 and Ξ^- , can now be obtained easily by replacing the s, u and d quarks in the Σ^0 with the required quark flavours.

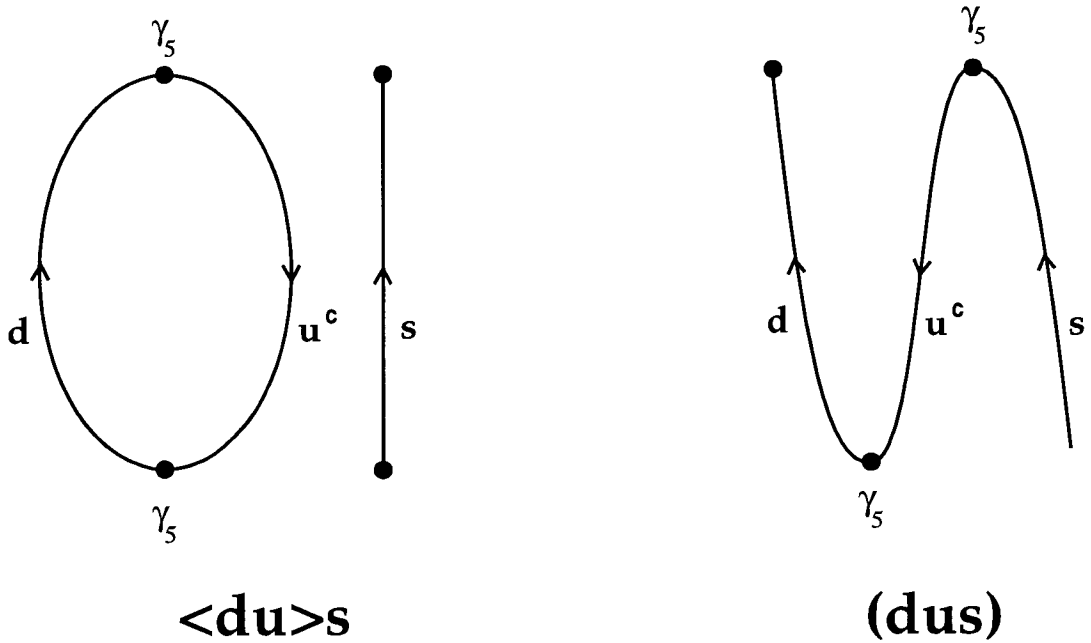


Figure 2.1: The two different types of contractions for the baryon states.

The Λ^0 state which is $S[DU] = S[UD]$, where the notation means that the wave function of this state is anti-symmetric in up and down flavours of quark. This state corresponds to the ‘ Λ like’ correlator which is the second type of correlator,

$$\begin{aligned}
 G_{\Lambda^0}(x, 0) &= \langle 0 | \Lambda_\epsilon^0(x) \overline{\Lambda}_\xi^0(0) | 0 \rangle \\
 &= \frac{1}{3} \langle 0 | (B_{uds,\epsilon}(x) - B_{dsu,\epsilon}(x)) (\overline{B}_{uds,\xi}(0) - \overline{B}_{dsu,\xi}(0)) | 0 \rangle \\
 &= \frac{1}{3} \{ \langle 0 | (B_{uds,\epsilon}(x) \overline{B}_{uds,\xi}(0)) | 0 \rangle - \langle 0 | (B_{uds,\epsilon}(x) \overline{B}_{dsu,\xi}(0)) | 0 \rangle \\
 &\quad - \langle 0 | (B_{dsu,\epsilon}(x) \overline{B}_{uds,\xi}(0)) | 0 \rangle + \langle 0 | (B_{dsu,\epsilon}(x) \overline{B}_{dsu,\xi}(0)) | 0 \rangle \}.
 \end{aligned}
 \tag{2.36}$$

Each of these terms will be looked at individually and the correlation function $G_{\Lambda^0}(x, 0)$ will be constructed at the end. Once again we shall suppress the Dirac

indices. The first term in equation (2.36) is

$$\begin{aligned}
\langle 0|B_{uds}(x)\overline{B_{uds}(0)}|0\rangle &= \langle 0|(\mathcal{O}_{(ud)s}(x) + \mathcal{O}_{(us)d}(x))(\overline{\mathcal{O}_{(ud)s}(0)} + \overline{\mathcal{O}_{(us)d}(0)})|0\rangle \\
&= \langle 0|\mathcal{O}_{(ud)s}(x)\overline{\mathcal{O}_{(ud)s}(0)}|0\rangle + \langle 0|\mathcal{O}_{(ud)s}(x)\overline{\mathcal{O}_{(us)d}(0)}|0\rangle \\
&\quad + \langle 0|\mathcal{O}_{(us)d}(x)\overline{\mathcal{O}_{(ud)s}(0)}|0\rangle + \langle 0|\mathcal{O}_{(us)d}(x)\overline{\mathcal{O}_{(us)d}(0)}|0\rangle \\
&= \langle ud\rangle_s + \langle dus\rangle + \langle sud\rangle + \langle us\rangle_d. \tag{2.37}
\end{aligned}$$

The second term in equation (2.36) is

$$\begin{aligned}
\langle 0|B_{uds}(x)\overline{B_{dsu}(0)}|0\rangle &= \langle 0|(\mathcal{O}_{(ud)s}(x) + \mathcal{O}_{(us)d}(x))(\overline{\mathcal{O}_{(ds)u}(0)} + \overline{\mathcal{O}_{(du)s}(0)})|0\rangle \\
&= \langle 0|\mathcal{O}_{(ud)s}(x)\overline{\mathcal{O}_{(ds)u}(0)}|0\rangle + \langle 0|\mathcal{O}_{(ud)s}(x)\overline{\mathcal{O}_{(du)s}(0)}|0\rangle \\
&\quad + \langle 0|\mathcal{O}_{(us)d}(x)\overline{\mathcal{O}_{(ds)u}(0)}|0\rangle + \langle 0|\mathcal{O}_{(us)d}(x)\overline{\mathcal{O}_{(du)s}(0)}|0\rangle \\
&= -\langle 0|\mathcal{O}_{(du)s}(x)\overline{\mathcal{O}_{(ds)u}(0)}|0\rangle - \langle 0|\mathcal{O}_{(ud)s}(x)\overline{\mathcal{O}_{(ud)s}(0)}|0\rangle \\
&\quad + \langle 0|\mathcal{O}_{(ds)u}(x)\overline{\mathcal{O}_{(sd)u}(0)}|0\rangle - \langle 0|\mathcal{O}_{(us)d}(x)\overline{\mathcal{O}_{(ud)s}(0)}|0\rangle \\
&= -\langle uds\rangle - \langle ud\rangle_s + \langle usd\rangle - \langle sud\rangle. \tag{2.38}
\end{aligned}$$

The third and fourth terms of (2.36) can be obtained through interchanging $u \leftrightarrow d$ in equations (2.37) and (2.38) respectively, thus

$$\begin{aligned}
G_{\Lambda^0}(x, 0) &= \frac{1}{3}[\langle us\rangle_d + \langle ds\rangle_u + 4\langle ud\rangle_s - \langle usd\rangle - \langle dsu\rangle \\
&\quad + 2\langle sud\rangle + 2\langle sdu\rangle + 2\langle uds\rangle + 2\langle dus\rangle]. \tag{2.39}
\end{aligned}$$

To extract the spin- $\frac{1}{2}$ positive parity Σ^0 and Λ^0 states from the correlations functions given in equations (2.34) and (2.39) we average the $(\epsilon\xi) = (11)$ and (22) components. The (33) and (44) components yield the spin- $\frac{1}{2}$ negative parity states. The signal of the negative parity states is noisy and makes it difficult to determine the ground state mass.

The representation containing the spin- $\frac{3}{2}$ baryons is simpler to construct. The

decuplet baryons are represented by a symmetric three-index tensor in QCD,

$$\mathcal{T}_{ijk}^\mu \propto [\psi_i^a \psi_j^{\alpha,b} \psi_k^{\beta,c} + \psi_i^{\alpha,a} \psi_j^{\beta,b} \psi_k^c + \psi_i^{\beta,a} \psi_j^b \psi_k^{\alpha,c}] \epsilon_{abc} (C\gamma^\mu)_{\alpha\beta}. \quad (2.40)$$

The interpolating operator $D_{ijk}^\mu = (\psi^a C\gamma^\mu \psi^b) \epsilon_{abc} \psi^c$ creates states in the $1 \otimes \frac{1}{2} \sim \frac{3}{2} \oplus \frac{1}{2}$ representation D has both a Lorentz and a Dirac index, and the tensor \mathcal{T} can be expressed in terms of the D operators as follows

$$\mathcal{T}_{ijk}^\mu \propto D_{ijk}^\mu + D_{jki}^\mu + D_{kij}^\mu. \quad (2.41)$$

For the decuplet baryons the relation to physical fields is just as for the usual tensor field, for example

$$\begin{aligned} \Delta^{++} &= \mathcal{T}_{111}, & \Sigma^{*,+} &= \sqrt{3}\mathcal{T}_{113} = \sqrt{3}\mathcal{T}_{131} = \sqrt{3}\mathcal{T}_{311} \\ \Omega^- &= \mathcal{T}_{333}, & \Xi^{*,0} &= \sqrt{3}\mathcal{T}_{133} = \sqrt{3}\mathcal{T}_{313} = \sqrt{3}\mathcal{T}_{331}. \end{aligned} \quad (2.42)$$

To calculate the correlation function for the decuplet baryons let us consider a generic state made of three non-degenerate quark flavours A, B and C which has the tensor field \mathcal{T}_{ABC} . Thus

$$\begin{aligned} G_{\{ABC\}}^\mu(x,0) &= 6 \langle 0 | \mathcal{T}_{ABC}^\mu(x) \overline{\mathcal{T}_{ABC}^\mu(0)} | 0 \rangle \\ &= 6 \langle 0 | [D_{ABC}^\mu(x) + D_{BCA}^\mu(x) + D_{CAB}^\mu(x)] \times \\ &\quad [\overline{D_{ABC}^\mu(0)} + \overline{D_{BCA}^\mu(0)} + \overline{D_{CAB}^\mu(0)}] | 0 \rangle \\ &= 6 \{ \langle 0 | D_{ABC}^\mu(x) \overline{D_{ABC}^\mu(0)} | 0 \rangle + \langle 0 | D_{ABC}^\mu(x) \overline{D_{BCA}^\mu(0)} | 0 \rangle \\ &\quad + \langle 0 | D_{ABC}^\mu(x) \overline{D_{CAB}^\mu(0)} | 0 \rangle + \dots \}, \\ &= 6 \{ \langle 0 | D_{ABC}^\mu(x) \overline{D_{ABC}^\mu(0)} | 0 \rangle - \langle 0 | D_{BAC}^\mu(x) \overline{D_{BCA}^\mu(0)} | 0 \rangle \\ &\quad - \langle 0 | D_{ABC}^\mu(x) \overline{D_{ACB}^\mu(0)} | 0 \rangle + \dots \}, \\ &= 6 \{ \langle \underline{AB} \rangle \underline{C} + \langle \underline{ABC} \rangle + \langle \underline{BAC} \rangle + \dots \}, \\ &= 6 \{ \langle \underline{AB} \rangle \underline{C} + \langle \underline{ABC} \rangle + \langle \underline{BAC} \rangle + \langle \underline{BC} \rangle \underline{A} + \langle \underline{BCA} \rangle + \langle \underline{ACB} \rangle \\ &\quad + \langle \underline{CA} \rangle \underline{B} + \langle \underline{CAB} \rangle + \langle \underline{CBA} \rangle \}. \end{aligned} \quad (2.43)$$

The abbreviated notation for the contractions used here is similar to that used in the spin- $\frac{1}{2}$ case, the underline denotes that γ^μ is used instead of γ_5 , and the μ index is suppressed. The correlation function for all decuplet states can be obtained by appropriate replacements of A, B, and C with the required quark flavours. Here again we average over the Dirac spinor combinations $(\epsilon\xi) = (11)$ and (22) . The fourth Lorentz component, $G_{\{ABC\}}^4$, is pure spin- $\frac{1}{2}$ and can be used to project out the desired pure spin- $\frac{3}{2}$ state: $G_{\{ABC\}}(\frac{3}{2}) = G_{\{ABC\}}^1 + G_{\{ABC\}}^2 + G_{\{ABC\}}^3 - G_{\{ABC\}}^4/3$.

Channel	$I(J^P)$	Operator	Lightest state (MeV)
N	$\frac{1}{2}(\frac{1}{2}^+)$	$\frac{1}{2}(1 + \gamma_4)\epsilon_{ijk}(u^i C \underline{\gamma}_5 d^j)u_\alpha^k$	nucleon(940)
N^{np}	$\frac{1}{2}(\frac{1}{2}^-)$	$\frac{1}{2}(1 - \gamma_4)\epsilon_{ijk}(u^i C \underline{\gamma}_5 d^j)u_\alpha^k$	N(1535)
$\Delta(\frac{3}{2})$	$\frac{3}{2}(\frac{3}{2}^+)$	$\frac{1}{2}(1 + \gamma_4)\epsilon_{ijk}(u^i C \underline{\gamma}_i u^j)u_\alpha^k$	$\Delta(1232)$
$\Delta^{np}(\frac{3}{2})$	$\frac{3}{2}(\frac{3}{2}^-)$	$\frac{1}{2}(1 - \gamma_4)\epsilon_{ijk}(u^i C \underline{\gamma}_i u^j)u_\alpha^k$	$\Delta(1700)$
$\Delta(\frac{1}{2})$	$\frac{3}{2}(\frac{1}{2}^+)$	$\frac{1}{2}(1 + \gamma_4)\epsilon_{ijk}(u^i C \underline{\gamma}_4 u^j)u_\alpha^k$	$\Delta(1750)$
$\Delta^{np}(\frac{1}{2})$	$\frac{3}{2}(\frac{1}{2}^-)$	$\frac{1}{2}(1 - \gamma_4)\epsilon_{ijk}(u^i C \underline{\gamma}_4 u^j)u_\alpha^k$	$\Delta(1900)$

Table 2.2: Summary of the baryon operators and their relationship to the lightest particle states.

2.1.6 Fitting Baryon Two-point Functions

In table 2.2 we show the basic operators which are used to interpolate the octet baryons and the Δ baryons. These simple operators couple to both parities and therefore the asymptotic form contains the lowest contributions of both parities, with masses m_{B^+} and m_{B^-} for the positive and negative parity states respectively. In the definition of the baryon operators, the factors of $(1 \pm \gamma_4)/2$ are the Dirac projection matrices arising from the spin sum at zero three-momentum. By extracting these factors from the baryons operator we can write the baryon two-point function as follows:

$$C_B(t) = \sum_{\vec{x}} \langle 0 | \mathcal{B}(\vec{x}, t) \overline{\mathcal{B}}(0) | 0 \rangle$$

$$\begin{aligned} \xrightarrow{t, T \rightarrow \infty} & (1 + \gamma_4) [C_{B+} e^{-m_{B+} t} - C_{B-} e^{-m_{B-} (T-t)}] \\ & + (1 - \gamma_4) [-C_{B+} e^{-m_{B+} (T-t)} + C_{B-} e^{-m_{B-} t}]. \end{aligned} \quad (2.44)$$

Thus we are able to see how the baryon operators couple to both parities. For example to fit the positive parity spin- $\frac{1}{2}$ Σ two-point function, given in equation (2.34), we fold for $t < T/2$ the $(\epsilon\xi)$ (11), (22) components anti-symmetrically with the (33), (44) for $t > T/2$ and fit this combination to

$$\lim_{t, T \rightarrow \infty} C_{B+}(t) = C_{B+} e^{-m_{B+} t} \quad (t \leq T/2). \quad (2.45)$$

It is fairly clear how one would fit the negative parity state, and the other baryon states.

2.1.7 Monte Carlo Measurements: Signal vs. Noise

Let us consider a general correlation function $C_H(t)$. A Monte Carlo estimate is formed by calculating $G_H(\vec{x}, t)$ from the quark propagators and averaging over all N gauge configurations. We can estimate the size of the statistical fluctuations in $C_H(t)$ using the standard formula for the variance:

$$\begin{aligned} N\sigma_H^2(t) & \approx \sum_{\vec{x}} [\langle G_H(\vec{x}, t) G_H(\vec{x}, t) \rangle - \langle G_H(\vec{x}, t) \rangle^2] \\ & \approx \sum_{\vec{x}} [\langle \langle 0 | \mathcal{O}_H(t) \mathcal{O}_H(t) \mathcal{O}_H^\dagger(0) \mathcal{O}_H^\dagger(0) | 0 \rangle \rangle] - (C_H(t))^2. \end{aligned} \quad (2.46)$$

Let us first consider the case of a meson; the first term involves four quark propagators going from time zero to time t , and so its falloff is governed by the lowest energy state containing at least two quarks and two anti-quarks, i.e two pions. Thus the first term falls off as $e^{-2m_\pi t}$. In the case of the pion also the second term falls off as $e^{-2m_\pi t}$. In the case of the rho the first term falls off more slowly at large t . Thus the signal to noise ratio for a meson is

$$\frac{C_M(t)}{\sigma_M(t)} \sim \sqrt{N} e^{-(m_M - m_\pi)t}. \quad (2.47)$$



For a pion this is a constant in time, but for a rho this means the statistical errors grow in time.

For the case of a baryon, in equation (2.46) the first term is dominated at large t by the lowest-energy state consisting of three quarks and three anti-quarks, that is, one composed of three pions, so up to constants we expect

$$\sigma_N(t) \sim e^{-(3m_\pi/2)t}. \quad (2.48)$$

Therefore the ratio of signal to noise in the case of a baryon is

$$\frac{C_B(t)}{\sigma_B(t)} \sim \sqrt{N} e^{-(m_B - 3m_\pi/2)t}. \quad (2.49)$$

As in the case of the rho meson, the statistical errors of the baryon correlators grow in time, which means the masses of these states are harder to measure than in the case of the pion.

2.2 Smearing

Equation (2.20) shows how the mass can be determined from the propagation of a hadronic state in Euclidean time. Provided sufficiently large Euclidean time t is taken, the mass determination is independent of the particular hadronic creation operator used, since the ground state always dominates. There are two approaches one can take to extract a good determination of the ground state mass.

- The first is to use a large temporal extent T for the lattice. This increases the computational overhead, in both memory and runtime for a simulation. Firstly the actual time for computing a single propagator increases. Secondly the fluctuations of the correlators, between configurations, increases with the propagation separation in Euclidean time from the creation point at the source. Therefore, if a correlator plateaus at large Euclidean time, more configurations will need to be generated for the signal to have the same statistical noise as one that plateaus at earlier Euclidean time, which

means an increase in runtime.

- The second approach is to enhance the overlap with the ground state wavefunction, $A_1 \gg A_n$ for $n > 1$, where $A_n = |\langle 0 | \Phi_M(0) | n \rangle|^2$ in equation (2.20). This is achieved using spatially extended interpolating field operators Φ_M . The ground state will then dominate at smaller Euclidean time t , with all the advantages of a better signal to noise ratio. This is the technique known as *Smearing*.

Obviously, the most economical way of achieving the desired goal, if the computation overhead involved is relatively small, is the second approach.

The original proposals [52, 53] for *smeared* interpolating fields comprised a sum of point operators over all spatial sites on the source timeslice and are non-gauge-covariant; while improving the signal at small times, they lead to increased noise at later times. The problem of statistical noise can be alleviated by fixing the gauge so that non-covariance is no longer an issue, yielding *cube* [54, 55] and *wall* [56] smeared operators. However, fixing the gauge on the lattice raises the possibility of Gribov copies [57]. Choosing gauge-covariant operators eliminates the possible problems in gauge-fixing; such operators were first discussed in [58, 59]. In this section, two different gauge-covariant-smearing techniques are investigated, which are *fuzzing* [60, 61] and *Jacobi smearing* [62, 63], and these techniques will be referred to in subsequent chapters. The Jacobi smearing algorithm is a variant of the *Wuppertal* smearing described by Güsken [58].

It is worth noting that these smearing algorithms are conceptually different.

- The Jacobi smearing algorithm aims to increase the overlap with the ground state by approximating the wave function of the S-wave ground state. Since the S-wave wave function is spherically symmetric with some characteristic non-zero radius, an acceptable choice of operator would be any finite sized operator with maximal reflection and rotation symmetry. The lattice only possesses a finite cubic sub-group of the usual reflection and rotation symmetries, this could be realised as some form of cube or octahedron.

- The fuzzing algorithm uses the observation that the main contamination to the ground state using point interpolating fields is from the first excited state. The fuzzing procedure constructs fuzzed gluon flux tubes and uses these, in the case of a meson, to join the quark and anti-quark by a colour flux string. The quark propagator is spatially extended at distance $\pm r$ along the lattice axes with the appropriate fuzzed gauge links and combined together in both the forward and backward spatial directions. The tunable distance r is taken to be the spatial extension at which the wave-function of the first excited state has a node.

2.2.1 Source and Sink Smearing

On the lattice two-point functions are calculated by creating the hadron at a point *source* and annihilating the hadron at all *sink* points, the location of the source is usually taken to be the origin of the lattice at $t=0$. The timesliced hadron correlator is calculated by summing together all the sink points in the three spatial directions on every timeslice. The mass of the hadron is calculated from the exponential decay of the hadron correlator. In the case of the meson this is represented by

$$C_{\mathcal{O}_1\mathcal{O}_2} = \sum_{\vec{x}} -Tr(G(x,0)(\gamma_4\Gamma_2^\dagger\gamma_4)\gamma_5 G^\dagger(x,0)\gamma_5\Gamma_1). \quad (2.50)$$

To smear a hadron, the quark propagators comprising it are smeared. The quark propagator can be either smeared at the source creation point, or sink annihilation point or both. Smearing at the source is computationally cheaper than sink smearing, as the source only lives a on single timeslice and sink smearing requires smearing at every annihilation point. In the limit of an infinite number of configurations the approaches of source and sink smearing will become equivalent. However, in practice this is not the case because smeared functions are constructed from the gauge fields and these fluctuate between timeslices. Thus the signal from timesliced correlators constructed from propagators smeared at

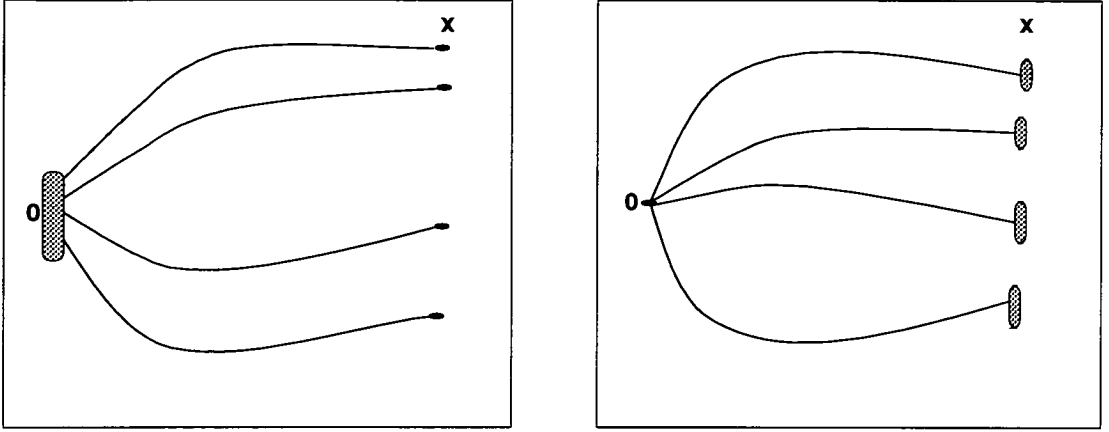


Figure 2.2: Schematic representation on the left of source smearing and on the right for sink smearing on a single timeslice. The hatched area indicates a smeared operator

the sink will be noisier than those constructed from source smeared propagators.

The smeared-quark field operators are defined as follows:

$$\psi^S(\vec{x}, t) = \sum_{\vec{y}} S(\vec{x}, \vec{y}) \psi(\vec{y}, t), \quad \bar{\psi}^S(\vec{x}, t) = \sum_{\vec{y}} \bar{\psi}(\vec{y}, t) S^\dagger(\vec{y}, \vec{x}), \quad (2.51)$$

for the sink and source quark fields respectively. A sink-smeared quark propagator is then

$$\begin{aligned} G^{LS}(x, 0) &= \langle 0 | \psi^S(x) \bar{\psi}(0) | 0 \rangle \\ &= \sum_{\vec{y}} \langle 0 | S(\vec{x}, \vec{y}) \psi(\vec{y}) \bar{\psi}(0) | 0 \rangle \\ &= \sum_{\vec{y}} S(\vec{x}, \vec{y}) M^{-1}(\vec{y}, 0) \\ &= \sum_{\vec{y}} \left(M(0, \vec{y}) S^{-1}(\vec{x}, \vec{y}) \right)^{-1}. \end{aligned} \quad (2.52)$$

Calculation of $G^{LS}(x, 0)$ is obtained from the solution of the matrix equation

$$\sum_{\vec{y}} \left[M(0, \vec{y}) S^{-1}(\vec{x}, \vec{y}) \right] G^{LS}(x, 0) = 1, \quad (2.53)$$

i.e.

$$M(0, y)G(y, 0) = 1, \quad (2.54)$$

where $G(y, 0)$ is the usual point to point propagator and

$$G^{LS}(x, 0) = \sum_{\vec{y}} S(\vec{x}, \vec{y})G(y, 0). \quad (2.55)$$

Thus a sink-smearred propagator can be obtained from a local propagator simply by convoluting with the smearing function.

The source-smearred propagator is obtained from

$$\begin{aligned} G^{SL}(x, 0) &= \langle 0 | \psi(x) \bar{\psi}^S(0) | 0 \rangle \\ &= \sum_{\vec{y}} \langle 0 | \psi(x) \bar{\psi}(y) S^\dagger(\vec{y}, \vec{0}) | 0 \rangle \\ &= \sum_{\vec{y}} M^{-1}(x, y) S^\dagger(\vec{y}, \vec{0}) \\ &= \sum_{\vec{y}} \left((S^\dagger(\vec{y}, \vec{0}))^{-1} M(y, x) \right)^{-1}. \end{aligned} \quad (2.56)$$

Thus, the propagator which must be solved is

$$\sum_{\vec{y}} \left(S^\dagger(\vec{y}, \vec{0}) \right)^{-1} M(y, x) G^{SL}(x, 0) = 1, \quad (2.57)$$

i.e.

$$M(y, x) G^{SL}(x, 0) = S^\dagger(\vec{y}, \vec{0}). \quad (2.58)$$

So in this case, the point source is replaced with a smearred source and to calculate the source-smearred propagator the above matrix equation must be solved.

At this point we will explain the nomenclature that will be used throughout the rest of this thesis when describing smearred propagators and correlators. The different smearing types are labelled by L, S and F, which are point or local, Jacobi smearred and fuzzed respectively. The smearing class of a propagator is described by the source and the sink, for example SL stands for a Jacobi smearred

source with a point sink. The naming conventions used for smeared correlators used in the thesis is shown schematically in figure 2.3. The meson (FL,FL), for example, has propagator one fuzzed at the source and sink, with propagator two being a point source and sink.

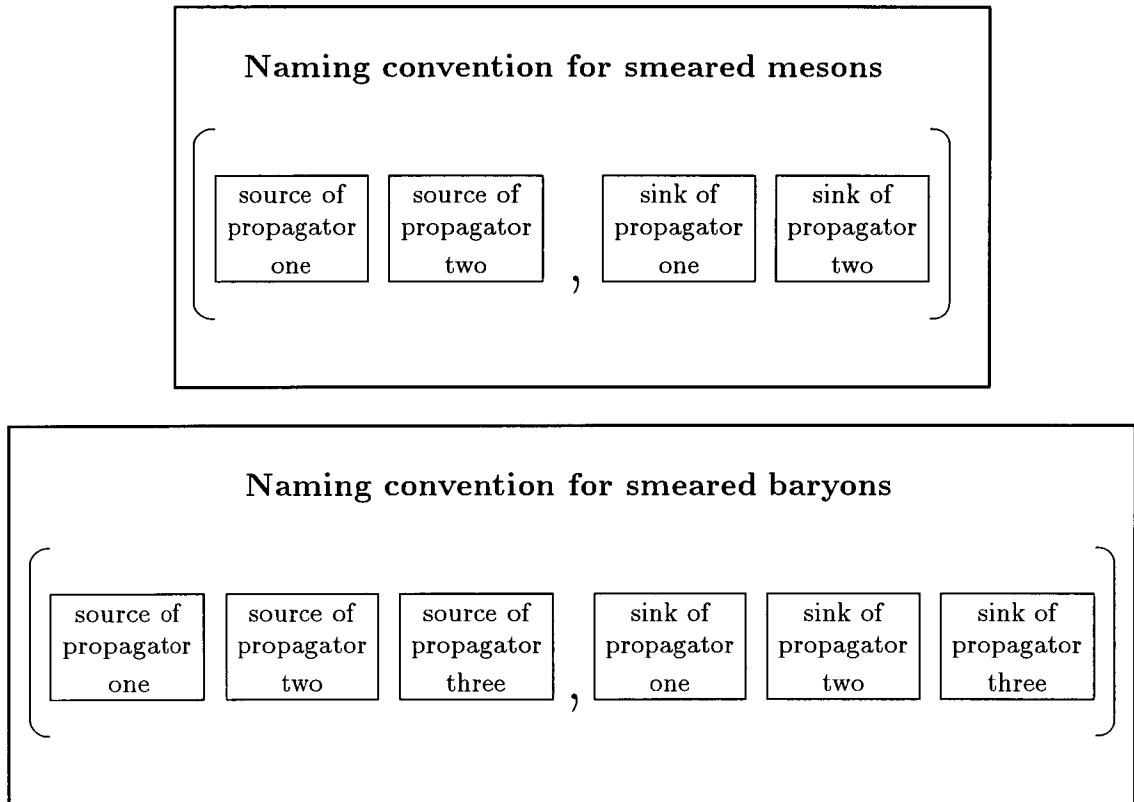


Figure 2.3: The conventions used for the smearing types of hadron correlators.

2.2.2 The Jacobi Smearing Algorithm

The Wuppertal group [58] proposed obtaining, for example, a smeared source, by solving the three dimensional Klein-Gordon equation

$$K(\vec{x}, \vec{y})S(\vec{y}, \vec{0}) = \delta_{\vec{x}, \vec{0}}, \quad (2.59)$$

where

$$K(\vec{x}, \vec{y}) = \delta_{\vec{x}, \vec{y}} - \kappa_{sc} \Delta_{\vec{x}\vec{y}}, \quad (2.60)$$

and

$$\Delta_{\vec{x}\vec{y}} = \sum \{ \delta_{\vec{y}, \vec{x} - \hat{\mu}} U_{\mu}^{\dagger}(\vec{x} - \hat{\mu}) + \delta_{\vec{y}, \vec{x} + \hat{\mu}} U_{\mu}(\vec{x}) \}. \quad (2.61)$$

Each quark is effectively localised about the origin in a region of radius r controlled by the scalar hopping parameter κ_{sc} . The rms radius, r , is defined by

$$r^2 = \frac{\sum_{\vec{x}} |\vec{x}|^2 |S(\vec{x}, \vec{0})|^2}{\sum_{\vec{x}} |S(\vec{x}, \vec{0})|^2}. \quad (2.62)$$

For each hadron ground state, an optimal radius is expected, corresponding to the smeared source which best approximates the lattice ground state. Wuppertal smearing was investigated in [62] at $\beta = 6.2$ for $\kappa_{sc} = 0.180$ and 0.184 , corresponded to $r \simeq 2$ and $r \simeq 4$ respectively. Large radii correspond to values of κ_{sc} that are close to a critical value κ_{sc}^{crit} , and the inversion of $K(\vec{x}, \vec{y})$ becomes computational expensive in computer time.

A computational inexpensive gauge-invariant smearing can be obtained by expanding equation (2.59) as a power series in κ_{sc} . This series can be obtained using the Jacobi iteration and results in the smearing function $J(\vec{x})$:

$$J(\vec{x}) = \sum_n^N \kappa_{sc}^n \Delta_{\vec{x}, \vec{y}}^n \delta_{\vec{y}, \vec{0}}. \quad (2.63)$$

For κ_{sc}^n less than κ_{sc}^{crit} , this series can be iterated to convergence, i.e. $N \rightarrow \infty$ and the resultant smearing function would be that of the Wuppertal algorithm. For κ_{sc} greater than κ_{sc}^{crit} , the series diverges, but nevertheless still provides a valid

smearing source, for any choice of N . The rms smearing radius is now dependent on N and κ_{sc} . Each successive iteration of the Jacobi procedure extends the smearing function along each axis by one link, and thus a minimum value of N exists for a particular radius.

For the Jacobi smearing algorithm, the rms smearing radius depends on two parameters κ_{sc} and N . In figure 2.4, the rms smearing radius is plotted against κ_{sc} for different N , it is clear that the rms smearing radius has little dependence on κ_{sc} when κ_{sc} is greater than 0.25. However, the rms smearing radius has strong dependence on N , which is the same conclusion reached in [63]. In figure 2.5, the smearing function

$$F(x, y) = \frac{1}{\text{Volume}} \sum_z \sqrt{\text{Tr } S^\dagger(x, y, z; (\vec{0})) S(x, y, z; (\vec{0}))}, \quad (2.64)$$

where x, y, z refer to the three Cartesian coordinate directions and the function is normalised by the the total volume

$$\text{Volume} = \sum_{x, y, z} \sqrt{\text{Tr } S^\dagger(x, y, z; (\vec{0})) S(x, y, z; (\vec{0}))}, \quad (2.65)$$

is plotted, which demonstrates that the Jacobi smearing algorithm produces an acceptable smearing function, as the reflection and rotation symmetries are clearly observable.

At this point it is useful to outline the various criteria one should adopt when choosing the parameters for Jacobi smearing κ_{sc} and N . This will ultimately depend on the computational resources available. In the ideal scenario of having a large amount of computational resources both in speed and memory one should compute all possible smearing combinations for a given state. Thus, for a meson correlator one could compute the following smeared correlators: (SL,LL), (SS,LL), (LL,SL), (LL,SS), (SL,SL) and (SS,SS) for example which requires the inversion of two quark propagators. There is an even larger number of smearing combinations for the baryon correlators. However, in the situation where computational resources are at a premium one could compute the (SS,LL) and (SS,SS)

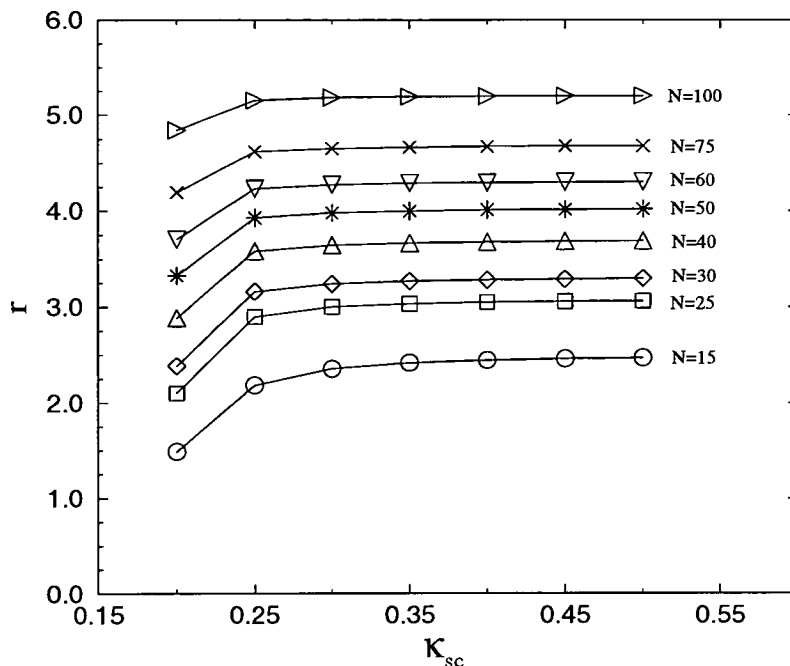


Figure 2.4: The rms smearing radius, r , against κ_{sc} for various values of N .

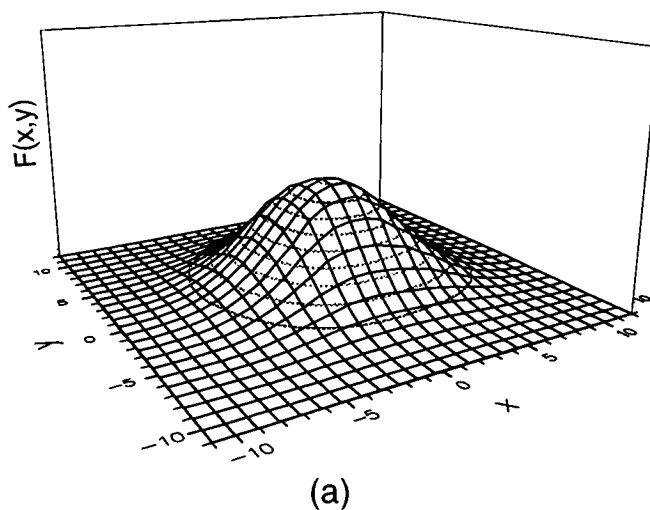


Figure 2.5: The smearing functions $F(x, y) = \sum_z \sqrt{|S|^2}$, normalised to unit volume, on a $24^3 \times 48$ lattice using Jacobi smearing with $\kappa_S = 0.250$, $N = 50$, taken from [62].

meson correlators, which only requires the inversion of one smeared propagator. If one wants to compute not only hadron masses, but also meson decay constants correlators constructed from propagators smeared at both the source and the sink will be required. This will have a large effect on the choice of Jacobi-smearing parameters as smearing at the sink produces a noisier signal. In the case where the only the (SS,LL) and (SS,SS) are computed the second correlator has approximately double the smearing radius, so it is impossible to get both correlators to have an ideal overlap with the lightest hadronic state required. In the case where all possible smearing combinations are computed these constraints are also relevant. However the signal-to-noise ratio for the (SL,SL) correlator, which is required for decay constants, will not be as bad as in the previous case.

To investigate the approach to the ground state plateau a comparison was made between correlators constructed from local propagators and from Jacobi-smeared quark propagators, in an attempt to find the optimal smearing radius for a given hadronic state. The study is based on an analysis of 41 configurations generated at $\beta = 6.0$ on a $16^3 \times 48$ lattice, using the non-perturbatively improved SW $O(a)$ -improved fermion action at two κ values 0.13344 and 0.13455.³ The Jacobi-smeared propagators were smeared at the sink using a point source with $\kappa_{sc} = 0.25$, and with a range of values of N corresponding to 10, 15, 30, 40, 50, 60, 75 and 100. Two sink smeared propagators (LS) were combined to form (LL,SS) meson correlators, and the baryons were constructed from three sink smeared propagators to form (LLL,SSS) baryon correlators. In the case of the meson the non-degenerate κ combination was calculated.

In figures 2.6, 2.7, 2.8 and 2.9, a selection of the values of N used in the sink smearing at the highest quark mass for the pion, rho, nucleon and Δ , are shown respectively. It is worth noting that the qualitative features of these effective mass plots are the same for all the simulated quark masses, except that, at the lighter quark masses, the data is noisier. The effect of changing the number of smearing

³The physical pion masses which these hopping parameters correspond are given in section 3.1.

iterations N on the approach to the ground state plateau is qualitatively the same for each of the hadrons. When N is increased the contamination from the excited states is reduced and the signal plateaus at an earlier timeslice. However, the signal becomes noisier as more gauge links are used in the smearing algorithm. For the pion the local correlator plateaus at timeslice 10. Sink smearing, with $N=60$, causes the plateau to start at timeslice 5. Increasing N beyond this causes the signal to be noisier with no additional gain in an earlier plateau. The rho meson has a similar behaviour to the pion except the signal is noisier and more statistics are needed to make a clear quantitative statement. The lack of statistics also makes it difficult to make a similar statement for the baryons except that with $N=100$, there is a clear plateau starting at timeslice 9, even though the signal, as anticipated, is noisier. This highlights one of the problems faced when choosing the optimal parameters for a particular smearing algorithm; they differ between the different hadronic states one would like to measure. Therefore in the case when one cannot compute all the different smearings one would like, a trade off has to be made, in choosing the smearing parameters to have a good overlap with the ground state of a number of hadrons.

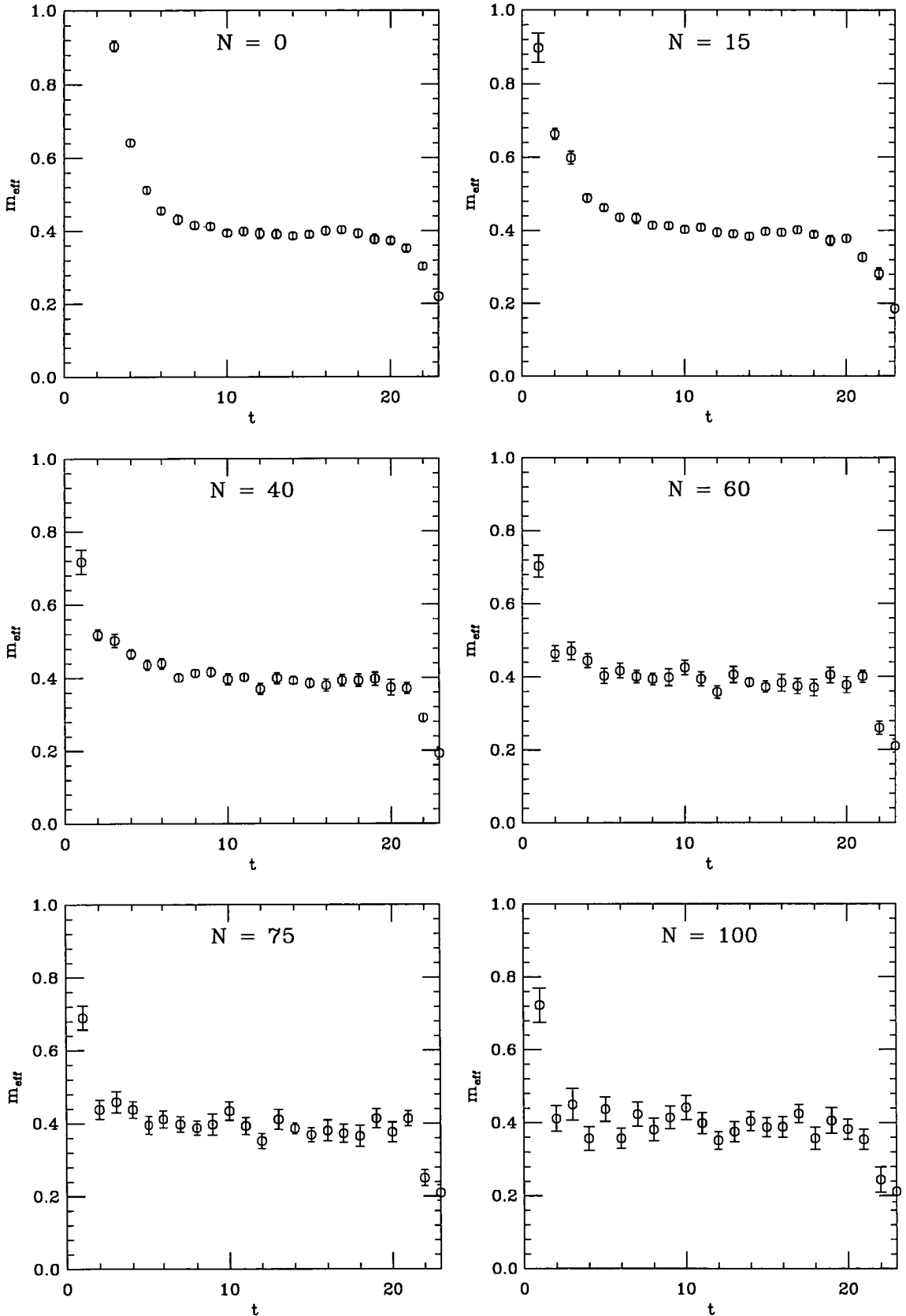


Figure 2.6: Effective masses for the pion, with varying numbers of smearing iterations N used in the Jacobi smearing procedure, $\kappa_{sc} = 0.25$, at $\beta = 6.0$ and $\kappa = 0.13344$ from 41 configurations, and the smeared correlators are (LL,SS).

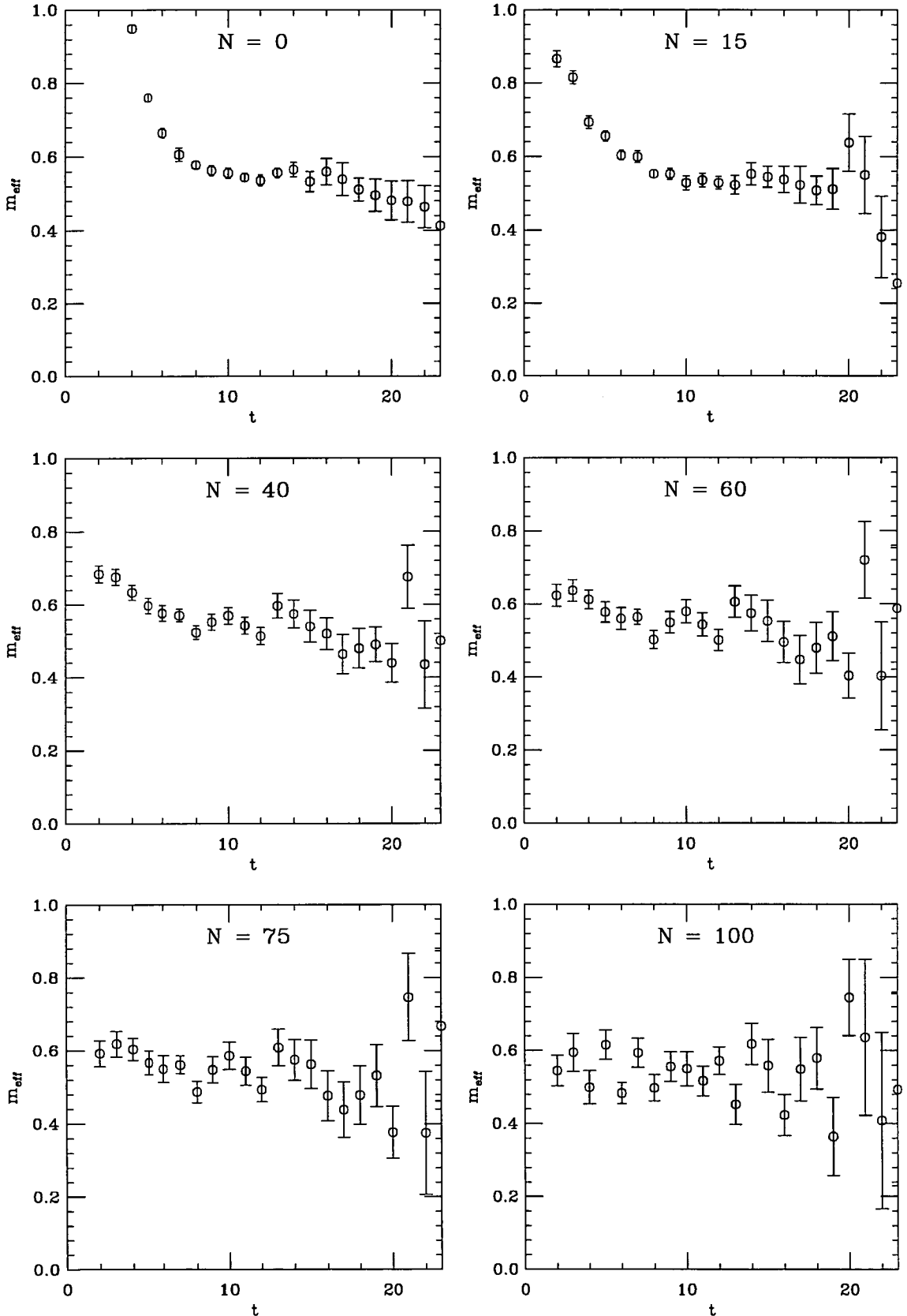


Figure 2.7: Effective masses for the rho, with varying numbers of smearing iteration N used in the Jacobi smearing procedure, $\kappa_{sc} = 0.25$, at $\beta = 6.0$ and $\kappa = 0.13344$ from 41 configurations, and the smeared correlators are (LL,SS).

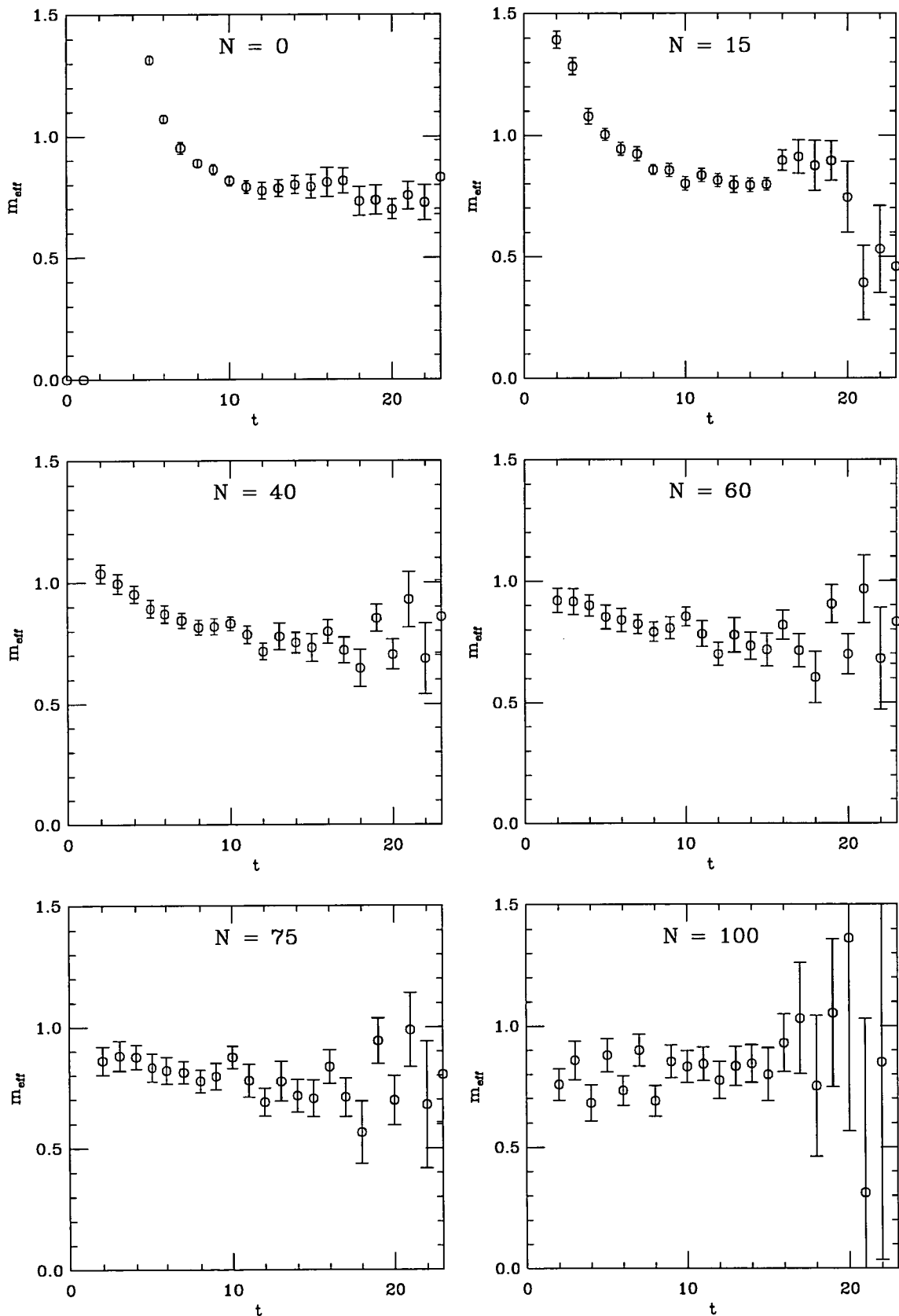


Figure 2.8: Effective masses for the nucleon, with varying numbers of smearing iteration N used in the Jacobi smearing procedure, $\kappa_{sc} = 0.25$, at $\beta = 6.0$ and $\kappa = 0.13344$ from 41 configurations, and the smeared correlators are (LLL,SSS).

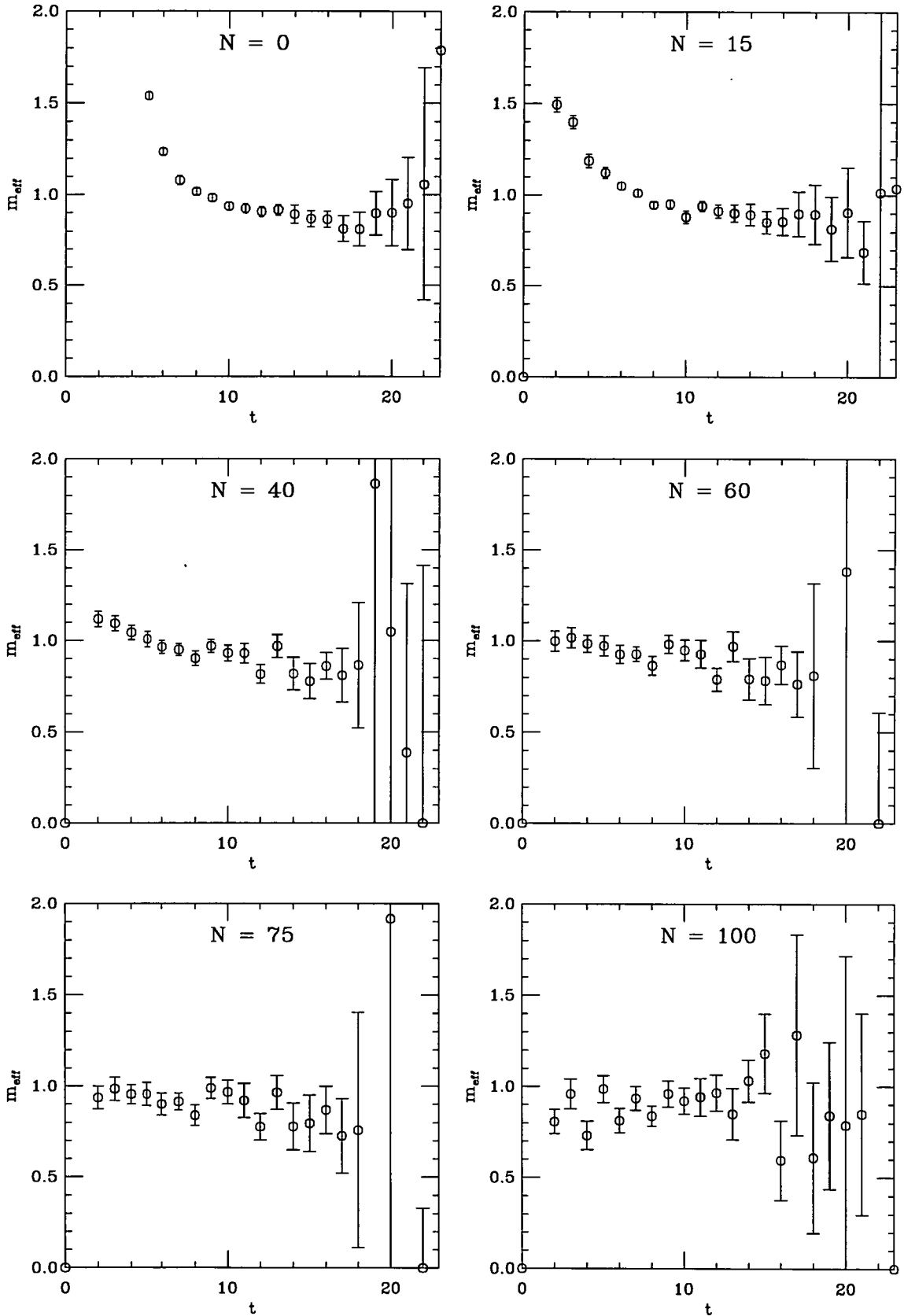


Figure 2.9: Effective masses for the Δ , with varying numbers of smearing iteration N used in the Jacobi smearing procedure, $\kappa_{sc} = 0.25$, at $\beta = 6.0$ and $\kappa = 0.13344$ from 41 configurations, and the smeared correlators are (LLL,SSS).

2.2.3 Fuzzing

The rationale behind fuzzing was discussed at the beginning of this section; the fuzzing method in detail is described as follows. Fuzzed gluon flux tubes are created through an iterative fuzzing scheme. At each iteration, a each spatial gauge link is replaced by a multiple of itself plus sum of the four neighbouring spatial staples:

$$U_\mu(n) \rightarrow U_\mu^1(n) = P_{SU(3)} \left\{ cU_\mu(n) + \sum_{\substack{\pm\nu \neq \mu \\ \nu \neq 4}} U_\nu(n)U_\mu(n + \hat{\nu})U_\nu^\dagger(n + \hat{\mu}) \right\}, \quad (2.66)$$

where a projection of a matrix M to the $SU(3)$ matrix U is carried out iteratively by maximising $\text{ReTr}(MU^\dagger)$ over U using a Cabibbo-Marinari approach. To generate the fat fuzzed gauge links we iterated equation (2.66) five times with $c = 2$. The idea of spatially smearing the gauge links was used successfully to measure glueballs masses and the string tension by Teper [64] and the APE Collaboration [65], and in the study of the static potentials of heavy quarks [66].

A fuzzed quark propagator at a site (\vec{x}, t) is defined as the average of the propagators to the sites given by the six spatial displacements of distance $\pm r$ from (\vec{x}, t) along the lattice axes, parallel transported in a gauge-covariant way using the fuzzed gauge links,

$$\psi_\alpha^{\prime a} = \sum_{\mu=1}^3 \left\{ \prod_{n=1}^r U_\mu^\dagger(x - n\hat{\mu})\psi_\alpha^a(x - r\mu) + \prod_{n=1}^r U_\mu^1(x + (n-1)\hat{\mu})\psi_\alpha^a(x + r\mu) \right\}. \quad (2.67)$$

The sum over all six orientations in the three forward and three backward directions results in an isotropic spatial dependence. This is illustrated in figure 2.10, which shows a schematic representation of a fuzzed source.

Meson propagators are formed analogously for the case of the Jacobi-smearred propagators. However, in [61], it was noted that contracting two fuzzed propagators with the same value of r is not likely to be useful since the fuzzed links will partially cancel giving a component which will have an overlap with the purely local hadronic operator. So these correlators were not studied.

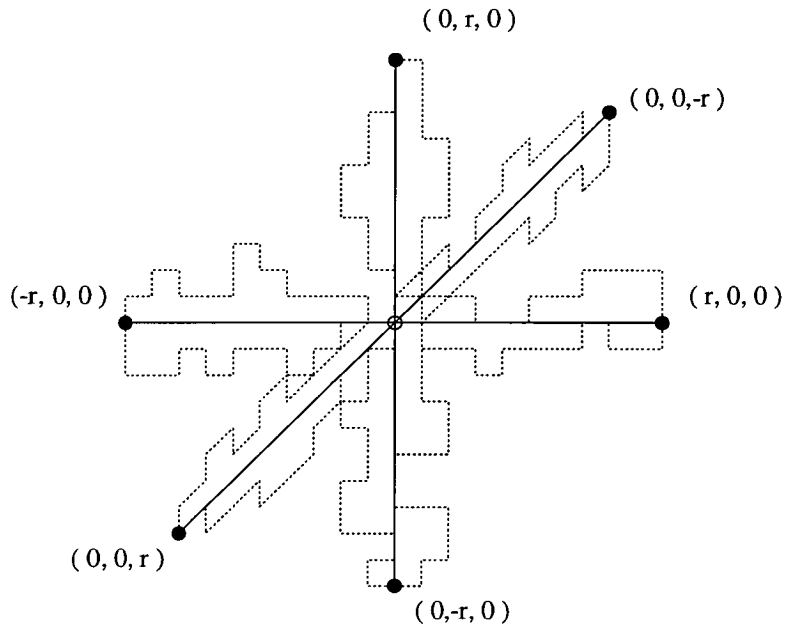


Figure 2.10: Schematic guide to fuzzing. The source is composed of six points around the origin. The dotted lines indicate typical paths that will be used in the average.

Once again, for the baryon states there are a large number of fuzzed correlators, made from combinations of fuzzed propagators and local propagators. In [61], it was again noted that a correlator composed of three fuzzed propagators has a component which is unfuzzed.

The benefit of using fat fuzzed gauge fields to join quark and anti-quark, is that if a straight-line path is used the signal from the correlator is noisy, as this has a poor overlap with the hadronic state because there is only a small probability amplitude for the gluon field to be so localised. As in the case of Jacobi smearing, with only a finite ensemble of configurations, the signal of the sink fuzzed correlators will be noisier, compared with, with those which are source fuzzed, due to the fluctuations between timeslices of the gauge fields which are used in the fuzzing algorithm. Thus, with a finite sample, to produce the cleanest signal or if we wish to measure meson decay constants, we require the inversion

of two quark propagators, with one been fuzzed at the source and the other as been local, which is computationally more expensive than the case of Jacobi smearing. However, the number of computations to create a fuzzed propagator is considerably less than the case of Jacobi smearing whether at the source or at the sink.

To investigate the fuzzing algorithm, sink fuzzed meson correlators (LL,FL) were computed, as the calculation of sink fuzzed propagators from a local propagator, is inexpensive computationally. The study is based on the analysis of 419 configurations generated at $\beta = 6.0$ on a $16^3 \times 48$ lattice, using the non-perturbatively improved SW $O(a)$ -improved fermion action at two κ values 0.13344 and 0.13455.⁴ The sink fuzzed propagators were computed with a fuzzing radius r from 0 to 14, however it was found that increasing the fuzzing radius beyond half of the spatial dimension of the lattice the signal becomes noisy. A selection of effective mass plots of the pion and rho calculated from meson correlators at different values of r are shown in figures 2.11 and 2.12 respectively. For the pion as r increases the effective mass begins to plateau at an earlier timeslice. Thus increasing the fuzzing radius is decreasing the overlap with the first excited state. On increasing r from 4 onwards the effective mass begins to approach the plateau first from below and then from above, which means that there is a negative overlap with one or even more of the higher excited states. When $r=6$ the effective mass approaches the plateau purely from below which means the amplitude of the first excited state is either negative or small in comparison with the other amplitudes. We can observe a similar picture for the rho effective mass plots, in this case there is an approach to the plateau purely from below when $r=7$ and it is easy to see that the signal becomes noisier than for the pion as r is increased, as expected.

The gauge invariant zero-momentum meson correlation function (LL,FL) is de-

⁴The physical pion masses which these hopping parameters correspond are given in section 3.1.

defined as

$$C(t, r) = \sum_{\vec{x}} \sum_{i=1} \langle 0 | \bar{\psi}(\vec{x} + r_i, t) \Gamma M(\vec{x}, t; r_i) \psi(\vec{x}, t) \bar{\psi}(\vec{0}, 0) \Gamma \psi(\vec{0}, 0) | 0 \rangle, \quad (2.68)$$

where $M(\vec{x}, t; r_i)$ denotes the product of fuzzed links of length r originating from site \vec{x} in direction i for a given timeslice t . The pion and rho correlation functions are fitted to a double exponential fit:

$$C(t, r) = c_1(r) \left[e^{-m_1 t} + e^{-m_1(T-t)} \right] + c_2(r) \left[e^{-m_2 t} + e^{-m_2(T-t)} \right], \quad (2.69)$$

where m_1 is the mass of the ground state and m_2 is the mass of the first excited state. A simultaneous fit was made to data of all r values from 0 to 8. Correlated least χ^2 fits were performed, over the largest number of timeslices that gave an acceptable $\chi^2/\text{d.o.f.}$. Uncorrelated fits were also used to check that the fitted parameters were consistent from both fits, and consistency in the fitted parameter through changing the minimum fitting timeslice by ± 1 were also taken in consideration. Statistical errors were determined by means of a bootstrap analysis, where 100 bootstrap samples were generated. The chosen fitting range⁵ was from [7,23] in most cases. Examples of these fits for the pion and rho are shown in figure 2.14, where the simultaneous fit is superimposed on top of the effective masses for all values of r in the fit, the quality of these fits are $\chi^2/\text{d.o.f.} \approx 1.4$ and $\chi^2/\text{d.o.f.} \approx 1.2$ respectively. The values obtained from the fit are normalised so that $c_1(0) + c_2(0) = 1$. The ground state and first excited state amplitudes are shown for all quark masses simulated for the pion and rho in figure 2.13. We can observe that changing the fuzzing radius, r , has a large effect on first excited state amplitude. The observations made from the effective masses plots are verified here in that, on increasing the fuzzing radius r from 0 to 6, the overlap with the first excited state decreases. The node in the first excited state wave function of the pion is around $r=6$ and for the rho is around $r=7$. This highlights again the problem faced when choosing the optimal parameters for a particular smearing

⁵The fitting range is specified as $[t_{min}, t_{max}]$, where these refer to the first and last timeslice in the fit.

algorithm; they differ between the different hadronic states one would like to measure. The optimal fuzzing radius suggested from [61] is $r=6$, this analysis shows that taking this value there still will be excited state contamination in the rho.

It has been observed by [67], that the optimal fuzzing radius may not occur at an integer value of the lattice spacing. To improve the fuzzing algorithm at a relatively small increase in computer time it is proposed that the contributions of propagators fuzzed to different radii are added together, each radius is weighted by a factor. The weighting factors are obtained through assuming that the wave functions of a particular system obey a particular model like the Quarkonium wave functions in the case of a heavy-heavy quark system, for example, therefore another tunable parameter is introduced into the smearing algorithm. This new smearing algorithm is called ‘‘Boyling’’ [67].

The relative amplitude is usually called the Bethe-Salpeter (or BS) wave function of the hadron. It is the overlap between a quark and antiquark at distance r apart and the hadronic state which is an eigenstate of the Hamiltonian, transfer matrix on a lattice. For a pion the Bethe-Salpeter wave function is defined as

$$\psi^{BS}(r) = \langle 0 | \bar{d}(\vec{x} + \vec{r}) M(\vec{x}; \vec{r}) u(\vec{x}) | \pi \rangle, \quad (2.70)$$

where $M(\vec{x}; \vec{r})$ is a path-ordered product of gauge links that joins points $\vec{x} + \vec{r}$ and \vec{x} and makes the amplitude gauge invariant. The Bethe-Salpeter amplitudes are normalised such that $\psi^{BS}(0) = 1$. There the ground state and first excited state Bethe-Salpeter wave functions are related to the fitted amplitudes as:

$$\psi_1^{BS}(r) = \frac{c_1(r)}{c_1(0)}, \quad \psi_2^{BS}(r) = \frac{c_2(r)}{c_2(0)}, \quad (2.71)$$

and are shown in figure 2.15 for the pion and rho. The results for the ground state wave function are in good agreement with [60, 68].

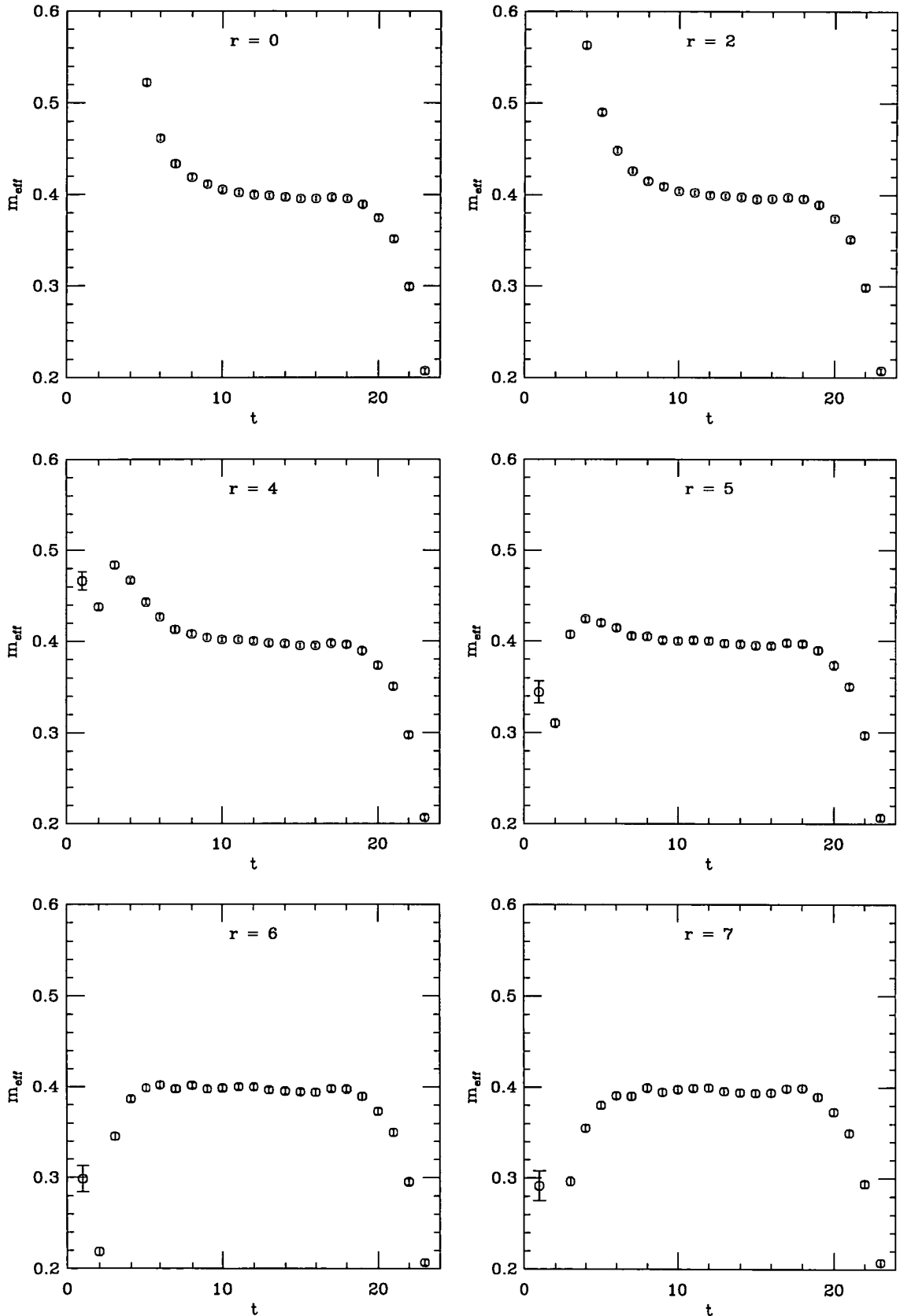


Figure 2.11: Effective mass of the pion from the (LL,FL) correlator using different values of r , the fuzzing radius, at $\beta = 6.0$ and $\kappa = 0.13344$ from 419 configurations.

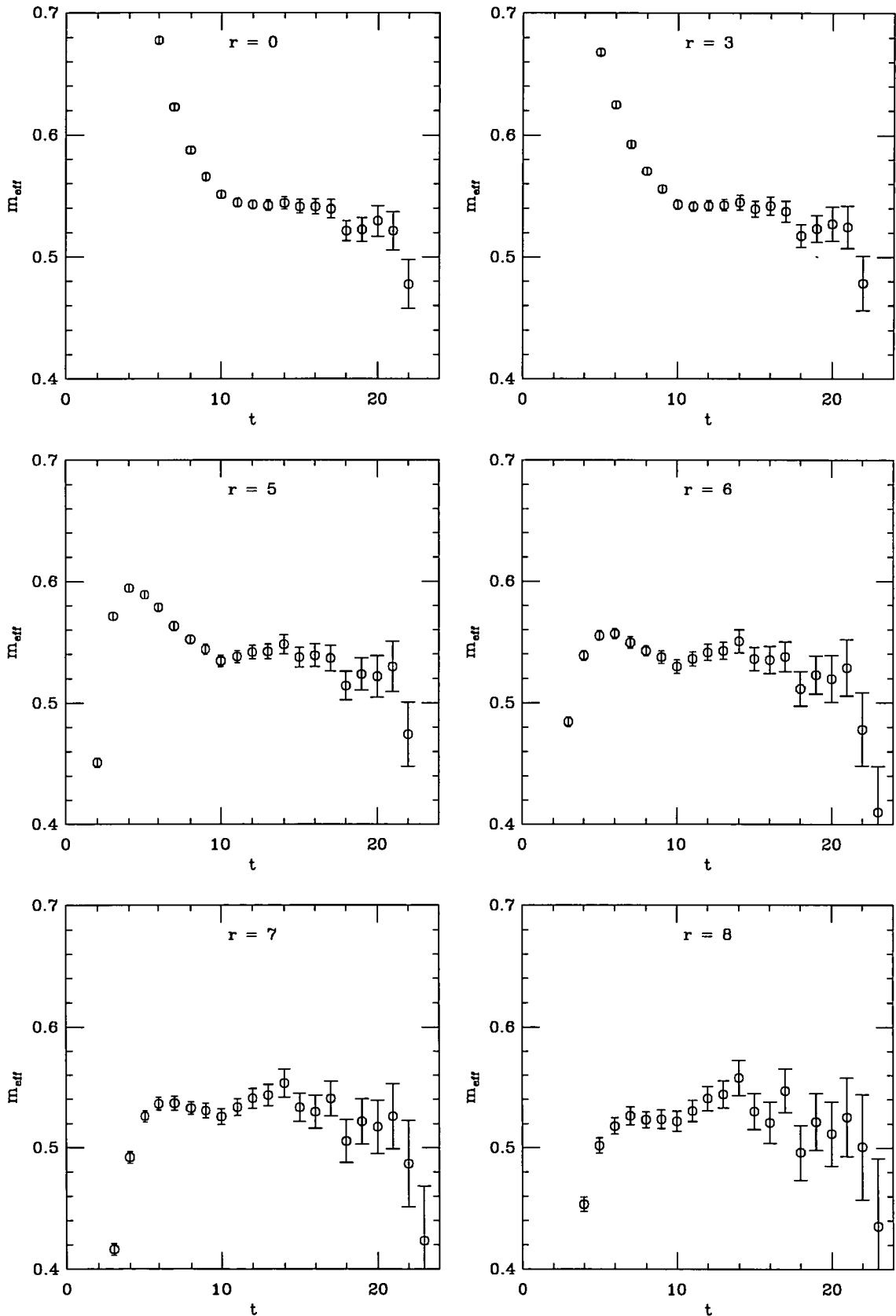


Figure 2.12: Effective mass of the rho from the (LL,FL) correlator using different values of r , the fuzzing radius, at $\beta = 6.0$ and $\kappa = 0.13344$ from 419 configurations.

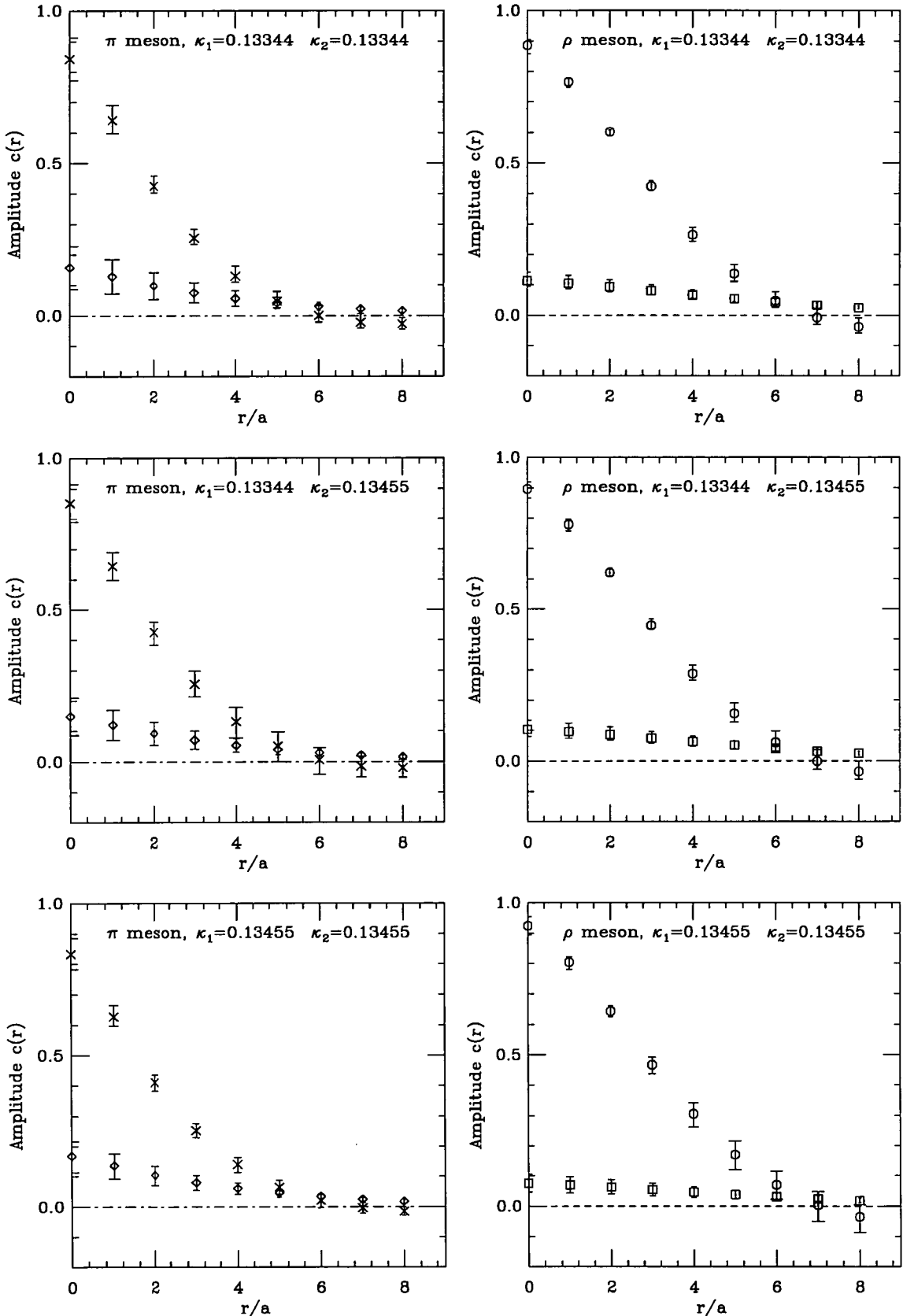


Figure 2.13: Fitted amplitudes for the π meson and ρ meson. The ground state and first excited amplitudes for the π meson are represented by the (\diamond) and (\times) respectively and for the ρ meson are represented by (\square) and (\circ) respectively.

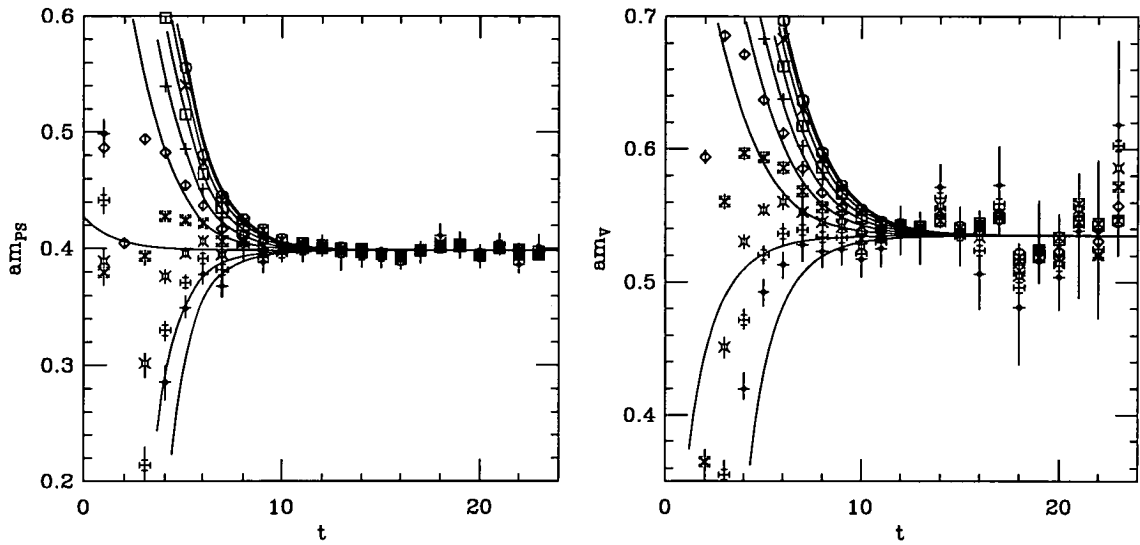


Figure 2.14: The effective mass plots for the pion and rho are shown on left and right respectively. Each plot contains values of r ranging from 0 to 8, at $\kappa = 0.13344$. The data is fitted from [7,23] using a double exponential fit, the results of which are shown.

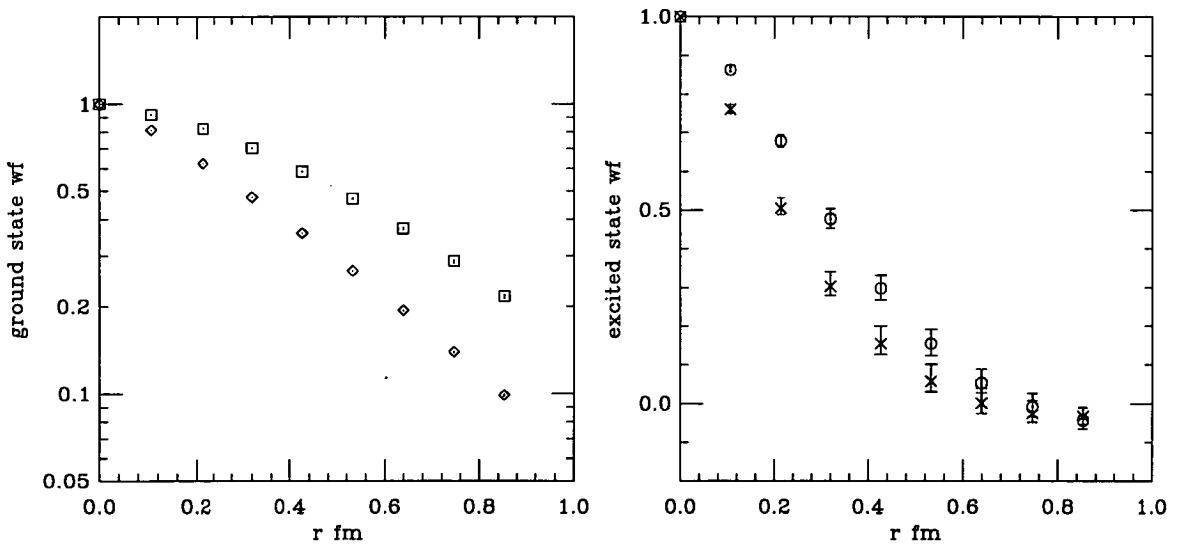


Figure 2.15: The ground state and excited state wave functions are shown on the left and right respectively at $\kappa = 0.13344$. The ground state and first excited Bethe-Salpeter wave functions for the π meson are represented by the (\diamond) and (\times) respectively and for the ρ meson are represented by (\square) and (\circ) respectively.

In the baryon sector a minor investigation of the effects of changing the fuzzing radius has been undertaken. The baryon data was generated using the same simulation data as previously, but source fuzzed propagators were generated at $\kappa = 0.13417$. The analysis is based on the study of 7 configurations, the fuzzed baryons correlators are of the type (FFL,LLL) and the following fuzzing radii were used: 2, 4, 5, 6 and 7. Effective mass plots for the nucleon and Δ with a selection of these fuzzing radii are shown in figure 2.16. We can observe that increasing the fuzzing radius causes both baryons to plateau at an earlier timeslice, the data with $r=7$ was not shown as this data was too noisy. A similar analysis as to that of the mesons will be need to find the optimal fuzzing radius.

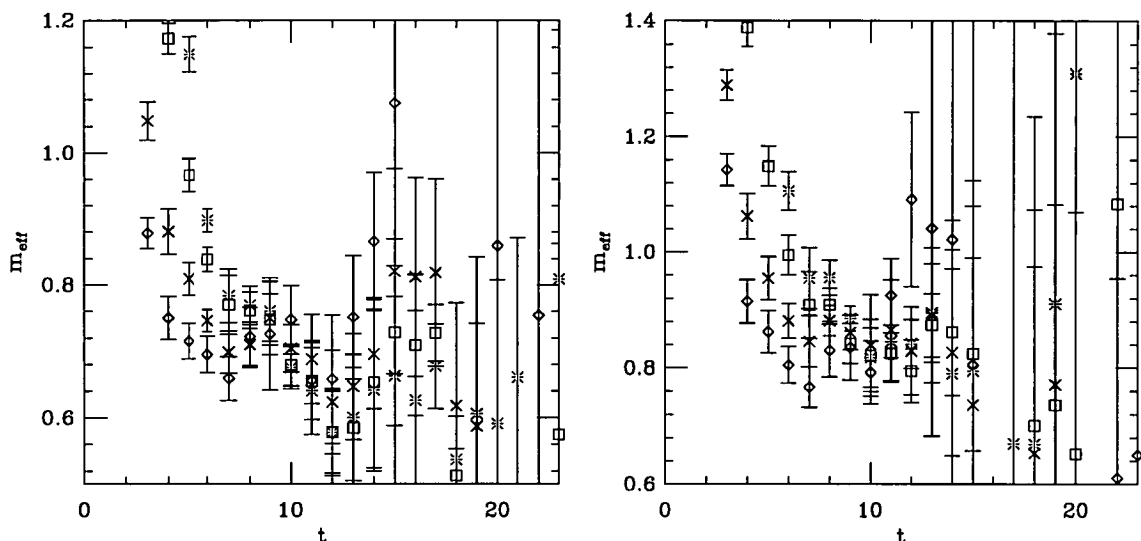


Figure 2.16: The effective mass plots for the nucleon and Δ are shown on left and right respectively. Each plot contains a number of different values for r , the fuzzing radius, = 0, 2, 4, and 6, and correspond to the symbols (*), (\square), (\times), and (\diamond). The data was generated at $\beta = 6.0$ and $\kappa = 0.13417$ from 7 configurations, using (FFL,LLL) correlators.

Chapter 3

Simulation Details and Fitting Hadron Masses

3.1 Simulation Details

Before going into detail about each of the data sets used in the simulation, it will be worthwhile giving a brief overview of the simulation and discussing the points which are common to each of the data sets. The gauge configurations were generated with the standard Wilson gauge action at three values of β , which are 5.7, 6.0 and 6.2. The lattice sizes were chosen so that the physical spatial length is fixed at around 1.8fm; any continuum extrapolation of $a \rightarrow 0$ is independent of finite size effects. To study finite size effects, at fixed a , gauge configurations were generated on larger lattices at $\beta = 5.7$ and 6.0.

Propagators have been generated with the Sheikholeslami-Wohlert $O(a)$ -improved Wilson fermion action¹ with two values of the clover coefficient corresponding to the tadpole prescription (C=TAD) and the non-perturbative value (C=NP), which removes all $O(a)$ discretisation errors. The tadpole improved propagators were generated at $\beta = 5.7, 6.0$ and 6.2, and on the larger volume at $\beta = 5.7$. The non-perturbative improved propagators were generated at $\beta = 6.0$ and 6.2, and on the larger volume at $\beta = 6.0$. Propagators were generated at am_π/am_ρ ratios of 0.5, 0.6 and 0.7 which corresponds to physical pion masses of 500, 600 and 800 MeV respectively, except at $\beta = 5.7$ where propagators were only generated at the two heaviest pion masses. In the following, the data on the smaller volumes will be referenced without specifying the lattice size, and the larger volumes will

¹The Sheikholeslami-Wohlert $O(a)$ -improved Wilson fermion action is discussed in detail in section 1.9.

be referenced by explicitly stating the volume.

β	$N_s^3 \times N_t$	$N_{OR}:N_{CM}$	N_{sep}	$a\sqrt{K}$	a^{-1} (Gev)	N_s fm	Number of configurations
5.7	$12^3 \times 24$	5:1	600	0.4099(23)	1.042	2.227	482
5.7	$16^3 \times 32$	5:1	600	0.4099(23)	1.042	3.029	145
6.0	$16^3 \times 48$	7:1	800	0.2265(55)	1.885	1.674	499
6.0	$32^3 \times 64$	7:1	1000	0.2265(55)	1.885	3.347	76
6.2	$24^3 \times 48$	5:1	2400	0.1619(19)	2.637	1.795	228

Table 3.1: Gauge configurations generated with the ratio of combination of OR and CM steps. N_{sep} is the total number of updates separating the configurations. The values of the string tension $a\sqrt{K}$ were taken from [69], the physical value is taken as 427 MeV.

The gauge configurations and propagators at $\beta = 5.7$ were calculated on a 16- and 64-node i860 Meiko Computing Surface at Edinburgh. At $\beta = 6.0$ and 6.2 the data were calculated on a 512-node Cray T3D at the Edinburgh Parallel Computing Centre. The gauge configurations were generated with a combination of the over-relaxation (OR) algorithm [70, 71] and the Cabbibo-Marinari (CM) algorithm [72]. The parameters used are listed in table 3.1, ² and periodic boundary conditions were imposed.

The quark propagators were generated with a number of different algorithms: Over-Relaxed Minimal Residual (MR) detailed in [73], bi-conjugate gradient (BiCG) exploiting γ_5 symmetry of the fermion matrix, quasi-minimal residual (QMR) again exploiting γ_5 symmetry of the fermion matrix, and stabilised bi-conjugate gradient (BiCGstab), all of which are detailed in [74]. All algorithms use a red-black preconditioner and the boundary conditions were set to periodic in space and anti-periodic in time.

The propagators generated on the i860 Meiko used the MR algorithm. The other algorithms were developed during the propagator generation program on the T3D. A considerable saving in computer time was found in using BiCGstab over MR

²The motivation for the physical value of the string tension is discussed in section 4.5.2.

when solving the quark propagator at the lighter quark mass. For example, at $\beta = 6.0$ in the case of the tadpole data set, the number of iterations required to invert the fermion matrix to a fixed residue were reduced by around 30%. In addition, computational savings were made by switching from 64-bit to 32-bit arithmetic and writing key routines, like matrix multipliers, in assembler for the T3D. This speeded up the code by around 70%. The computational resource required to generate this data set, which is about 5 Tbytes in size, is well over a million processor hours of computer time.

In table 3.2 are listed the parameters which were used to generate the propagators. For C=NP at $\beta = 6.0$, *exceptional configurations* were found on both the small and large volume, at the lightest quark mass simulated. The presence of these exceptional configurations was initially found through the inability of the BiCGstab solver to solve to a fixed residual, certain spin and colour components of the quark propagator, even after a large number of iterations. On these configurations the MR and BiCG solver algorithms were used with the lightest quark mass and a similar behaviour of the algorithms breaking down and not been able to converge the quark propagator was observed. However the quark propagator was calculated successfully using QMR(γ_5). In [74] other solver algorithms have been investigated to solve the quark propagators on these configurations.

Data-set	β	$N_s^3 \times N_t$	Number of configurations	C	κ	Parameters used in smearing	Propagators types
C=TAD	5.7	$12^3 \times 24$	482	1.5678	0.13843, 0.14077	$\kappa_{sc} = 0.25, N=16$	LL,SL
	5.7	$16^3 \times 32$	145	1.5678	0.13843, 0.14077	$\kappa_{sc} = 0.25, N=16$	LL,SL
	6.0	$16^3 \times 48$	499	1.4785	0.13856, 0.13810, 0.13700	r=6	LL,FL,LF,FF
	6.0	$16^3 \times 48$	218	1.4424	0.13745, 0.13710, 0.13640	r=8	LL,FL,LF,FF
C=NP	6.0	$16^3 \times 48$	496(3)	1.7692	0.13455, 0.13417, 0.13344	r=6	LL,FL,FL,FF
	6.0	$32^3 \times 64$	70(2)	1.7692	0.13455, 0.13417, 0.13344	$\kappa_{sc} = 0.25, N=30$	SL, SS
	6.2	$24^3 \times 48$	216	1.6138	0.13530, 0.13510, 0.13460	r=8	LL,FL,LF,FF

Table 3.2: List of all propagators generated. The smearing of the propagator is denoted source/sink, where the different smearing types L, F, and S are point, fuzzed and Jacobi smeared respectively. The number of exceptional configurations which were found is given in brackets, and is additional to the quoted number of configurations.

These exceptional configurations present us with a problem; let us consider the pion two-point function $G_p(x) = \text{Tr}\{G(x,0)G^\dagger(x,0)\}$. For an ensemble of N configurations the pion propagator fluctuates about $\tilde{G}_p(x) = \frac{1}{N} \sum_{n=1}^N G_p^{(n)}(x)$ with some variance σ^2 . The problem occurs when the generated ensemble of gauge configurations contains a few exceptional configurations, where $G_p(x)$ shoots up to values that are orders of magnitude above the normal level of fluctuations characterised by σ . A reliable estimation of $\tilde{G}_p(x)$ is impossible. The lowest eigenvalue of the exceptional configurations are orders of magnitude lower than the normal size of the lowest eigenvalue [75]. In figure 3.1, a comparison is made between the pion effective mass plot on a non-exceptional configuration and a exceptional one. For the exceptional configuration, the lowest eigenvalue of the fermion matrix, called a *zero mode*, dominates the quark propagator, and hence the pion propagator. From the pion effective mass plot we can observe that the zero mode is localised between timeslices 11 and 12 due to the change in sign in the effective mass. As these exceptional configurations cause unbounded fluctuations on the measurement of $\tilde{G}_p(x)$, these configurations have been removed from the ensemble where measurements have been undertaken. This is in-line with the idea that the presence of these zero modes is one of the pathologies of quenched QCD. In full QCD the zero modes are suppressed by the fermion determinant, and so eliminating these exceptional configurations which are an artifact of quenching, is not so bad. In [76, 77], a procedure for correcting these quenching artifacts by first isolating the contributions of zero mode poles to the quark propagator and then shifting the sub-critical poles to the critical point, is described. This procedure results in a Modified Quenched Approximation (MQA), where it is stated that “calculations can be carried out for arbitrarily small quark mass”.

The presence of these exceptional configurations is in agreement with the observations of [38], where it is stated that the fraction of exceptional configurations grows as g , C , or N_s/a is increased, or as the quark mass is made smaller. For the exceptional configurations small changes were made in the values of C and the hopping parameter κ . However, it is difficult to make an quantitative study as parameters like κ_{crit} will be needed to calculate the quark mass at each value of

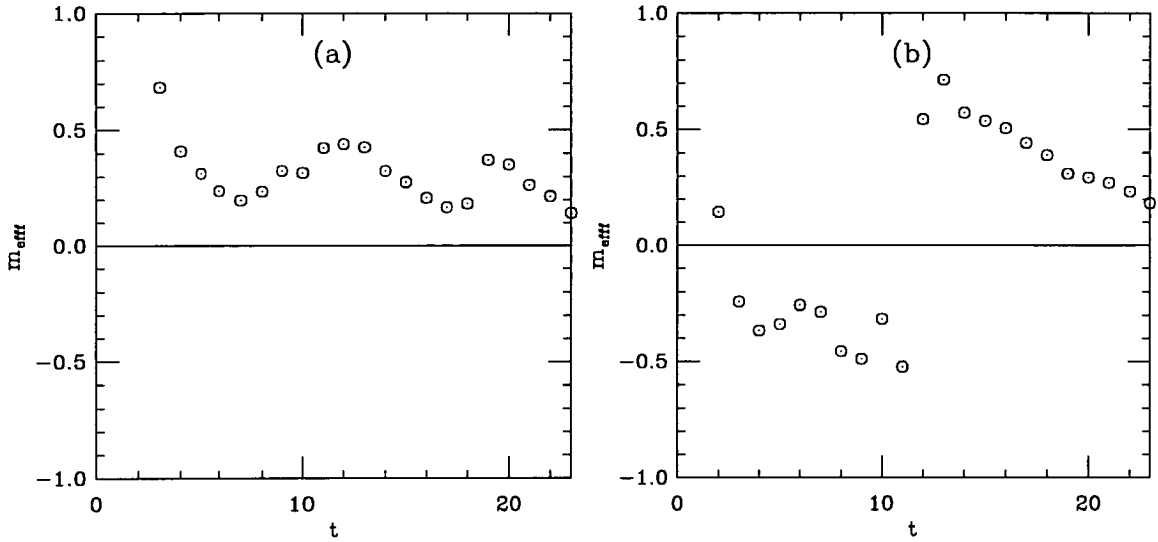


Figure 3.1: Plot (a) shows the effective mass of the pion for one normal configuration at $\beta = 6.0$, $16^3 \times 48$, with C=NP and $\kappa = 0.13455$. Plot (b) shows the data for an *exceptional configuration*. For the exceptional configuration we can observe that the effective mass is negative for t less than timeslice 11 and is positive at t greater than timeslice 12. Therefore there is a change in sign of the effective mass between timeslices 11 and 12. This is consistent with the picture that the pion propagator is dominated by its lowest eigenmode.

C, which requires simulations for a number of configurations. But either a small decrease in C at $\kappa = 0.13455$ or decreasing κ at fixed C alleviated the problem.

The propagators in table 3.2 were contracted together to form meson and baryon two-point functions. Meson correlators were formed with degenerate and non-degenerate quark mass combinations. The smearing combinations will be described shortly. Degenerate quark mass baryon correlators were generated at all β values, and on the $\beta = 6.0$ and 6.2 data sets, the non-degenerate quark mass combinations were computed. At $\beta = 6.2$ with C=TAD, there was an initial problem with the code which meant for the first 18 configurations some of the non-degenerate baryon correlators were not generated and so these configurations have not been used in the analysis.

The smearing combinations of the meson and baryon correlators are shown in the effective mass plots in figures 3.3 to 3.9, for each of the data sets. The (LL,LF) meson correlators are not shown in these plots as they approach the plateau along the same path as the (FL,LL) meson, and would cause the figures to be messy. For the non-degenerate baryons, the sink fuzzed correlators were not calculated, due to the computational overhead required to calculate them, but these smearing combinations were computed with the degenerate code and are shown in figure 3.2 for the nucleon. These correlators supply us with only a limited amount of additional information that one could use in a determination of the nucleon mass, as these correlators are noisier than those which are already computed.

The tadpole-improved data have been analysed by other members of the UKQCD Collaboration; the $\beta = 5.7$ data have been analysed with other values of $C=1$ and $C=0$ the Wilson case, to look at the effects on spectral quantities of changing the clover coefficient at fixed a , and appears in [78]. Preliminary results of the $C=TAD$ data set have appeared in [79, 80, 81]. The analysis of both the $C=TAD$ and $C=NP$ data sets presented here is independent of all these publications, and therefore any conclusion reached is independent of these.

The effective mass plots are shown in figures 3.3 to 3.9 at the heaviest quark mass simulated, for each of the data sets. There is no significant change in their behaviour in going from the heaviest to lightest quark mass, except that the signal becomes noisier. In comparing the effective mass plots for the $C=TAD$ data at all β values, using the (LL,LL) pion as an example, it can be observed that the pion reaches the plateau, at timeslice 7, 12, and 16, for $\beta = 5.7, 6.0$ and 6.2 respectively. The explanation of this is that in the continuum, the zero three-momentum pion propagator, with a physical ground state mass in the range of pion masses simulated, takes a fixed amount of time to decay exponentially to the ground state state. The physical length scale, which on the lattice can be obtained through multiplying these timeslices by the lattice spacing,³ is roughly 6 (GeV)^{-1} . The consequence of this is that simulations at higher β values require

³The inverse lattice spacings are listed in table 3.1.

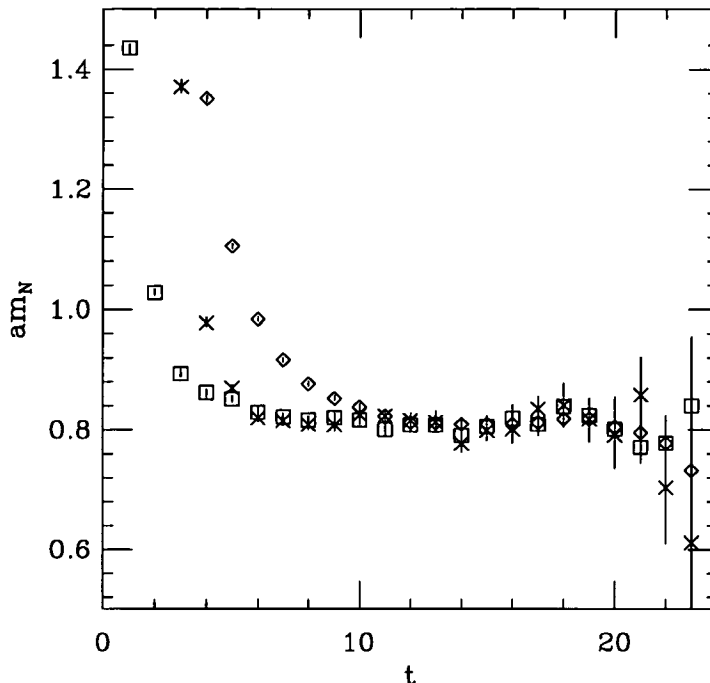


Figure 3.2: Effective masses for the nucleon at $\beta = 6.0$, with $C=TAD$ and $\kappa = 0.13700$, (\diamond), (\square), and (\times), are the (LL,LL), (LL,FF) and (FF,FF) correlators respectively. These correlators were computed with the degenerate baryon code, in comparison with the nucleon in figure 3.5 the (LL,FF) is only noisier at the final timeslices, in comparison with (FF,LL), but the (FF,FF) gives a far noisier signal.

a larger temporal component, in comparison with those at lower β values, in order for the correlators to decay to the ground state, and means that any measurement of a hadron mass will be statistically noisier, at higher β values. Smearing will significantly improve the determination of hadron masses from these lattices. From the effective masses one can observe that, as expected, the sink smeared data produces a noisier signal in-comparison with the source smeared data, irrespective of whether one uses fuzzing or Jacobi smearing.

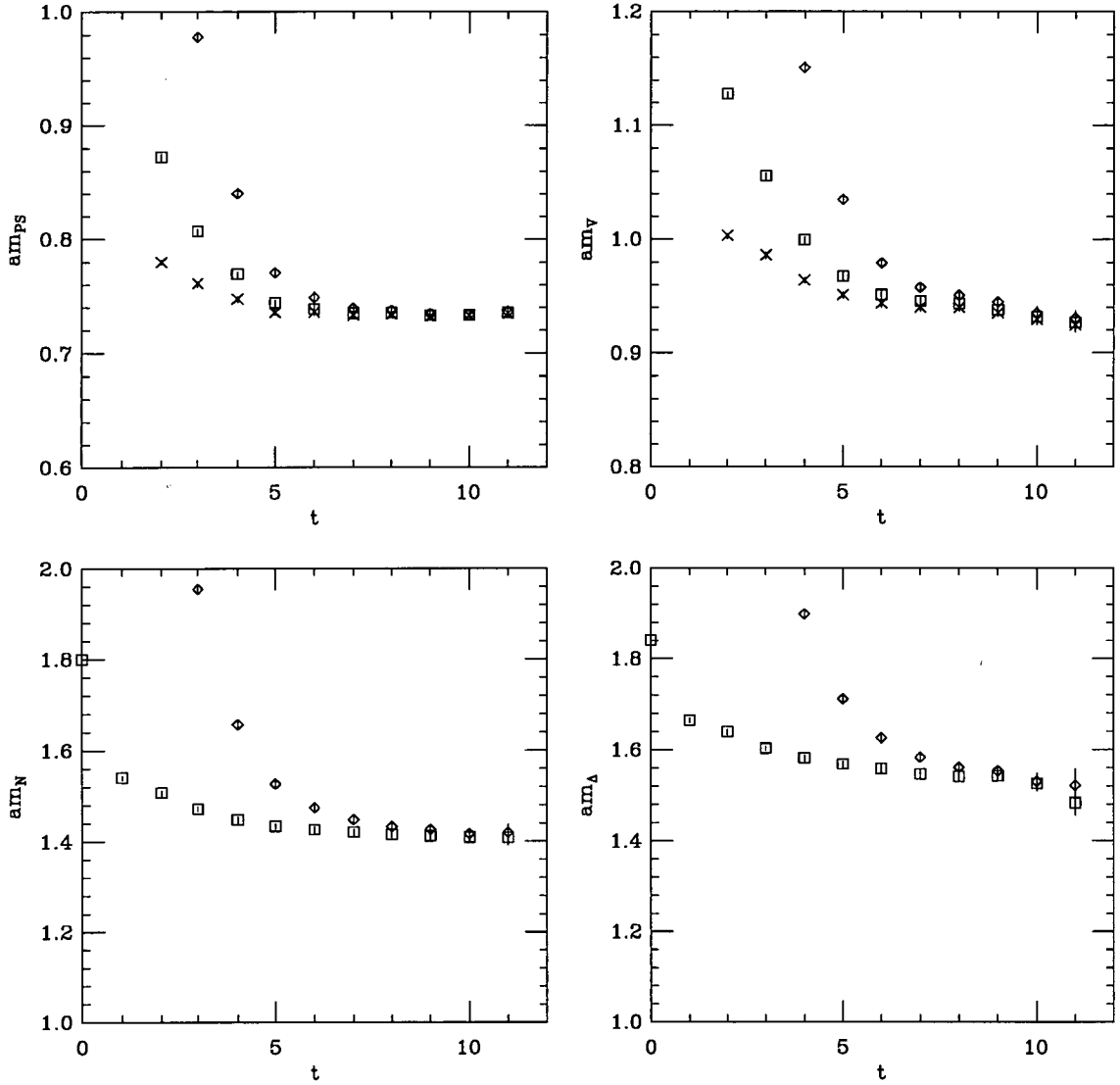


Figure 3.3: Effective masses for the pion, rho, nucleon and delta particles at $\beta = 5.7$, with C=TAD and $\kappa = 0.13843$. For the pion and rho plots the (\diamond), (\square), and (\times), are the masses obtained from the (LL,LL), (SL,LL) and (SS,LL) correlators respectively. For the nucleon and delta plots the (\diamond) and (\square) are the masses obtained from the (LLL,LLL) and (SSS,LLL) correlators respectively.

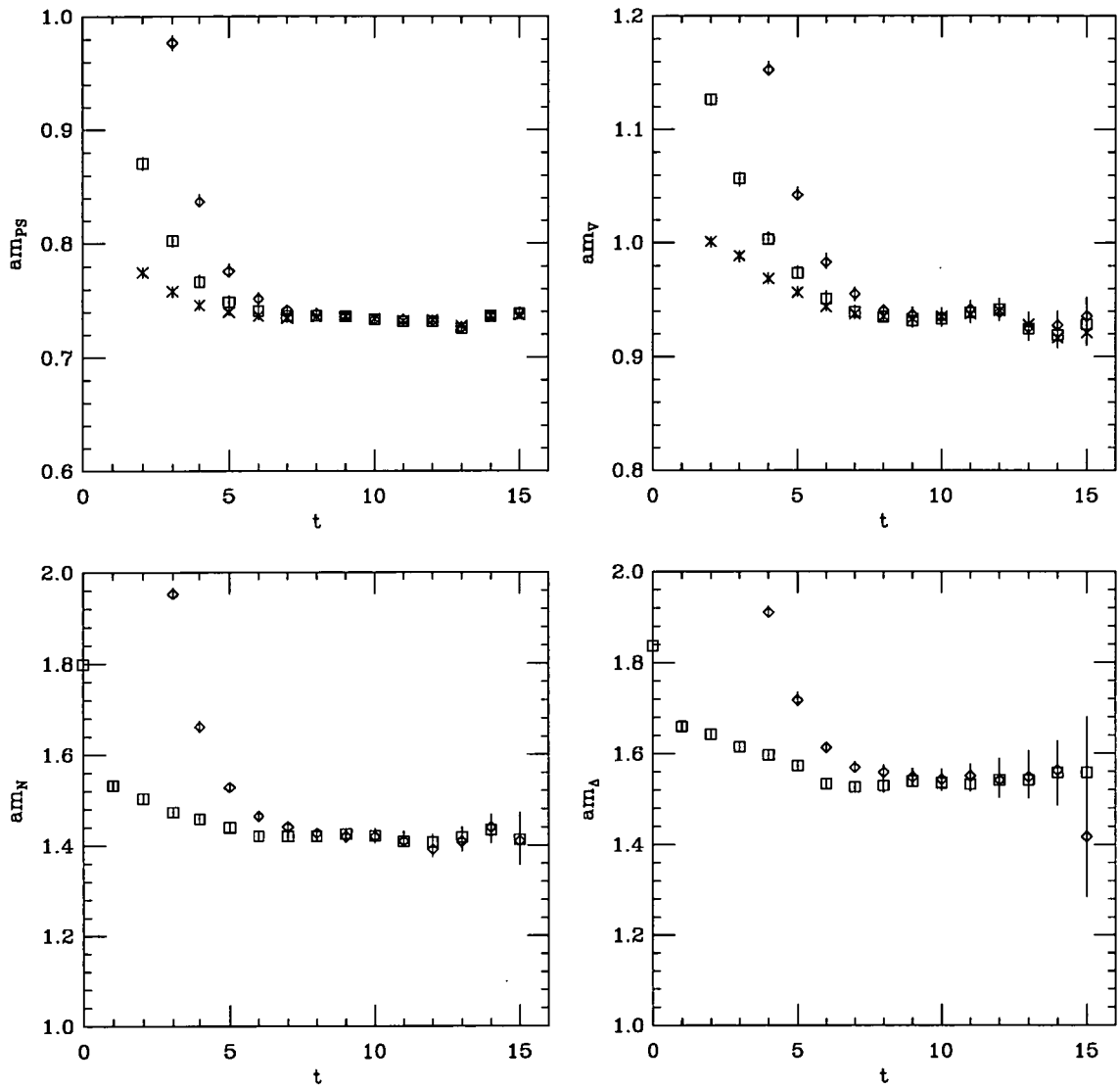


Figure 3.4: Effective masses for the pion, rho, nucleon and delta particles on the $16^3 \times 32$ lattice at $\beta = 5.7$, with $C=TAD$ and $\kappa = 0.13843$. For the pion and rho plots the (\diamond), (\square), and (\times), are the masses obtained from the (LL,LL), (SL,LL) and (SS,LL) correlators respectively. For the nucleon and delta plots the (\diamond) and (\square) are the masses obtained from the (LLL,LLL) and (SSS,LLL) correlators respectively.

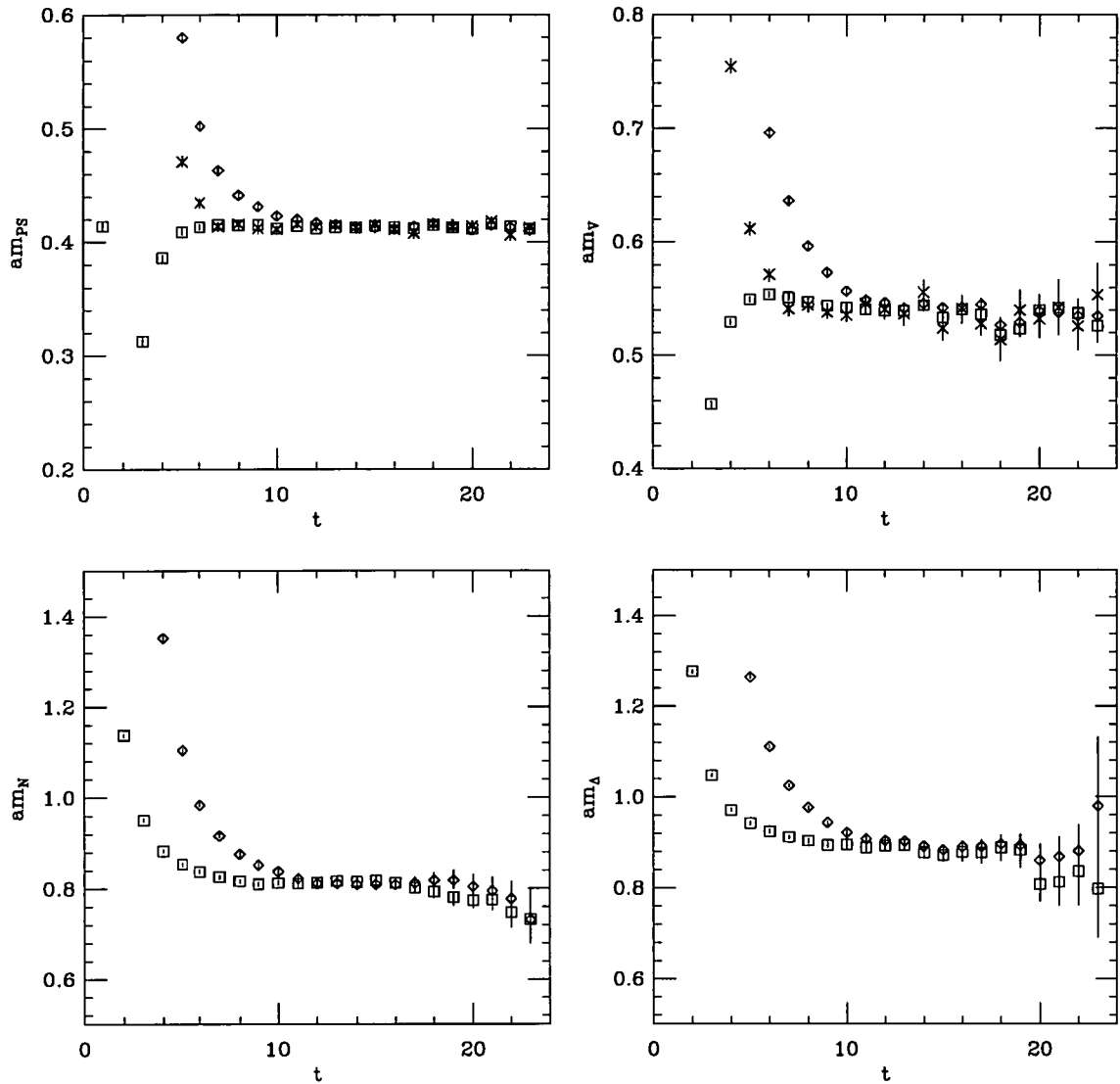


Figure 3.5: Effective masses for the pion, rho, nucleon and delta particles at $\beta = 6.0$, with $C=TAD$ and $\kappa = 0.13700$. For the pion and rho plots the (\diamond), (\square), and (\times), are the masses obtained from the (LL,LL), (FL,LL) and (FL,FL) correlators respectively. For the nucleon and delta plots the (\diamond) and (\square) are the masses obtained from the (LLL,LLL) and (FFL,LLL) correlators respectively.

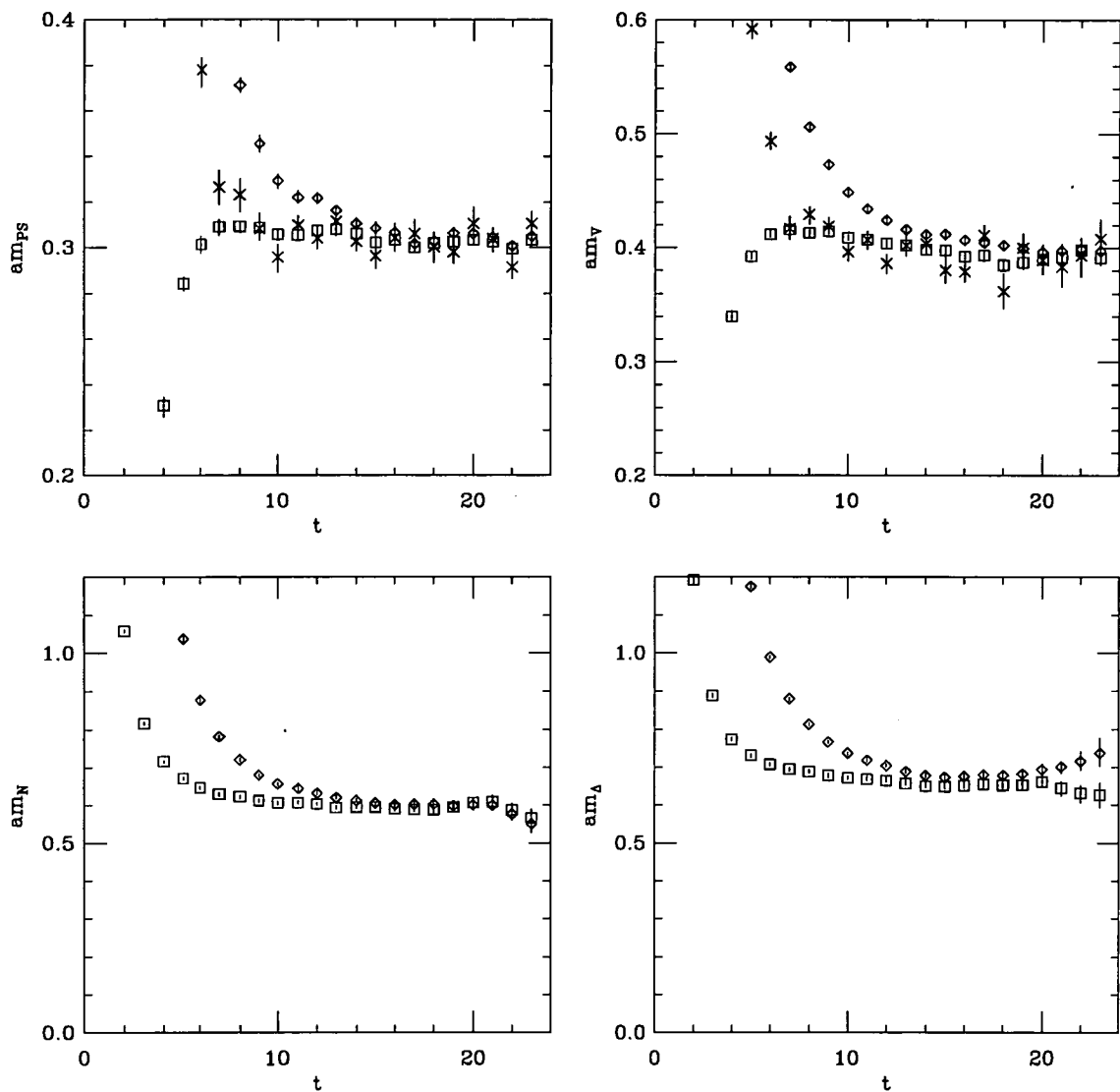


Figure 3.6: Effective masses for the pion, rho, nucleon and delta particles at $\beta = 6.2$, with C=TAD and $\kappa = 0.13640$. For the pion and rho plots the (\diamond), (\square), and (\times), are the masses obtained from the (LL,LL), (FL,LL) and (FL,FL) correlators respectively. For the nucleon and delta plots the (\diamond) and (\square) are the masses obtained from the (LLL,LLL) and (FFL,LLL) correlators respectively.

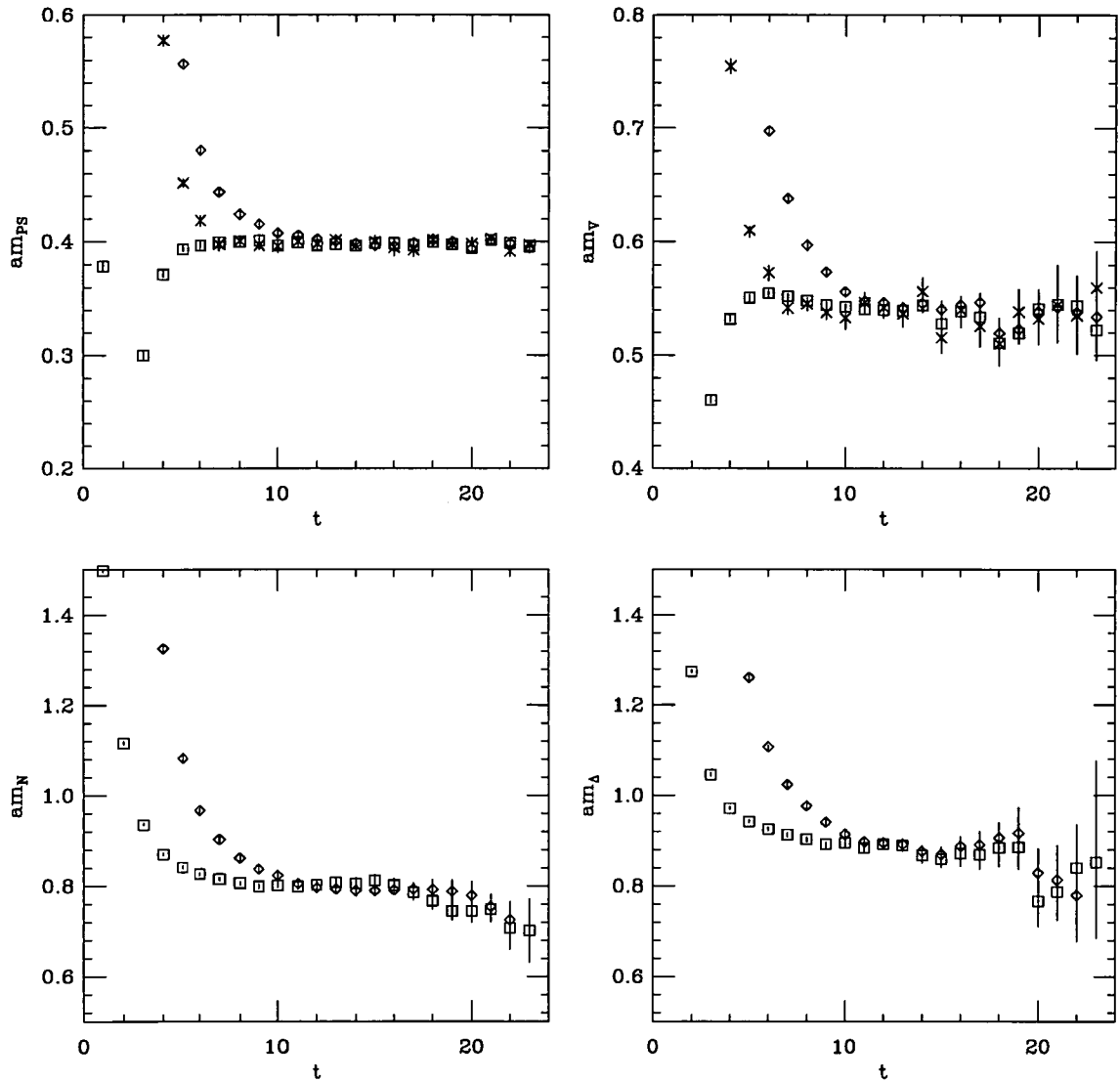


Figure 3.7: Effective masses for the pion, rho, nucleon and delta particles at $\beta = 6.0$, with $C=NP$ and $\kappa = 0.13344$. For the pion and rho plots the (\diamond), (\square), and (\times), are the masses obtained from the (LL,LL), (FL,LL) and (FL,FL) correlators respectively. For the nucleon and delta plots the (\diamond) and (\square) are the masses obtained from the (LLL,LLL) and (FFL,LLL) correlators respectively.

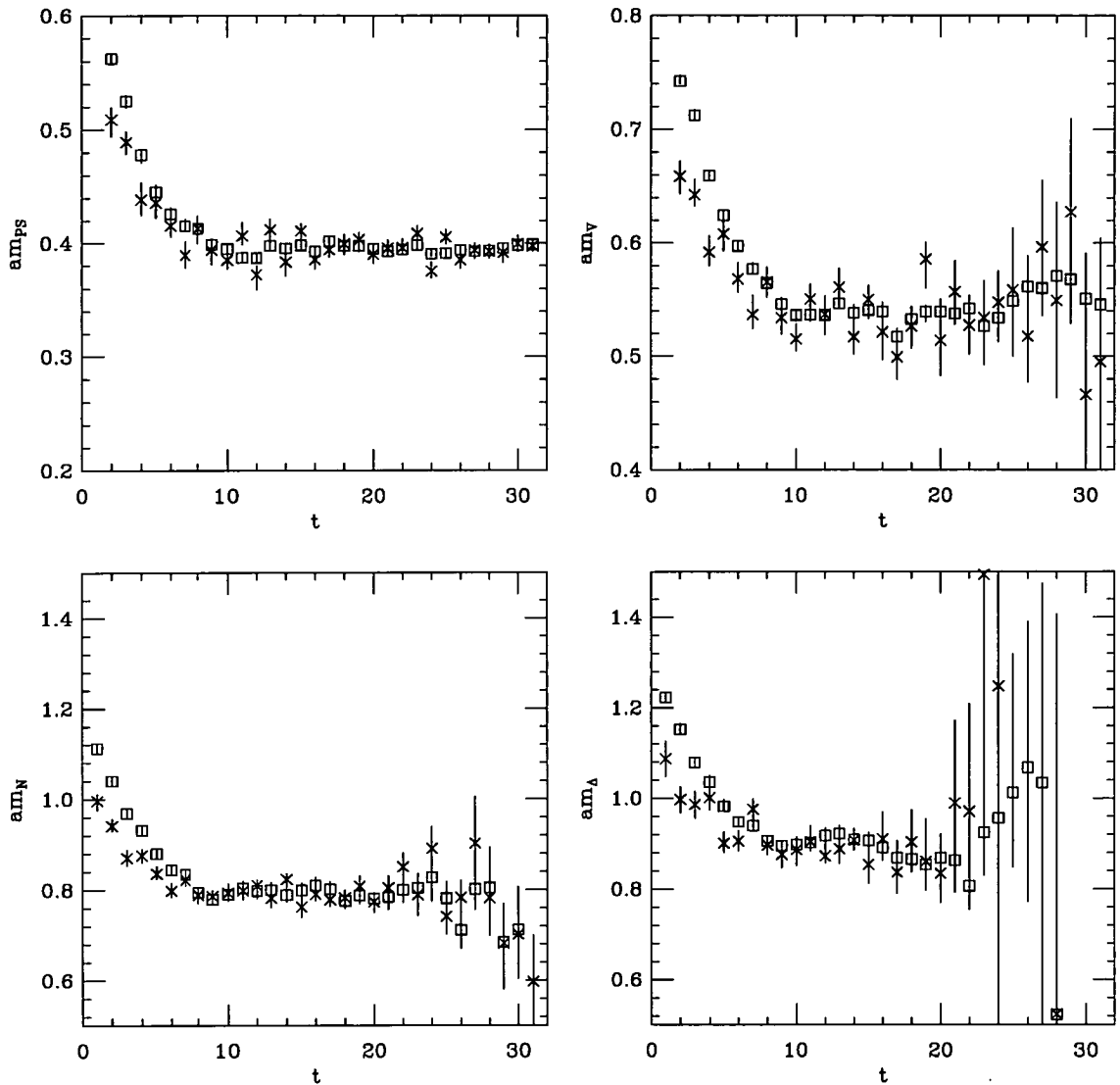


Figure 3.8: Effective masses for the pion, rho, nucleon and delta particles on the $32^3 \times 64$ lattice at $\beta = 6.0$, with $C=NP$ and $\kappa = 0.13344$. For the pion and rho plots the (\square), and (\times), are the masses obtained from the (SS,LL) and (SS,SS) correlators respectively. For the nucleon and delta plots the (\square) and (\times) are the masses obtained from the (SSS,LLL) and (SSS,SSS) correlators respectively.

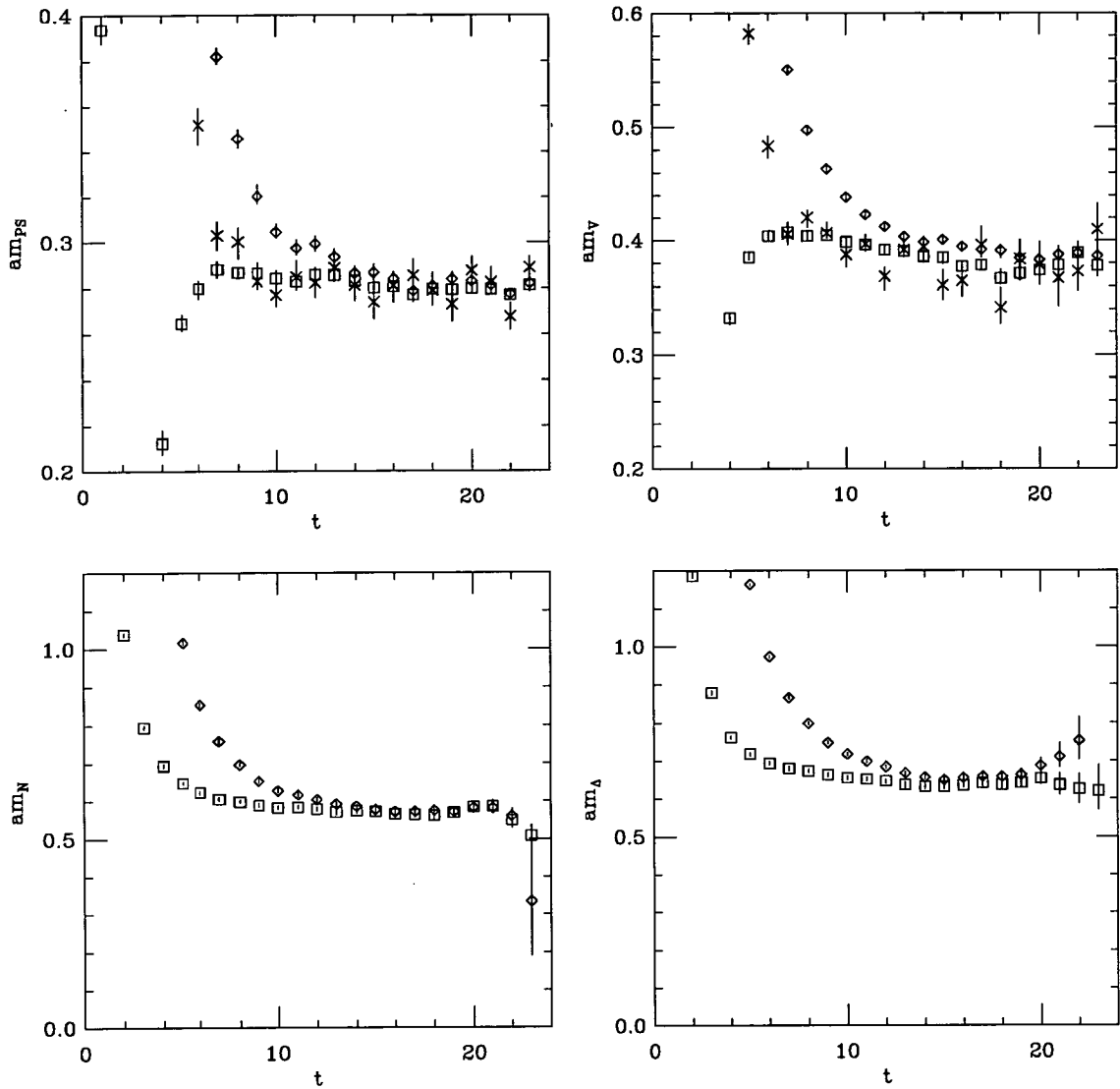


Figure 3.9: Effective masses for the pion, rho, nucleon and delta particles at $\beta = 6.2$, with $C=NP$ and $\kappa = 0.13460$. For the pion and rho plots the (\diamond) , (\square) , and (\times) , are the masses obtained from the (LL,LL), (FL,LL) and (FL,FL) correlators respectively. For the nucleon and delta plots the (\diamond) and (\square) are the masses obtained from the (LLL,LLL) and (FFL,LLL) correlators respectively.

3.2 Fitting Hadron Masses

Determining accurate measurements of the hadron masses from fitting the appropriate two-point functions and investigating the systematic errors involved in such a procedure is an essential part of any hadron spectrum calculation. This section first covers the principles involved in a general procedure, then explains the specific procedure which has been adopted in fitting the correlators which were computed.

3.2.1 The Multi-Exponential Fitting Procedure

In [82], effective mass plots from an ensemble of 1000 configurations at $\beta = 6.0$ on a $24^3 \times 64$ lattice, with Wilson fermions, show the phenomena of “wiggles” in the ground state plateau for point and wall sources, where by in the region of the plateau there are fluctuations on neighbouring timeslices larger than one standard deviation. Wiggles are present in the plateaux of the fitted mass plots shown in figures 3.3 to 3.9. The wiggles are explained through modelling the averaged propagator of a hadronic particle state for an ensemble of N configurations as a combination of the true propagator (obtained from a two exponential fit to the data) and independent random eigenvectors of the data covariance matrix (which was generated in the fit to the data) which are Gaussian distributed on every timeslice. The effective mass plots for any finite sample exhibit deviations from the plateau by more than one standard deviation, as does the real data. Thus the existence of such large fluctuations is a property of the covariance matrix, through having a finite ensemble size N . The consequences of this are that a plateau⁴ is rarely long lived and the definition of such a region is questionable. This causes problems when choosing the range of timeslices $[t_{\min}, t_{\max}]$ for fitting the hadron correlator to a single exponential in order to obtain the ground state mass. As more than one plateau could exist, stability of the fitted mass over different fitting ranges is a problem. This causes various groups [83, 51, 84, 85, 86] to adopted a number of different procedures to determine the fitting range, such as choosing

⁴In this context the plateau is defined to be where the effective mass $m_{eff}(t)$ does not fluctuate more than one standard deviation between timeslices in that region.

the start of the fitting range at the timeslice where the plateau begins and the end of the fitting range is chosen where either the errors of effective mass have doubled in size or the signal shows a clear break, is the procedure used in [51].

Clearly a reliable method is needed for the determination of the ground state mass. It is clear in figures 3.3 to 3.9 that fitting the hadron correlators to a single exponential in the region of the plateau, does not make the most of all the timeslices computed and at later timeslices the signal becomes noisier for the rho, nucleon and delta. Therefore, one would like to move t_{min} to earlier timeslices and push the fitting range as far out as possible while still maintaining a good chi-squared. However, a multi-exponential fit to a single correlator is usually unstable. It is much easier to do multi-exponential fits to several correlators simultaneously, and if each exponential has a significant amplitude in at least one correlator, life becomes a lot easier. At lower β , values the ground state plateau appears at earlier times and the use of many exponentials to get to early times is not as important at $\beta = 5.7$ as at $\beta = 6.2$

The method which we shall investigate makes use of multi-correlator multi-exponential fits, which are detailed in [87, 88] as follows. The general method which has been adopted to fit most of the data sets is to compute the local (point) correlators, denoted as L here, and the smeared correlators which have a good overlap with the ground 1 S-state, denoted as 1 here. Ideally one would like the smeared correlators which have a good overlap with the first excited state, called the 2 S-state, and even those which had an overlap with the higher radial excitations too, which would push t_{min} even further out,⁵ and would be useful at the higher β values.

The information provided by our fits cannot make any firm predictions for the masses and amplitudes of the 2 S-state, when fitting to more than one exponential and this is treated purely as noise, as there is no correlator included in the fit with a good overlap with this state. For mesons, in most cases all combinations of smearing types are computed, such that all elements of the 2×2 matrix

⁵Pushing t_{min} out means in this context starting the fit at an earlier timeslice.

M_S with entries {correlator source n_{sc} correlator sink n_{sk} } and $n_{sc}=n_{sk}=L,1$ are constructed. To expand on this further, the smearing matrix in the case of fuzzing is

$$M_S = \begin{pmatrix} LL & L1 \\ 1L & 11 \end{pmatrix} = \begin{pmatrix} LL & LF \\ FL & FF \end{pmatrix}. \quad (3.1)$$

The first type of fit one can do is to a matrix of correlation functions:

$$C_M(n_{sc}n_{sk}; t) = \sum_{n=1}^{N_{exp}} a(n_{sc}, n)a^*(n_{sk}, n)(e^{-m_n t} + e^{-m_n(T-t)}), \quad (3.2)$$

here one is assuming that $\eta_1\eta_2 = 1$ in equation (2.23), i.e. the case of a pion. The 2×2 matrix is fitted with $N_{exp} = 1$ and 2. The second type of fit is a row of correlation functions, which are fitted to

$$C_M(n_{sc}n_{sk}; t) = \sum_{n=1}^{N_{exp}} b(n_{sc}n_{sk}, n)(e^{-m_n t} + e^{-m_n(T-t)}). \quad (3.3)$$

This can be used to fit simultaneously a number of different combinations of correlation functions ($n_{sc}n_{sk}$), with $N_{exp} = 1$ and 2; usually the (LL) and ($1L$) correlators are fitted together. The second type of fit can be used for the baryon correlators. The four correlators which are the elements of the (2×2) matrix that are fitted in a matrix fit can be fitted in a row fit too, the fitted amplitudes are related through $b(n_{sc}n_{sk}, n) = a(n_{sc}, n)a^*(n_{sk}, n)$; the matrix fit reduces the number of fitting parameters by constraining the amplitudes such that $b(L1, n) = b(1L, n)$.

Another approach, which may prove fruitful, would be to include all the operators which had the overlap with the same state. In the case of the pion, this would correspond to fitting simultaneously the correlators with the Γ structure of the usual pseudoscalar (γ_5) operator together with the axial-vector ($\gamma_4\gamma_5$) and the corresponding cross correlators at the source and sink; here $\eta_1\eta_2 = -1$ in equation (2.23). However in the case of the pion, the correlators introduced into the fit are noisier, so the additional information provided by these channels is limited and therefore does not reduce the error in the fitted masses.

The numerical procedure to determine the fit parameters from minimising the χ^2 is the Levenberg-Marquardt algorithm [89, 90]. When fitting a number of correlators to more than one exponential, problems were experienced with this algorithm due to near-degeneracy of the minimum, so that the algorithm wanders around doing steepest descent in rather flat degenerate valleys. In [91], a number of different schemes are proposed to circumvent these problems with modifications to the algorithm. However these were found to be difficult to implement in practice. To tackle this problem a different approach was taken. The parameter space of variables,⁶ which the algorithm relied upon, were investigated by spanning the space of these variables and finding the region where the fitted parameters were consistent, and the variables were chosen from this region which did not unduly cause the algorithm to take a long time to converge. This study was carried out on all the different fits to the different hadron correlators. Different fitting ranges were used, so not to bias a particular value of $[t_{min}, t_{max}]$. The resultant fitting algorithm is not optimal, and rogue fits do occur, but they are infrequent and can be identified after looking at all the fitted parameters in a sliding window analysis when $[t_{min}, t_{max}]$ are varied.

An alternative procedure one can use to determine the initial fitting parameters, which are used as input to start the fitting algorithm, is to use the fitted parameters which have been obtained from a particular fitting range, and use this in the fits on all other fitting ranges; we denote this procedure as a ‘hard-wired guess’. It was found that using a hard-wired guess caused the fits using the other fitting ranges to be biased in some way, as the fitted masses obtained in a sliding window analysis were relatively stable whilst the amplitudes varied wildly. The

⁶In the algorithm itself, using the notation of [89] on page 683 onwards, there is the starting value of λ and the amount by which λ is increased or decreased when finding the global maximum. It was found in this case, starting with a larger value of λ around 1 rather than 0.001 suggested, and reducing the increment factor from 10 to 5, were a better choice in most cases. Secondly, the initial estimate of the fit parameters, which were used as input in the algorithm, played a rôle in finding the global minimum and these was investigated too. The main problem, encountered in the routines, is that it is difficult to find a relatively good estimate of the excited state mass and amplitude. The excited state mass was estimated to be some multiple of the ground state mass, hence introducing another variable, the excited state amplitudes could then easily be determined through modelling the correlator in the fit.

procedure that is implemented, to determine the initial fitting parameters was to determine a good estimate for the ground state mass and amplitudes from all the correlators in the region of the plateau, and to determine the excited state masses and amplitudes from these. After some work on the routines, it was found that the fits converged over the fitting range without any human intervention required to tune the fits, such as hard-wire guesses. Correlations between all time slices, and types of operator for simultaneous fits, were included. The covariance matrix was inverted using Singular Value Decomposition, without eliminating any eigenvalues. A comparison was made between using correlated and uncorrelated fits, and the two were found to be consistent, but as one might expect the errors from the correlated fit were smaller. The bootstrap algorithm [22], using 1000 bootstrap subsamples, was used to estimate the error on the fitted parameters at the 68% confidence levels, regenerating the covariance matrix for each subsample.

On performing all the possible multi-exponential fits to the hadron correlators on a given data set, using a sliding-window, a fitting range was chosen satisfying the following criteria:

- acceptable values for the quality of fit, Q , and $\chi^2/\text{d.o.f.}$;
- stability of the result for the ground state mass;
- agreement between the results obtained using a single exponential and a double exponential fit, and the fitting ansätze of using a row or matrix fit;
- ability of the fitting algorithm to resolve two masses;
- good agreement in the range of fitting window visually looking by eye at a plot of the fitted masses obtained from each of the correlators used in the fit and the appropriate curves produced from the fit parameters.

The variable Q , which is a function of χ^2 and $\nu = \text{d.o.f.}$ is defined [89] as

$$Q(\nu, \chi^2) = \frac{1}{\Gamma(\nu/2)} \int_{\chi^2/2}^{\infty} e^{-t} t^{\nu/2-1} dt. \quad (3.4)$$

It represents the probability that ν normal, random, uncorrelated variables, with a mean of 0 and unit variance, have a sum of squares which is greater than χ^2 . An acceptable value for Q lies around 0.5; a much smaller value indicates that the model used is incorrect, whereas a value approaching 1 indicates that too many parameters are being used. The stability criterion which we used is that the mass obtained does not change noticeably when the minimum time slice of the fit is changed slightly.

Fits to the hadron masses at $\beta = 6.0$ and $\beta = 6.2$

The data sets at both these β values and with the clover coefficients C=TAD and C=NP, on the smaller volume at $\beta = 6.0$, have the common feature that the meson and baryon correlators have been computed with the same smearing combinations using local and fuzzed propagators. It therefore seems appropriate to discuss these data sets together. The (LL,LL), (FL,LL), (LL,FL) and (FL,FL) meson correlators have been fitted in a row fit to the first two correlators alone and to all four correlators. In addition a matrix fit has been performed to all the correlators. Single exponential and double exponential were used with each of the fitting ansätze. Using more than two exponentials in the row fits is unstable, as there is no correlation with a strong overlap with the first excited state, so such a fit is unstable and the algorithm experiences problems with convergence. Sliding window plots for the pion and rho at $\beta = 6.0$ with C=TAD at the heaviest computed quark mass are shown in figures 3.10 and 3.11 respectively; the value of t_{max} has been set to timeslice 23 and t_{min} , is varied. For the case of the pion the signal is very clean out to this timeslice, and for the rho the error bars grow with time. Therefore the choice of t_{max} should not have any real affect on the fit. The sliding window plots display the fitted ground and excited state masses, Q, $\chi^2/\text{d.o.f.}$, and the ground state amplitudes for (LL,LL) and (FL,LL) correlators against t_{min} . The amplitudes are given in the form which would be obtained from the row fit. Thus the fitted amplitudes from the matrix fit are related as follows:

$$\text{G.S } A_{LL} = b(\text{LL}, 1) = a(\text{L}, 1)a^*(\text{L}, 1), \quad (3.5)$$

$$\text{G.S } A_{\text{FL}} = b(1L, 1) = a(1, 1)a^*(L, 1). \quad (3.6)$$

In the case of the pion, the fitted ground-state masses become stable after the excited state contamination has died away at $t_{\text{min}} = 5$ for the double exponential fit and $t_{\text{min}} = 12$ for the single exponential fit. There is agreement in the fitted mass between these regions. In these regions, we see there is clear agreement for the masses at the 1σ level, between all three fitting ansätze used, which is a good indication that the systematic errors in this procedure are under control. However the fitted amplitudes only agree within 2σ between the three fitting ansätze, which could indicate some minor systematic effects in this procedure. As the statistical noise does not grow with time for the pion, the errors on the fitted parameters are roughly equal for all t_{min} . The $\chi^2/\text{d.o.f.}$ in the stable regions are constant with t_{min} . The fit which was chosen for the pion was a row fit to (LL,LL) and (FL,LL) correlators using a double exponential with the fitting range [6,23]; as this fit has the smallest $\chi^2/\text{d.o.f.}$ and the best Q value, and one can see that this gives a good fit to the data in figure 3.17.

In the case of the rho, there is a similar picture to the pion for the t_{min} at which the fits stabilise, and for the agreement between the different fitting ansätze. However there are a number of clear differences: the single exponential fitted masses are not as stable as for the pion with varying t_{min} . In this case the statistical errors do grow with time, so there are advantages in using a double exponential fit over using a single exponential fit, both in the stability of the fitted mass and in the size of the error bars. There is no qualitative difference in the quality of the fit in the stable regions; the row fit to the (LL,LL) and (FL,LL) correlators was chosen, as the errors bars from this fit are smaller and are more symmetric than the other fits. Here again we can see that this choice gives a good fit to the data in figure 3.17. The fitted masses from this analysis are tabulated in appendix A. The data at the different clover coefficients C=TAD and C=NP have been generated with similar pion masses and the same smearing parameters, and it is no surprise that the type of fits chosen and fitting ranges are very similar.

The sliding window plots which have been discussed so far are at fixed β and at

a fixed quark mass which is the heaviest computed. On going to lighter quark masses, the only visible difference in the sliding window plots is that the quality of the fits becomes worse, as one would expect as the data becomes noisier. The fitting range and type of fit is the same at all the computed quark masses. To illustrate these last two points the chosen fits for the rho at all quark masses for $C=NP$ and $\beta = 6.0$ are shown in figure 3.12.

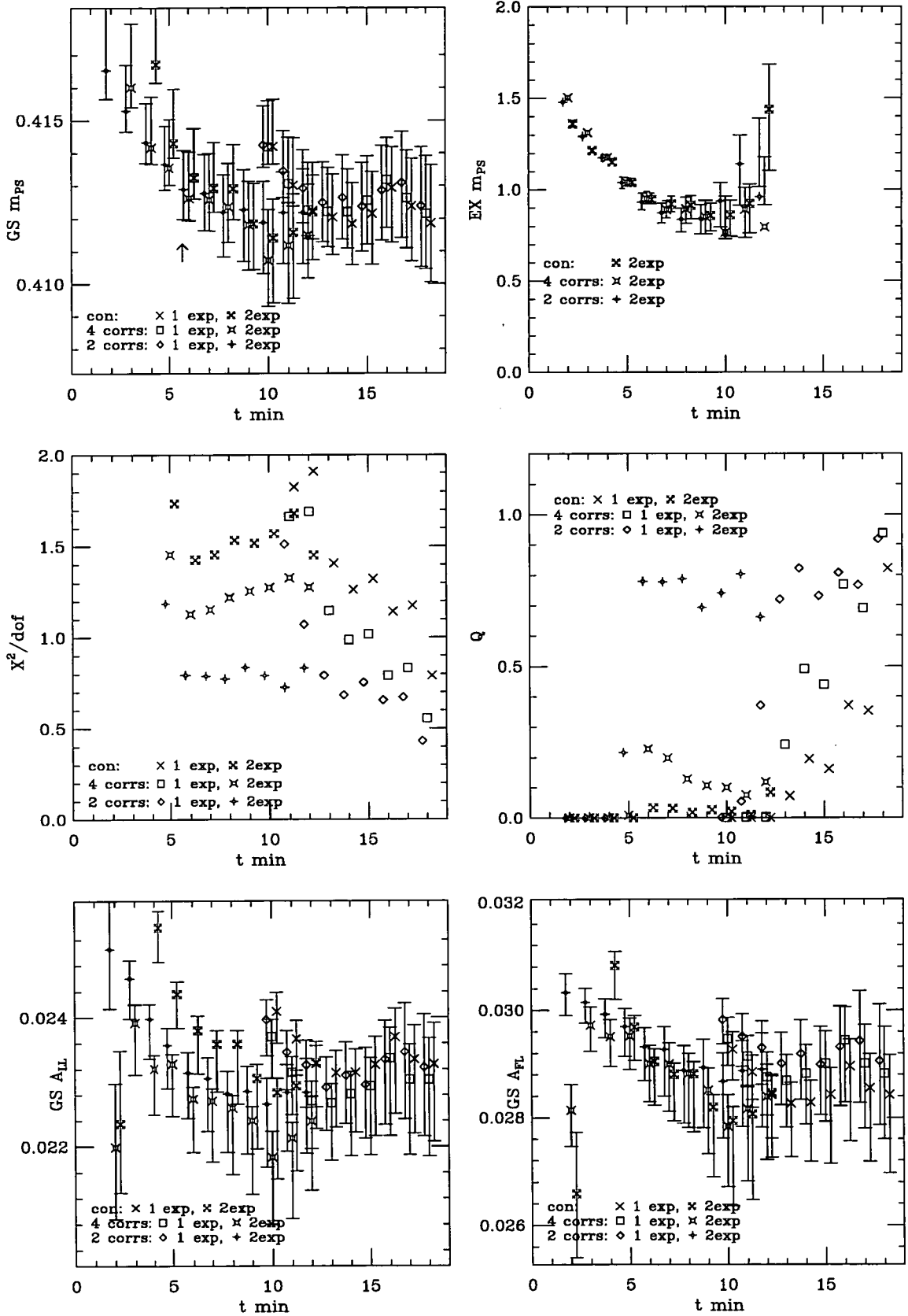


Figure 3.10: Sliding window plots for the pion at $\beta = 6.0$, with $C=TAD$ and $\kappa = 0.13700$. The fits corresponding to fitting the various combinations of the following correlators (LL,LL), (FL,LL), (LL,FL) and (FL,FL). The **2 corrs** fit is a row fit to the first two correlators, the **4 corrs** fit is a row fit to all the correlators and the **con** fit is a (2×2) matrix fit to all correlators. The chosen fit is a 2 corrs fit over the range $[6,23]$, with 2 exponentials.

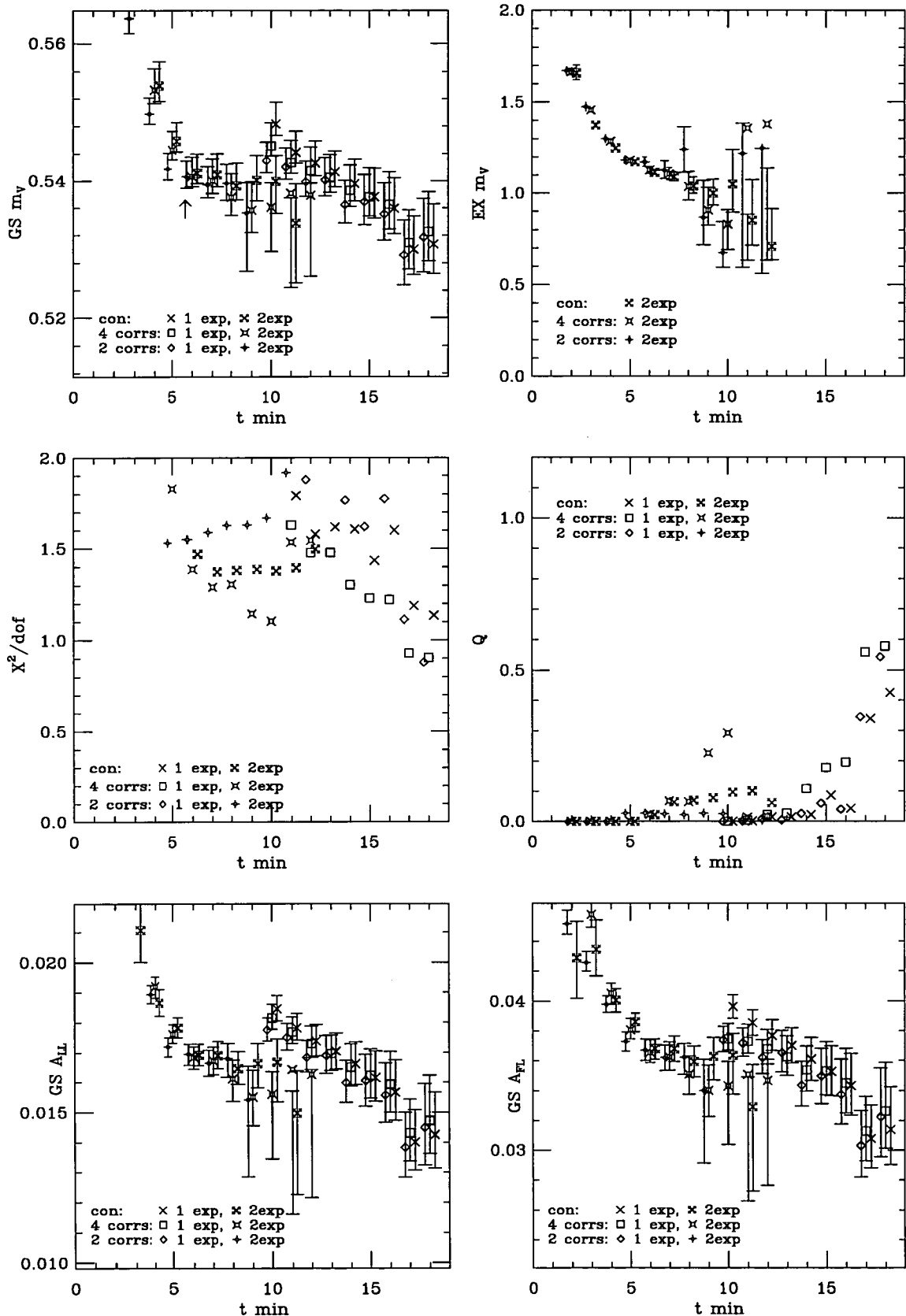


Figure 3.11: Sliding window plots for the rho at $\beta = 6.0$, with $C=TAD$ and $\kappa = 0.13700$. The fits corresponding to fitting the various combinations of the following correlators (LL,LL), (FL,LL), (LL,FL) and (FL,FL). The **2 corr** fit is a row fit to the first two correlators, the **4 corr** fit is a row fit to all the correlators and the **con** fit is a (2×2) matrix fit to all correlators. The chosen fit is a 2 corr fit over the range $[6,23]$, with 2 exponentials.

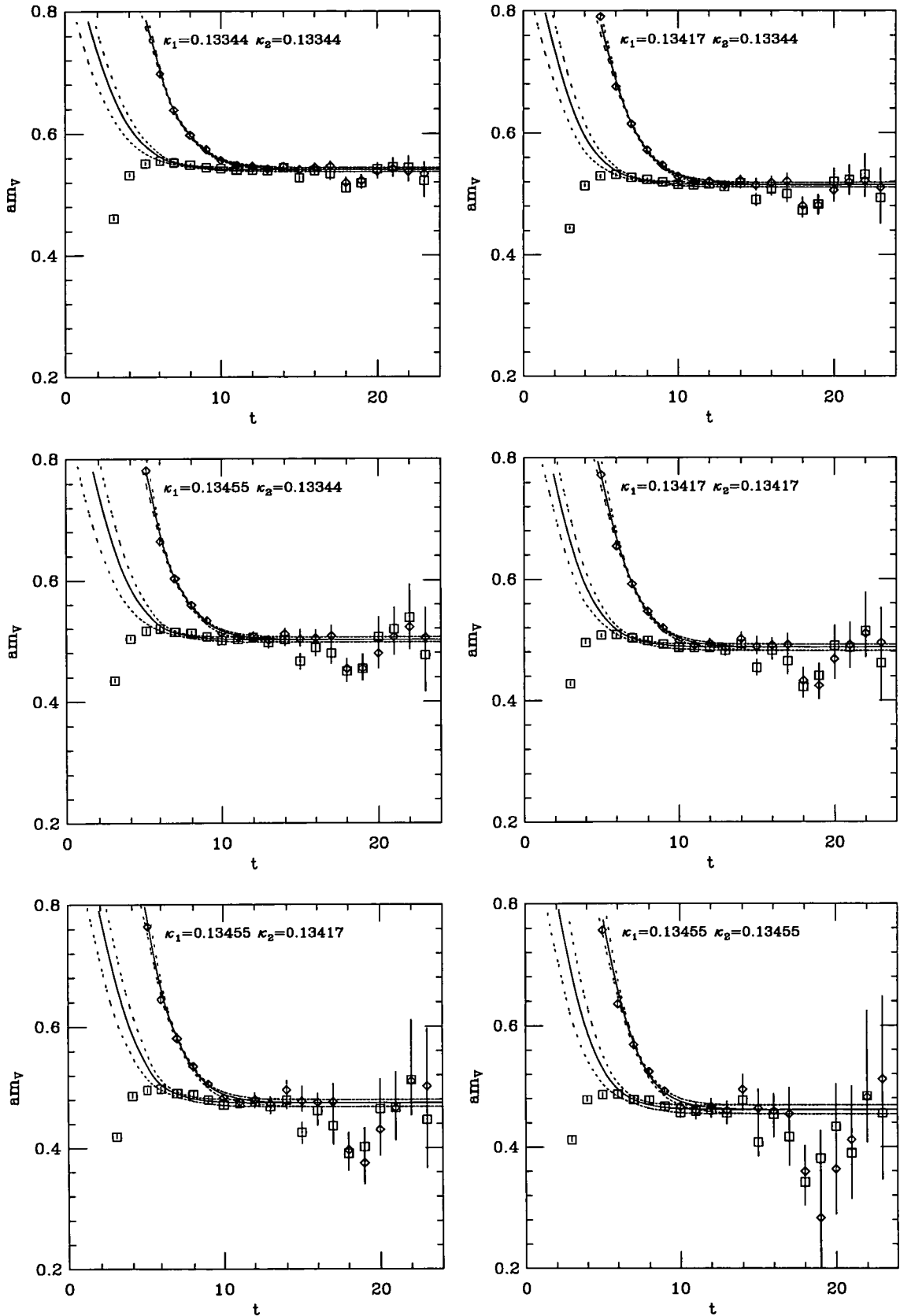


Figure 3.12: The plots show the row fits to the rho at $\beta = 6.0$, with $C=NP$ and on the $16^3 \times 48$ lattice. There is a plot for each of the computed quark masses. The (LL,LL) and (FL,LL) correlators are fitted with 2 exponentials from [6,23], the masses obtained from these correlators are represented by the (\diamond), and the (\square) respectively.

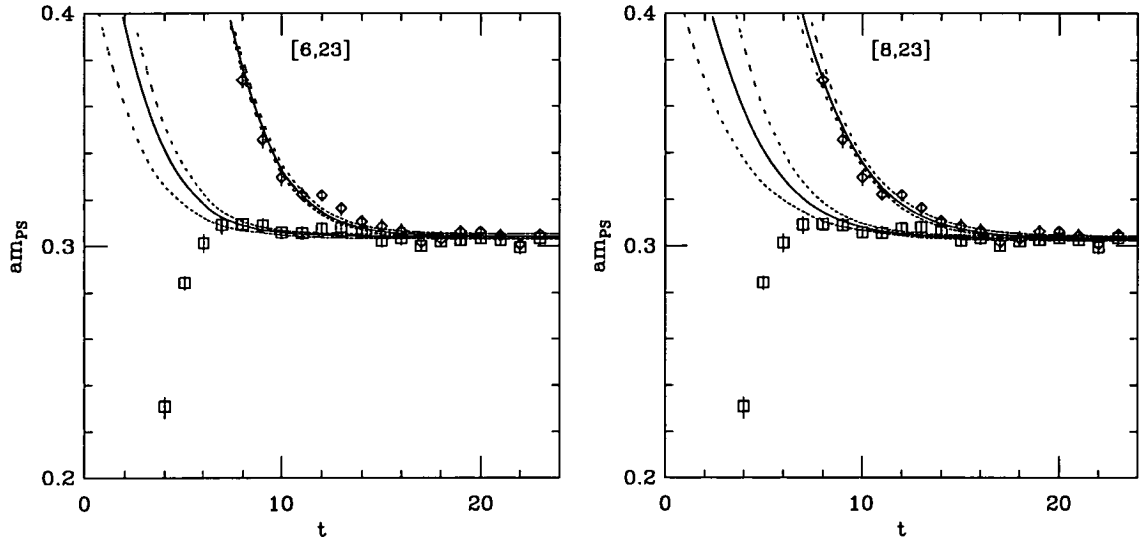


Figure 3.13: The plots show the row fits to the pion at $\beta = 6.2$, with $C=TAD$, and $\kappa = 0.13640$. The (LL,LL) and (FL,LL) correlators are fitted with 2 exponentials from [6,23] and [8,23] in the plot on the left and right respectively. The masses obtained from these correlators are represented by the (\diamond), and the (\square) corresponding to (LL,LL) and (FL,LL) correlators respectively.

At $\beta = 6.2$, in the sliding window plots for the pion, which have not been shown here, the ground state mass stabilises at a larger value of t_{min} for both the single exponential and double exponential fits, as the local correlator takes longer to plateau. Therefore trying to push t_{min} out further in the fit will contain excited state contamination, as the local correlator has an overlap with all the S-states, so contains contamination from the second excited state in this case. Taking this into consideration the sliding window plots are essentially similar to the case of pion at $\beta = 6.0$, and therefore a row fit is chosen to the standard two correlators from [8,23]. The sliding window plots for the rho at $\beta = 6.2$, with $C=TAD$, are shown in figure 3.14. The same situation applies here in comparing the sliding window plots at $\beta = 6.2$ and $\beta = 6.0$, as just described. Again the row fit to the same correlators over the same fitting range as in the case of the pion is preferred. In figures 3.13 and 3.14, using the chosen row fit, a comparison is made between fitting from [6,23] and [8,23] for the pion and rho respectively. For

the pion one can see that the fit from [8,23] gives a slightly better fit to the data. For the rho there is a large difference between the fits to the data over these two ranges and this highlights the danger of not fitting over the right window. The plateau for the rho (FL,LL) correlator is not as good for the pion, and looks to still contain contamination from the first excited state, as there is a small rise in the plateau, before falling off with second excited state. To push t_{min} further out at $\beta = 6.2$, one would be required to fit to more than two exponentials and this was not undertaken as there was no correlation computed which had a good overlap with the first excited state, and therefore fits to three exponentials would become unstable, but should be considered if one wanted to improve this study.

The baryon correlators are fitted to a simultaneous multi-correlator multi-exponential fit as follows:

$$C_B(n_{sc}, n_{sk}; t) = \sum_{n=1}^{N_{exp}} b(n_{sc}n_{sk}, n) e^{-m_n t}. \quad (3.7)$$

At $\beta = 6.0$ with C=TAD, sliding window plots for the simultaneous fit to the (LLL,LLL) and (FFL,LLL) correlators to one and two exponentials for the ‘ Σ -like’ and Δ correlators are shown in figures 3.15 and 3.16. The fits stabilise at a similar t_{min} as for the case of the pion at this β value. In the figures, the chosen fitting range is indicated by an arrow, and the double exponential fit is chosen, as the error bars are smaller than for the single exponential fit. We can see how well these fitted parameters fit the masses obtained from the correlators in figure 3.17. Sliding window plots have not been shown for the fits of ‘ Λ -like’ correlators as they show quantitatively the same features as the ‘ Σ -like’ plots.

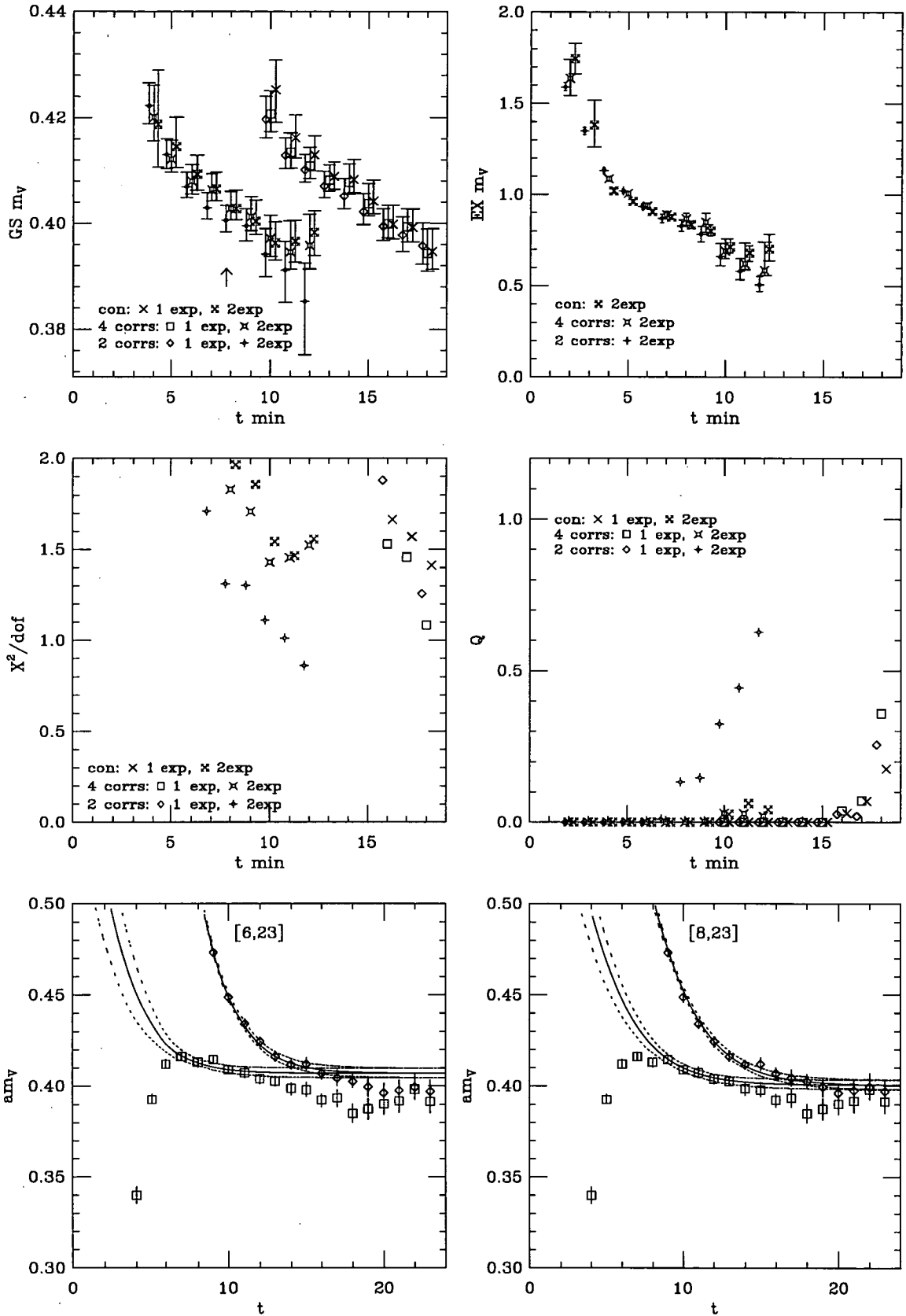


Figure 3.14: Sliding window plots for the rho at $\beta = 6.2$, with $C=TAD$ and $\kappa = 0.13640$. The fits correspond to the same as given in the caption of figure 3.11. The plots are the bottom show effective mass plots for the rho, superimposed are curves that correspond to fitted parameters which are both obtained with a row fit to the (LL,LL), (FL,LL) correlators using a double exponential fit, the fitting ranges are labelled on each graph.

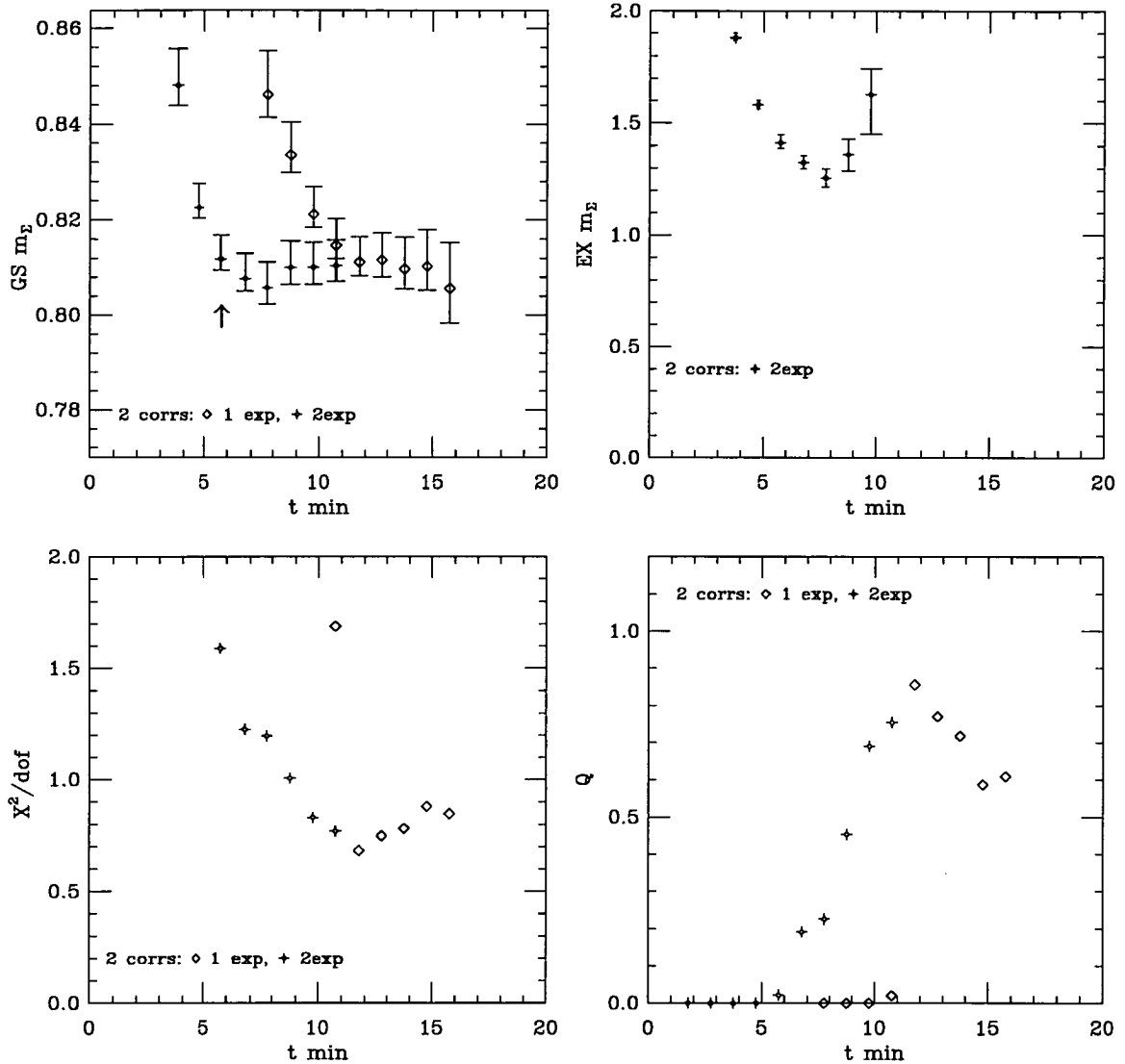


Figure 3.15: Sliding window plots for the ‘ Σ -like’ baryon at $\beta = 6.0$, with $C=TAD$ and $\kappa = 0.13700$. The fits corresponding to fitting the (LLL,LLL) and (FFL,LLL) correlators to a single and a double exponential row fit. The chosen fitting range is $[6,23]$, with 2 exponentials.

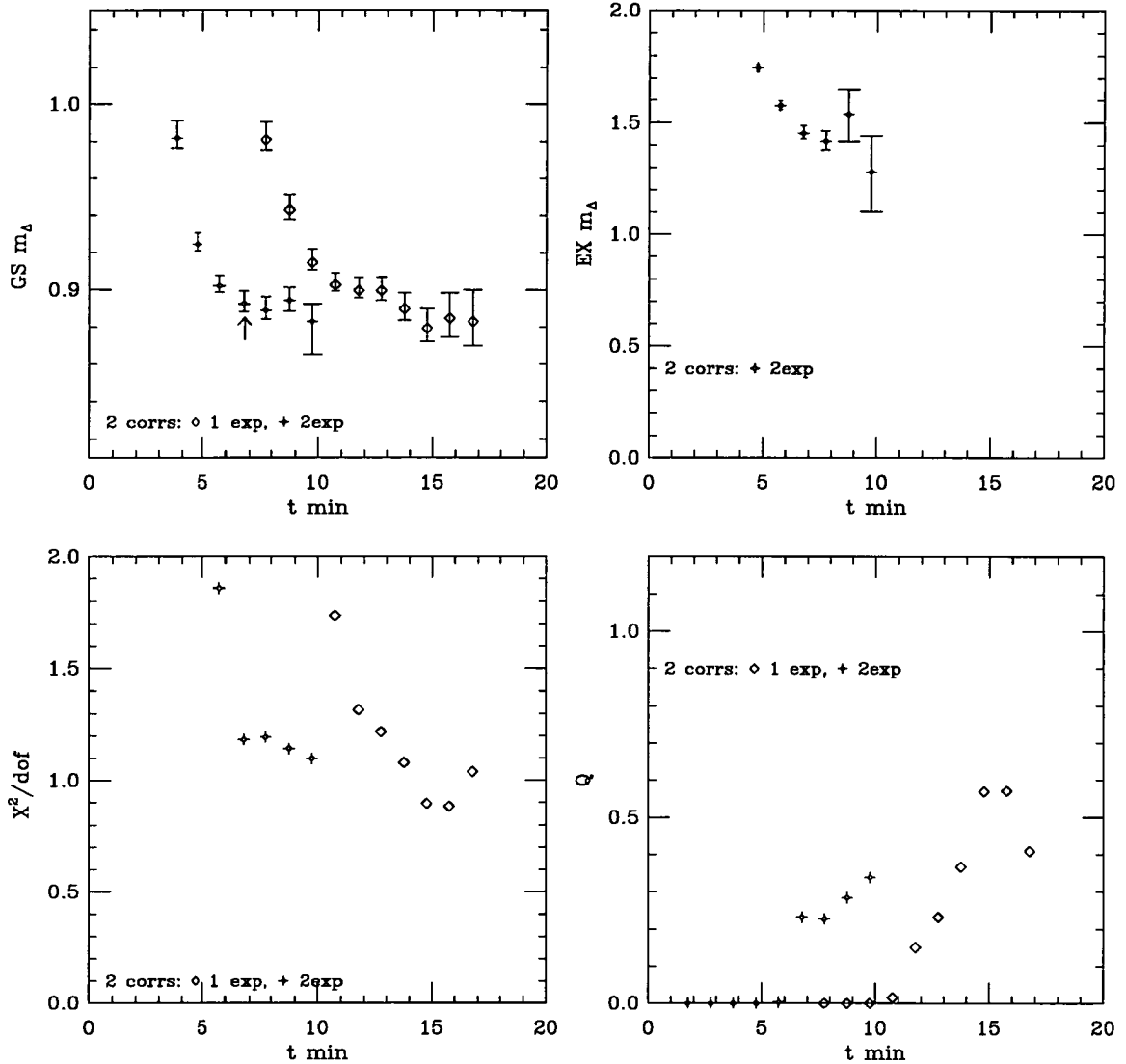


Figure 3.16: Sliding window plots for the Δ baryon at $\beta = 6.0$, with $C=TAD$ and $\kappa = 0.13700$. The fits corresponding to fitting the (LLL,LLL) and (FFL,LLL) correlators to a single and a double exponential row fit. The chosen fitting range is $[7,23]$, with 2 exponentials.

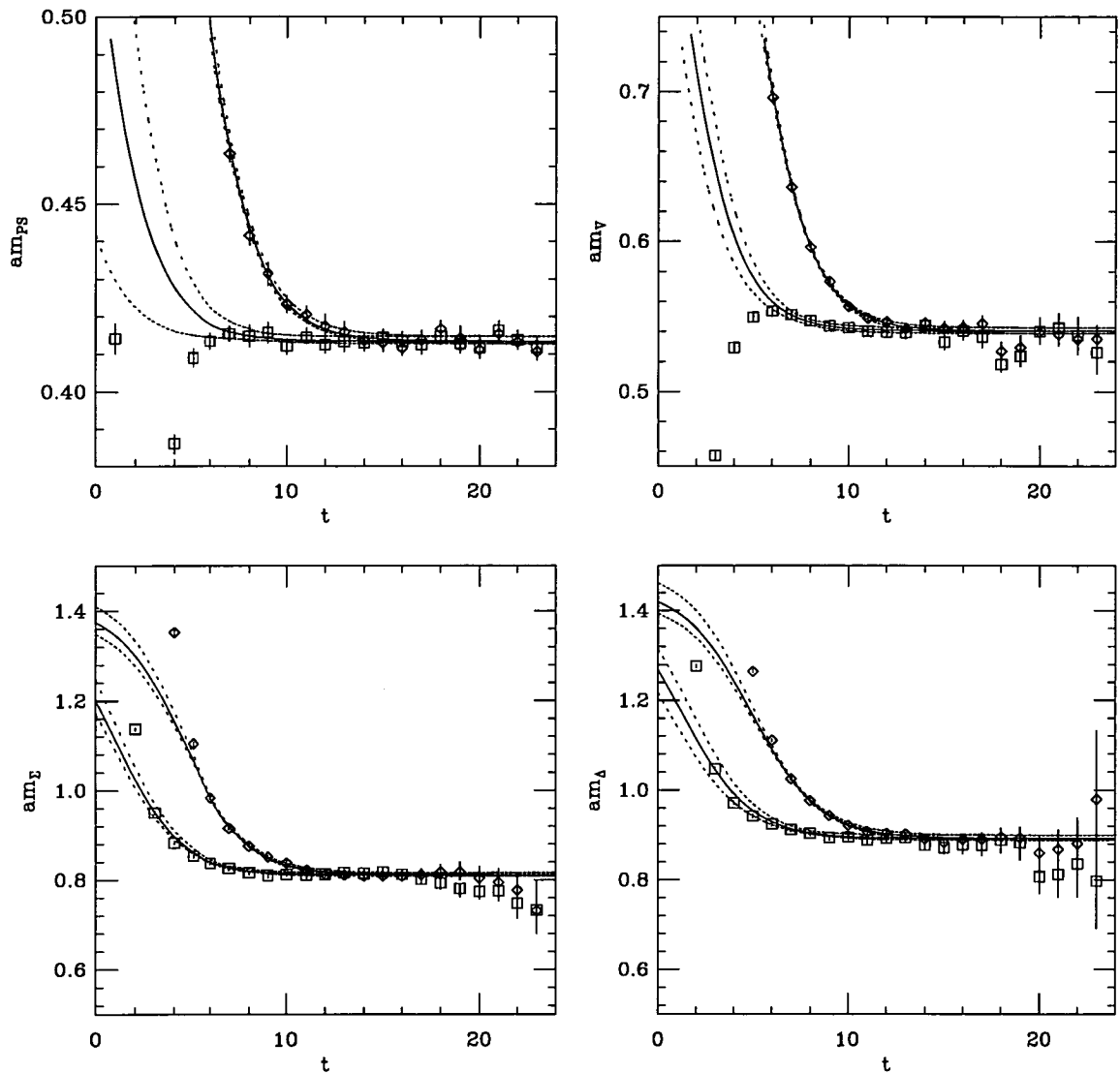


Figure 3.17: Fitted masses for the pion, rho, sigma and delta particles at $\beta = 6.0$, with C=TAD and $\kappa = 0.13700$. The pion and rho masses obtained from the (LL,LL), (FL,LL) correlators correspond to the (\diamond), and (\square), respectively. The ‘ Σ -like’ and Δ masses obtained from the (LLL,LLL) and (FFL,LLL) correlators correspond to the (\diamond) and (\square), respectively. Displayed are the curves corresponding to the fitted parameters obtained from the row fits to the data with the chosen fitting ranges given in figures 3.10 to 3.16.

Fits to the hadron masses at $\beta = 5.7$, with C=TAD

Using the (LL,LL), (SL,LL) and (SS,LL) meson correlators row fits were performed to the first two correlators and to all correlators for the pion and vector. It was found that double exponential fits started to stabilise at $t_{min} = 3$ and single exponential fits at $t_{min} = 6$. In this region there is good agreement between the single and double exponential fits and between both types of row fit. A typical sliding window plot is shown for the heaviest pion on the small volume is shown in figure 3.18. The double exponential fit to the (LL,LL) and (SL,LL) correlators using the range [3,12] for the pion and [4,12] for the vector on the small volume and [3,16] for the pion and [4,16] for the vector on the large volume were chosen, ⁷ as these fits had better $\chi^2/d.o.f.$ and slight smaller error bars in the fitted masses over the other fits. In the case of the rho on the smaller volume, it was found that fitting simultaneously the interpolating operators which have an overlap with the rho and correspond to interpolating operators bi-linear in quark fields with Γ structures $\vec{\gamma}$ and $\vec{\gamma}\gamma_4$, reduced the error on the fitted ground state mass.

Like the rho on the small volume, the best fit to the nucleon is obtained by fitting the (SSS,LLL) to a double exponential fitting simultaneous the interpolating operators

$$\mathcal{O}_{(ij)k}(x) = (\psi_i^a(x)C\gamma_5\psi_j^b(x))\psi_k^c(x)\epsilon_{abc}, \quad (3.8)$$

and

$$\mathcal{O}_{(ij)k}(x) = (\psi_i^a(x)C\gamma_4\gamma_5\psi_j^b(x))\psi_k^c(x)\epsilon_{abc}, \quad (3.9)$$

reduced the error in the fitted mass. The fitting ranges chosen are [2,11] and [2,15] for the small and large volume respectively. The spin- $\frac{3}{2}$ decuplet masses were fitted using the (LLL,LLL) and (SSS,LLL) correlators with a double exponential with the fitting range of [5,11] and [6,15] on the small and large volume respectively.

⁷The data on both lattices was studied extensively in [78], we draw slightly different conclusions on the choice of fit and fitting ranges, because of a slightly different fitting procedure. However the results of the fitted masses are consistent with their results.

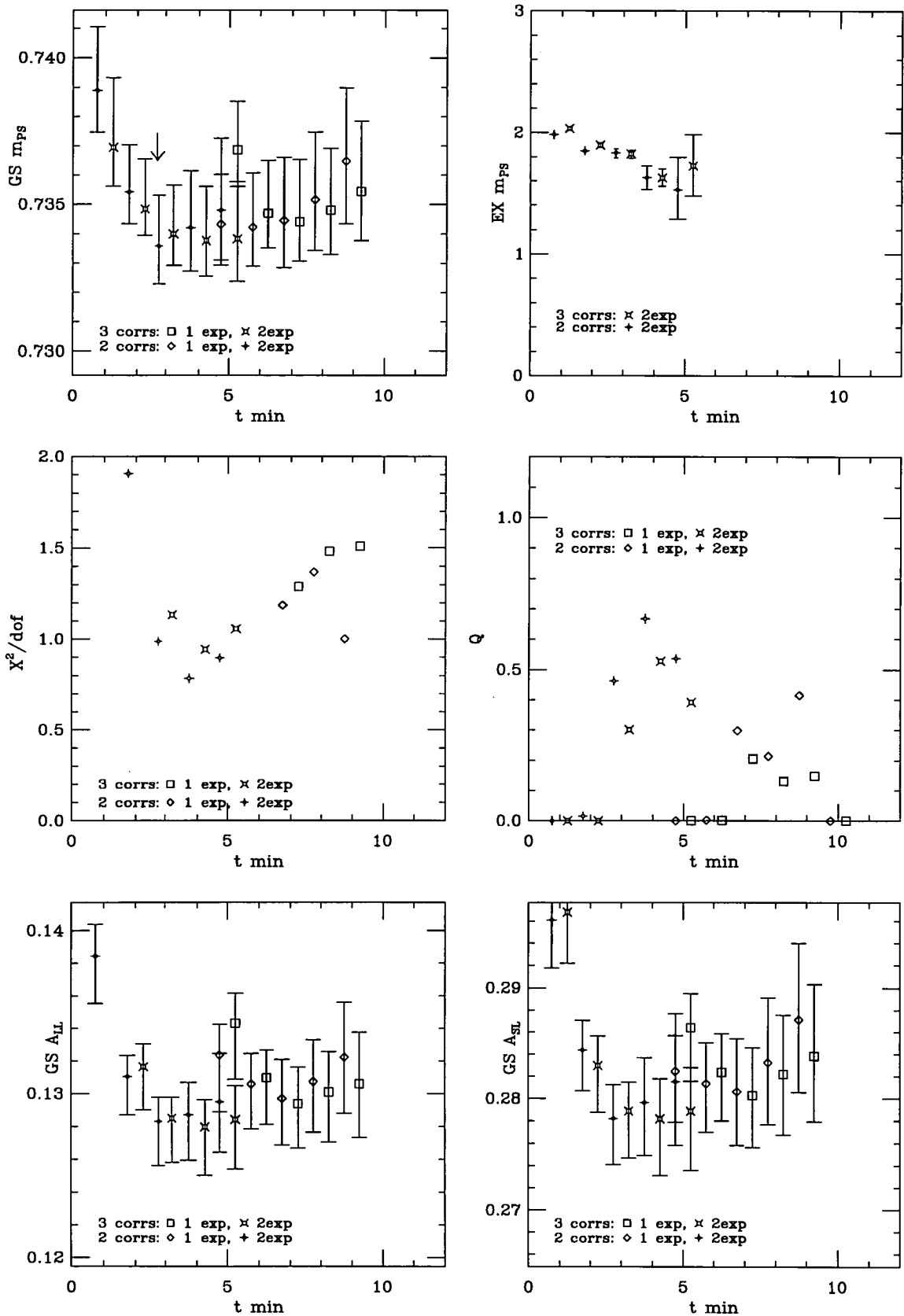


Figure 3.18: Sliding window plots for the pion on the $12^3 \times 24$ lattice at $\beta = 5.7$, with C=TAD and $\kappa = 0.13843$. The fits corresponding to fitting the various combinations of the following correlators (LL,LL), (SL,LL), and (SS,LL). The **2 corr**s fit is a row fit to the first two correlators, the **3 corr**s fit is a row fit to all correlators. The chosen fit is a 2 corr fit over the range [3,12], with 2 exponentials.

Fits to the hadron masses on the $32^3 \times 64$ lattice at $\beta = 6.0$, with C=NP

This data set is unique in that only smeared propagators were computed. Therefore in general multi-exponential multi-correlator fits could not be used. For the pion and rho a single exponential was fitted to (SS,LL) correlator from [9,19] and [10,15], respectively, and these fits are shown in figure 3.19. Double exponential fits to these correlators were unstable and including the (SS,SS) correlators caused the error bars to increase on the fitted masses. The fitting ranges were chosen by fixing t_{min} at where the effective mass begins to plateau, the value of t_{max} was taken at an acceptable value of $\chi^2/\text{d.o.f.}$ and where the error bars on the fitted mass were relatively symmetric. It is worth commenting that the central value of the fitted mass is stable on changing t_{max} . Increasing t_{max} to later timeslices; reduces the errors for the pion, but the error bars become asymmetric and the error on the fitted rho mass is unchanged. This procedure is not as systematic as the multi-exponential fitting procedure at determining the fitting range and therefore taking the result with the larger errors is the safest option.

The ‘ Σ -like’ correlators and the ‘ Λ -like’ correlators are similar, so they are included in this discussion. It was found that the best fit was to the (SSS,LLL) and (SSS,SSS) with a double exponential from [2,18], after considering fitting the correlators to a single or double exponential fit, and including in the fit the additional interpolating operators to the one given in equation (2.26) that have an overlap with spin- $\frac{1}{2}$ baryons, like

$$\mathcal{O}_{(ij)k}(x) = (\psi_i^a(x) C \gamma_4 \gamma_5 \psi_j^b(x)) \psi_k^c(x) \epsilon_{abc}, \quad (3.10)$$

which has a good overlap with with the spin- $\frac{1}{2}$ baryons. For the Δ correlators a double exponential fit from [2,16] to the (SSS,LLL) correlators was found to be the best.

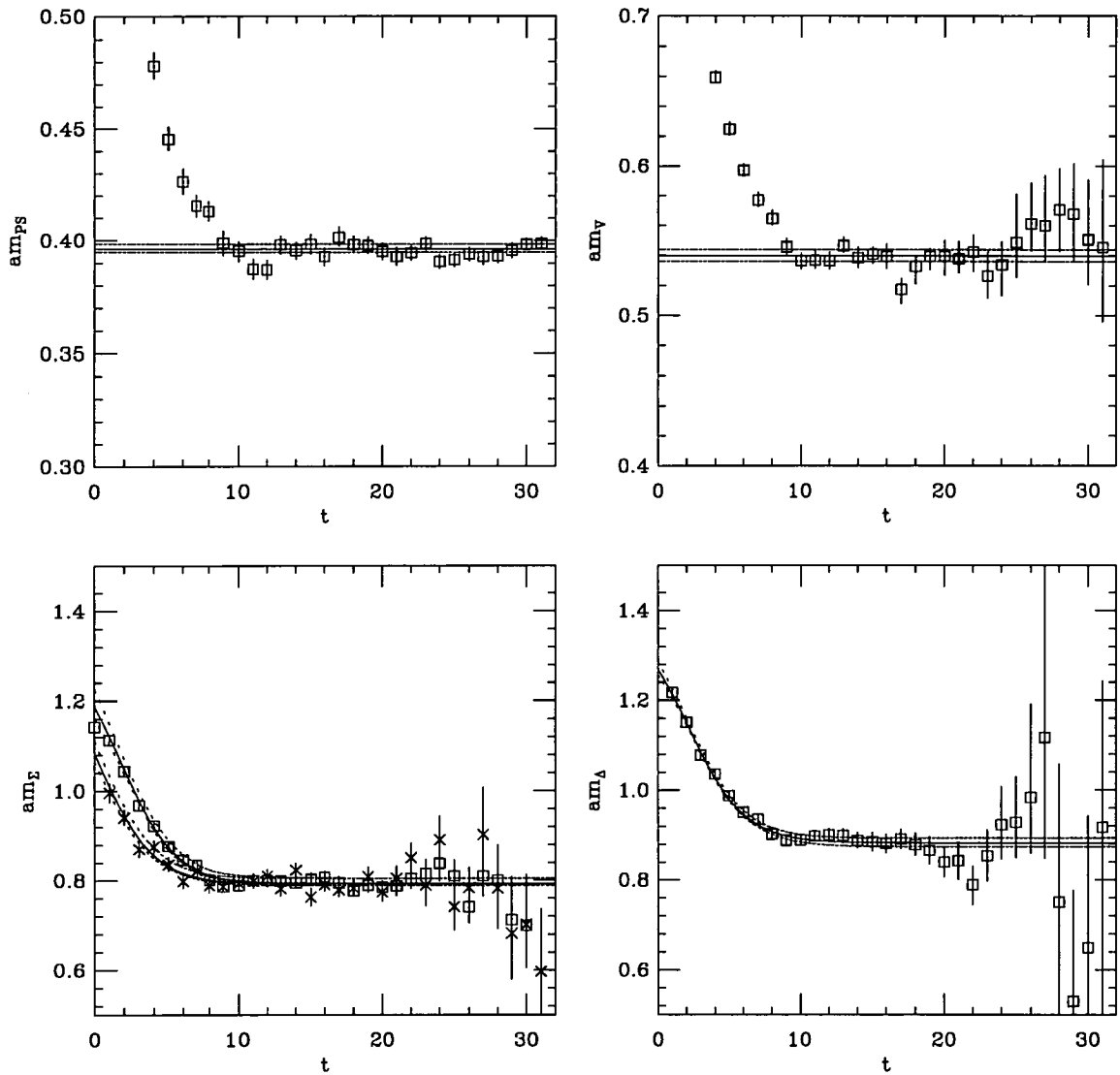


Figure 3.19: Fitted masses for the pion, rho, sigma and delta particles on the $32^3 \times 64$ lattice at $\beta = 6.0$, with $C=NP$, $\kappa = 0.13344$. For the pion and rho plots the (\square), are the masses obtained from the (SL,LL) correlator. For the sigma and delta plots the (\square) and (\times) are the masses obtained from the (SSS,LLL) and (SSS,SSS) correlators respectively. The fitted curves to the masses, in each of the plots, are from row fits to the data with the chosen fitting range, given in appendix A.

3.2.2 Some comments on the other hadronic states measured

To finish this section it is worth mentioning the other particles which were calculated. In the meson sector there are the scalar $S(0^{++})$, axial $A(1^{++})$, and tensor $T(1^{+-})$ operators, which have an overlap with the a_0 , a_1 and b_1 meson states, respectively. The effective masses of these states at $\beta = 6.0$ and C=TAD are shown in figure 3.20. At the heaviest quark mass computed we can see there is a clear signal at earlier timeslices which become noisy at later timeslices, but can be fitted successfully with multi-correlator multi-exponential fits. At lighter quark masses the signals for the $S(0^{++})$ and $T(1^{+-})$ become very poor, as can be seen in the effective masses at $\kappa = 0.13856$. At this quark mass the signal for the $A(1^{++})$ is also very poor too, but can be fitted using multi-exponential multi-correlator fits. We will not discuss fits to these states any further.

The other baryon states which are calculated in addition to those which have been already mention in this chapter are listed in table 2.2 with the interpolating field operators used to create each state. The additional baryon states are as follows: the $\Delta(\frac{1}{2})$ with $I(J^P) = \frac{3}{2}(\frac{1}{2}^+)$, the negative parity partner of this state $\Delta^{np}(\frac{1}{2})$ with $I(J^P) = \frac{3}{2}(\frac{1}{2}^-)$ and the negative parity partners of the ‘ Σ -like’, ‘ Λ -like’ and $\Delta(\frac{3}{2})$ correlators. In figure 3.21, examples of the effective masses of these correlators are shown which were calculated at $\beta = 6.0$ with C=TAD, at degenerate quark masses, so the parity partners of ‘ Σ -like’ and ‘ Λ -like’ correlators are represented by N^{np} . The picture here is similar to the mesonic correlators just discussed, in that the signal disappears in going to lighter quark masses for the N^{np} and $\Delta^{np}(\frac{3}{2})$ correlators. In the case of $\Delta(\frac{1}{2})$ correlator and its negative-parity partner the signal at the heaviest quark mass $\kappa = 0.13700$, is very poor and it seems there is a discrepancy between the effective masses obtained from the (LLL,LLL) and the (FFL,LLL) correlators. In light of these problems of the poor quality of signal, these states shall no longer be considered in this analysis.

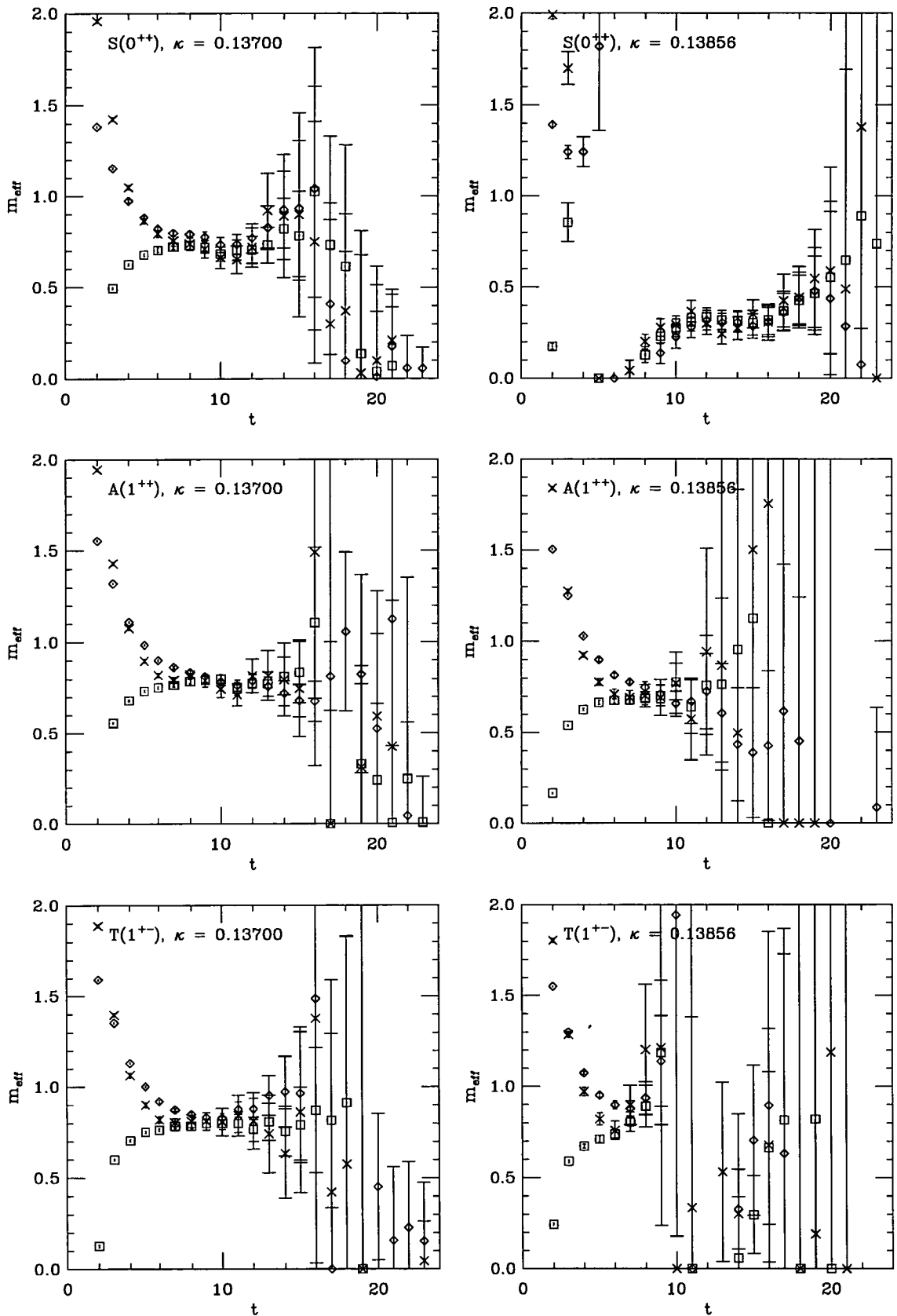


Figure 3.20: Effective masses at $\beta = 6.0$ and $C=TAD$ for the $S(0^{++})$, $A(1^{++})$, and $T(1^{+-})$, mesons calculated with degenerate quark propagators at the heaviest and lightest quark masses simulated corresponding to $\kappa = 0.13700$ and $\kappa = 0.13856$. The (\diamond), (\square) and (\times) correspond to the masses obtained from (LL,LL), (FL,LL) and (FL,FL) respectively.

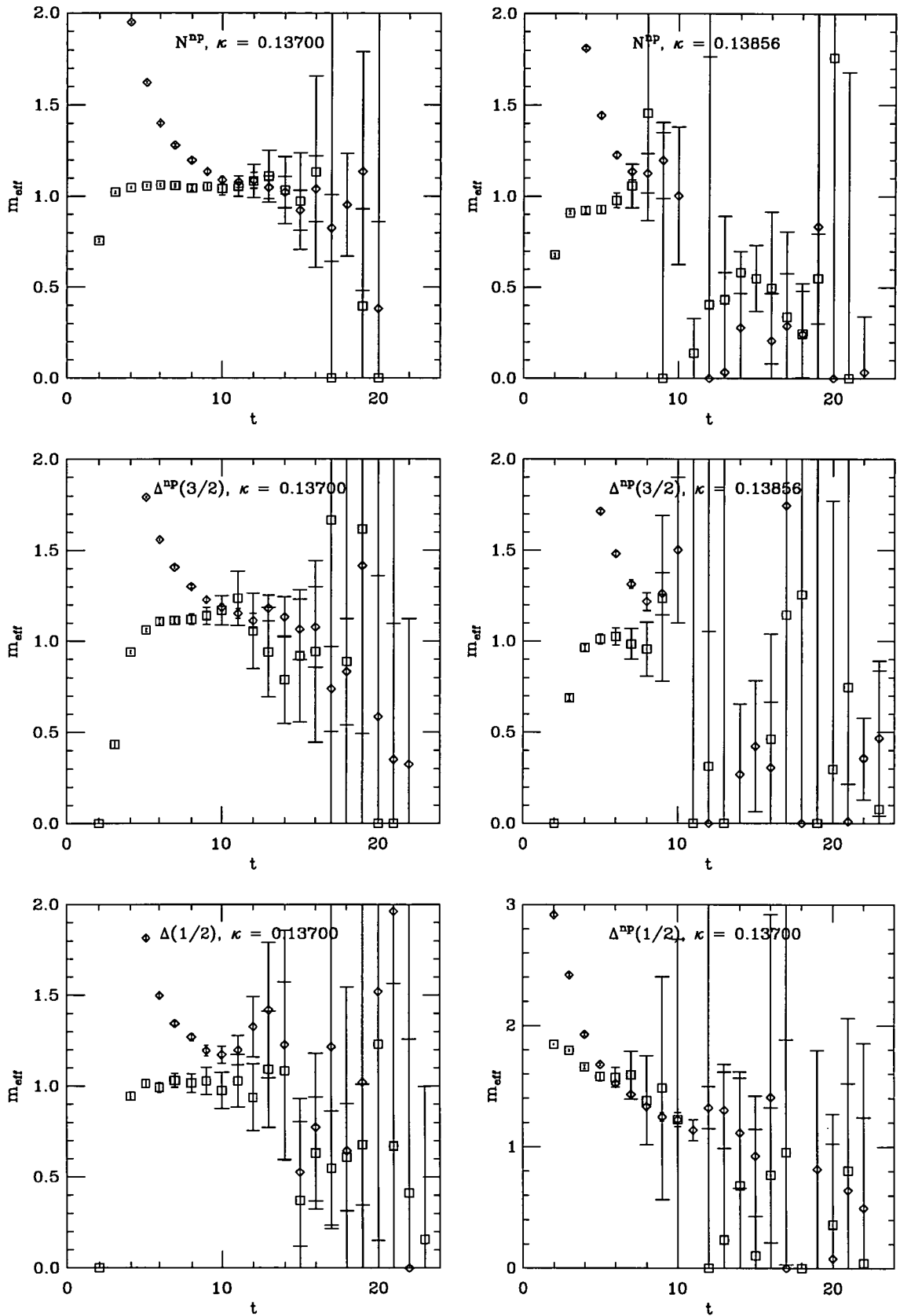


Figure 3.21: Effective masses at $\beta = 6.0$ and C=TAD for the N^{np} , $\Delta^{\text{np}}(\frac{3}{2})$, $\Delta^{\text{np}}(\frac{1}{2})$, and $\Delta^{\text{np}}(\frac{1}{2})$ baryons calculated with degenerate quark propagators at the heaviest and lightest quark masses computed corresponding to $\kappa = 0.13700$ and $\kappa = 0.13856$. The (\diamond), and (\square), correspond to the masses obtained from (LL,LLL) and (FFL,LLL) respectively.

Chapter 4

The Light Hadron Spectrum

4.1 Finite Volume Effects

An extensive theoretical study of finite volume effects on field theoretic calculations has been carried out by Lüscher [92]. Consider, for example, the effect on the mass of a particle, m_p . For large enough volume, the leading effect is due to the propagation of the lightest mass meson (e.g. pion) “around the world,” leading to the expression for $m(N_s)$, the particle mass in an $N_s \times N_s \times N_s$ box,

$$m_P(N_s) = m_P(\infty) + A \frac{e^{-\lambda N_s}}{N_s}, \quad (4.1)$$

where the exponent λ is determined by the mass of the pion, and A is given in terms of the on-shell πPP coupling. This finite volume correction can be interpreted as the effect of squeezing the pion cloud surrounding the particle. A somewhat different situation takes place when the particle P is a loosely bound state of constituents. In this case, the finite size effect is caused by the squeezing of the bound-state wave function [93]. As pointed out by Lüscher [92], this situation falls into the same general framework as that which led to equation (4.1), except that, in this case, the particle that travels around the world is one of the constituents of the bound state. Recently, it has been argued [94] that, in intermediate ranges of volume, where the asymptotic behaviour predicted by Lüscher’s volume formula has not yet set in, the volume dependence might be expected to exhibit a power law dependence of the form

$$m(N_s) = m(\infty) + \frac{\text{const.}}{N_s^3}, \quad (4.2)$$

instead of the exponential falloff of Lüscher's result. This power law form is also found by the authors of [94] to fit better to their data on light hadron masses (in full QCD). At this stage we are unable to quote infinite volume results from fitting to either form for the volume dependence, as we have only two volumes at β values 5.7 and 6.0. Thus we can only investigate the presence of a finite volume effect in our calculations. Therefore to improve this study will require additional volumes at both β values.

4.2 Chiral Extrapolations

4.2.1 Pion Chiral Extrapolations

The bare unrenormalised quark mass, m_q , is defined as follows:

$$am_q = \frac{1}{2} \left(\frac{1}{\kappa} - \frac{1}{\kappa_c} \right), \quad (4.3)$$

where κ_c is the critical hopping parameter and is an undetermined function of β . It is important to obtain an accurate determination of the critical hopping parameter, as the extrapolation or interpolation of the calculated hadron masses to the physical point are all reliant on the quark mass. Therefore any systematic effects in the determination of κ_c will pass over to the lattice measurements of physical states like the nucleon and rho meson, for example. The method to determine κ_c here is to express m_{PS}^2 in terms of m_q , and so determine κ_c from the fit. However this is dependent on the chiral behaviour of the pion mass. The chiral behaviour is modified due to quenching effects, and is the subject of quenched chiral perturbation theory QCPT [95, 96, 97], where there are two distinct effects.

1. Quenching removes loops which, at the underlying quark level, involve internal quark loops. This changes the values of the coefficients in the chiral expansion and may remove some terms completely.
2. Because of the absence of an anomaly, the η' is a pseudo-Goldstone boson in quenched QCD, so there are new contributions coming from η' loops

that give rise to chiral logarithms which make the quenched approximation singular in the chiral limit.

The result of QCPT for the mass of a pion composed of quarks of mass m_1 and m_2 is

$$m_{PS}^2 = c_\pi(m_1 + m_2)(1 - \delta \log[(m_1 + m_2)]) + e_\pi m_q^2 + \dots, \quad (4.4)$$

with c_π , e_π and δ constants, and the ellipsis represents higher order terms in the chiral expansion. The m_q^2 term is shorthand for analytic terms, i.e. those proportional to the quadratic terms $(m_1 + m_2)^2$, m_1^2 and m_2^2 , and non-analytic chiral logarithms of general form $m_q^2 \log(m_q)$. The δ term is an artifact of quenching; it arises from η' loops, and is divergent in the chiral limit, but its effect is small, and becomes noticeable only at quark masses smaller than those we use. Thus when fitting the pion masses we ignore the δ term. The pion masses for each data set tabulated in appendix A are fitted to following ansätze.

- **Fit 1:** The three lightest pion masses are fitted to

$$m_{PS}^2 = C_1 \left(\frac{1}{2\kappa_1} + \frac{1}{2\kappa_2} - C_0 \right). \quad (4.5)$$

- **Fit 2:** All pion masses are fitted to

$$m_{PS}^2 = C_1 \left(\frac{1}{2\kappa_1} + \frac{1}{2\kappa_2} - C_0 \right). \quad (4.6)$$

- **Fit 3:** All pion masses are fitted to

$$m_{PS}^2 = C_1 \left(\frac{1}{2\kappa_1} + \frac{1}{2\kappa_2} - C_0 \right) + C_2 \left(\frac{1}{2\kappa_1} + \frac{1}{2\kappa_2} - C_0 \right)^2. \quad (4.7)$$

- **Fit 4:** All pion masses are fitted to

$$m_{PS}^2 = C_1 \left(\frac{1}{2\kappa_1} + \frac{1}{2\kappa_2} - C_0 \right) + C_3 \left(\frac{1}{2\kappa_1} + \frac{1}{2\kappa_2} - C_0 \right)^3. \quad (4.8)$$

- **Fit 5:** All pion masses are fitted to

$$m_{PS}^2 = C_1 \left(\frac{1}{\kappa_{eff}} - C_0 \right) + C_2 \left(\frac{1}{\kappa_{eff}} - C_0 \right)^2 + C_3 \left(\frac{1}{\kappa_{eff}} - C_0 \right)^3. \quad (4.9)$$

- **Fit 6:** All pion masses are fitted to

$$m_{PS}^2 = C_1 \left(\frac{1}{\kappa_{eff}} - C_0 \right) + C_2 \left(\frac{1}{\kappa_{eff}} - C_0 \right)^2 + C_4 \left(\frac{1}{\kappa_{eff}} - C_0 \right)^2 \log \left[\left(\frac{1}{\kappa_{eff}} - C_0 \right) \right]. \quad (4.10)$$

- **Fit 2':** All pion masses are fitted to

$$m_{PS}^2 = C_1 \left(\frac{1}{2\kappa_1} + \frac{1}{2\kappa_2} - C_0 \right) + C'_1 \left| \frac{1}{2\kappa_1} - \frac{1}{2\kappa_2} \right|. \quad (4.11)$$

- **Fit 3':** All pion masses are fitted to

$$m_{PS}^2 = C_1 \left(\frac{1}{2\kappa_1} + \frac{1}{2\kappa_2} - C_0 \right) + C_2 \left(\frac{1}{2\kappa_1} + \frac{1}{2\kappa_2} - C_0 \right)^2 + C'_1 \left| \frac{1}{2\kappa_1} - \frac{1}{2\kappa_2} \right| + C'_2 \left| \frac{1}{2\kappa_1} - \frac{1}{2\kappa_2} \right|^2. \quad (4.12)$$

- **Fit 4':** All pion masses are fitted to

$$m_{PS}^2 = C_1 \left(\frac{1}{2\kappa_1} + \frac{1}{2\kappa_2} - C_0 \right) + C_3 \left(\frac{1}{2\kappa_1} + \frac{1}{2\kappa_2} - C_0 \right)^3 + C'_1 \left| \frac{1}{2\kappa_1} - \frac{1}{2\kappa_2} \right| + C'_3 \left| \frac{1}{2\kappa_1} - \frac{1}{2\kappa_2} \right|^3. \quad (4.13)$$

The critical hopping parameter, $\kappa_c = 1/C_0$, and the effective κ is defined as

$$\frac{1}{\kappa_{eff}} = \left(\frac{1}{2\kappa_1} + \frac{1}{2\kappa_2} \right). \quad (4.14)$$

The parameterisation of these fits is in terms of quark masses m_1 and m_2 , such that fit 2' is

$$m_{PS}^2 = C_1(m_1 + m_2) + C_2(m_1 + m_2)^2 + C'_1|m_1 - m_2| + C'_2(m_1 - m_2)^2. \quad (4.15)$$

One could have written all of these fits 1-9 in terms of m_1 and m_2 , but it is important to stress the relationship with the fitted parameters.

The results for all of these pion chiral extrapolations using correlated fits at $\beta = 6.0$ with C=TAD are given in table 4.1. This data set will be discussed as an example; the results for fits 1-5 on all the data sets are in given in appendix B. The results indicate the inclusion of these higher order terms in m_q in equation (4.4) is important. As an example, the linear fit to all six quark masses (fit 2) gives a $\chi^2/\text{d.o.f.}$ of 7 which is large. This significantly decreases when going to the higher order fits in m_q (fits 3 and 4), for example, where the $\chi^2/\text{d.o.f.}$ are 2 and 1 respectively. The coefficients of the higher order terms are a large number of σ from zero and there is a significant change in κ_c from fit 2. Therefore the statistical quality of the data is sufficiently good to merit the use of these higher order fits. However is the data good enough to determine which of these chiral forms to use?

A linear fit in m_q to three lightest quark masses gives a good fit to the data and a low $\chi^2/\text{d.o.f.}$, a consequence of the larger statistical errors on the pions calculated at these lighter quark masses. The higher order terms in m_q in equation (4.4) become more important as the quark mass is increased. Therefore one criteria one can use in comparing the higher order fits is that there is relatively good agreement between the κ'_c s determined from that fit and fit 1. Before going any further it would be worthwhile eliminating some of the fits. The fits which are denoted by the prime after the number test the assumption that the mass of a meson made from different masses m_1 and m_2 is exactly the same as one composed of identical quarks of mass $\frac{1}{2}(m_1 + m_2)$. The last assumption has been made in the fits without the prime. In all three cases where this assumption is tested, the primed fits have a larger $\chi^2/\text{d.o.f.}$ and the coefficients of all terms which are

some power of $|m_1 - m_2|$ are within 2σ of zero. Thus the assumption made in fits 1-6 is valid at the current level of statistics. Fit 6, which includes a non-analytic term, gives the lowest $\chi^2/\text{d.o.f.}$ of the fits to all the quark masses. However the coefficient of the $m_q^2 \log(m_q)$ is within 2σ of zero, and on reducing the number of quark masses in the fit there is a significant change in the fit coefficients, indicating that this fit is unstable. Including more quark masses in the fit may will remedy this problem, and one should consider this in further studies.

Fits 3 and 4 which include quadratic and cubic terms in m_q , in addition to the linear term, have acceptable $\chi^2/\text{d.o.f.}$ of 2 and 1 respectively. The coefficients of these higher order terms are a larger number of σ from zero and these fits are stable under removing quark masses from the fit. In fit 5 a full cubic fit is performed. However, the coefficients from this fit differ considerably from those obtained for the higher order terms in fits 3 and 4, and this fit is unstable to removing quark masses from the fit. Hence, although we are seeing curvature in the pion chiral extrapolation, as can be seen in figure 4.1, the number of quark masses is insufficient to discriminate between fits 3 and 4. The values of κ_c obtained from fits 3 and 4 are within 1σ , and these are within 2σ of the value obtained from fit 1.

The value κ_c which has been taken is that obtained from fit 3 over the one from fit 4, as one could argue that the higher order terms follow order by order in equation (4.4) when going to higher quark masses, and one should take the difference between these κ'_c 's as the systematic error in this procedure.

Fit	κ_c	C_1	C_2	C_3	C_4	C'_1	C'_2	C'_3	$\chi^2/\text{d.o.f}$
1	0.139267 $\begin{smallmatrix} +21 \\ -11 \end{smallmatrix}$	1.415 $\begin{smallmatrix} +14 \\ -21 \end{smallmatrix}$							0.2/1
2	0.139245 $\begin{smallmatrix} +14 \\ -9 \end{smallmatrix}$	1.463 $\begin{smallmatrix} +7 \\ -9 \end{smallmatrix}$							28.1/4
3	0.139305 $\begin{smallmatrix} +22 \\ -16 \end{smallmatrix}$	1.323 $\begin{smallmatrix} +31 \\ -35 \end{smallmatrix}$	0.77 $\begin{smallmatrix} +16 \\ -16 \end{smallmatrix}$						6.0/3
4	0.139288 $\begin{smallmatrix} +19 \\ -14 \end{smallmatrix}$	1.379 $\begin{smallmatrix} +19 \\ -21 \end{smallmatrix}$		3.14 $\begin{smallmatrix} +58 \\ -63 \end{smallmatrix}$					3.2/3
5	0.139262 $\begin{smallmatrix} +32 \\ -17 \end{smallmatrix}$	1.462 $\begin{smallmatrix} +56 \\ -87 \end{smallmatrix}$	-1.03 $\begin{smallmatrix} +105 \\ -69 \end{smallmatrix}$	7.24 $\begin{smallmatrix} +277 \\ -414 \end{smallmatrix}$					1.8/2
6	0.139243 $\begin{smallmatrix} +38 \\ -19 \end{smallmatrix}$	1.580 $\begin{smallmatrix} +9 \\ -14 \end{smallmatrix}$	2.45 $\begin{smallmatrix} +61 \\ -97 \end{smallmatrix}$		1.66 $\begin{smallmatrix} +56 \\ -97 \end{smallmatrix}$				1.3/2
2'	0.139247 $\begin{smallmatrix} +14 \\ -9 \end{smallmatrix}$	1.457 $\begin{smallmatrix} +7 \\ -9 \end{smallmatrix}$				0.0142 $\begin{smallmatrix} +52 \\ -50 \end{smallmatrix}$			19.9/3
3'	0.139285 $\begin{smallmatrix} +28 \\ -15 \end{smallmatrix}$	1.350 $\begin{smallmatrix} +32 \\ -44 \end{smallmatrix}$	0.62 $\begin{smallmatrix} +22 \\ -17 \end{smallmatrix}$			-0.0003 $\begin{smallmatrix} +37 \\ -27 \end{smallmatrix}$	-0.081 $\begin{smallmatrix} +63 \\ -31 \end{smallmatrix}$		3.1/1
4'	0.139278 $\begin{smallmatrix} +23 \\ -13 \end{smallmatrix}$	1.386 $\begin{smallmatrix} +20 \\ -26 \end{smallmatrix}$		2.93 $\begin{smallmatrix} +81 \\ -74 \end{smallmatrix}$		0.0001 $\begin{smallmatrix} +31 \\ -32 \end{smallmatrix}$		0.54 $\begin{smallmatrix} +29 \\ -53 \end{smallmatrix}$	1.6/1

Table 4.1: Chiral extrapolations for the pion calculated at $\beta = 6.0$, C=TAD and on the $16^3 \times 48$ lattice.

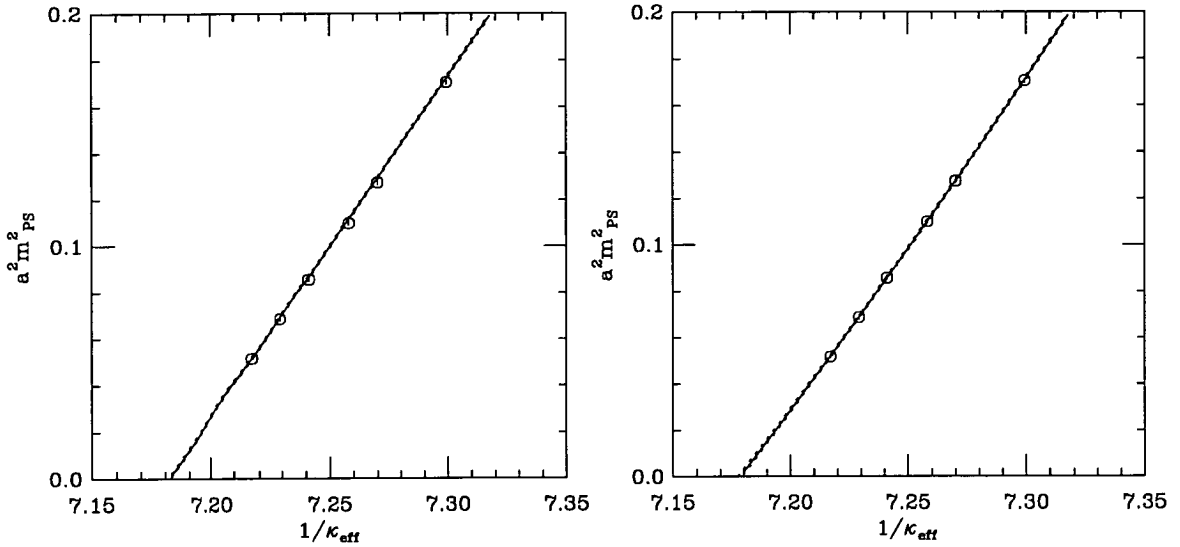


Figure 4.1: Chiral extrapolations of the pion at $\beta = 6.0$ and C=TAD; the plot on the left is a linear extrapolation in m_q , and the plot on the right is for an extrapolation with a linear and quadratic term in m_q . In comparing the two plots the quadratic fit is clearly giving a better fit to the data.

At $\beta = 5.7$, with only three quark-mass combinations, the information that one can obtain is limited, as not all the fits can be performed. For the quadratic fit the coefficients are obtained from solving the equations and no minimisation procedure is performed, which explains the large error bars on the fitted parameters in this case. The data at $\beta = 6.2$ lend support for the need to include higher order terms in m_q in the pion chiral extrapolation. There is no difference in the overall picture when comparing the different fits between C=TAD and C=NP at fixed β .

Finite Volume Effects in the Pion

The pion masses on the two volumes at each of $\beta = 5.7$ and $\beta = 6.0$ are shown in figure 4.2.1. At $\beta = 6.0$, C=NP, the masses decrease between the small and larger volume by 0.5% at the heaviest quark masses and by 3% at the lightest quark mass. At $\beta = 5.7$, C=TAD, the masses increase by 0.6% between the small and large volume at the lightest quark mass computed. Therefore the results are

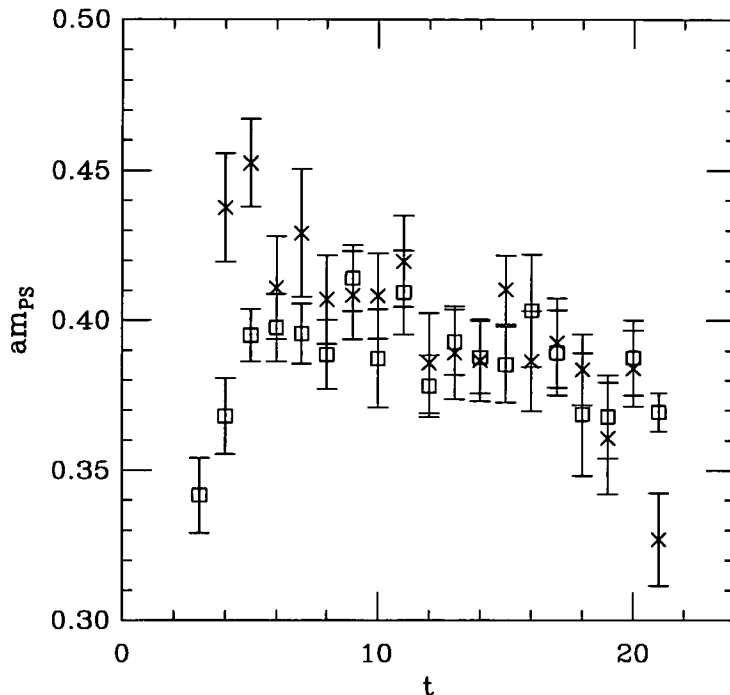


Figure 4.2: Comparison of the effective masses of the heaviest pion at $\beta = 6.0$, with C=NP on the $16^3 \times 48$ lattice, computed from a sink-fuzzed correlator (LL,FL) with $r = 6$ and a sink smeared correlator (LL,SS) with the number of smearing iterations $N = 30$ and $\kappa_{sc} = 0.25$, corresponding to the (\square) and the (\times) respectively. The results were computed from 21 configurations.

somewhat conflicting, but the physical volumes of the lattices at both β values are different and at $\beta = 6.0$ the lightest quark mass computed is considerably smaller in physical units. At $\beta = 6.0$ the finite volume effect is in the direction that the mass decreases in going to a larger volume, which has been observed by [86] and is what you would expect. The effective masses for the pion at the lightest quark mass with both volumes superimposed is shown in figure 4.4. It is questionable as to whether a finite volume effect is observed here, more volumes and higher statistics are required. Another possible source of discrepancy between the pion masses on the two volumes at $\beta = 6.0$ is the different smearing procedures used for each volume, i.e. fuzzing on the small volume and Jacobi smearing on the large

volume. To investigate this further, the smearing study in section 2.2 generated data on the small volume using both Jacobi smearing and fuzzing. Therefore, at the smearing parameters used in this simulation, the effective masses for heaviest¹ pion computed with the different smearing types superimposed are shown in figure 4.2. We can observe that in the region of the plateau there is good agreement in the central values of the masses from both smearing types. Thus, this results suggests that the discrepancy between the small and large volume cannot be attributed to using different smearing types at each volume.

Simulation	$N_s^3 \times N_t$	κ_c	
$\beta = 5.7, C=TAD$	$12^3 \times 24$	0.143519	$^{+104}_{-93}$
	$16^3 \times 32$	0.143543	$^{+66}_{-42}$
$\beta = 6.0, C=NP$	$16^3 \times 48$	0.135335	$^{+20}_{-17}$
	$32^3 \times 64$	0.135290	$^{+27}_{-12}$

Table 4.2: Finite volume effects on κ_c . κ_c is determined from fitting the pion masses to equation (4.7).

At $\beta = 5.7$ the κ'_c s measured in the two volumes are within statistical errors, while at $\beta = 6.0$ there is roughly a 2σ difference between the two volumes. The consequences of this difference at $\beta = 6.0$ are as follows. In the calculation of lattice hadron masses there is another possible source of discrepancy between the two volumes which is different from a finite volume effect in that, for a fixed κ value, the bare unrenormalised quark mass m_q which this corresponds to is different on the two volumes. Therefore, in the extrapolation or interpolation of the calculated hadron masses to the physical point, the quark mass to which this corresponds will be different on the two volumes.

¹Though we are primarily concerned with the discrepancy at the lightest pion mass, one of the results of the smearing study was that the optimal smearing parameters were unchanged in the range of quark masses simulated here.

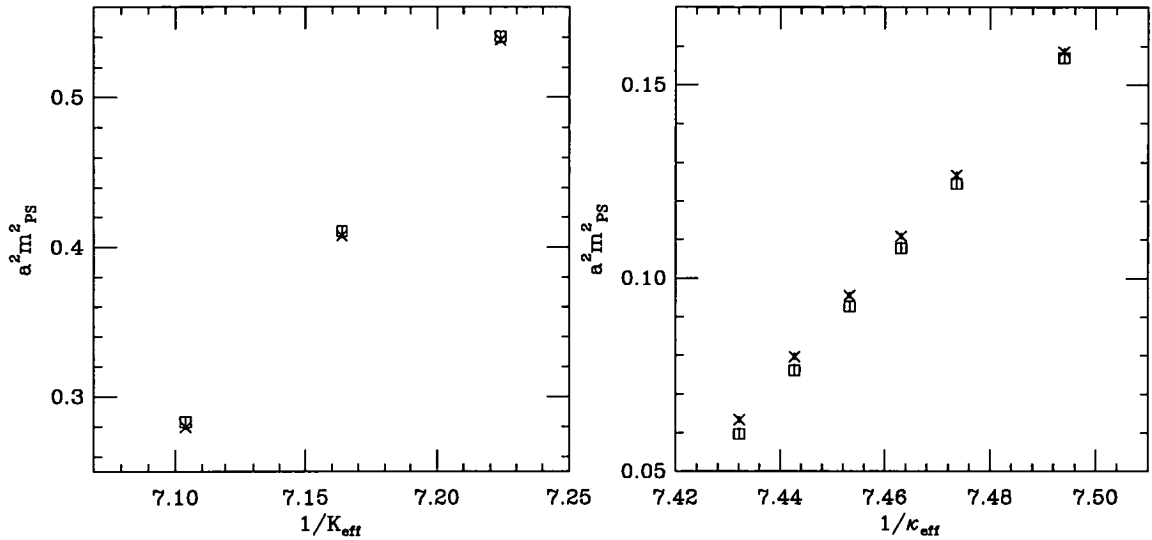


Figure 4.3: Investigation of finite volume effects in the pion. The plot on the left shows the pion masses calculated at $\beta = 5.7$ with C=TAD, the (\square) and the (\times) corresponding to the $16^3 \times 32$ and $12^3 \times 24$ lattices respectively. The plot on the right shows the pion masses calculated at $\beta = 6.0$ with C=NP, the (\square) and the (\times) corresponding to the $32^3 \times 64$ and $16^3 \times 48$ lattices respectively.

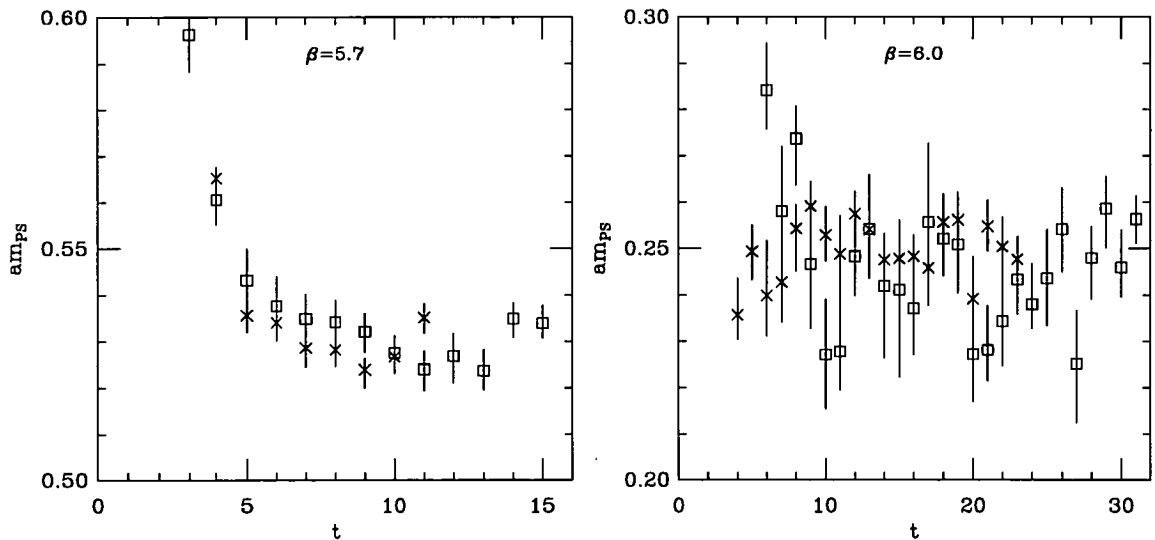


Figure 4.4: Each plot contains a comparison between the effective masses for the lightest pion calculated at each of the two lattice volumes at $\beta = 5.7$ and $\beta = 6.0$. The effective masses are represented by a (\times) and a (\square) for the small and large volume, respectively. The masses are obtained from the (SL,LL) correlator at $\beta = 5.7$, and from the (SS,LL) and (FL,LL) correlators on the large and small volumes, respectively at $\beta = 6.0$.

Measure of the $O(a^2)$ effects in the Non-perturbatively improved action

β	κ_c	
	This simulation	ALPHA [38]
6.0	0.135335 $^{+20}_{-17}$	0.135196(14)
6.2	0.135895 $^{+14}_{-55}$	0.135795(13)

Table 4.3: Comparison of the measured value of κ_c on the small volumes with C=NP from this simulation with those obtained from a different non-perturbative procedure given in the text. This gives an indication of the residual $O(a^2)$ discretisation errors.

The ALPHA collaboration [38] have determined the value of κ_c through a different procedure. This procedure uses the PCAC relation² on the lattice

$$\langle \frac{1}{2}(\partial_\mu^* + \partial_\mu)(A^I)_\mu(x)\mathcal{O} \rangle = 2\tilde{m}\langle (P^I)(x)\mathcal{O} \rangle, \quad (4.16)$$

where P^I and A^I are the on-shell $O(a)$ -improved pseudoscalar density and the improved axial current respectively, and \mathcal{O} denotes an on-shell $O(a)$ -improved field localised in a region not containing x . The κ value at which the unrenormalised current quark mass \tilde{m} vanishes is taken to be κ_c . This calculation has been performed in the framework of the non-perturbatively $O(a)$ -improved fermion action, so we can compare the results for κ_c computed in this simulation and those calculated with C=NP, as shown in table 4.3. The PCAC in equation (4.16) holds to $O(a)$ therefore the discrepancy between the two values of κ_c acts as an indication of the residual discretisation errors at each of the β values, modulo systematic errors in the case of the results from our simulation.

4.2.2 Vector Meson Chiral Extrapolations

The quenched chiral expansion for the vector-mesons masses, predicted in [51] from the chiral expansion in full QCD [98], has now been calculated using the

²The improved fields are defined in section 1.9.

formalism of quenched chiral perturbation theory [99] giving

$$m_\rho = a_\rho + \delta b_\rho m_q^{1/2} + c_\rho(m_1 + m_2) + d_\rho m_q^{3/2} + e_\rho m_q^2 + \dots \quad (4.17)$$

Once again we drop the δ term arising from quenched chiral logarithms. The vector meson masses are fitted to the following ansätze:

- Fit 1 : $m_V = m_\rho^c + C_1 m_q$ fitted to the three lightest quark masses,
- Fit 2 : $m_V = m_\rho^c + C_1 m_q$ fitted all quark masses,
- Fit 3 : $m_V = m_\rho^c + C_1 m_q + C_2 m_q^{3/2}$ fitted to all quark masses,
- Fit 4 : $m_V = m_\rho^c + C_1 m_q + C_3 m_q^2$ fitted to all quark masses,
- Fit 5 : $m_V = m_\rho^c + C_1 m_q + C_2 m_q^{3/2} + C_3 m_q^2$ fitted to all quark masses.

Here again, the results of the fits at $\beta = 6.0$ and C=TAD are used as the representative data set and are shown in table 4.4. A linear fit to all six quark masses gives a good $\chi^2/\text{d.o.f.} \approx 0.7$. The higher order fits, 3-5, give a lower $\chi^2/\text{d.o.f.}$ as would be expected, but the values of m_ρ^c from these fits are still within 1σ of fit 2. The coefficients of the higher order terms are non-zero, but have large error bars, and are a little over 1σ from zero. Therefore the statistical quality of the data is not yet good enough to support these higher order fits. However non-linear terms have been observed by other groups [51, 100]. The linear chiral extrapolations are shown in figure 4.5 for this data set and for that at $\beta = 6.2$ with C=TAD. In both cases we can observe that the fits appear reasonable. The chiral expansion for the rho we shall use in the rest of the analysis is fit 2:

$$m_V = m_\rho^c + C_1 m_q, \quad \text{fitted to all quark masses.} \quad (4.18)$$

Finite Volume Effects in the Rho

In figure 4.6 are plotted the rho masses at volumes at both $\beta = 5.7$ and $\beta = 6.0$. Once again, the results of this finite volume comparison are conflicting. For $\beta = 5.7$, at the heaviest quark mass, the rho mass is over 1σ smaller on the larger volume than on the smaller volume; this increases to 2σ , at the lightest quark

Fit	m_ρ^c	C_1	C_2	C_3	$\chi^2/\text{d.o.f}$
Fit 1	0.391 $^{+14}_{-12}$	2.42 $^{+33}_{-36}$			0.02/1
Fit 2	0.391 $^{+7}_{-9}$	2.47 $^{+8}_{-9}$			2.64/4
Fit 3	0.377 $^{+15}_{-13}$	3.24 $^{+62}_{-73}$	-2.2 $^{+20}_{-18}$		1.41/3
Fit 4	0.379 $^{+13}_{-10}$	2.91 $^{+33}_{-42}$		-4.0 $^{+36}_{-31}$	1.29/3
Fit 5	0.396 $^{+30}_{-34}$	0.50 $^{+451}_{-349}$	15.1 $^{+214}_{-284}$	-30.4 $^{+498}_{-365}$	0.90/2

Table 4.4: Chiral extrapolations for the rho calculated at $\beta = 6.0$, with C=TAD on the $16^3 \times 48$ lattice.

mass. However at $\beta = 6.0$ the rho masses are within statistical errors at all quark masses, as can be observed in figure 4.6. The effective masses for the rho with both volumes superimposed is shown in figure 4.7, here once again it is unclear whether a finite volume effect is observed, which is in line with [101, 102].

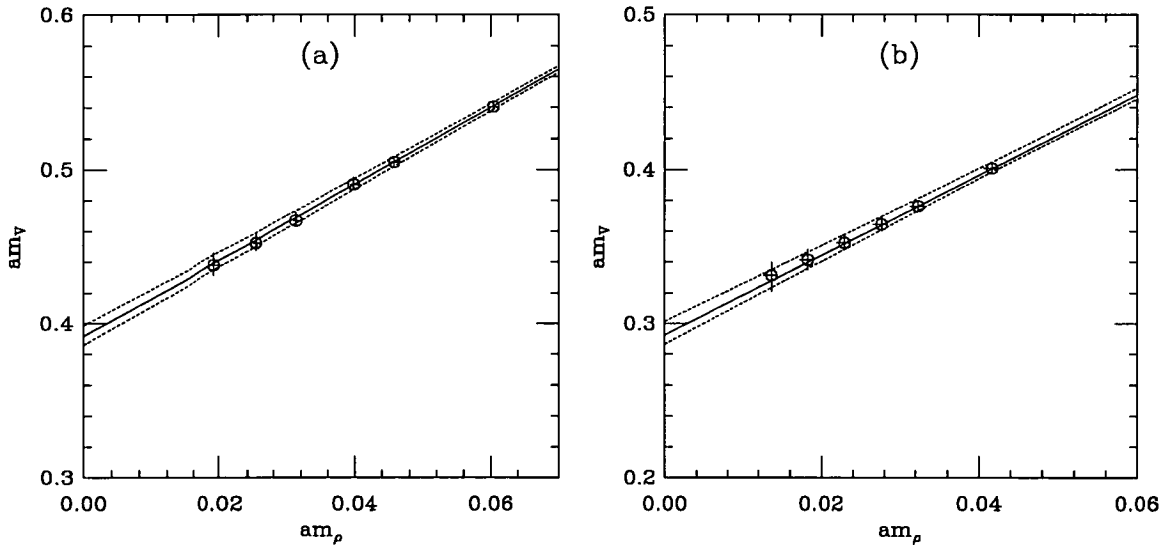


Figure 4.5: Linear chiral extrapolation of the rho, plot (a) shows the data at $\beta = 6.0$ and C=TAD and plot (b) shows the data at $\beta = 6.2$ and C=TAD.

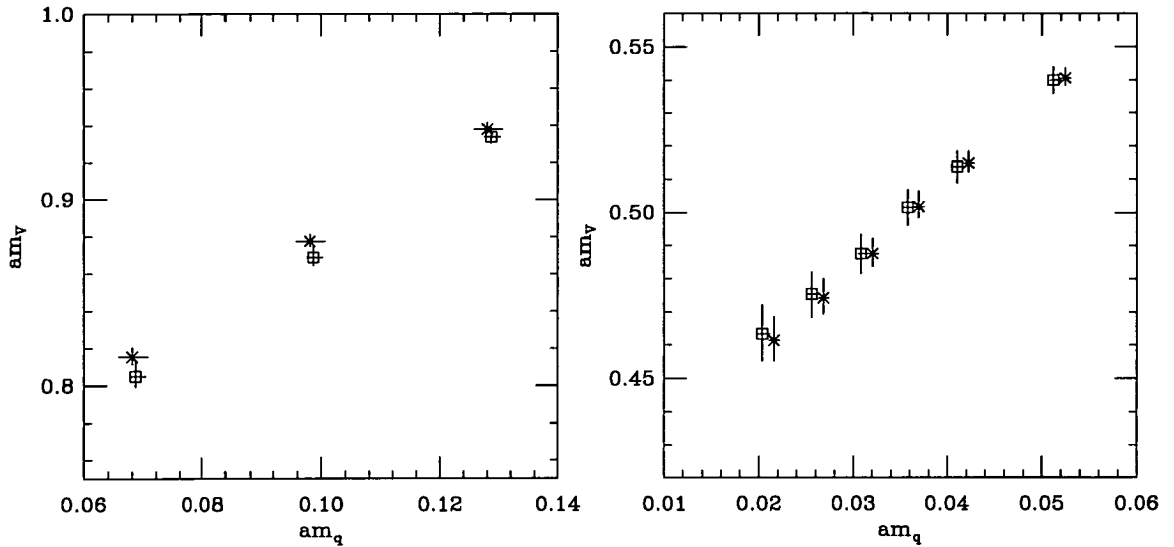


Figure 4.6: Investigation of finite volume effects in the rho. The plot on the left shows the rho masses calculated at $\beta = 5.7$ with $C=TAD$, the (\square) and the (\times) corresponding to the $16^3 \times 32$ and $12^3 \times 24$ lattices respectively. The plot on the right shows the rho masses calculated at $\beta = 6.0$ with $C=NP$, the (\square) and the (\times) corresponding to the $32^3 \times 64$ and $16^3 \times 48$ lattices respectively.

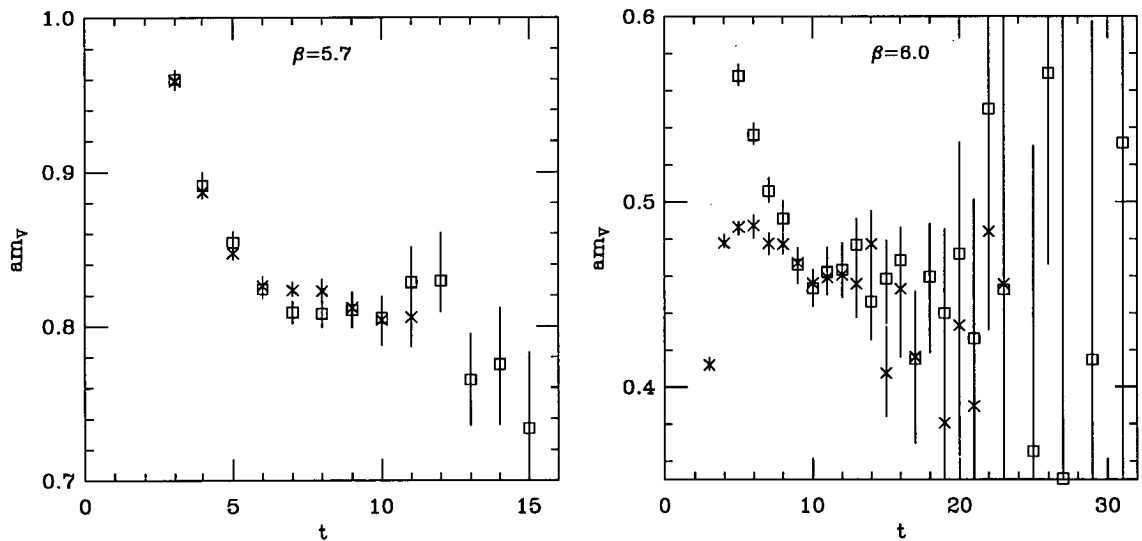


Figure 4.7: Each plot contains a comparison between the effective masses for the lightest rho calculated at each of the two lattice volumes at $\beta = 5.7$ and $\beta = 6.0$. The effective mass are represented by a (\times) and a (\square) for the small and large volume, respectively. The masses are obtained from the (SL,LL) correlator at $\beta = 5.7$, and from the (SS,LL) and (FL,LL) correlators on the large and small volumes, respectively at $\beta = 6.0$.

4.2.3 Spin- $\frac{1}{2}$ Octet Baryons Chiral Extrapolations

The two types of spin- $\frac{1}{2}$ correlator were computed with all the combinations of computed quark masses, but not all these correlators are independent, as the correlators of the form $A[AB]$ and $A\{AB\}$ are related through

$$\begin{aligned} A[AB] &= \frac{1}{4}(3B[AA] + B\{AA\}), \\ A\{AB\} &= \frac{3}{4}(B[AA] + 3B\{AA\}). \end{aligned} \quad (4.19)$$

We can think of the results for the masses of $A\{BB\}$ and $A[BB]$ as being those for the Σ and Λ , respectively, with $m_s = m_A$ and $m_u = m_d = m_B$. Unlike in the real world, we have the freedom to set $m_A = m_B$. However, in this case the Σ and Λ are also degenerate, i.e. $m(A\{AA\}) = m(A[AA])$; the contractions in the two cases are identical, the contractions are given in equations (2.34) and (2.39), respectively. There is agreement between the fitted masses of the Σ and Λ correlators, which are degenerate in quark mass at $\beta = 6.0$, C=NP and on the $32^3 \times 64$ lattice; see tables A.29 and A.30 respectively. But, we can observe up to a 2σ discrepancy between the fitted masses for the Σ and Λ correlators which are degenerate in quark mass on the smaller volume $16^3 \times 48$; see tables A.24 and A.25 respectively. How can we explain this? On the larger volume the correlators are computed using Jacobi smearing algorithm and are of the type (SSS,LLL) and (SSS,SSS), but on the smaller volume the correlators are computed using the fuzzing algorithm and are of type (FFL,LLL). Therefore in the case of the fuzzed baryon correlators even though the correlators are constructed from propagators that are degenerate in quark mass there still exists a non-degeneracy between the propagator types. Thus, when there is a finite sample, $m(A_F\{A_F A_L\}) \approx m(A_F[A_F A_L])$, and this will only agree in the case of an infinite ensemble.

The interpretation of the results for the completely non-degenerate correlators, $A[BC]$ and $A\{BC\}$, requires more thought, as the situation is complicated. Because isospin is broken, the Σ^0 - and Λ -like states mix, with both correlators containing contributions from physical states. Let M_+ and M_- be the masses of

the heavier and lighter states, respectively, and δM the mass difference. At long times, the effective masses for both correlators will asymptote to M_- . However, at times short compared to the inverse mass difference, i.e. $\delta M t \ll 1$, there will be an approximate plateau at a value which is a weighted average of the two masses. To see this, we pick the Λ correlator and write it as

$$C_\Lambda(t) = A e^{-M_- t} (\cos^2 \theta + \sin^2 \theta e^{-\delta M t}) + \dots, \quad (4.20)$$

where $\tan \theta$ is the ratio of the amplitudes to create the two mixed states, and the ellipsis represents excited states. The effective mass is

$$\begin{aligned} m(\Lambda)_{eff}(t) &= -\frac{d \ln C_\Lambda(t)}{dt} = M_- + \sin^2 \theta \delta M (1 + O(\delta M t)) \\ &\approx \cos^2 \theta M_- + \sin^2 \theta M_+ + \dots, \end{aligned} \quad (4.21)$$

Thus the effective mass is almost constant, and given our errors, we cannot distinguish it from a plateau. We discuss below the interpretation of the resulting “mass”.

The chiral form for the baryon masses is [49],

$$m_N = a_N + \delta [b_N m_q^{1/2} + b'_N m_q \ln(m_q)] + c_N m_q + d_N m_q^{3/2} + e_N m_q^2 + \dots, \quad (4.22)$$

where δ is the same constant as in equation (4.4), while $a_N - e_N$ are additional constants. The expansion has the same form in full QCD, except that the δ term, which again comes from η' loops, is absent. Like the pion and rho, we ignore the δ term in all fits. If we keep only constants and linear terms in quark masses, then it is straightforward to show, using quenched chiral perturbation theory [49], that

$$\begin{aligned} m(\Sigma^+) = M(S\{UU\}) &= M_0 + 4F m_u + 2(F - D) m_s, \\ m(\Lambda) = M(S[UU]) &= M_0 + 4\left(F - \frac{2D}{3}\right) m_u + 2\left(F + \frac{D}{3}\right) m_s. \end{aligned} \quad (4.23)$$

Here M_0 is the spin-1/2 baryon mass in the chiral limit, and F and D are the usual

reduced matrix elements of scalar densities. Note that there is no dependence on m_d , since the d quark does not enter the correlators. These formulae apply to all the states that are considered, for example, the proton mass is $m(D\{UU\})$, and is obtained by replacing m_s with m_d in the formula for $m(\Sigma^+)$.

At this order in the chiral expansion, it is simple to extend the results to baryons composed of three non-degenerate quarks. The mass matrix in the $(\Sigma^0, \Lambda) = (S\{UD\}, S[UD])$ basis is

$$\begin{pmatrix} \alpha & \gamma \\ \gamma & \beta \end{pmatrix} = \begin{pmatrix} M_0 + 4F\bar{m} + 2(F - D)m_s & \frac{2D}{\sqrt{3}}(m_u - m_d) \\ \frac{2D}{\sqrt{3}}(m_u - m_d) & M_0 + 4(F - \frac{2D}{3})\bar{m} + 2(F + \frac{D}{3})m_s \end{pmatrix} \quad (4.24)$$

Diagonalising this matrix gives the eigenvalues M_{\pm} , with mixing angle θ . If we assume that the same mixing angle applies for the interpolating fields, then θ is the angle appearing in the previous expressions for the Λ correlator equation (4.20). The ‘‘short-time effective mass’’, equation (4.21), is then

$$M(\Lambda)_{eff} \approx \cos^2 \theta M_- + \sin^2 \theta M_+ = \beta. \quad (4.25)$$

A similar argument shows that

$$m(\Sigma)_{eff} \approx \sin^2 \theta M_- + \cos^2 \theta M_+ = \alpha. \quad (4.26)$$

Thus we find the surprising result that the short-time effective masses are insensitive to the isospin breaking term γ . Furthermore, the expressions for α and β are exactly the same as the formulae applicable when isospin is unbroken, except that m_u is replaced by the average mass, \bar{m} . Thus we assume that for baryons composed of completely non-degenerate quarks, the effective masses satisfy

$$m(A\{BC\}) = m(A\{DD\}) \text{ and } m(A[BC]) = m(A[DD]), \quad (4.27)$$

where $m_D = (m_B + m_C)/2$. We make clear in the following where we are using this assumption and where not.

Following the discussion below equation (4.19), the degenerate nucleon masses are taken as the average of the fitted Λ and Σ mass at the appropriate quark mass. The degenerate nucleon masses were fitted to the following ansätze, following equation (4.22)

$$\text{Fit 1 : } m_N = M_0 + C_l m_q,$$

$$\text{Fit 2 : } m_N = M_0 + C_l m_q + C_{nl} m_q^{3/2},$$

$$\text{Fit 3 : } m_N = M_0 + C_l m_q + C_{nl} m_q^2.$$

The ‘ Σ -like’ $A\{BC\}$ are fitted to the following ansätze, assuming the relation in equation (4.27)

$$\text{Fit 4 : } m_\Sigma = M_0 + C_l^A m_A + C_l^D m_D$$

fitted to all ‘ Σ -like’ masses of type $A\{BB\}$,

$$\text{Fit 5 : } m_\Sigma = M_0 + C_l^A m_A + C_l^D m_D$$

fitted to all ‘ Σ -like’ masses of type $A\{BC\}$

$$\text{Fit 6 : } m_\Sigma = M_0 + C_l^A m_A + C_{nl}^A m_D^{3/2} + C_l^A m_D + C_{nl}^D m_D^{3/2}$$

fitted to all ‘ Σ -like’ masses of type $A\{BC\}$,

$$\text{Fit 7 : } m_\Sigma = M_0 + C_l^A m_A + C_{nl}^A m_D^2 + C_l^A m_D + C_{nl}^D m_D^2$$

fitted to all ‘ Σ -like’ masses of type $A\{BC\}$.

The ‘ Λ -like’ $A[BC]$ masses were fitted to the same form as fits 4-7, but here we expect the coefficients to be different. The higher order fits which are used in the extrapolations of the ‘ Σ -like’ masses do not have any firm theoretical foundation, but enable an investigation of the presence of non-linearity in the chiral expansion. A detailed investigation of the octet mass splitting has been performed in [51], in which the fits to the mass splittings have a greater sensitivity to the higher order terms in the chiral expansion than in the case of the chiral extrapolations of the nucleon masses. Therefore the mass splitting should be investigated in a further studies.

The results of the fits at $\beta = 6.0$ with C=TAD, are shown in tables 4.5 to 4.7. In the case of the linear chiral extrapolation to the ‘ Σ -like’ masses, there is consistency between the nine point fit to masses of type $A\{BB\}$ and the eighteen-

Fit	#points	M_0	C_l	C_{nl}	$\chi^2/\text{d.o.f}$
1	3	0.534 $^{+10}_{-10}$	4.58 $^{+15}_{-14}$		0.2/1
2	3	0.521 $^{+27}_{-40}$	5.42 $^{+254}_{-159}$	-2.6 $^{+49}_{-79}$	
3	3	0.523 $^{+24}_{-34}$	5.07 $^{+146}_{-94}$	-5.2 $^{+96}_{-158}$	

Table 4.5: Chiral extrapolations for the degenerate nucleon masses calculated at $\beta = 6.0$, C=TAD and on the $16^3 \times 48$ lattice.

Fit	#points	M_0	C_l^A	C_{nl}^A	C_l^D	C_{nl}^D	$\chi^2/\text{d.o.f}$
4	9	0.533 $^{+11}_{-9}$	1.73 $^{+6}_{-6}$		2.92 $^{+9}_{-10}$		3.6/6
5	18	0.536 $^{+9}_{-9}$	1.71 $^{+5}_{-5}$		2.89 $^{+9}_{-8}$		8.8/15
6	18	0.542 $^{+14}_{-14}$	1.81 $^{+42}_{-40}$	-0.3 $^{+12}_{-13}$	2.45 $^{+49}_{-49}$	1.3 $^{+14}_{-15}$	8.0/13
7	18	0.541 $^{+13}_{-13}$	1.77 $^{+23}_{-23}$	-0.7 $^{+24}_{-26}$	2.65 $^{+27}_{-28}$	2.3 $^{+26}_{-26}$	8.0/13

Table 4.6: Chiral extrapolations for the ‘ Σ -like’ masses calculated at $\beta = 6.0$, C=TAD and on the $16^3 \times 48$ lattice.

point fit to $A\{BC\}$ under the assumption that $m_D = (m_B + m_C)/2$. This is an indication that this assumption is reasonable, and this is also seen in the fits to the ‘ Λ -like’ masses. We can see that in the chiral limit there is consistency between the extrapolations of the degenerate nucleon, ‘ Λ -like’ and ‘ Σ -like’ masses, as expected.

The non-linear chiral extrapolations yield higher $\chi^2/\text{d.o.f}$.’s than the linear fit, and the coefficients of the higher order terms are within 1σ of zero. Furthermore, the chirally extrapolated masses agree with those from the linear fit. Therefore we use the linear chiral extrapolations. In figure 4.8 the linear chiral extrapolation of the degenerate nucleon masses is shown, and an indication of linearity of the extrapolation of all eighteen ‘ Σ -like’ $A\{BC\}$ masses is shown through extrapolating in m_D keeping m_A fixed.

Finite Volume Effects in the Spin- $\frac{1}{2}$ Octet Baryons

The masses of the degenerate nucleon for both volumes at $\beta = 5.7$ are plotted in figure 4.9, together with a plot of the ‘ Σ -like’ masses computed at degenerate quark mass at both volumes from $\beta = 6.0$ with C=NP. At $\beta = 5.7$ the masses

Fit	#points	M_0	C_l^A	C_{nl}^A	C_l^D	C_{nl}^D	$\chi^2/\text{d.o.f}$
4	9	0.534 $^{+12}_{-12}$	1.39 $^{+7}_{-7}$		3.13 $^{+12}_{-11}$		1.0/6
5	18	0.537 $^{+12}_{-11}$	1.36 $^{+6}_{-6}$		3.11 $^{+10}_{-10}$		7.0/15
6	18	0.544 $^{+17}_{-18}$	1.05 $^{+61}_{-56}$	1.0 $^{+18}_{-19}$	2.96 $^{+64}_{-66}$	0.4 $^{+18}_{-19}$	6.7/13
7	18	0.543 $^{+16}_{-16}$	1.19 $^{+36}_{-33}$	1.9 $^{+35}_{-37}$	3.04 $^{+35}_{-36}$	0.7 $^{+33}_{-35}$	6.7/13

Table 4.7: Chiral extrapolations for the ‘ Λ -like’ masses calculated at $\beta = 6.0$, $C=\text{TAD}$ and on the $16^3 \times 48$ lattice.

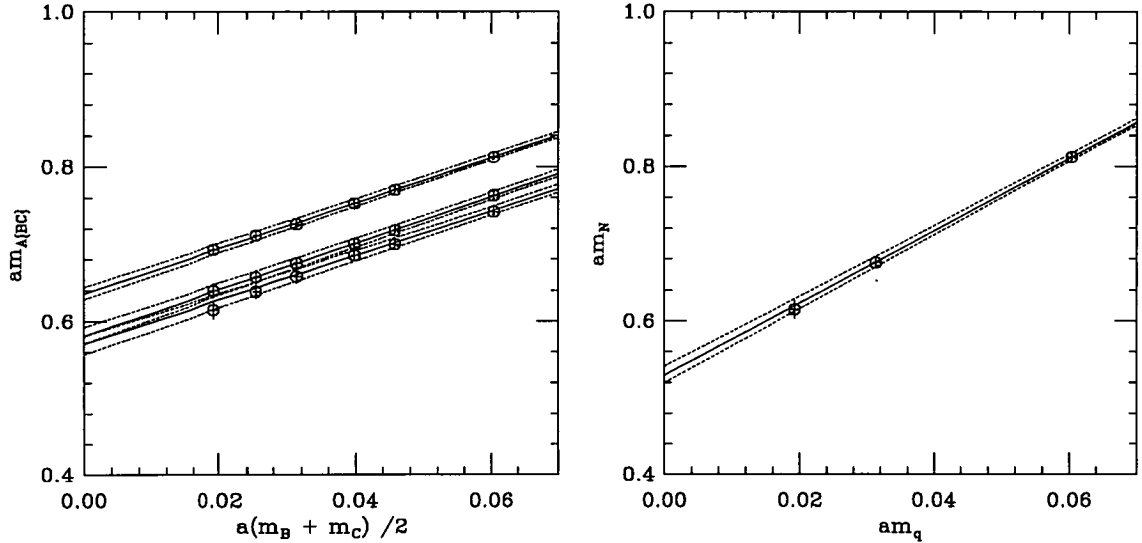


Figure 4.8: Chiral extrapolations for spin- $\frac{1}{2}$ octet baryons at $\beta = 6.0$ and $C=\text{TAD}$. The plot on the left shows part of the chiral extrapolation for the ‘ Σ -like’ $A\{BC\}$ masses, keeping m_A fixed, and extrapolating in $m_D = \frac{1}{2}(m_B + m_C)$. The plot on the right shows the chiral extrapolation for the degenerate nucleon masses.

from both volumes agree within statistical errors. At $\beta = 6.0$, there is agreement between the masses computed at heavier quark mass. At the lightest quark mass computed at $\beta = 6.0$ there is a 2σ discrepancy between the masses, with the ‘ Σ -like’ being lighter in the larger volume by 5%; although the error bars on the fitted masses from 32×64 lattice are a factor of two larger than those on the smaller volume. The effective mass plots for this case are shown in figure 4.10, and indicate that we are observing a finite volume effect in this case in the direction observed by [101], but smaller error bars are required to be certain.

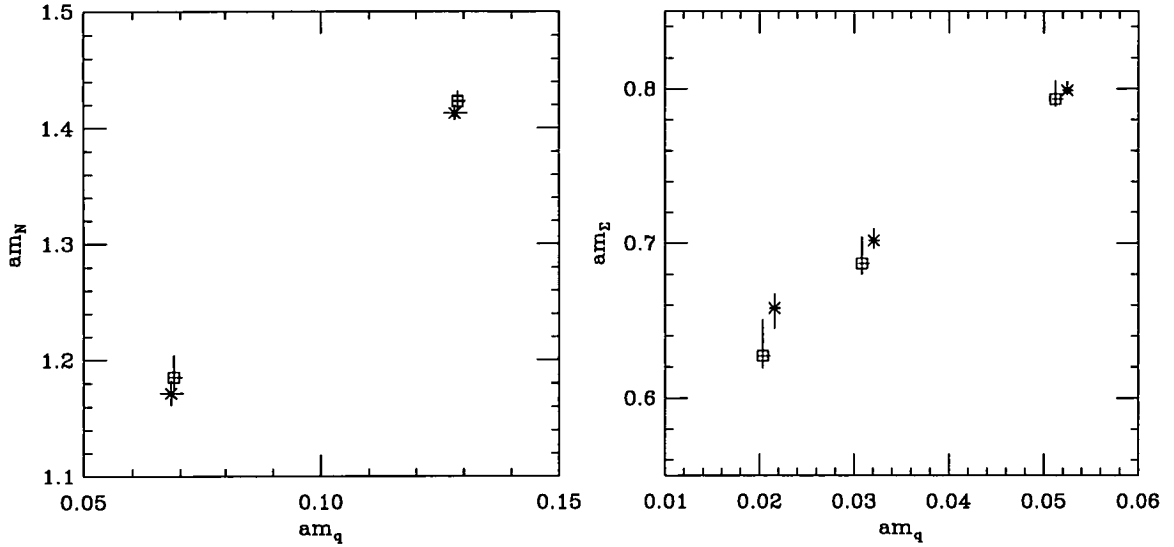


Figure 4.9: Investigation of finite volume effects in the spin- $\frac{1}{2}$ baryons. The plot on the left shows the nucleon masses calculated at $\beta = 5.7$ with $C=TAD$, the (\square) and the (\times) corresponding to the $16^3 \times 32$ and $12^3 \times 24$ lattices respectively. The plot on the right shows the ‘ Σ -like’ masses calculated at $\beta = 6.0$ with $C=NP$, the (\square) and the (\times) corresponding to the $32^3 \times 64$ and $16^3 \times 48$ lattices respectively.

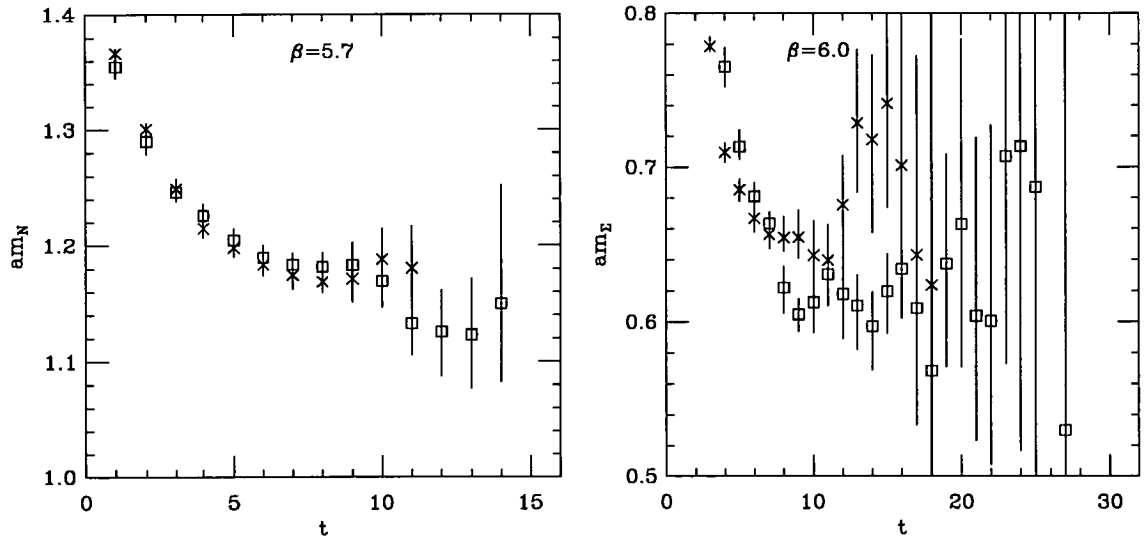


Figure 4.10: Each plot contains a comparison between the effective masses calculated at each of the two lattice volumes at $\beta = 5.7$ and $\beta = 6.0$ for the lightest nucleon. The effective masses are represented by a (\times) and a (\square) for the small and large volume, respectively. The masses are obtained from the (SSS,LLL) correlator at $\beta = 5.7$, and from the (SSS,LLL) and (FFL,LLL) correlators on the large and small volumes, respectively at $\beta = 6.0$.

4.2.4 Spin- $\frac{3}{2}$ Baryons Chiral Extrapolations

The chiral expansion for the spin- $\frac{3}{2}$ masses for the case of 3 non-degenerate quarks is [50, 51],

$$\begin{aligned}
 m_{\{ABC\}} &= M'_0 + c^\Delta(m_A + m_B + m_C) \\
 &\quad d_1^\Delta(M_{AB}^3 + M_{BC}^3 + M_{CA}^3) + d_2^\Delta(M_{AA}^3 + M_{BB}^3 + M_{CC}^3) \\
 &\quad e_1^\Delta(m_A m_B + m_B m_C + m_C m_A) + e_2^\Delta(m_A^2 + m_B^2 + m_C^2), \quad (4.28)
 \end{aligned}$$

where terms like M_{AB} are for the mass of the non-degenerate pion made with quarks A and B, and terms due to quenched chiral logarithms have been ignored. The Δ masses are fitted to the following ansätze:

Fit 1 : $m_\Delta = M'_0 + C_1 m_q$ fitted to all masses of type $\{AAA\}$,

Fit 2 : $m_\Delta = M'_0 + C_1 m_q$ fitted to all masses of type $\{ABC\}$,

Fit 3 : $m_\Delta = M'_0 + C_1 m_q + C_2 m_q^{3/2}$
fitted to all masses of type $\{ABC\}$,

Fit 4 : $m_\Delta = M'_0 + C_1 m_q + C_3 m_q^2$
fitted to all masses of type $\{ABC\}$,

Fit 5 : $m_\Delta = M'_0 + C_1 m_q + C_2 m_q^{3/2} + C_3 m_q^2$
fitted to all masses of type $\{ABC\}$,

in all fits we take $m_q = (m_A + m_B + m_C)/3$. The higher order fits, 3-5, are to enable a test for non-linearity in the chiral expansion and originate through making some assumptions in the chiral expansion (4.28) that do not have any firm theoretical foundations. Once again a detailed investigation of equation (4.28) would require a study of the mass splittings between the spin- $\frac{3}{2}$ baryons.

The results of the fits at $\beta = 6.0$ with C=TAD are shown in table 4.8. The picture here is the same as for the spin- $\frac{1}{2}$ octet baryon extrapolations in that there is consistency between the fits to data with degenerate and non-degenerate quark masses, and the data do not support the use of the higher order fits. The linear chiral extrapolations to the ten non-degenerate spin- $\frac{3}{2}$ baryons masses for C=TAD at $\beta = 6.0$ and $\beta = 6.2$ is shown in figure 4.11.

Fit	#points	M_0	C_1	C_2	C_3	$\chi^2/\text{d.o.f.}$
1	3	0.676 $^{+15}_{-18}$	3.57 $^{+27}_{-20}$			0.9/1
2	10	0.668 $^{+17}_{-16}$	3.73 $^{+21}_{-20}$			7.8/8
3	10	0.680 $^{+30}_{-35}$	3.03 $^{+188}_{-130}$	2.07 $^{+382}_{-544}$		7.6/7
4	10	0.679 $^{+26}_{-29}$	3.31 $^{+103}_{-72}$		4.13 $^{+679}_{-972}$	7.5/7
5	10	0.645 $^{+66}_{-66}$	8.28 $^{+803}_{-898}$	-32.0 $^{+569}_{-490}$	61 $^{+86}_{-103}$	7.2/6

Table 4.8: Chiral extrapolations for the Δ masses calculated at $\beta = 6.0$, C=TAD on the $16^3 \times 48$ lattice.

Finite Volume Effects in the Spin- $\frac{3}{2}$ baryons

In figure 4.12 the spin- $\frac{3}{2}$ baryon masses are plotted for both volumes at $\beta = 5.7$ with C=TAD and $\beta = 6.0$ with C=NP. There is excellent agreement between the masses from both volumes at $\beta = 6.0$ and the masses agree within statistical errors at $\beta = 5.7$, as can be observed in the effective mass plots for this state calculated at the lightest quark masses and shown in figure 4.13. Therefore we can conclude that there are no observable finite volume effects in the spin- $\frac{3}{2}$ baryon masses on our lattices.

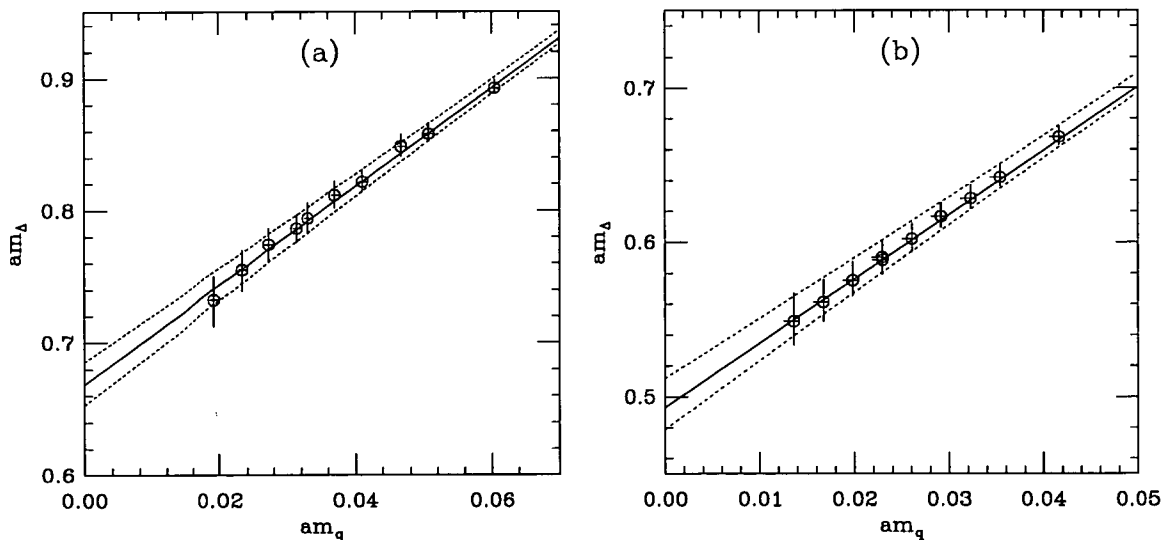


Figure 4.11: Linear chiral extrapolation of the Δ ; plot (a) shows the data at $\beta = 6.0$ and C=TAD and plot (b) shows the data at $\beta = 6.2$ and C=TAD.

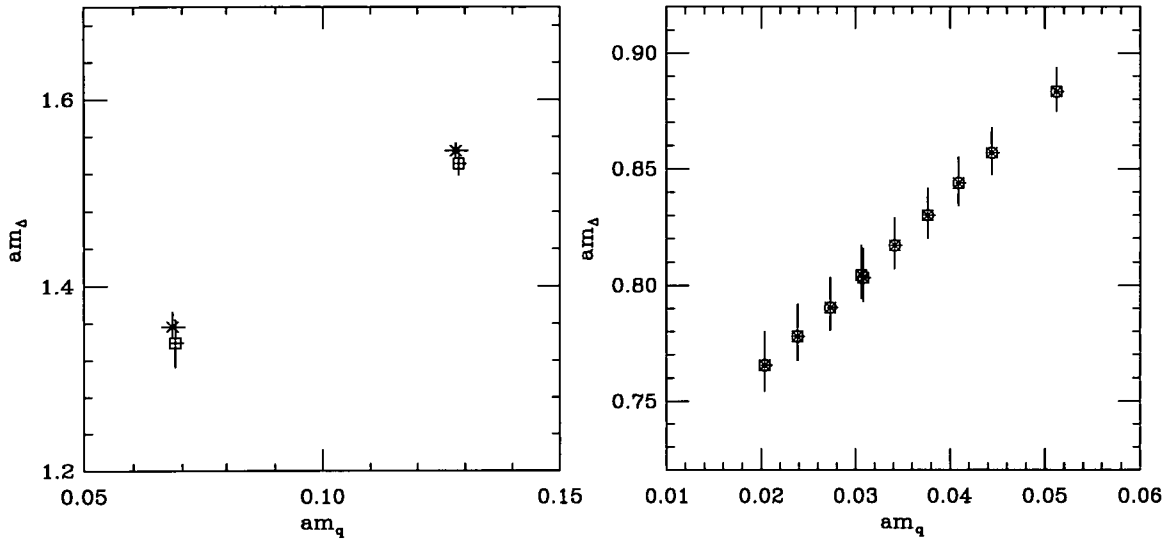


Figure 4.12: Investigation of finite volume effects in the Δ . The plot on the left shows the Δ masses calculated at $\beta = 5.7$ with C=TAD, the (\square), and the (\times) corresponding to the $16^3 \times 32$ and $12^3 \times 24$ lattices respectively. The plot on the right shows the degenerate Δ masses calculated at $\beta = 6.0$ with C=NP, the (\square) and the (\times) correspond to the $32^3 \times 64$ and $16^3 \times 48$ lattices respectively.

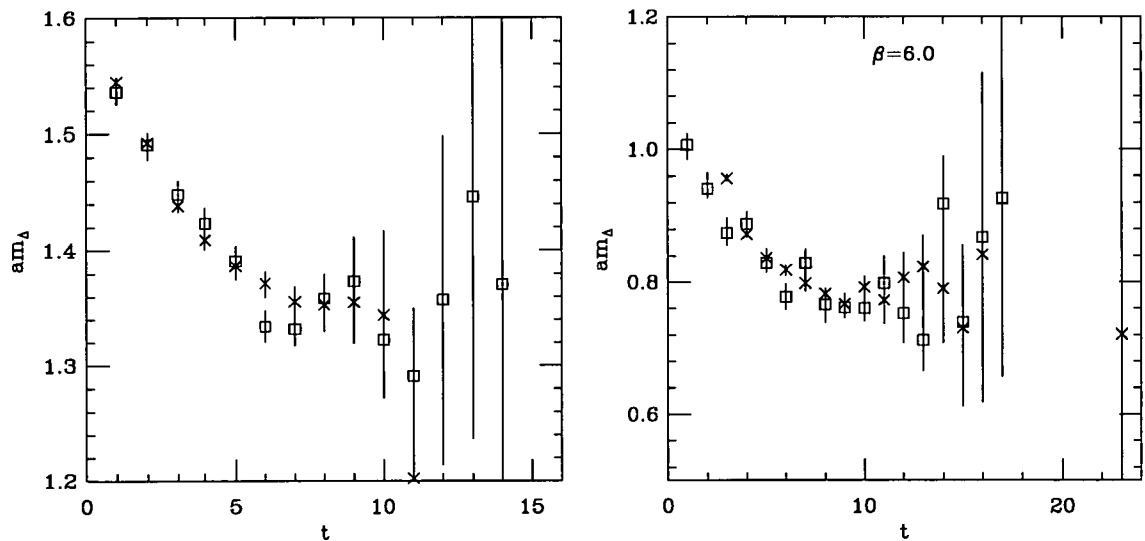


Figure 4.13: Each plot contains a comparison between the effective masses calculated at each of the two lattice volumes at $\beta = 5.7$ and $\beta = 6.0$ for the lightest Δ . The effective masses are represented by a (\times) and a (\square) for the small and large volume, respectively. The masses are obtained from the (SSS,LLL) correlator at $\beta = 5.7$, and from the (SSS,LLL) and (FFL,LLL) correlators on the large and small volumes, respectively at $\beta = 6.0$.

4.3 A Brief Investigation of Scaling

Section 1.7 describes the renormalisation group prediction for the approach to the continuum i.e. $g(a) \rightarrow 0$ as $a \rightarrow 0$. In this regime, ratios of dimensionless quantities should be independent of the coupling. QCD should have a well-defined continuum limit for any specific choice of quark masses.

Simulations are usually carried out for a range of quark masses and the data extrapolated/interpolated to physical quark mass values. For simplicity, if we consider a single quark flavour, then we can fix the quark mass by fixing m_{PS}/m_V , say. The spectra obtained at different lattice spacings may be compared in an Edinburgh Plot [103] in which one mass ratio, m_N/m_V is plotted versus the ratio used to fix the quark mass, m_{PS}/m_V . Scaling corresponds to these data falling on a universal curve independent of a . The data are compared with a phenomenological quark model [104]

$$M_{baryon} = M_b + \sum_{i=1}^3 m_i + \xi_b \sum_{i>j} \frac{\vec{s}_i \cdot \vec{s}_j}{m_i m_j}, \quad (4.29)$$

$$M_{meson} = M_m + \sum_{i=\bar{q},q} m_i + \xi_m \frac{\vec{s}_{\bar{q}} \cdot \vec{s}_q}{m_{\bar{q}} m_q}, \quad (4.30)$$

where the parameters, M , m and ξ are taken from experiment. This is expected to be a good model, for large quark mass, but does not have the correct chiral behaviour.

The Edinburgh Plot is shown in figure 4.14, for data from the small volumes at all β values with $C=TAD$ and $C=NP$. To illustrate the effects of using an improved fermion action we also show data with $C=0$, taken from [86]. We first observe that there is extremely good agreement between the data at all β values using the $O(a)$ -improved fermion actions. This is not observed in the case of when $C=0$, where there are clear scaling violations, the points lie above the phenomenological curve, which is well reproduced by the data from the $O(a)$ -improved fermion actions.

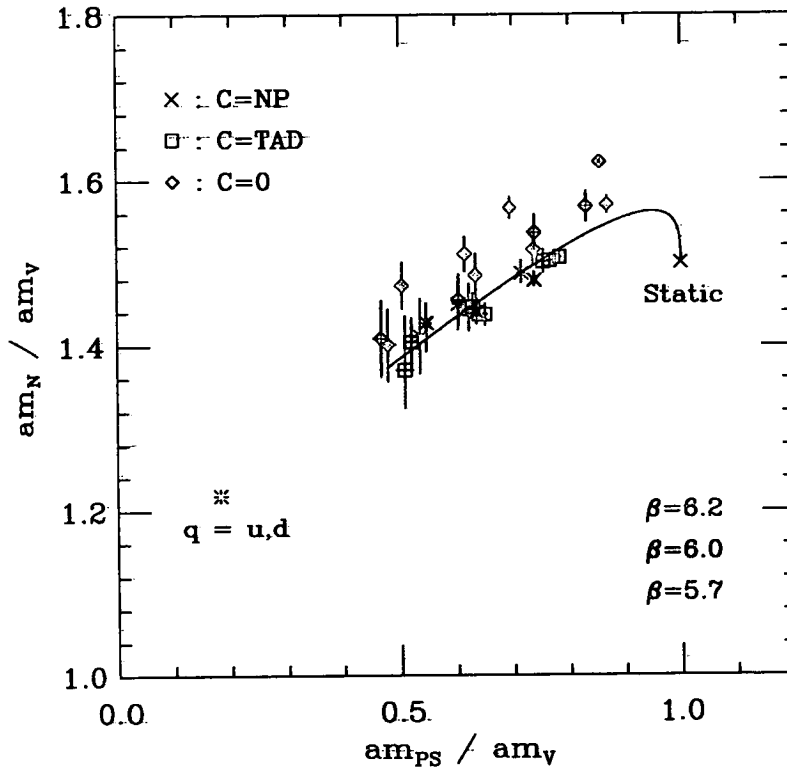


Figure 4.14: The Edinburgh plot for $C=NP$, $C=TAD$ and $C=0$ at all β values. The $C=0$ data are taken from [86], the β values in this case correspond to 5.7, 5.93 and 6.17. There is clearly improved scaling behaviour for the $O(a)$ -improved fermion actions where there is extremely good agreement between the results at all β values, which is not observed in the case of $C=0$.

A novel way of looking at the possible scaling violations in the meson sector is to take a chiral extrapolation for a pion, for example, and set the scale using the string tension \sqrt{K} , given in table 3.1. A similar plot is made for the rho data and these are both shown in figure 4.15, for data from the small volumes at all β values with $C=TAD$ and $C=NP$. We observe excellent agreement between the data for the pion with $C=NP$; the data at $C=TAD$ are not in as good agreement, and there is indication of scaling violations at $\beta=5.7$. For the rho we again observe that the scaling violations are reduced using $C=NP$ over that with $C=TAD$.

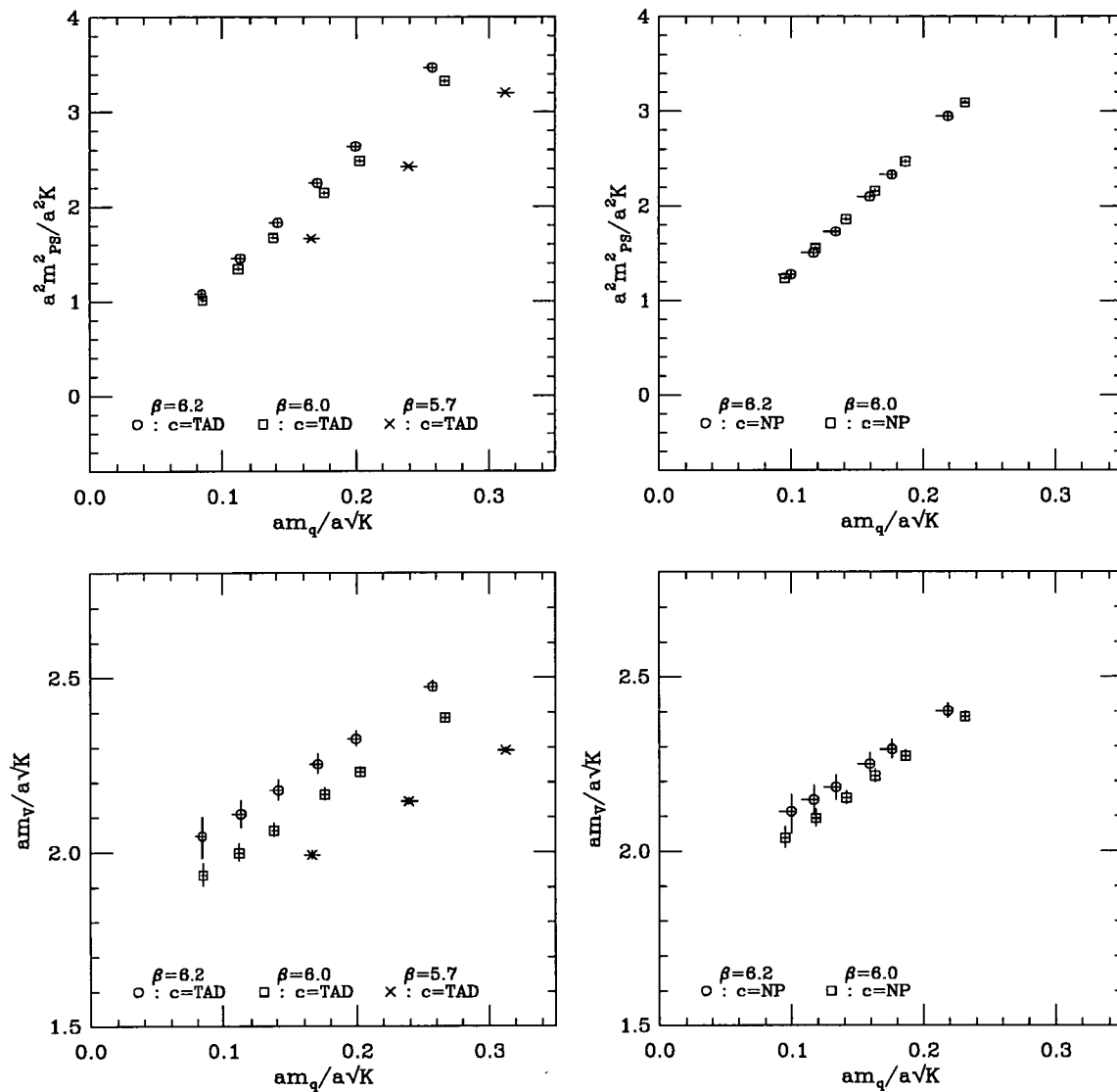


Figure 4.15: Comparison of the chiral behaviour of $am_{PS}/a\sqrt{K}$ and $am_V/a\sqrt{K}$, between the β values with C=TAD and C=NP and all the quark masses computed.

4.4 Determination of the Light Quark Masses

We have obtained the chiral behaviour of the computed hadron masses, as a function of the bare, unrenormalised quark mass in section 4.2. The next step is to calculate the masses of physical states like the π meson, which requires the interpolation/extrapolation to quark masses of the constituent quarks of these states, in this case an extrapolation to the mass average of the up and down quarks. Therefore the masses of the light quarks on the lattice are required as input.

4.4.1 The Normal Quark Mass

In early lattice calculations, the masses of hadrons containing light quarks were obtained by extrapolating the up and down-quark mass to the chiral limit, $m_\pi = 0$, i.e. setting $\kappa_u = \kappa_d = \kappa_c$. Of course, the physical mass of the π meson is 137 MeV, which is non-zero. Hence, a somewhat more reasonable procedure is to extrapolate to the so called “normal” quark mass, which corresponds to the isospin symmetric mass $\bar{m} = (m_u + m_d)/2$, since electromagnetic effects are not included in the simulations. We fix \bar{m} to be at the experimental³ ratio of M_π with M_ρ , through solving the chosen chiral expansions of the pion and rho given in equations (4.7) and (4.18), respectively, at

$$\frac{am_{PS}}{am_V} = \frac{M_\pi}{M_\rho} = 0.1786. \quad (4.31)$$

The normal quark mass \bar{m} can be related to κ_n through the bare unrenormalised quark mass

$$a\bar{m} = \frac{1}{2} \left(\frac{1}{\kappa_n} - \frac{1}{\kappa_c} \right), \quad (4.32)$$

and is tabulated in appendix B. The systematic errors in determining κ_n could be investigated using a different experimental ratio of hadron masses composed of up and down quarks. If we use, for example, M_π/M_N , the statistical errors in

³The convention which is adopted here is that masses denoted by, “M”, refer to experimental quantities whereas, “m”, refers to lattice values. All experimental values are taken from [105], unless otherwise stated.

the determination of κ_n are large and so this was not taken any further. However, the advantage of using the ratio M_π/M_N over M_π/M_ρ is that, in full QCD, the ρ meson decays, whereas the π meson and nucleon are stable.

4.4.2 The Strange Quark Mass

A similar procedure to the above is adopted in the determination of the strange quark mass, m_s . In this particular case we use experimental values of mesons composed not only of strange quarks, but also those composed of a strange quark and either an up or down quark. Though in the latter we need to use \bar{m} , we can then investigate the systematic errors in the determination of m_s .

In the determination of m_s we have again set the lattice scale from $M_\rho = 769$ MeV. The experimental masses we use are the strange pseudoscalar meson mass $M_K = 494$ MeV, where K is composed of a strange quark and a normal quark, the corresponding vector meson mass $M_K^* = 894$ MeV, and the $\bar{s}s$ vector meson⁴ $M_\phi = 1019$ MeV. In the case of the pseudoscalar, the ratio m_{PS}^2/m_ρ^2 , where am_ρ is the vector chirally extrapolated to the normal quark mass, is interpolated to the experimental ratio M_K^2/M_ρ^2 , using the chiral form given in equation (4.7) thus obtaining $m_q = (\bar{m} + m_s)/2$. Similar interpolations are performed in the case of the vector channels. The results for m_s are given for $\beta = 6.0$ with C=TAD in table 4.9, and in appendix B for all data sets. The strange quark mass quoted in the final column is calculated from

$$m_s(a) = \frac{1}{2a} \left(\frac{1}{\kappa_s} - \frac{1}{\kappa_c} \right), \quad (4.33)$$

At fixed lattice spacing a , there is a 10% difference between the values of m_s and they are not within statistical errors, presumably because of a combination of quenching and discretisation errors.

⁴In full QCD, there is mixing between the omega and phi vector mesons which means that the phi might not be a pure $\bar{s}s$ state, see [105] page 99. This does not occur in the valence approximation. However this is another source of systematic error, which has been neglected here.

Qty	κ_s	m_s (MeV)
M_K/M_ρ	0.13754 $\begin{smallmatrix} +6 \\ -6 \end{smallmatrix}$	90 $\begin{smallmatrix} +2 \\ -2 \end{smallmatrix}$
M_{K^*}/M_ρ	0.13739 $\begin{smallmatrix} +9 \\ -11 \end{smallmatrix}$	98 $\begin{smallmatrix} +4 \\ -3 \end{smallmatrix}$
M_ϕ/M_ρ	0.13732 $\begin{smallmatrix} +9 \\ -11 \end{smallmatrix}$	102 $\begin{smallmatrix} +4 \\ -4 \end{smallmatrix}$

Table 4.9: κ_s determined using different mass ratios at $\beta = 6.0$ with C=TAD. The strange quark mass m_s is determined in the lattice regularisation scheme.

4.5 Scaling Behaviour

4.5.1 How to set the mass scale

In quenched Lattice QCD, the inverse bare coupling β is the only free parameter. Thus the value of β fixes the mass scale (or lattice spacing a), which is determined by measuring a physical mass m in lattice units, and comparing with the corresponding experimental value M_{phys} yielding $a(\beta) = M_{phys}/m(\beta)$. On repeating this procedure for various β we can determine the dependence of the lattice spacing on the bare coupling $a(g^2)$, or, by inverting the relation, extract a running coupling $g^2(a)$. As soon as behaviour according to perturbation theory is observed (asymptotic scaling), the running lattice coupling can be translated into any other renormalisation scheme perturbatively.

4.5.2 The String Tension

We shall also fix the physical mass scale from the string tension $\sigma = K/a^2$ which is defined to be the slope of the potential between heavy quark sources $V(R)$ at large $q\bar{q}$ -separations

$$K = - \lim_{r \rightarrow \infty} F(r), \quad F(r) = - \frac{\partial V(r)}{\partial r}. \quad (4.34)$$

The advantages of using the string tension are that it is a purely gluonic quantity and therefore the discretisation errors are of $O(a^2)$, finite size effects are small, and the string tension is the most accurately measured dimensionful quantity on

the lattice [69], The draw-back in using the string tension is that the experimental value is ambiguous:

- Regge trajectories suggest a value $\sqrt{\sigma} \approx 400 - 450$ MeV [106].
- Potential related information can be gained from the Charmonium and Bottomium spectra by integration of the Schrödinger equation [107, 108, 109]. The spectra are determined predominately by the potential between distances r about 0.2 fm and 1 fm, since the corresponding wave functions almost vanish for smaller or larger separations. This is fortunate as for smaller r relativistic corrections to the Schrödinger equation have to be taken into account. For larger separations, differences between the quenched potential and full QCD potential are expected due to creation of a $q\bar{q}$ pair from the vacuum, a phenomena known as “string breaking”. The phenomenological potential is well described by the Cornell parameterisation

$$V(r) = V_0 - \frac{e}{r} + Kr. \quad (4.35)$$

Before the discovery of the Υ' , typical fit parameters were $\sqrt{\sigma} = 455$ MeV, and $e = 0.25$ [107]. After inclusion of the Υ mass splitting, these parameters moved rapidly to values like $\sqrt{\sigma} = 412$ MeV, $e = 0.51$ [108], or $\sqrt{\sigma} = 427$ MeV, $e = 0.52$ [109].

We take $\sqrt{\sigma} = 427$ MeV as, the physical value of the string tension and assume the error in this value is of the order of 5%.

4.6 Light Hadron Masses and Continuum Extrapolations

4.6.1 The ρ mass in the continuum

The lattice value of the rho mass is calculated by a chiral extrapolation of the vector masses, m_V , to the normal quark mass, $m_q = \bar{m}$, and is tabulated in appendix B. The lattice spacing dependence of the ρ mass in units of the \sqrt{K} is shown in figure 4.16, where the results from other simulations with different

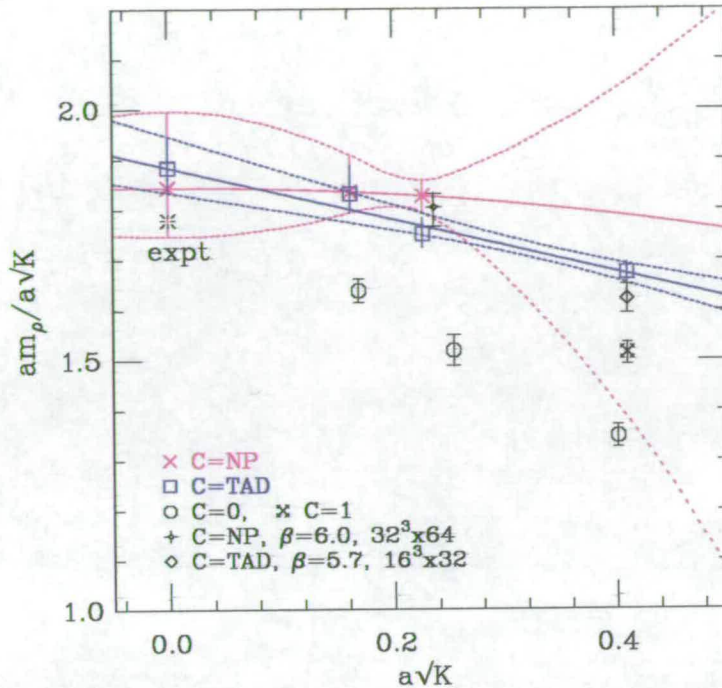


Figure 4.16: Continuum extrapolation of the am_ρ with the lattice scale set by the string tension $a\sqrt{K}$, for the $C=TAD$ and $C=NP$ data sets. Also shown, to demonstrate the scaling behaviour of different fermion actions, are data for the Wilson fermion action $C=0$ [86] and the tree-level-improved Sheikholeslami-Wohlert fermion action $C=1$ [78]. The physical value is shown by a burst, as will be in the case in all other plots unless otherwise stated.

values of the clover coefficient in the fermion action are plotted for comparison. We observe a reduced lattice-spacing dependence for the $O(a)$ -improved fermion actions, compared to the Wilson case, $C=0$.

The tadpole-improved prescription is expected to reduce the leading discretisation error in physical quantities, but not to eliminate it completely, so that some $O(a)$ -dependence should remain in this data. Therefore we perform a continuum extrapolation with

$$am_\rho^{TAD}/a\sqrt{K} = C_0 + C_1^F a\sqrt{K}. \quad (4.36)$$

In contrast, the leading lattice spacing dependence for the non-perturbative im-

provement prescription is $O(a^2)$, so we fit to

$$am_\rho^{NP}/a\sqrt{K} = C_0 + C_2^N a^2 K. \quad (4.37)$$

The continuum extrapolations are performed using uncorrelated fits. The errors from the fit to the C=NP data are large as no minimisation procedure has been performed, since there are no remaining degrees of freedom. The ratios $m_\rho/\sqrt{K}(a=0)$ obtained from the continuum extrapolations to the NP and the tadpole-improved data are in very good agreement, and consistent with a linear extrapolation to the Wilson data. The data using the Wilson fermion action shows a much stronger lattice-spacing dependence. At a fixed lattice-spacing $\beta \approx 6.0$ there is a 20% increase in this quantity towards the physical value in using C=NP over C=0. The plot of $am_\rho/a\sqrt{K}$ is a very good demonstration of the efficiency of $O(a)$ -improvement.

The errors in the values of $a\sqrt{K}$, listed in table 3.2, were not included in the continuum extrapolations. Therefore the errors in the extrapolated values are underestimated, but on changing the values of $a\sqrt{K}$ consistently to $a\sqrt{K} \pm \sigma$, the central values of these fits are within the statistical errors of the values quoted.

Investigation of the Continuum Extrapolations of $am_\rho/a\sqrt{K}$

To investigate the systematic errors in the continuum extrapolations, more β values are required so that higher-order terms in a can be included in the fit. In the case of the tadpole-improved data the need for higher order terms can be justified by the fact that, while $O(a)$ discretisation errors have been significantly reduced the $O(a^2)$ discretisation errors are important. We have already observed when fitting both actions independently the continuum values are consistent. Therefore a simultaneous fit to both actions constraining the continuum value to be the same is worth exploring. This procedure allows a $\chi^2/\text{d.o.f.}$ to be quoted in the following fits: a fit including the C=TAD data set to a full quadratic fit in a and a fit including the C=NP data set to the form given in equation (4.37).

A number of different independent and simultaneous fits were performed to the

Independent fit to the C=TAD data set	
Fit 1 :	$am_\rho^{TAD}/a\sqrt{K} = C_0 + C_1^T a\sqrt{K}$
Fit 2 :	$am_\rho^{TAD}/a\sqrt{K} = C_0 + C_2^T a^2K$
Fit 3 :	$am_\rho^{TAD}/a\sqrt{K} = C_0 + C_1^T a\sqrt{K} + C_2^T a^2K$
Independent fit to the C=NP data set	
Fit 4 :	$am_\rho^{NP}/a\sqrt{K} = C_0$
Fit 5 :	$am_\rho^{NP}/a\sqrt{K} = C_0 + C_2^N a^2K$
Simultaneous fit to both the C=TAD and C=NP data sets	
Fit 6 :	$am_\rho^{NP}/a\sqrt{K} = C_0$
	$am_\rho^{TAD}/a\sqrt{K} = C_0 + C_1^T a\sqrt{K}$
Fit 7 :	$am_\rho^{NP}/a\sqrt{K} = C_0$
	$am_\rho^{TAD}/a\sqrt{K} = C_0 + C_2^T a^2K$
Fit 8 :	$am_\rho^{NP}/a\sqrt{K} = C_0 + C_2^N a^2K$
	$am_\rho^{TAD}/a\sqrt{K} = C_0 + C_1^T a\sqrt{K}$
Fit 9 :	$am_\rho^{NP}/a\sqrt{K} = C_0 + C_2^N a^2K$
	$am_\rho^{TAD}/a\sqrt{K} = C_0 + C_2^T a^2K$
Fit 10 :	$am_\rho^{NP}/a\sqrt{K} = C_0 + C_2^N a^2K$
	$am_\rho^{TAD}/a\sqrt{K} = C_0 + C_1^T a\sqrt{K} + C_2^N a^2K$
Fit 11 :	$am_\rho^{NP}/a\sqrt{K} = C_0 + C_2^N a^2K$
	$am_\rho^{TAD}/a\sqrt{K} = C_0 + C_1^T a\sqrt{K} + C_2^T a^2K$

Table 4.10: Ansätze used in the continuum extrapolations of $am_\rho/a\sqrt{K}$. For fits 12-15 we repeat fits 6-9 but without the point at $\beta = 5.7$ for the C=TAD data set, the fits are repeated in the same order.

C=TAD and C=NP data sets for the continuum extrapolations of $am_\rho/a\sqrt{K}$, the ansätze which were used are given in table 4.10. The results of the fits are given in table 4.11 and the extrapolated values are shown in figure 4.17. In the simultaneous fits there are correlations between the C=TAD and C=NP data as they were generated from the same gauge configurations. However, by looking at the data-covariance matrix we find these correlations to be very small, and therefore do not include them in the fits.

We first observe that with the exception of fit 3 all the extrapolated values are roughly consistent. The errors on the fitted parameters are large and therefore

Fit	C_0	C_1^T	C_2^T	C_3^N	$\chi^2/\text{d.o.f.}$
1	1.884 ⁺⁶² ₋₅₀	-0.50 ⁺¹⁴ ₋₁₇			0.79/1
2	1.812 ⁺³⁹ ₋₃₀		-0.82 ⁺²⁴ ₋₂₉		1.24/1
3	2.155 ⁺³⁶⁸ ₋₂₅₇	-2.52 ⁺¹⁹² ₋₂₆₈	3.33 ⁺⁴³⁹ ₋₃₁₄		
4	1.829 ⁺³³ ₋₂₅				0.02/1
5	1.844 ⁺¹⁵² ₋₉₇			-0.32 ⁺²¹⁷ ₋₃₃₃	
6	1.841 ⁺²⁸ ₋₂₀	-0.39 ⁺⁷ ₋₉			1.66/3
7	1.821 ⁺²⁵ ₋₁₈		-0.88 ⁺¹⁶ ₋₂₁		1.41/3
8	1.877 ⁺⁵⁸ ₋₃₉	-0.49 ⁺¹² ₋₁₇		-1.03 ⁺¹⁰⁵ ₋₁₄₀	0.88/2
9	1.814 ⁺³⁹ ₋₂₇		-0.83 ⁺²² ₋₂₈	0.29 ⁺⁸⁶ ₋₁₀₁	1.30/2
10	1.847 ⁺³⁰ ₋₂₁	-0.26 ⁺¹⁹ ₋₁₈	-0.36 ⁺⁴³ ₋₅₂	-0.36 ⁺⁴³ ₋₅₂	0.99/2
11	1.886 ⁺¹⁵¹ ₋₈₉	-0.56 ⁺⁷² ₋₁₁₁	0.13 ⁺¹⁸⁷ ₋₁₂₃	-1.20 ⁺¹⁹⁹ ₋₃₁₆	0.87/1
12	1.834 ⁺³¹ ₋₂₄	-0.30 ⁺¹⁸ ₋₁₈			1.33/2
13	1.835 ⁺³⁰ ₋₂₄		-1.51 ⁺⁷⁴ ₋₇₈		0.73/2
14	1.905 ⁺¹³⁴ ₋₇₅	-0.63 ⁺³⁸ ₋₆₅		-1.61 ⁺¹⁷¹ ₋₂₇₈	0.78/1
15	1.887 ⁺⁹⁷ ₋₅₇		-2.60 ⁺¹³⁴ ₋₂₀₉	-1.23 ⁺¹³⁷ ₋₂₁₁	0.20/1

Table 4.11: Results for continuum extrapolations of $am_\rho/a\sqrt{K}$, from fitting the C=TAD and C=NP data sets to a number of different ansätze given in the table 4.10. The physical value of $M_\rho/\sqrt{K} = 1.800$.

we cannot rule out one fit as been better than any other; smaller errors bars on the points in the fit and more points are required in the fit to do this. The results of the independent fits to the C=TAD data indicate the following: the linear extrapolation (fit 1) and the extrapolation to $C_0 + C_1^T a^2$ (fit 2) give good $\chi^2/\text{d.o.f.}$'s, slightly better in the linear case; there is a 2σ discrepancy in the extrapolated values between the fits. The full quadratic fit to the C=TAD data gives coefficients with large error bars. The results of the independent fits to the C=NP data set show that the fit to the constant term only (fit 4) gives a very low $\chi^2/\text{d.o.f.}$ which shows this model is incorrect, and the extrapolated value from fit 5, given in equation (4.37), is consistent with the values obtained from the

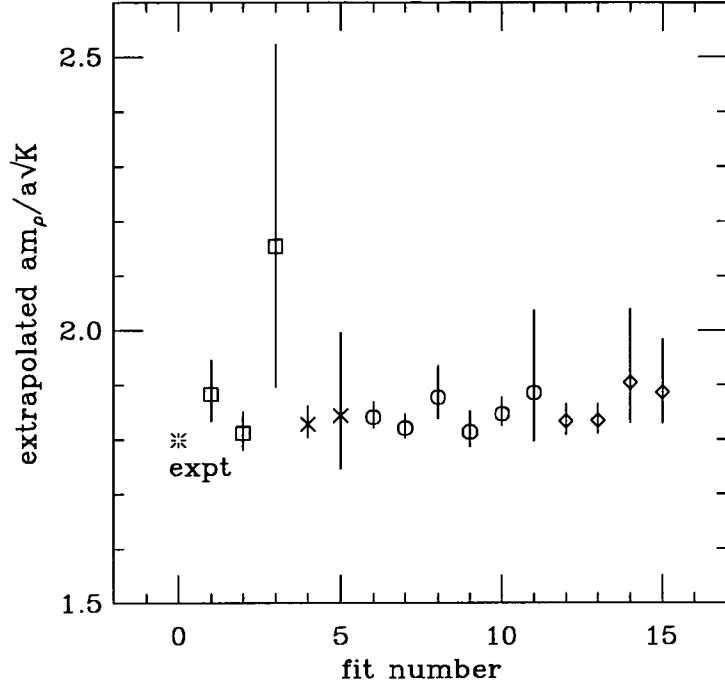


Figure 4.17: Results from continuum extrapolations of $am_\rho/a\sqrt{K}$ to $a \rightarrow 0$, from fitting the C=TAD and C=NP data sets, to a number of different ansätze given in the table 4.10.

other fits. The extrapolated values obtained from the simultaneous fits to both C=TAD and C=NP data sets are within 2σ of each other.

The point at $\beta = 5.7$ with C=TAD has the smallest errors of all the points in the simultaneous fits, and has the largest scaling violations, so simultaneous fits were investigated without this point in fits 12 to 15. The continuum values from these fits are within errors of the other fits, so we can conclude at the current level of statistics including the point at $\beta = 5.7$ is not introducing any systematic error in the fit though including a point not the scaling region. Fit 11 has the best $\chi^2/\text{d.o.f.}$ of the simultaneous fits and is within errors of most of the other fits, this fit is shown in figure 4.18 This fit is consistent to order $O(a^2)$ and following the discussion above is the fit which one would derive from the leading discretisation

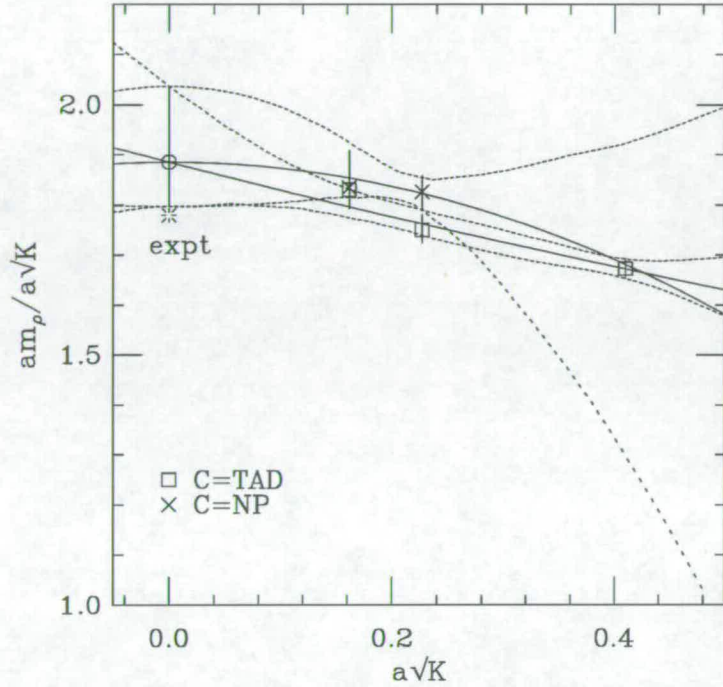


Figure 4.18: Continuum extrapolation of $am_\rho/a\sqrt{K}$ to $a \rightarrow 0$, fitting the C=TAD and C=NP data sets simultaneously, corresponding to fit 11, which is consistent to $O(a^2)$, given in table 4.10.

errors present in each action. However, the quality of the data is insufficient to draw any firm conclusions on the continuum extrapolations one should use. Therefore in the continuum extrapolations for the other physical states calculated we shall proceed as follows.

4.6.2 Conventions used in future continuum extrapolations

Before going on to look at other physical states, it will be worth stating in light of the results of the continuum extrapolations which have been investigated thus far, how future fits are going to be presented. For a lattice determination of the physical state aR , with the lattice scale is set by the quantity aS , the continuum extrapolated value of the ratio R/S will be obtained, in the first instance, from an

independent fit for each action to the lowest order of their discretisation errors i.e.

$$\frac{aR^{TAD}}{aS^{TAD}} = C_0 + C_1^T a, \quad \frac{aR^{NP}}{aS^{NP}} = C_0 + C_2^N a^2, \quad (4.38)$$

to check that both actions are consistent in the continuum limit. If any plot of continuum extrapolations is shown it will correspond to the independent fits in equation (4.38). Whenever a simultaneous fit to both actions is mentioned it will refer to fit 11 above, which corresponds to the fit:

$$\frac{aR^{TAD}}{aS^{TAD}} = C_0 + C_1^T a + C_2^T a^2 \quad \text{and} \quad \frac{aR^{NP}}{aS^{NP}} = C_0 + C_2^N a^2. \quad (4.39)$$

4.6.3 Strange Meson Masses

The K pseudoscalar meson is calculated by interpolating the pion chiral expansion to $m_1 = \bar{m}$ and $m_2 = m_s$, which we shall denote by the expression $m_{PS}^2(\bar{m}, m_s)$. The K^* vector meson is calculated at $m_V(\bar{m}, m_s)$ and the ϕ is calculated at $m_V(m_s, m_s)$. In section 4.4, it was observed that, at fixed a , there is a large systematic error in the calculated value of am_s , which may be attributable to quenching effects and discretisation errors. To investigate this further, we chose to consider the lattice value of the K^* mass. The computed values of am_s by matching lattice and experimental values of M_K/M_ρ , M_ϕ/M_ρ and M_ϕ/M_ρ , are given in table 4.9. The value of am_s computed from M_{K^*}/M_ρ is in between the values computed from M_K/M_ρ and M_{K^*}/M_ρ . Therefore the discrepancy between the lattice value of the K^* mass determined from the two remaining definitions of the am_s will be the largest.

The continuum extrapolations of K^* mass from the two definitions of the strange quark mass using $a\sqrt{K}$ to set the scale is shown in figure 4.19, and the same quantity using am_ρ to set the scale is shown in figure 4.20, but without the continuum extrapolations, which are however listed in tables 4.12 and 4.13 respectively. We observe the improved scaling behaviour for $am_{K^*}/a\sqrt{K}$ of the action with C=NP over that with C=TAD which was seen for $am_\rho/a\sqrt{K}$. This improved scaling behaviour is not observed in the case when the rho mass is used set the scale.

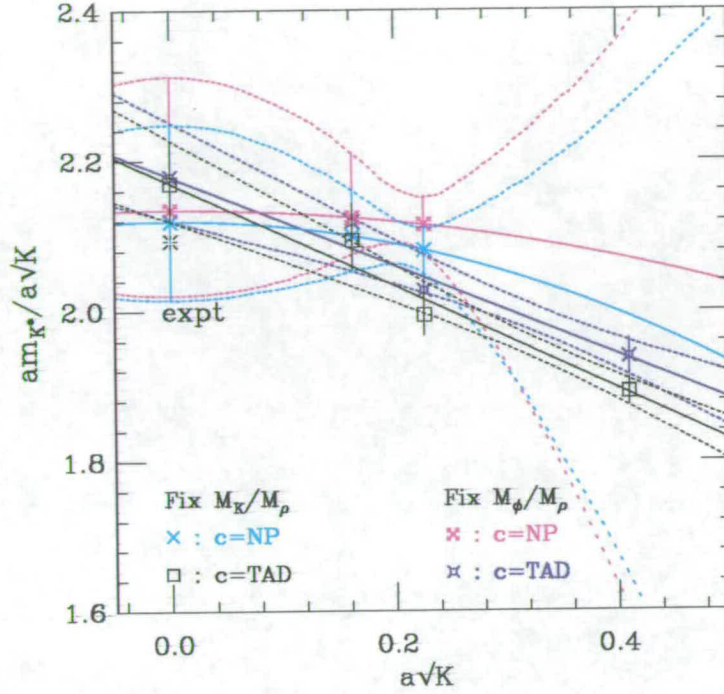


Figure 4.19: Continuum extrapolation of am_{K^*} with the lattice scale set by the string tension $a\sqrt{K}$, for $C=TAD$ and $C=NP$, using two different definitions of the strange quark mass.

How can this be explained? The approach to the continuum for the K^* mass, ρ mass and the string tension \sqrt{K} , can be written as

$$\begin{aligned}
 m_\rho^{TAD} &= C_{T,\rho}^0 + C_{T,\rho}^1 a + C_{T,\rho}^2 a^2 + \dots, \\
 m_\rho^{NP} &= C_{N,\rho}^0 + C_{N,\rho}^2 a^2 + C_{N,\rho}^3 a^3 + \dots, \\
 m_{K^*}^{TAD} &= C_{T,K^*}^0 + C_{T,K^*}^1 a + C_{T,K^*}^2 a^2 + \dots, \\
 m_{K^*}^{NP} &= C_{N,K^*}^0 + C_{N,K^*}^2 a^2 + C_{N,K^*}^3 a^3 + \dots, \\
 \sqrt{K} &= C_{\sqrt{K}}^0 + C_{\sqrt{K}}^2 a^2 + C_{\sqrt{K}}^3 a^3 + \dots,
 \end{aligned} \tag{4.40}$$

where the coefficients C are dependent on whatever quantity is used to set the scale; let's suppose the scale was set from a quantity with no discretisation errors.

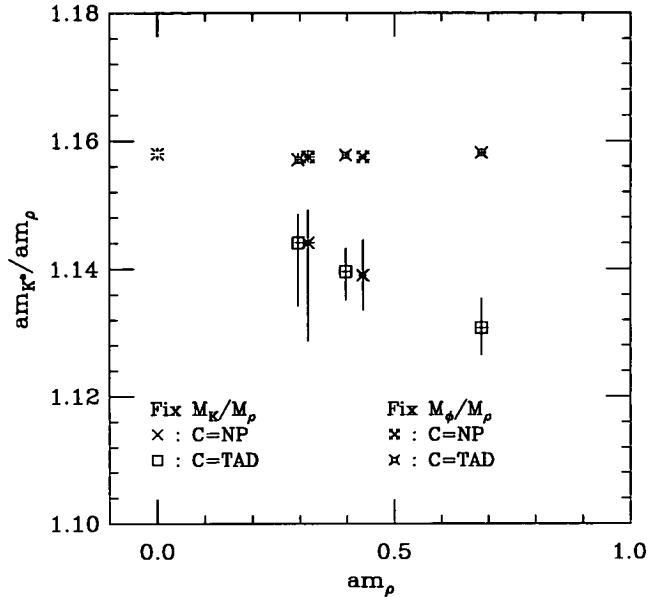


Figure 4.20: K^* mass in units of m_{ρ} , calculated using from two different definitions of the strange quark mass as input.

Using the expansions in equation (4.40) we examine how the tadpole-improved K^* mass approaches the continuum when the scale is set from the ρ mass

$$\frac{m_{K^*}^{TAD}}{m_{\rho}^{TAD}} = \frac{C_{T,K^*}^0}{C_{T,\rho}^0} + \left(\frac{C_{T,K^*}^1}{C_{T,\rho}^0} - \frac{C_{T,\rho}^1}{C_{T,K^*}^0} \right) a + \left(\frac{(C_{T,K^*}^1)^2}{C_{T,\rho}^0 C_{T,K^*}^0} - \frac{C_{T,\rho}^1 C_{T,K^*}^1}{(C_{T,\rho}^0)^2} \right) a^2 + \dots \quad (4.41)$$

The K^* and ρ were calculated from the same channel. Therefore one would expect that these states will have a similar approach to the continuum limit and C_{T,K^*}^1 and $C_{T,\rho}^1$ to be of the same size, as can be seen comparing tables 4.11 and 4.12. Thus the $O(a)$ term is small, and corresponding cancellations could be occurring for the higher order terms. For the C=NP case the K^* mass approaches the continuum when the scale is set from the ρ mass as

$$\frac{m_{K^*}^{NP}}{m_{\rho}^{NP}} = \frac{C_{N,K^*}^0}{C_{N,\rho}^0} + \left(\frac{C_{N,K^*}^2}{C_{N,\rho}^0} - \frac{C_{N,\rho}^2}{C_{N,K^*}^0} \right) a^2$$

$$+ \left(\frac{C_{N,K^*}^3}{C_{N,\rho}^0 (C_{N,K^*}^0)^2} - \frac{C_{N,\rho}^3 C_{N,K^*}^0}{(C_{N,\rho}^0)^4} \right) a^3 + \dots \quad (4.42)$$

We can use an analogous argument to that above to explain why the $O(a^2)$ term and possibly higher order terms are small. The tadpole-improved K^* mass approaches the continuum when the scale is set from the \sqrt{K} as

$$\frac{m_{K^*}^{TAD}}{\sqrt{K}} = \frac{C_{T,K^*}^0}{C_{\sqrt{K}}^0} + \frac{C_{T,K^*}^1}{C_{\sqrt{K}}^0} a + \left(\frac{C_{T,K^*}^2}{C_{\sqrt{K}}^0 C_{T,K^*}^0} - \frac{C_{\sqrt{K}}^2 C_{T,K^*}^0}{(C_{\sqrt{K}}^0)^3} \right) a^2 + \dots, \quad (4.43)$$

and the $O(a)$ term is dependent on the leading cut off effects of this action. The same quantity for the NP case approaches the continuum as

$$\begin{aligned} \frac{m_{K^*}^{NP}}{\sqrt{K}} &= \frac{C_{N,K^*}^0}{C_{\sqrt{K}}^0} + \left(\frac{C_{N,K^*}^2}{C_{\sqrt{K}}^0} - \frac{C_{\sqrt{K}}^2}{C_{N,K^*}^0} \right) a^2 \\ &+ \left(\frac{C_{N,K^*}^3}{C_{\sqrt{K}}^0 (C_{N,K^*}^0)^2} - \frac{C_{\sqrt{K}}^3 C_{N,K^*}^0}{(C_{\sqrt{K}}^0)^4} \right) a^3 + \dots, \end{aligned} \quad (4.44)$$

in this case the $O(a^2)$ term is dependent on the leading cut off effects of the NP action and the action from which the string tension was computed,⁵ we would expect the two to have different approaches to the continuum limit and therefore no cancellations to take place in the $O(a^2)$ term.

The next observation that we make is that the two definitions of the strange quark mass agree in the continuum limit for both actions, and the quoted values from the two actions for m_{K^*}/\sqrt{K} and m_{K^*}/m_ρ agree within one standard deviation. To investigate this further, the strange quark mass was fixed from the ratios $(m_K - m_\pi)/m_\rho$ and $(m_\phi - m_\rho)/m_\rho$. The K^* mass in units of am_ρ , obtained using these definitions of am_s , are plotted in figure 4.21 and the values in continuum limit are listed in table 4.14.

The authors of [85] proposed a different procedure to determine the K^* mass which does not use the bare unrenormalised quark mass m_q , and so is not de-

⁵The string tension is computed from a lattice version of the gluonic action as discussed in section 4.5.2.

Qty.	m_s fixed from	C_0	C_1^T	C_2^N	$\chi^2/\text{d.o.f.}$
$m_{K^*}^{\text{TAD}}/\sqrt{K}$	M_K/M_ρ	2.169 $^{+57}_{-50}$	-0.68 $^{+15}_{-16}$		1.2/1
	M_ϕ/M_ρ	2.177 $^{+73}_{-60}$	-0.59 $^{+17}_{-20}$		0.7/1
$m_{K^*}^{\text{NP}}/\sqrt{K}$	M_K/M_ρ	2.118 $^{+28}_{-105}$		-0.75 $^{+34}_{-282}$	
	M_ϕ/M_ρ	2.133 $^{+77}_{-113}$		-0.39 $^{+54}_{-388}$	

Table 4.12: Results for continuum extrapolations of $am_{K^*}/a\sqrt{K}$, from fitting the C=TAD and C=NP data to the form in equation (4.38). The physical value of $M_{K^*}/\sqrt{K} = 2.093$.

Qty.	m_s fixed from	C_0	C_1^T	C_2^N	$\chi^2/\text{d.o.f.}$
$m_{K^*}^{\text{TAD}}/m_\rho^{\text{TAD}}$	M_K/M_ρ	1.1526 $^{+66}_{-11}$	-0.032 $^{+21}_{-13}$		0.03/1
	M_ϕ/M_ρ	1.1567 $^{+10}_{-9}$	0.002 $^{+2}_{-2}$		0.40/1
$m_{K^*}^{\text{NP}}/m_\rho^{\text{NP}}$	M_K/M_ρ	1.1494 $^{+104}_{-339}$		-0.061 $^{+216}_{-71}$	
	M_ϕ/M_ρ	1.1574 $^{+210}_{-152}$		-0.0003 $^{+93}_{-127}$	

Table 4.13: Results for continuum extrapolations of am_{K^*}/am_ρ , from fitting the C=TAD and C=NP data to the form in equation (4.38). The physical value of $M_{K^*}/M_\rho = 1.1631$.

pendent on the determination of κ_c ; we denote this method the ‘‘APE method’’. This method plots aM_V against $(am_{PS})^2$ and imposes that the ratio M_{K^*}/M_K attains its physical value C_{sl} . This corresponds to finding the intercept of the curve

$$aM_V = C_{sl}\sqrt{(am_{PS})^2}. \quad (4.45)$$

The intercept of the curve and computed data defines aM_K and aM_{K^*} , but only one of these is an independent prediction. The values aM_{K^*} using both linear and non-linear fits to the data were found to be in agreement within statistical errors; we take the value from the linear fit due to the smaller statistical errors.

In the continuum limit, the different definitions of the strange-quark mass yield

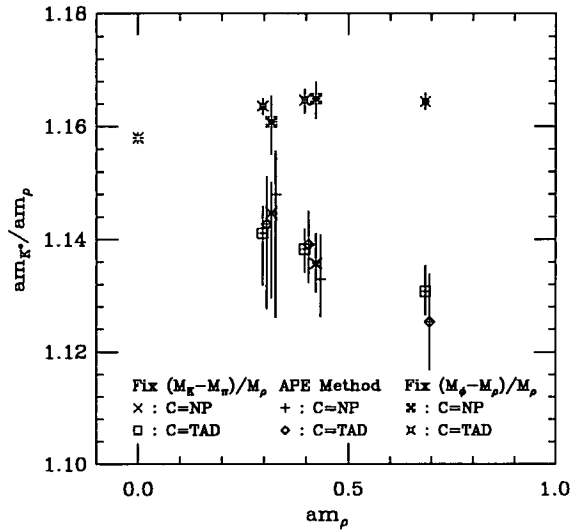


Figure 4.21: K^* mass units of m_{ρ} , calculated using from two different definitions of the strange quark mass as input and results for the APE method of determining the lattice K^* mass are shown.

values for m_{K^*}/m_{ρ} agreeing to within two standard deviations. This is very good agreement, and suggests that at fixed a the differences between the different definitions of the strange quark mass are a discretisation effect which extrapolates away in the continuum limit. Furthermore, agreement between the APE method and the definitions using the bare unrenormalised quark mass, m_q , is a verification of the chiral expansions used for the vector and pion. To illustrate this further, a pion chiral extrapolation which was linear in quark mass, $(am_{PS})^2 = bm_q$, was used instead of the non-linear fit, $(am_{PS})^2 = bm_q + cm_q^2$. Using the linear fit, κ_c , am_s and am_{K^*} , were recalculated and the K^* mass in units of m_{ρ} is plotted in figure 4.22. We observe that the K^* mass determined from the two definitions of the strange-quark mass do not agree in the continuum limit, and if a continuum extrapolation were done by eye for the K^* mass calculated using m_s fixed from M_K/M_{ρ} , its value would not agree with that of K^* mass calculated the APE method.

Qty	am_{K^*}/am_ρ extrapolated to $a \rightarrow 0$	
	C=TAD	C=NP
M_K/M_ρ	1.153 $\begin{smallmatrix} +6 \\ -12 \end{smallmatrix}$	1.149 $\begin{smallmatrix} +10 \\ -34 \end{smallmatrix}$
M_ϕ/M_ρ	1.157 $\begin{smallmatrix} +1 \\ -1 \end{smallmatrix}$	1.157 $\begin{smallmatrix} +2 \\ -2 \end{smallmatrix}$
$(M_K - M_\pi)/M_\rho$	1.149 $\begin{smallmatrix} +7 \\ -11 \end{smallmatrix}$	1.154 $\begin{smallmatrix} +10 \\ -33 \end{smallmatrix}$
$(M_\phi - M_\phi)/M_\rho$	1.163 $\begin{smallmatrix} +2 \\ -3 \end{smallmatrix}$	1.156 $\begin{smallmatrix} +10 \\ -12 \end{smallmatrix}$
APE method	1.157 $\begin{smallmatrix} +13 \\ -18 \end{smallmatrix}$	1.163 $\begin{smallmatrix} +14 \\ -49 \end{smallmatrix}$

Table 4.14: The results of the continuum extrapolations of am_{K^*}/am_ρ at $a = 0$, using the various prescriptions to fix am_s , for both actions. The physical isospin averaged value of $M_{K^*}/M_\rho = 1.163$.

4.6.4 The J parameter

The J parameter is defined as [110]

$$J = m_V \frac{\partial M_V}{\partial m_{PS}^2}, \quad (4.46)$$

and is determined at the experimental ratio

$$\frac{M_{K^*}}{M_K} = 1.8. \quad (4.47)$$

The motivation for the introduction of the parameter J is that it allows a comparison of lattice spectrum results with experimental data, without an extrapolation to the chiral limit. The experimental value of J, using the the K^* , ρ and K , π with differences to determine $\partial m_V/\partial m_{PS}^2$, is $J = 0.48(2)$.

In figure 4.24, we show the values of J determined on the lattice using a variety of methods and the continuum values from a linear fit to the C=TAD data set are given in table 4.15. The first method uses a linear fit to am_V against $(am_{PS})^2$, and J is the slope multiplied by am_V at $m_V = 1.8m_{PS}$. The continuum extrapolation of J shows little a dependence, and extrapolates to a value many standard deviations below the experimental value. This is surprising since the ρ

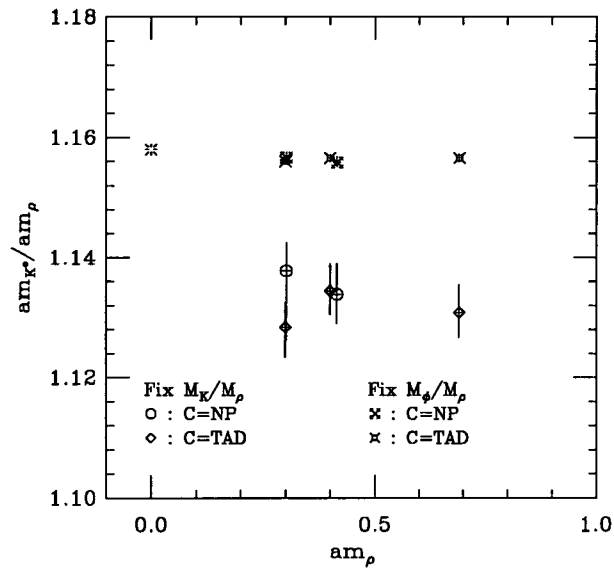


Figure 4.22: K^* mass units of m_ρ . This plot highlights the dependence of the chiral expansion used has on outcome of predictions of hadron masses, in this case the pion was fitted using a linear fit to the quark mass, therefore results in changes of κ_c and m_s which are used to determine the K^* mass.

and K^* mass extrapolated to the continuum are not that far from experiment. The chiral expansions used for the pion and the rho, as a function of the quark mass, imply that

$$am_V = b a^2 m_{PS}^2 + c a^4 m_{PS}^4. \quad (4.48)$$

This non-linear fit to the lattice data is the second method, a plot of equation (4.48) at $\beta = 6.0$ with C=TAD is shown in figure 4.23 and suggests that there is some non-linearity in the data, which is supported by [51, 100, 111, 112, 113]. The values of J calculated using this non-linear fit have larger errors as a result of the relatively large errors on the vector masses, and differ from the values calculated using a linear fit; on extrapolating to the continuum yields a value in better agreement with experiment. The J parameter inspired the authors of [85] to develop the APE method, used in the last section. The reason why the J parameter is more sensitive to the fitting ansatz used than the APE method,

is through the dependence on the slope of the vector to the square of the pion mass.

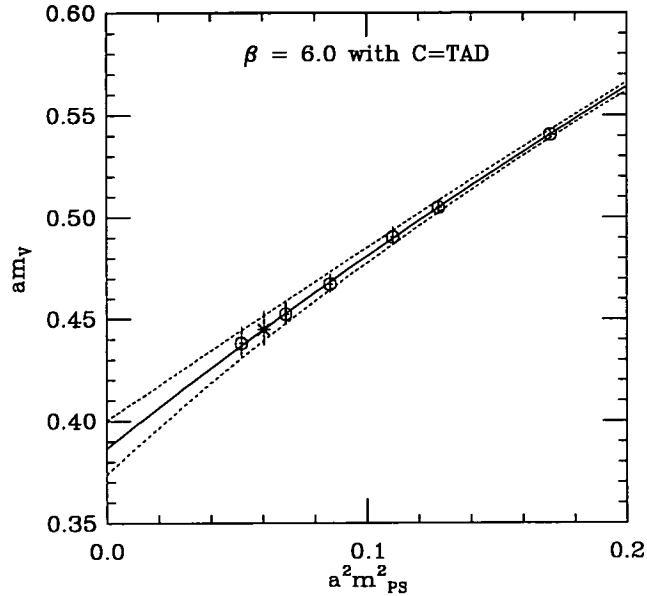


Figure 4.23: Plot shows a quadratic fit to am_V against $a^2 m_{PS}^2$, calculated at $\beta = 6.0$ with $C=TAD$.

The final method determines J using

$$J = am_{K^*} \frac{(am_{K^*} - am_{\rho})}{(a^2 m_K^2 - a^2 m_{\pi}^2)}, \quad (4.49)$$

where m_{K^*} , m_{ρ} , m_K and m_{π} are obtained from our lattice simulations. Here we use m_s determined by ratio m_{ϕ}/m_{ρ} . The errors in J from this method are relatively small and the value extrapolated to the continuum limit is within errors of the experimental value. This lends further support to the chiral expansions used in the case of the pion and vector.

Method	J
Linear fit to am_V .vs. $(am_{PS})^2$	0.387 $\begin{smallmatrix} +8 \\ -10 \end{smallmatrix}$
Quadratic fit to am_V .vs. $(am_{PS})^2$	0.423 $\begin{smallmatrix} +122 \\ -132 \end{smallmatrix}$
From am_{K^*} , am_ρ and am_K , am_π like expt.	0.462 $\begin{smallmatrix} +19 \\ -35 \end{smallmatrix}$

Table 4.15: Results of the linear continuum extrapolation to the C=TAD data set for the J parameter, which is determined using a number of different methods, as described in the text.

4.6.5 The Hyperfine Splitting

Heavy Quark Effective Theory (HQET) predicts that for heavy-light mesons, the vector-pseudoscalar mass splitting, $\Delta_{V-PS} = m_V^2 - m_{PS}^2$, is constant. This is borne out by experiment; $M_{D^*}^2 - M_D^2 \approx 0.53\text{GeV}^2$ and $M_{B^*}^2 - M_B^2 \approx 0.49\text{GeV}^2$. A somewhat unexpected experimental result is that the trend is continued into the light quark regime, where the hyperfine splitting, Δ_{V-PS} , remains approximately constant at 0.55GeV^2 , for example $M_\rho^2 - M_\pi^2 = 0.57\text{GeV}^2$ and $M_{K^*}^2 - M_K^2 = 0.55\text{GeV}^2$

The vector-pseudoscalar mass splittings for both C=TAD and C=NP at all β values computed, together with data at $\beta = 6.0$ with C=0 and C=1 from [51] and [85] respectively, are shown in figure 4.25. The mass-splittings are plotted with the scale set from am_K ,⁶ which is obtained from $am_K = (M_K/M_\rho) \times m_\rho$ and $a\sqrt{K}$. Once again we observe in the case where the scale is set from the string tension that increasing the value of the clover coefficient causes Δ_{V-PS} to increase towards the experimental values, a further demonstration of the improved scaling behaviour of the $O(a)$ -improved fermion actions. Using the ρ mass to set the scale, we can observe little difference between the different actions. Note that the slope $\partial(a^2\Delta_{V-PS})/\partial(am_{PS})^2$ is independent of the clover coefficient. The worry is the decrease in Δ_{V-PS} with increasing quark mass and the implications

⁶The scale is set using am_K instead of am_ρ as it easier to compare the results with the case when the scale set from $a\sqrt{K}$.

this has for the charmonium system. There are two possible sources for this feature, either discretisation errors or quenching effects; as we observe no change in the slope with the different fermion actions, it is more likely to be an artifact of the quenched approximation.

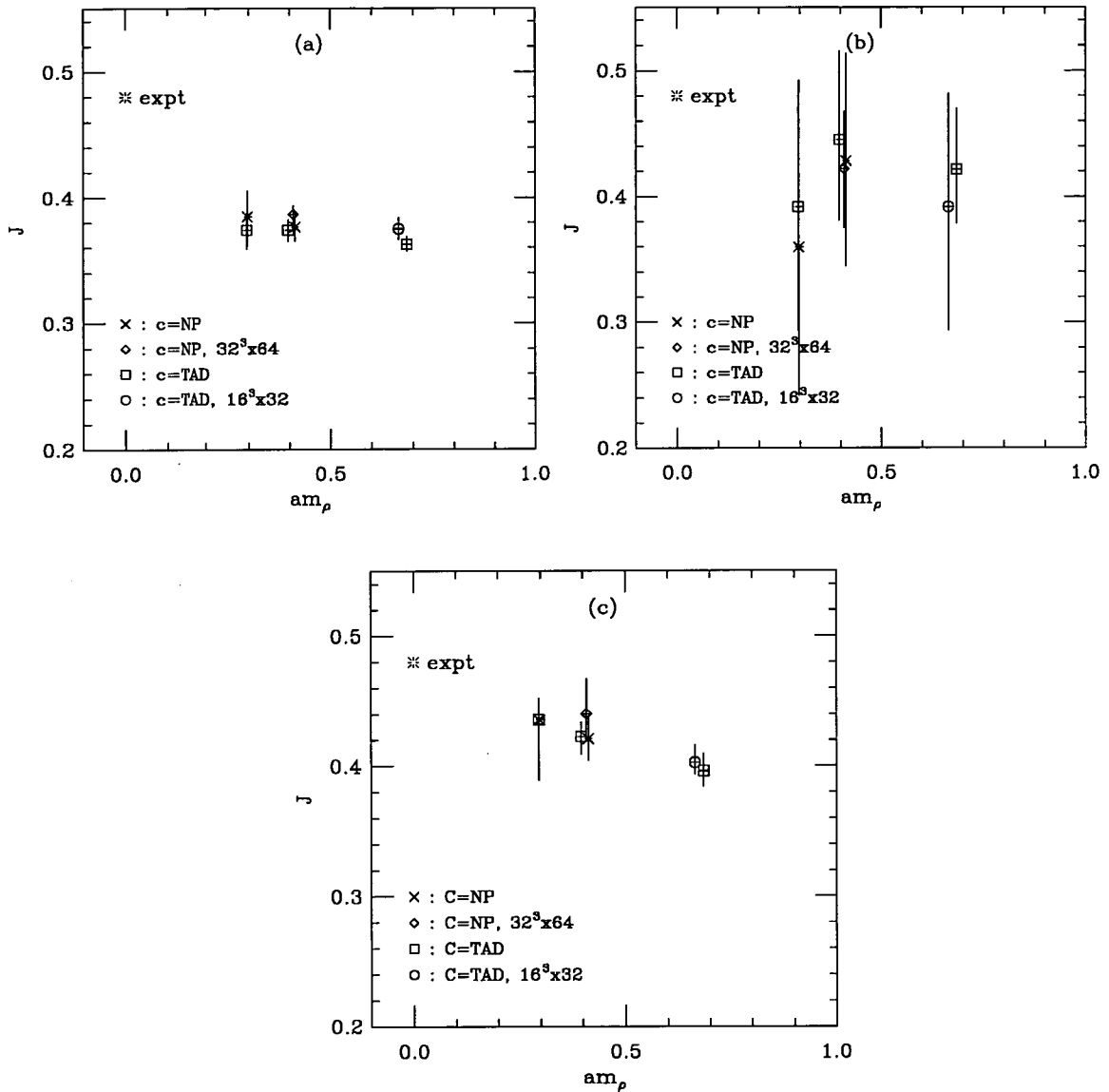


Figure 4.24: Plots (a), (b) and (c) show the J parameter. In plots (a) and (b), $dm_V/dm_{P_S}^2$ is computed using a linear and a quadratic chiral extrapolations respectively as described in the text. The plot (c) corresponds to J calculated from the lattice determination of am_π , am_K , am_ρ , and am_{K^*} .

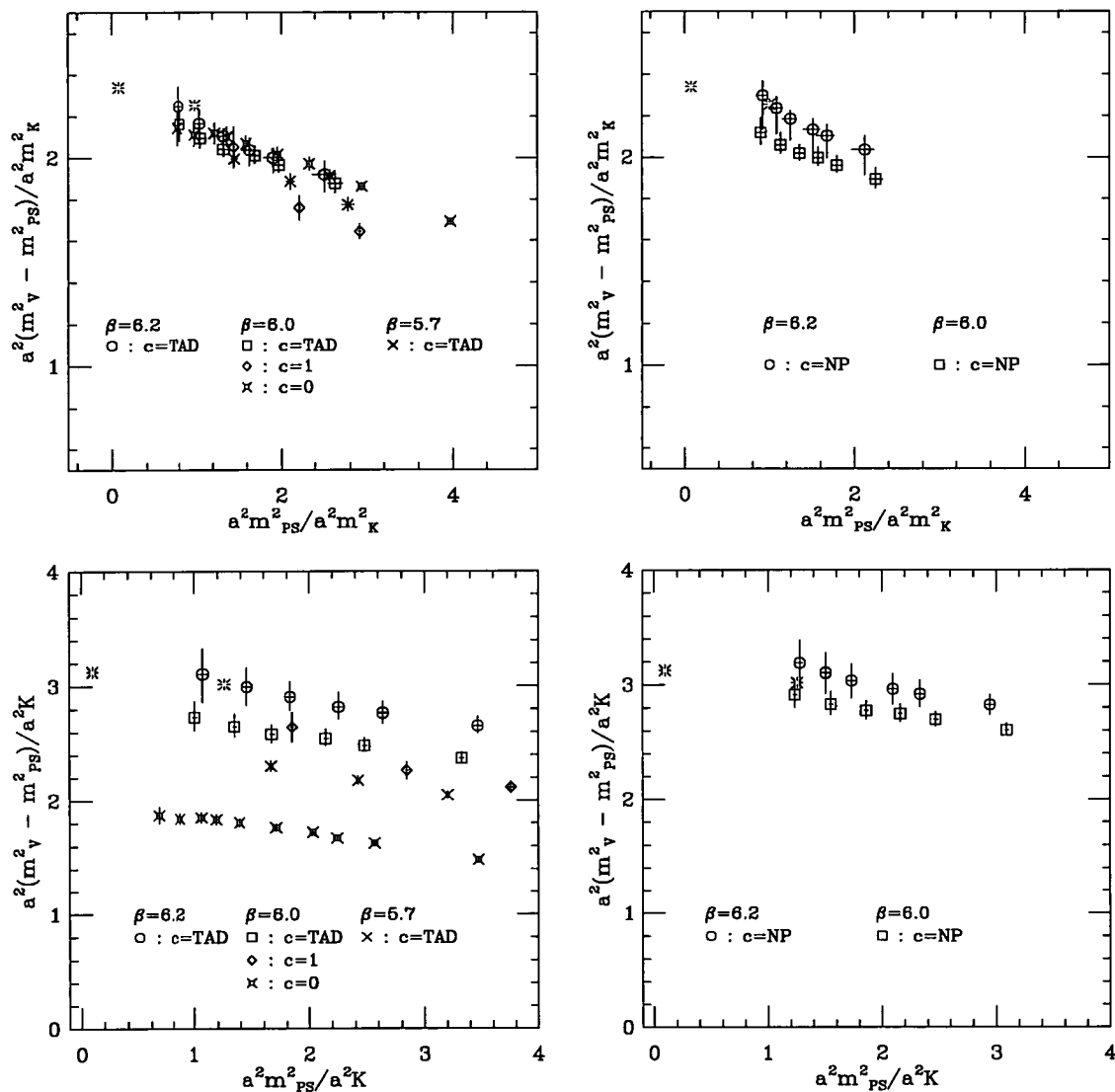


Figure 4.25: The vector-pseudoscalar mass splitting as a function of quark mass. The scale is set in two ways, the first uses the am_K which is derived from the am_ρ , and the second uses the string tension $a\sqrt{K}$. The data at $\beta = 6.0$ with $C=0$ and $C=1$ are taken from [51] and [85], respectively.

4.7 Light Baryons Masses

4.7.1 Spin- $\frac{1}{2}$ Octet Baryons

Using the preferred form of the chiral expansion of the ‘ Σ -like’ $A\{BC\}$ masses,

$$m_{\Sigma_{A\{BC\}}} = M_0 + C_l^A m_A + C_l^D m_D, \quad (4.50)$$

where $m_D = \frac{1}{2}(m_B + m_C)$, the lattice isospin-averaged masses of physical spin- $\frac{1}{2}$ octet baryons are calculated by extrapolating/interpolating the chiral expansion to the following

$$\begin{aligned} am_A &\rightarrow a\bar{m}, am_D \rightarrow a\bar{m} \text{ yielding } am_N, \\ am_A &\rightarrow am_s, am_D \rightarrow a\bar{m} \text{ yielding } am_\Sigma, \\ am_A &\rightarrow a\bar{m}, am_D \rightarrow am_s \text{ yielding } am_\Xi. \end{aligned} \quad (4.51)$$

The lattice value of the Λ^0 mass is obtained through an interpolation of the chiral expansion of the ‘ Λ -like’ masses to the constituent quark masses $am_A \rightarrow am_s$ and $am_D \rightarrow a\bar{m}$. At $\beta = 5.7$ baryon masses were obtained only for degenerate quark masses, and therefore these lattices can only be used to determine the nucleon mass and none of the strange-octet masses. The continuum extrapolations of the nucleon mass, am_N , with the scale set from both the string tension and the ρ mass, are plotted in figure 4.26. The Σ and Λ^0 masses are plotted in units of the string tension in 4.27.

Like the meson sector we observe that at $\beta = 6.2$ the central values for the octet-baryon masses computed with C=TAD and C=NP are in very good agreement. In comparing the nucleon mass scaled by the string tension at $\beta = 6.0$ computed with C=TAD and C=NP there is only a small improvement towards the continuum value for the NP case, and the values are within statistical errors. However, in the meson sector we observe a noticeable improved scaling behaviour for the masses computed with C=NP over that with C=TAD. The relative magnitude of the statistical errors are smaller for the meson masses than in the baryon sector.

Therefore, on increased statistics the effects of improvement may become noticeable for the nucleon at $\beta=6.0$. The spin- $\frac{1}{2}$ strange octet-baryons, the Σ and Λ , show conflicting scaling behaviour when displayed in units of the string tension. We observe an improved scaling behaviour in the case of the Σ computed with $C=NP$ over that with $C=TAD$, but for the Λ a similar trend is observed as in the nucleon. When the nucleon masses are scaled by the m_ρ , we observe a milder a dependence in the approach to the continuum limit, like the meson sector.

The values in the continuum limit for m_N/m_ρ are given in table 4.16, where a comparison is made with $C=0$ data; there is agreement within statistical errors between all these values. However, another β value is really required with the $C=NP$ action, to reduce the error bars and increase the confidence in these fits. Increasing the number of quark masses computed at $\beta = 5.7$, and calculating the baryons which non-degenerate are in quark mass, would increase the confidence in the chirally extrapolated value of the nucleon mass on this data set.

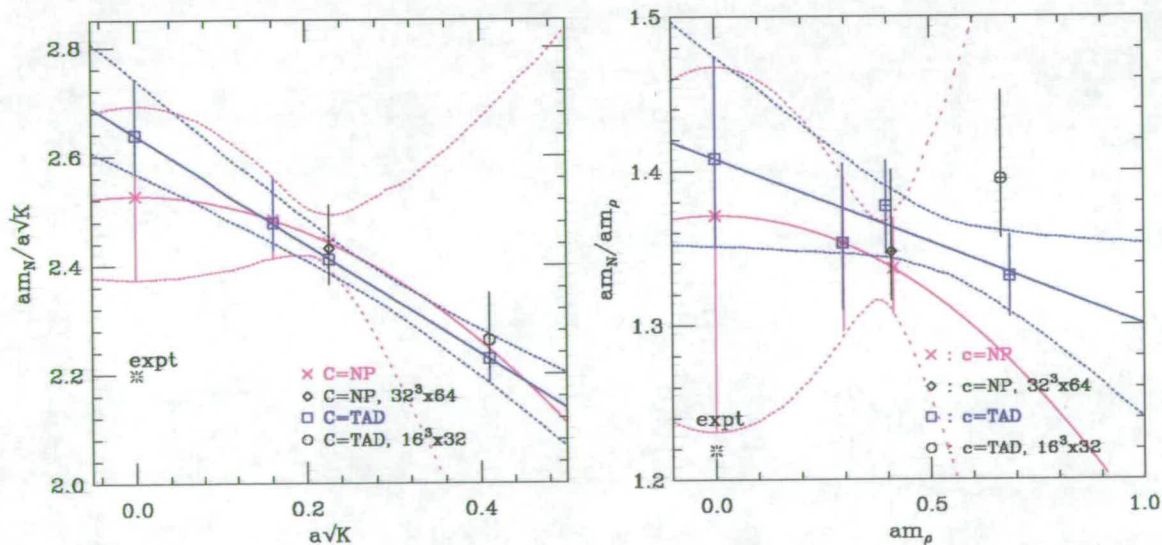


Figure 4.26: Continuum extrapolations of the am_N with the lattice scale set by the string tension $a\sqrt{K}$ and the rho mass am_ρ in the right plot are shown in the left and right plots respectively.

Physical quantity	Extrapolated value to $a \rightarrow 0$				expt. value
	C=TAD	C=NP	Simult.	C=0	
m_N/m_ρ	1.41(6)	1.37(12)	1.35(11)	1.38(7)	1.22
m_Δ/m_ρ	1.71(8)	1.71(18)	1.71(18)	1.73(10)	1.60
m_Δ/m_N	1.22(6)	1.26(13)	1.27(13)		1.31

Table 4.16: A comparison between the physical values in the continuum limit of baryons obtained from these simulations with $O(a)$ -improved fermion actions, using independent and simultaneous fits to both actions, with the results obtained using a Wilson fermion action presented in [51] and the experimental values.

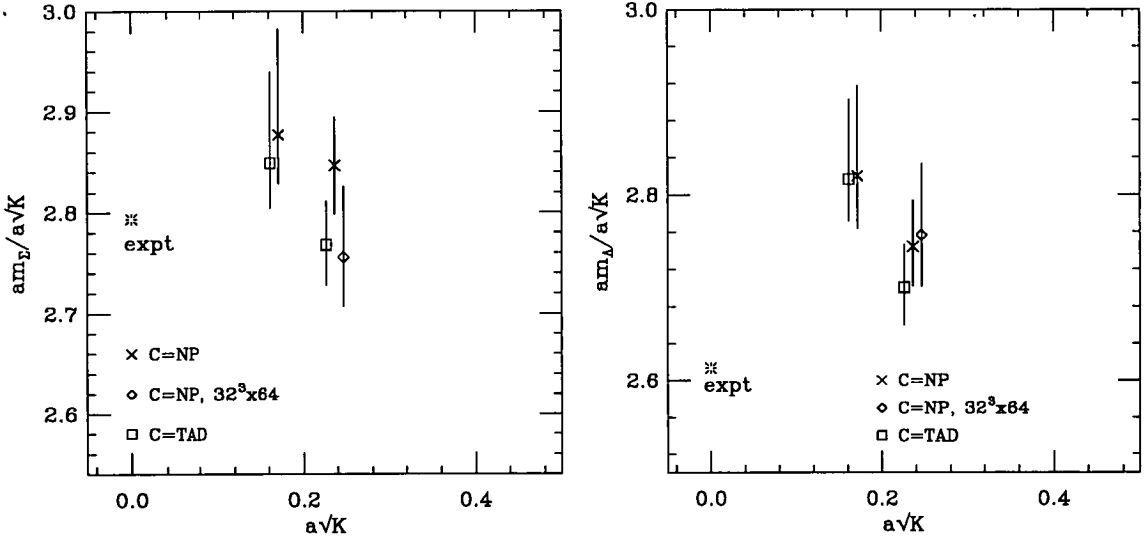


Figure 4.27: Plot are am_Σ and am_Λ masses in units of the string tension $a\sqrt{K}$, in the left and right figures, respectively.

4.7.2 Spin- $\frac{3}{2}$ Decuplet Baryons

As these states are symmetric in flavour the lattice values of the physical masses are calculated by an extrapolation/interpolation of the linear chiral expansion, $m_{\Delta\{ABC\}} = M'_0 + C_1 m_q$ where $m_q = (m_A + m_B + m_C)/3$, to

$$\begin{aligned}
 am_q &\rightarrow a\bar{m} && \text{yielding} && am_{\Delta}, \\
 am_q &\rightarrow a(m_s + 2\bar{m})/3 && \text{yielding} && am_{\Sigma^*}, \\
 am_q &\rightarrow a(2m_s + \bar{m})/3 && \text{yielding} && am_{\Xi^*}, \\
 am_q &\rightarrow am_s && \text{yielding} && am_{\Omega}.
 \end{aligned} \tag{4.52}$$

Continuum extrapolations for m_{Δ} are shown in figure 4.29, where the scale is set from the string tension, m_{ρ} and m_N . In figure 4.28, the am_{Σ^*} and am_{Ω} masses are shown scaled by the string tension. The approaches to the continuum limit obey the same behaviour as the meson sector: when the masses are scaled by \sqrt{K} we observe improved scaling for the masses computed with C=NP over that with C=TAD, and a much reduced a dependence when the scale is set from either am_{ρ} or am_N . There is excellent agreement between both actions in the continuum limit, which can be seen for the values given in table 4.16.

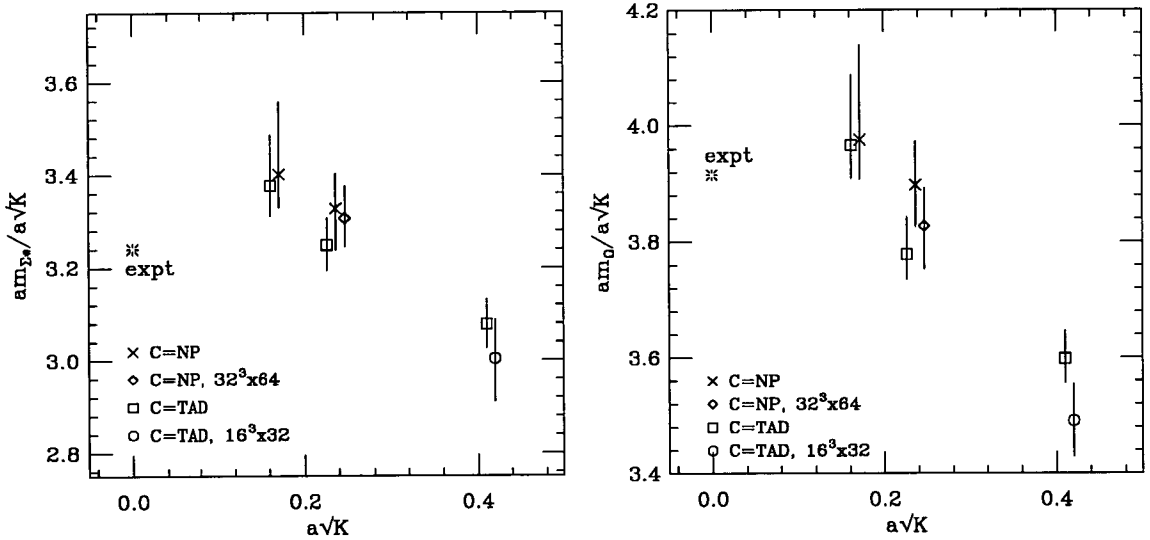


Figure 4.28: Plot are am_{Σ^*} and am_{Ω} masses in units of the string tension $a\sqrt{K}$, in the left and right figures, respectively. The strange quark mass was fixed from M_{K^*}/M_{ρ} .

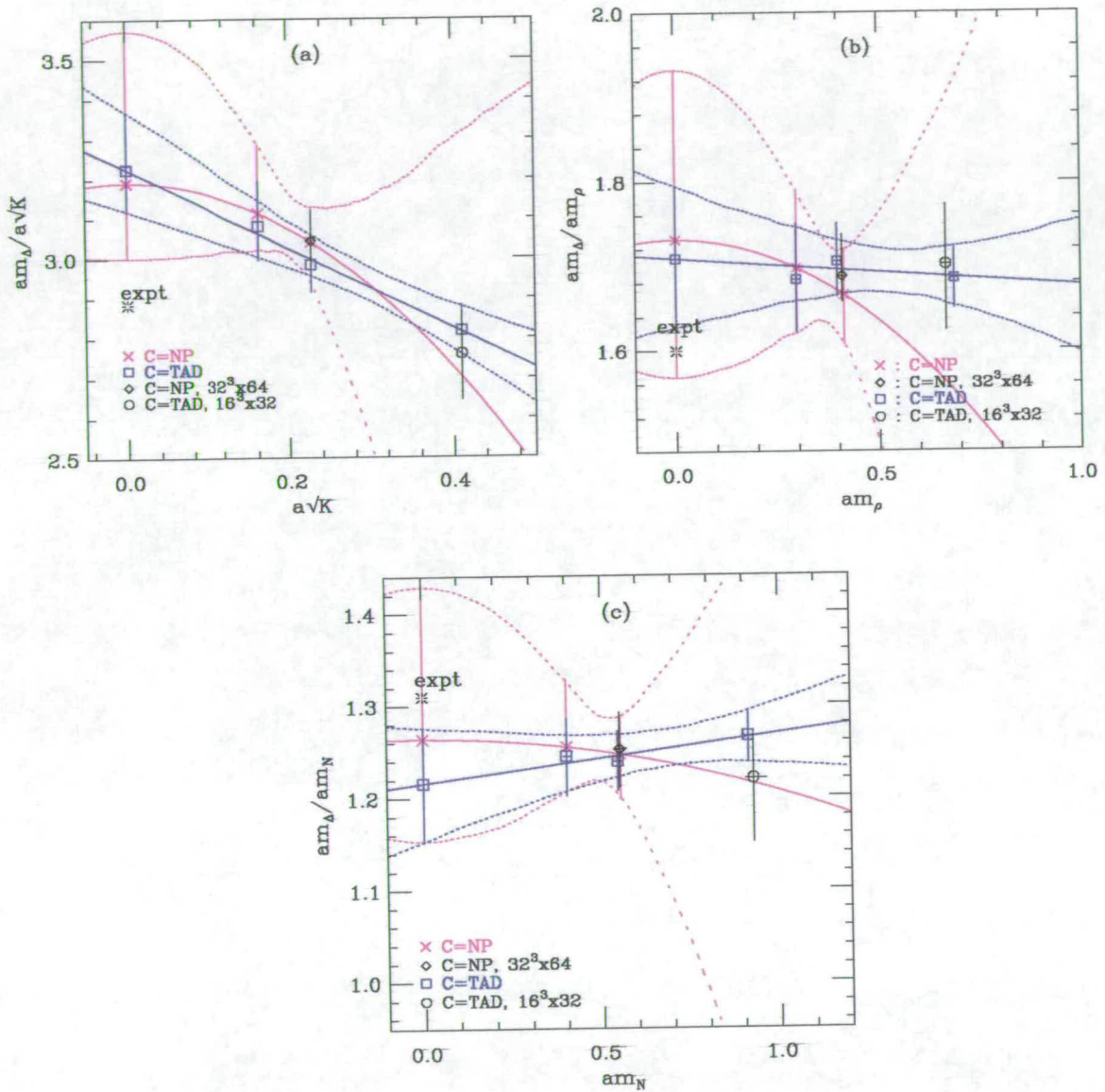


Figure 4.29: Continuum extrapolations of am_Δ with the lattice scale set by the string tension $a\sqrt{K}$, the rho mass am_ρ and the nucleon mass am_N are shown in plots (a), (b) and (c) respectively.

Chapter 5

Summary and Conclusions

5.1 Improvement and the continuum limit

We have calculated the light spectrum using the Sheikholeslami-Wohlert (SW) $O(a)$ -improved fermion action with two choices for the clover coefficient $C=TAD$ and $C=NP$, and we have compared the results from these simulations with simulations using Wilson fermions, $C=0$, and tree-level improved SW fermions, $C=1$. We have observed in the approach to the continuum the following behaviour:

- hadron masses scaled by the string tension show an improved scaling behaviour for the $O(a)$ -improved fermion actions, in comparison with the Wilson fermion data. There is no visible difference at $\beta = 6.2$ between the hadron masses computed with $C=TAD$ and $C=NP$. But there is a noticeable improvement at $\beta = 6.0$ for the meson masses computed with $C=NP$ over that with $C=TAD$ and there is improvement in the baryon sector towards the continuum value;
- hadron masses scaled by a different hadron mass, calculated from the same action, show a milder a dependence, and in some cases there is no a dependence at all, which has been observed by [51];
- hadron masses extrapolated to the continuum limit are consistent between the different fermion actions.

We conclude from this behaviour that there is some evidence that the improvement program is working and reducing the cutoff effects for the $O(a)$ -improved

fermions. But, further calculations are required to further support this. Computing the light hadron spectrum at additional β values will reduce the errors in the fitted parameters for the continuum extrapolations and increase our confidence in the fits. A stronger test to verify that $O(a)$ -improvement is working is through comparing the matrix elements (decay constants) calculated with the different actions. Improvement of the matrix elements is not only dependent on the improvement of the lattice action, but also on the improvement of the correlation functions (composite fields), as discussed in section 1.9. The improved correlation functions are dependent on the improvement coefficients (c_A, b_A, \dots). Comparing the continuum results obtained from the different actions for the matrix elements is not as straight forward as in the case of the hadron masses, renormalisation constants are required to match the lattice and the continuum theories, see [42], which need to be calculated so introduce additional systematic errors in their determination. The results of such an analysis are presented in [114].

5.2 Can we see the effects of the Quenched Approximation?

The continuum results for the quenched light hadron mass spectrum are presented, so that a comparison can be made with the experimental data. Continuum extrapolations are performed independently to the C=TAD and C=NP data sets and a simultaneous fit is performed to both data sets. The lattice scale is set in each continuum extrapolation using different quantities: the ρ mass, \sqrt{K} and the nucleon mass. The results are shown in figure 5.1 and tabulated in tables 5.1 and 5.2.

In comparing the extrapolated results between when the scale is set from the ρ mass and the string tension, we find there is a small discrepancy, but taking into account the 5% uncertainty in the physical value of \sqrt{K} which has not been included, the values agreement within statistical errors. In contrast when the scale is set from the nucleon mass the extrapolated results differ by up to 15% from those when the scale is set from either the ρ mass or \sqrt{K} . This can be explained by the fact the continuum quenched nucleon mass is 15% larger than

the experimental value. Can this discrepancy be attributed to quenching errors? In [115, 116, 117], results are reported from the CP-PACS Collaboration. They simulate with Wilson fermions, $C=0$, at m_π/m_ρ ratios of 0.75, 0.7, 0.6, 0.5 and 0.4 on lattices with $N_s \approx 3\text{fm}$ and at β values of 5.9, 6.1, 6.25 and 6.47. The number of configurations generated vary from 800 to 100 going from the lowest to highest β , so the statistical quality of their data is superior to ours. They find curvature in the nucleon and Λ chiral extrapolations, and chirally extrapolating the nucleon with a cubic fit in quark mass. This reduces the continuum extrapolated value obtained from a linear fit by 15%. The curvature in the spin- $\frac{1}{2}$ octet chiral extrapolations is observed on going to lighter quark mass and only became apparent on including the point at $m_\pi/m_\rho = 0.4^1$ in the fit. This claim needs to be checked in our simulations by simulating at lighter quark masses, ² and improving the statistical quality of our results. We shall now concentrate on the continuum extrapolated results when the scale is set from the ρ mass. There is agreement between the continuum extrapolated result for the Δ baryon from our and their simulation which is 5% larger than the experimental value. With the exception of the Λ baryon the extrapolated values for the other strange baryons are in relatively good agreement with the experimental values. In the meson sector the extrapolated values are in good agreement with the experimental values.

In light of these points the question still remains open as to how much quenching affects the light hadron mass spectrum, our results show that quenching effects could be as large as 15% in some quantities. But as already mentioned higher statistics, smaller quark masses and additional points in the continuum extrapolation are needed to quantify this.

¹This is smaller than any quark mass in our simulations.

²However this presents problems using $C=NP$ and possibly using $C=TAD$, in that simulating with a lighter quark mass increases the possibility of generating exceptional configurations, as explained in section 3.1 and therefore the method mentioned in that section for correcting these quenched artifacts need to be investigated.

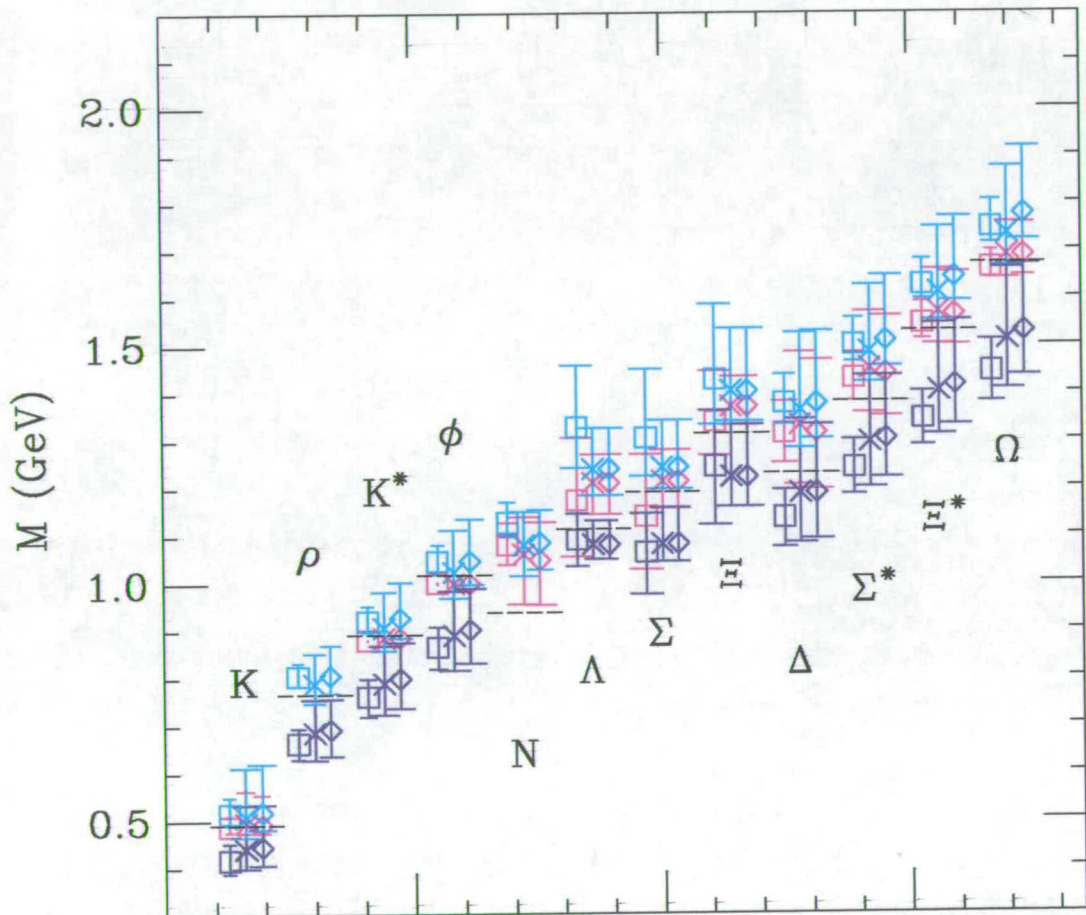


Figure 5.1: A comparison of the quenched light hadron mass spectrum with the experimental data indicated by horizontal lines. The continuum extrapolated values represented by (\square) , (\times) and (\diamond) correspond to an independent fit to the $C=TAD$ data, an independent fit to the $C=NP$ data and a simultaneous fit to both data sets $C=TAD$ and $C=NP$, respectively. The scale in the continuum extrapolations was set from the ρ mass, \sqrt{K} and the nucleon mass, which corresponded to the symbols coloured in red, green and blue respectively. Strange hadrons were calculated using m_s fixed from M_{K^*}/M_ρ .

Light Meson Masses in GeV								
Hadron	Fit	Scale set in cont. extrap. from			expt.			
		m_ρ	\sqrt{K}	m_N				
K	C=TAD	0.488	$^{+22}_{-13}$	0.515	$^{+35}_{-24}$	0.417	$^{+35}_{-29}$	0.494
	C=NP	0.495	$^{+67}_{-20}$	0.508	$^{+103}_{-43}$	0.441	$^{+92}_{-42}$	
	C=TAD and C=NP	0.492	$^{+63}_{-17}$	0.518	$^{+101}_{-36}$	0.445	$^{+90}_{-39}$	
ρ	C=TAD			0.805	$^{+27}_{-22}$	0.663	$^{+31}_{-35}$	0.768
	C=NP			0.788	$^{+65}_{-42}$	0.685	$^{+69}_{-58}$	
	C=TAD and C=NP			0.806	$^{+65}_{-38}$	0.692	$^{+65}_{-56}$	
K^*	C=TAD	0.880	$^{+1}_{-1}$	0.921	$^{+31}_{-25}$	0.761	$^{+37}_{-43}$	0.894
	C=NP	0.884	$^{+3}_{-2}$	0.906	$^{+76}_{-49}$	0.788	$^{+81}_{-66}$	
	C=TAD and C=NP	0.885	$^{+3}_{-2}$	0.927	$^{+75}_{-44}$	0.799	$^{+76}_{-64}$	
ϕ	C=TAD	1.000	$^{+2}_{-2}$	1.046	$^{+35}_{-28}$	0.865	$^{+42}_{-47}$	1.019
	C=NP	0.999	$^{+6}_{-3}$	1.023	$^{+88}_{-55}$	0.890	$^{+93}_{-74}$	
	C=TAD and C=NP	0.999	$^{+5}_{-2}$	1.047	$^{+87}_{-50}$	0.901	$^{+88}_{-71}$	

Table 5.1: A comparison of the quenched light meson spectrum with the experimental data. The ansätze used in the independent fits to the C=NP and C=TAD data sets is given in equation (4.38) and the ansatz used in the simultaneous fit to both data sets is given in equation (4.39). Strange hadrons were calculated using m_s fixed from M_{K^*}/M_ρ .

Light Baryon Masses in GeV								
Hadron	Fit	Scale in cont. extrap. set from			expt.			
		m_ρ	\sqrt{K}	m_N				
N	C=TAD	1.080	$^{+46}_{-43}$	1.127	$^{+44}_{-30}$	0.940		
	C=NP	1.060	$^{+78}_{-106}$	1.079	$^{+70}_{-66}$			
	C=TAD and C=NP	1.048	$^{+79}_{-95}$	1.085	$^{+69}_{-58}$			
Λ	C=TAD	1.173	$^{+131}_{-119}$	1.327	$^{+131}_{-87}$	1.091	$^{+55}_{-57}$	1.116
	C=NP	1.210	$^{+60}_{-66}$	1.239	$^{+86}_{-57}$	1.080	$^{+50}_{-31}$	
	C=TAD and C=NP	1.210	$^{+60}_{-66}$	1.239	$^{+86}_{-57}$	1.080	$^{+50}_{-31}$	
Σ	C=TAD	1.139	$^{+130}_{-112}$	1.304	$^{+146}_{-80}$	1.063	$^{+82}_{-89}$	1.193
	C=NP	1.213	$^{+66}_{-57}$	1.242	$^{+98}_{-47}$	1.082	$^{+76}_{-38}$	
	C=TAD and C=NP	1.213	$^{+66}_{-57}$	1.242	$^{+98}_{-47}$	1.082	$^{+76}_{-38}$	
Ξ	C=TAD	1.338	$^{+108}_{-71}$	1.428	$^{+159}_{-96}$	1.244	$^{+118}_{-124}$	1.315
	C=NP	1.370	$^{+63}_{-40}$	1.403	$^{+131}_{-65}$	1.222	$^{+110}_{-64}$	
	C=TAD and C=NP	1.370	$^{+63}_{-40}$	1.403	$^{+131}_{-65}$	1.222	$^{+110}_{-64}$	
Δ	C=TAD	1.314	$^{+66}_{-63}$	1.377	$^{+61}_{-45}$	1.136	$^{+59}_{-63}$	1.232
	C=NP	1.331	$^{+154}_{-126}$	1.362	$^{+162}_{-81}$	1.188	$^{+155}_{-104}$	
	C=TAD and C=NP	1.315	$^{+152}_{-121}$	1.377	$^{+152}_{-75}$	1.188	$^{+144}_{-97}$	
Σ^*	C=TAD	1.430	$^{+54}_{-48}$	1.501	$^{+55}_{-36}$	1.241	$^{+58}_{-57}$	1.383
	C=NP	1.450	$^{+120}_{-95}$	1.486	$^{+139}_{-65}$	1.295	$^{+140}_{-96}$	
	C=TAD and C=NP	1.441	$^{+120}_{-91}$	1.509	$^{+136}_{-55}$	1.302	$^{+132}_{-82}$	
Ξ^*	C=TAD	1.545	$^{+45}_{-34}$	1.626	$^{+54}_{-31}$	1.344	$^{+58}_{-57}$	1.532
	C=NP	1.569	$^{+89}_{-68}$	1.609	$^{+137}_{-59}$	1.402	$^{+142}_{-92}$	
	C=TAD and C=NP	1.565	$^{+88}_{-65}$	1.641	$^{+127}_{-51}$	1.415	$^{+136}_{-85}$	
Ω	C=TAD	1.661	$^{+36}_{-23}$	1.746	$^{+58}_{-33}$	1.443	$^{+66}_{-64}$	1.673
	C=NP	1.687	$^{+69}_{-50}$	1.733	$^{+141}_{-69}$	1.510	$^{+151}_{-104}$	
	C=TAD and C=NP	1.688	$^{+66}_{-44}$	1.775	$^{+141}_{-55}$	1.528	$^{+141}_{-93}$	

Table 5.2: A comparison of the quenched light baryon spectrum with the experimental data. The ansatz used in the independent fits to the C=NP and C=TAD data sets is given in equation (4.38) and the ansatz used in the simultaneous fit to both data sets is given in equation (4.39). Strange hadrons were calculated using m_s fixed from M_{K^*}/M_ρ .

5.3 What have we achieved?

The main aim of this work has been achieved which is the *ab initio* calculation of the light hadron spectrum using Lattice QCD.

One of the main achievements of this calculation are that the systematic errors have been thoroughly investigated:

- a systematic approach has been applied to fitting the hadron two-point functions to determine the lattice hadron masses;
- the chiral behaviour of each of the different particles has been investigated by fitting to a number of different ansätze; motivated from quenched chiral perturbation theory;
- finite volume effects have been studied;
- continuum extrapolations have been performed using different fits and we have checked that the different actions are consistent in the continuum limit.

We state the conclusions from this analysis as follows:

- we observe that there are no significant finite volume effects in the hadron masses computed using the volumes in these simulations;
- we have demonstrated that $O(a)$ -improvement seems to be working and reducing the cut off effects for light hadron masses;
- we observe a discrepancy between the different ways of fixing the strange quark mass m_s at a fixed lattice spacing, but these all agree in the continuum limit, i.e. taking $a \rightarrow 0$;
- we find that the continuum value of the J parameter is in agreement with the experimental value;

- we find that vector-pseudoscalar mass splitting is not constant with the quark mass as is seen with the experimental data, but there is a small slope which means that this quantity is smaller at higher quark masses. We find the size of this slope to be the same for unimproved Wilson fermions and $O(a)$ -improved fermions, which suggests that this is a quenching effect and not a discretisation effect;
- the quenched spectrum disagrees with experiment by as much as 15% for some particles, like the nucleon and Λ , but is in better agreement for the meson sector.

Appendix A

Fitted Lattice Hadron Masses

The fitting procedure described in detail in section 3.2, have been implemented thoroughly on each of the data-sets. Multi-correlator multi-exponential simultaneous fits have been made to as many different combinations of the correlators as possible. After careful examination of the sliding window plots, which have been produced for each entry in the proceeding tables and examples of which are shown in figures 3.10 to 3.16, the type of fitting ansatz is chosen together with the appropriate fitting range. This appendix contains tables for the fitted masses obtained from fitting the pion, rho, Δ , ‘ Σ -like’ and ‘ Λ -like’ correlators, for each of the data-sets as listed in table 3.2.

κ_1	κ_2	am_{PS}	Fit Range	$\chi^2/\text{d.o.f}$
0.13843	0.13843	0.7336 $^{+17}_{-13}$	3–12	13.8/14
0.14077	0.13843	0.6385 $^{+18}_{-12}$	3–12	9.0/14
0.14077	0.14077	0.5290 $^{+22}_{-15}$	3–12	6.1/14

Table A.3: Pion masses on the 12×24 lattice at $\beta = 5.7$, with C=TAD, obtained from a double exponential fit to the (LL,LL) and (SL,LL) correlators.

κ_1	κ_2	am_V	Fit Range	$\chi^2/\text{d.o.f}$
0.13843	0.13843	0.9381 $^{+33}_{-21}$	4–12	46.2/26
0.14077	0.13843	0.8776 $^{+39}_{-26}$	4–12	39.6/26
0.14077	0.14077	0.8153 $^{+50}_{-38}$	4–12	39.6/26

Table A.4: Rho masses on the 12×24 lattice at $\beta = 5.7$, with C=TAD, obtained from a double exponential fit to the channels $\sum_{i=1}^3 \bar{\psi}^a \gamma_i \psi^a$ and $\sum_{i=1}^3 \bar{\psi}^a \gamma_4 \gamma_i \psi^a$ with the (LL,LL) and (SL,LL) correlators.

κ	am_{Δ}	Fit Range	$\chi^2/\text{d.o.f}$
0.13843	1.545 $^{+9}_{-7}$	5–11	8.3/8
0.14077	1.357 $^{+16}_{-13}$	5–11	3.2/8

Table A.5: Degenerate delta masses on the 12×24 lattice at $\beta = 5.7$, with C=TAD, obtained from a double exponential fit to the (LLL,LLL) and (SSS,LLL) correlators.

κ	am_N	Fit Range	$\chi^2/\text{d.o.f}$
0.13843	1.413 $^{+7}_{-6}$	2–11	2.4/14
0.14077	1.172 $^{+11}_{-10}$	2–11	6.8/14

Table A.6: Degenerate nucleon masses on the 12×24 lattice at $\beta = 5.7$, with C=TAD, obtained from a double exponential fit to the (SSS,LLL) correlators. A simultaneous fit was to both the interpolating operators $\epsilon_{abc}(\psi^a C \gamma_5 \psi^b) \psi^c$ and $\epsilon_{abc}(\psi^a C \gamma_4 \gamma_5 \psi^b) \psi^c$, which have an overlap with the nucleon.

κ_1	κ_2	am_{PS}	Fit Range	$\chi^2/\text{d.o.f}$
0.13843	0.13843	0.7352^{+19}_{-14}	3–16	20.2/22
0.14077	0.13843	0.6409^{+20}_{-15}	3–16	21.4/22
0.14077	0.14077	0.5322^{+22}_{-15}	3–16	25.4/22

Table A.7: Pion masses on the 16×32 lattice at $\beta = 5.7$, with, obtained from a double exponential fit to the (LL,LL) and (SL,LL) correlators.

κ_1	κ_2	am_V	Fit Range	$\chi^2/\text{d.o.f}$
0.13843	0.13843	0.9338^{+50}_{-33}	4–16	10.2/20
0.14077	0.13843	0.8689^{+59}_{-47}	4–16	11.7/20
0.14077	0.14077	0.8052^{+77}_{-58}	4–16	15.1/20

Table A.8: Rho masses on the 16×32 lattice at $\beta = 5.7$, with, obtained from a double exponential fit to the $\sum_{i=1}^3 \bar{\psi}^a \gamma_i \psi^a$ channel with the (LL,LL) and (SL,LL) correlators.

κ	am_Δ	Fit Range	$\chi^2/\text{d.o.f}$
0.13843	1.531^{+15}_{-13}	6–15	8.0/14
0.14077	1.340^{+25}_{-27}	6–15	11.0/14

Table A.9: Degenerate delta masses on the 16×32 lattice at $\beta = 5.7$, with, obtained from a double exponential fit to the (LLL,LLL) and (SSS,LLL) correlators.

κ	am_N	Fit Range	$\chi^2/\text{d.o.f}$
0.13843	1.424^{+9}_{-8}	2–15	17.6/22
0.14077	1.186^{+19}_{-12}	2–15	23.1/22

Table A.10: Degenerate nucleon masses on the 16×32 lattice at $\beta = 5.7$, with C=TAD, obtained from a double exponential fit to the (SSS,LLL) correlators. A simultaneous fit was made to both the interpolating operators $\epsilon_{abc}(\psi^a C \gamma_5 \psi^b) \psi^c$ and $\epsilon_{abc}(\psi^a C \gamma_4 \gamma_5 \psi^b) \psi^c$, which have an overlap with the nucleon.

κ_1	κ_2	am_{PS}	Fit Range	$\chi^2/\text{d.o.f}$
0.13700	0.13700	0.4129 $^{+12}_{-10}$	6-23	23.8/30
0.13810	0.13700	0.3569 $^{+14}_{-10}$	6-23	26.7/30
0.13856	0.13700	0.3317 $^{+17}_{-12}$	6-23	32.6/30
0.13810	0.13810	0.2930 $^{+16}_{-12}$	6-23	34.3/30
0.13856	0.13810	0.2625 $^{+18}_{-13}$	6-23	39.2/30
0.13856	0.13856	0.2276 $^{+22}_{-14}$	6-23	44.1/30

Table A.11: Pion masses on the 16×48 lattice at $\beta = 6.0$, with C=TAD, obtained from a double exponential fit to the (LL,LL) and (FL,LL) correlators.

κ_1	κ_2	am_V	Fit Range	$\chi^2/\text{d.o.f}$
0.13700	0.13700	0.5406 $^{+24}_{-17}$	6-23	46.5/30
0.13810	0.13700	0.5048 $^{+34}_{-24}$	6-23	44.8/30
0.13856	0.13700	0.4903 $^{+46}_{-31}$	6-23	40.1/30
0.13810	0.13810	0.4671 $^{+48}_{-37}$	6-23	45.5/30
0.13856	0.13810	0.4525 $^{+63}_{-48}$	6-23	40.7/30
0.13856	0.13856	0.4382 $^{+79}_{-68}$	6-23	35.6/30

Table A.12: Rho masses on the 16×48 lattice at $\beta = 6.0$, with C=TAD, obtained from a double exponential fit to the channel $\sum_{i=1}^3 \bar{\psi}^a \gamma_i \psi^a$ with the (LL,LL) and (FL,LL) correlators.

κ_1	κ_2	κ_3	am_Δ	Fit Range	$\chi^2/\text{d.o.f}$
0.13700	0.13700	0.13700	0.893 $^{+7}_{-5}$	7-23	33.1/28
0.13700	0.13700	0.13810	0.858 $^{+8}_{-6}$	7-23	34.8/28
0.13700	0.13700	0.13856	0.849 $^{+9}_{-8}$	7-23	38.6/28
0.13700	0.13810	0.13810	0.822 $^{+9}_{-8}$	7-23	37.1/28
0.13700	0.13810	0.13856	0.812 $^{+11}_{-10}$	7-23	41.6/28
0.13700	0.13856	0.13856	0.794 $^{+12}_{-12}$	7-23	39.9/28
0.13810	0.13810	0.13810	0.787 $^{+11}_{-11}$	7-23	43.4/28
0.13810	0.13810	0.13856	0.775 $^{+12}_{-14}$	7-23	47.4/28
0.13810	0.13856	0.13856	0.756 $^{+15}_{-17}$	7-23	46.8/28
0.13856	0.13856	0.13856	0.733 $^{+18}_{-20}$	7-23	44.7/28

Table A.13: Delta ($\{\kappa_1\kappa_2\kappa_3\}$) masses on the 16×48 lattice at $\beta = 6.0$, with C=TAD, obtained from a double exponential fit to the (LLL,LLL) and (FFL,LLL) correlators.

κ_1	κ_2	κ_3	am_Σ	Fit Range	$\chi^2/\text{d.o.f}$
0.13700	0.13700	0.13700	0.812 $^{+5}_{-3}$	6–23	47.7/30
0.13700	0.13700	0.13810	0.770 $^{+6}_{-3}$	6–23	53.8/30
0.13700	0.13700	0.13856	0.753 $^{+6}_{-4}$	6–23	53.5/30
0.13700	0.13810	0.13810	0.726 $^{+6}_{-5}$	6–23	52.6/30
0.13700	0.13810	0.13856	0.712 $^{+7}_{-6}$	6–23	45.7/30
0.13700	0.13856	0.13856	0.693 $^{+7}_{-7}$	6–23	37.9/30
0.13810	0.13700	0.13700	0.763 $^{+6}_{-4}$	6–23	45.3/30
0.13810	0.13700	0.13810	0.718 $^{+6}_{-5}$	6–23	59.0/30
0.13810	0.13700	0.13856	0.701 $^{+7}_{-6}$	6–23	58.3/30
0.13810	0.13810	0.13810	0.676 $^{+7}_{-6}$	6–23	48.2/30
0.13810	0.13810	0.13856	0.658 $^{+9}_{-7}$	6–23	47.9/30
0.13810	0.13856	0.13856	0.640 $^{+9}_{-10}$	6–23	41.8/30
0.13856	0.13700	0.13700	0.742 $^{+7}_{-5}$	6–23	48.8/30
0.13856	0.13700	0.13810	0.700 $^{+7}_{-7}$	6–23	49.7/30
0.13856	0.13700	0.13856	0.686 $^{+9}_{-7}$	6–23	43.1/30
0.13856	0.13810	0.13810	0.658 $^{+9}_{-8}$	6–23	47.2/30
0.13856	0.13810	0.13856	0.639 $^{+12}_{-9}$	6–23	51.8/30
0.13856	0.13856	0.13856	0.615 $^{+11}_{-12}$	6–23	42.1/30

Table A.14: ‘ Σ -like’ ($\kappa_1\{\kappa_2\kappa_3\}$) masses on the 16×48 lattice at $\beta = 6.0$, with C=TAD, obtained from a double exponential fit to the (LLL,LLL) and (FFL,LLL) correlators.

κ_1	κ_2	κ_3	am_Λ	Fit Range	$\chi^2/\text{d.o.f}$
0.13700	0.13700	0.13700	0.809 $^{+5}_{-3}$	7-23	25.0/28
0.13700	0.13700	0.13810	0.762 $^{+6}_{-4}$	7-23	37.8/28
0.13700	0.13700	0.13856	0.741 $^{+6}_{-6}$	7-23	41.0/28
0.13700	0.13810	0.13810	0.719 $^{+6}_{-6}$	7-23	39.1/28
0.13700	0.13810	0.13856	0.695 $^{+7}_{-8}$	7-23	45.3/28
0.13700	0.13856	0.13856	0.683 $^{+8}_{-11}$	7-23	42.3/28
0.13810	0.13700	0.13700	0.767 $^{+6}_{-5}$	7-23	44.0/28
0.13810	0.13700	0.13810	0.724 $^{+7}_{-6}$	7-23	41.5/28
0.13810	0.13700	0.13856	0.703 $^{+7}_{-8}$	7-23	44.7/28
0.13810	0.13810	0.13810	0.678 $^{+8}_{-8}$	7-23	41.3/28
0.13810	0.13810	0.13856	0.657 $^{+9}_{-10}$	7-23	43.1/28
0.13810	0.13856	0.13856	0.641 $^{+9}_{-13}$	7-23	45.4/28
0.13856	0.13700	0.13700	0.751 $^{+7}_{-6}$	7-23	46.7/28
0.13856	0.13700	0.13810	0.705 $^{+8}_{-8}$	7-23	52.0/28
0.13856	0.13700	0.13856	0.685 $^{+7}_{-14}$	7-23	47.1/28
0.13856	0.13810	0.13810	0.657 $^{+11}_{-11}$	7-23	48.4/28
0.13856	0.13810	0.13856	0.635 $^{+11}_{-17}$	7-23	44.7/28
0.13856	0.13856	0.13856	0.623 $^{+12}_{-15}$	7-23	48.5/28

Table A.15: ‘ Λ -like’ ($\kappa_1[\kappa_2\kappa_3]$) masses on the 16×48 lattice at $\beta = 6.0$, with C=TAD, obtained from a double exponential fit to the (LLL,LLL) and (FFL,LLL) correlators.

κ_1	κ_2	am_{PS}	Fit Range	$\chi^2/\text{d.o.f}$
0.13640	0.13640	0.3015 $^{+17}_{-14}$	8-23	39.5/26
0.13710	0.13640	0.2630 $^{+20}_{-16}$	8-23	32.3/26
0.13745	0.13640	0.2430 $^{+21}_{-18}$	8-23	27.6/26
0.13710	0.13710	0.2191 $^{+20}_{-18}$	8-23	25.5/26
0.13745	0.13710	0.1955 $^{+19}_{-23}$	8-23	24.9/26
0.13745	0.13745	0.1682 $^{+20}_{-27}$	8-23	27.5/26

Table A.16: Pion masses on the 24×48 lattice at $\beta = 6.2$, with C=TAD, obtained from a double exponential fit to the (LL,LL) and (FL,LL) correlators.

κ_1	κ_2	am_V	Fit Range	$\chi^2/\text{d.o.f}$
0.13640	0.13640	0.4006 $^{+28}_{-22}$	8-23	34.1/26
0.13710	0.13640	0.3764 $^{+37}_{-31}$	8-23	29.3/26
0.13745	0.13640	0.3646 $^{+48}_{-42}$	8-23	25.4/26
0.13710	0.13710	0.3526 $^{+50}_{-45}$	8-23	27.2/26
0.13745	0.13710	0.3417 $^{+63}_{-63}$	8-23	24.7/26
0.13745	0.13745	0.3314 $^{+86}_{-102}$	8-23	28.4/26

Table A.17: Rho masses on the 24×48 lattice at $\beta = 6.2$, with C=TAD, obtained from a double exponential fit to the channel $\sum_{i=1}^3 \bar{\psi}^a \gamma_i \psi^a$ with the (LL,LL) and (FL,LL) correlators.

κ_1	κ_2	κ_3	am_Δ	Fit Range	$\chi^2/\text{d.o.f}$
0.13640	0.13640	0.13640	0.669 $^{+7}_{-5}$	9–23	37.9/24
0.13640	0.13640	0.13710	0.642 $^{+8}_{-6}$	9–23	35.2/24
0.13640	0.13640	0.13745	0.629 $^{+9}_{-7}$	9–23	34.3/24
0.13640	0.13710	0.13710	0.617 $^{+9}_{-7}$	9–23	32.6/24
0.13640	0.13710	0.13745	0.603 $^{+10}_{-9}$	9–23	31.8/24
0.13640	0.13745	0.13745	0.589 $^{+12}_{-10}$	9–23	30.2/24
0.13710	0.13710	0.13710	0.591 $^{+10}_{-9}$	9–23	29.4/24
0.13710	0.13710	0.13745	0.576 $^{+12}_{-11}$	9–23	28.2/24
0.13710	0.13745	0.13745	0.562 $^{+14}_{-13}$	9–23	27.0/24
0.13745	0.13745	0.13745	0.549 $^{+18}_{-16}$	9–23	26.7/24

Table A.18: Delta ($\{\kappa_1\kappa_2\kappa_3\}$) masses on the 24×48 lattice at $\beta = 6.2$, with C=TAD, obtained from a double exponential fit to the (LLL,LLL) and (FFL,LLL) correlators.

κ_1	κ_2	κ_3	am_Σ	Fit Range	$\chi^2/\text{d.o.f}$
0.13640	0.13640	0.13640	0.602 $^{+5}_{-5}$	8–23	54.5/26
0.13640	0.13640	0.13710	0.572 $^{+6}_{-5}$	8–23	49.7/26
0.13640	0.13640	0.13745	0.556 $^{+7}_{-6}$	8–23	44.1/26
0.13640	0.13710	0.13710	0.543 $^{+8}_{-6}$	8–23	50.0/26
0.13640	0.13710	0.13745	0.530 $^{+9}_{-7}$	8–23	40.6/26
0.13640	0.13745	0.13745	0.512 $^{+10}_{-9}$	8–23	35.5/26
0.13710	0.13640	0.13640	0.566 $^{+7}_{-4}$	8–23	56.1/26
0.13710	0.13640	0.13710	0.538 $^{+7}_{-6}$	8–23	45.2/26
0.13710	0.13640	0.13745	0.520 $^{+9}_{-6}$	8–23	37.4/26
0.13710	0.13710	0.13710	0.509 $^{+9}_{-7}$	8–23	45.7/26
0.13710	0.13710	0.13745	0.492 $^{+11}_{-8}$	8–23	39.0/26
0.13710	0.13745	0.13745	0.477 $^{+12}_{-12}$	8–23	33.2/26
0.13745	0.13640	0.13640	0.547 $^{+8}_{-5}$	8–23	51.8/26
0.13745	0.13640	0.13710	0.515 $^{+9}_{-6}$	8–23	46.6/26
0.13745	0.13640	0.13745	0.498 $^{+13}_{-7}$	8–23	46.8/26
0.13745	0.13710	0.13710	0.480 $^{+11}_{-7}$	8–23	45.0/26
0.13745	0.13710	0.13745	0.457 $^{+16}_{-7}$	8–23	45.3/26
0.13745	0.13745	0.13745	0.454 $^{+15}_{-14}$	8–23	30.5/26

Table A.19: ‘ Σ -like’ ($\kappa_1\{\kappa_2\kappa_3\}$) masses on the 24×48 lattice at $\beta = 6.2$, with C=TAD, obtained from a double exponential fit to the (LLL,LLL) and (FFL,LLL) correlators.

κ_1	κ_2	κ_3	am_Λ	Fit Range	$\chi^2/\text{d.o.f}$
0.13640	0.13640	0.13640	0.601 $^{+6}_{-4}$	8-23	60.5/26
0.13640	0.13640	0.13710	0.568 $^{+7}_{-4}$	8-23	58.5/26
0.13640	0.13640	0.13745	0.550 $^{+8}_{-5}$	8-23	52.8/26
0.13640	0.13710	0.13710	0.537 $^{+8}_{-5}$	8-23	56.4/26
0.13640	0.13710	0.13745	0.515 $^{+9}_{-6}$	8-23	43.5/26
0.13640	0.13745	0.13745	0.496 $^{+12}_{-6}$	8-23	41.8/26
0.13710	0.13640	0.13640	0.574 $^{+6}_{-5}$	8-23	40.8/26
0.13710	0.13640	0.13710	0.539 $^{+8}_{-5}$	8-23	61.7/26
0.13710	0.13640	0.13745	0.520 $^{+9}_{-6}$	8-23	51.8/26
0.13710	0.13710	0.13710	0.504 $^{+9}_{-6}$	8-23	58.7/26
0.13710	0.13710	0.13745	0.483 $^{+11}_{-7}$	8-23	47.3/26
0.13710	0.13745	0.13745	0.459 $^{+15}_{-8}$	8-23	43.1/26
0.13745	0.13640	0.13640	0.560 $^{+8}_{-6}$	8-23	33.9/26
0.13745	0.13640	0.13710	0.528 $^{+9}_{-7}$	8-23	31.0/26
0.13745	0.13640	0.13745	0.507 $^{+10}_{-9}$	8-23	26.7/26
0.13745	0.13710	0.13710	0.495 $^{+11}_{-9}$	8-23	30.4/26
0.13745	0.13710	0.13745	0.476 $^{+11}_{-13}$	8-23	25.8/26
0.13745	0.13745	0.13745	0.435 $^{+18}_{-10}$	8-23	37.0/26

Table A.20: ‘ Λ -like’ ($\kappa_1[\kappa_2\kappa_3]$) masses on the 24×48 lattice at $\beta = 6.2$, with C=TAD, obtained from a double exponential fit to the (LLL,LLL) and (FFL,LLL) correlators.

κ_1	κ_2	am_{PS}	Fit Range	$\chi^2/\text{d.o.f}$
0.13344	0.13344	0.3982 $^{+12}_{-8}$	6-23	34.8/30
0.13417	0.13344	0.3560 $^{+13}_{-9}$	6-23	31.1/30
0.13455	0.13344	0.3330 $^{+13}_{-11}$	6-23	29.8/30
0.13417	0.13417	0.3090 $^{+15}_{-10}$	6-23	29.4/30
0.13455	0.13417	0.2822 $^{+15}_{-12}$	6-23	28.3/30
0.13455	0.13455	0.2517 $^{+17}_{-14}$	6-23	32.6/30

Table A.21: Pion masses on the 16×48 lattice at $\beta = 6.0$, with C=NP, obtained from a double exponential fit to the (LL,LL) and (FL,LL) correlators.

κ_1	κ_2	am_V	Fit Range	$\chi^2/\text{d.o.f}$
0.13344	0.13344	0.5406 $^{+30}_{-22}$	6-23	40.8/30
0.13417	0.13344	0.5149 $^{+35}_{-28}$	6-23	39.1/30
0.13455	0.13344	0.5018 $^{+45}_{-34}$	6-23	36.2/30
0.13417	0.13417	0.4877 $^{+45}_{-39}$	6-23	40.4/30
0.13455	0.13417	0.4743 $^{+58}_{-49}$	6-23	37.9/30
0.13455	0.13455	0.4615 $^{+73}_{-62}$	6-23	35.3/30

Table A.22: Rho masses on the 16×48 lattice at $\beta = 6.0$, with C=NP, obtained from a double exponential fit to the channel $\sum_{i=1}^3 \bar{\psi}^a \gamma_i \psi^a$ with the (LL,LL) and (FL,LL) correlators.

κ_1	κ_2	κ_3	am_Δ	Fit Range	$\chi^2/\text{d.o.f}$
0.13344	0.13344	0.13344	0.889 ⁺⁸ ₋₆	7-23	37.0/28
0.13344	0.13344	0.13417	0.865 ⁺⁹ ₋₈	7-23	41.0/28
0.13344	0.13344	0.13455	0.857 ⁺¹⁰ ₋₁₁	7-23	45.8/28
0.13344	0.13417	0.13417	0.838 ⁺¹⁰ ₋₁₀	7-23	42.3/28
0.13344	0.13417	0.13455	0.830 ⁺¹¹ ₋₁₃	7-23	45.7/28
0.13344	0.13455	0.13455	0.815 ⁺¹² ₋₁₆	7-23	43.3/28
0.13417	0.13417	0.13417	0.812 ⁺¹¹ ₋₁₃	7-23	45.2/28
0.13417	0.13417	0.13455	0.802 ⁺¹² ₋₁₆	7-23	47.8/28
0.13417	0.13455	0.13455	0.785 ⁺¹⁴ ₋₁₈	7-23	47.0/28
0.13455	0.13455	0.13455	0.767 ⁺¹⁷ ₋₂₁	7-23	46.0/28

Table A.23: Delta ($\{\kappa_1\kappa_2\kappa_3\}$) masses on the 16×48 lattice at $\beta = 6.0$, with C=NP, obtained from a double exponential fit to the (LLL,LLL) and (FFL,LLL) correlators.

κ_1	κ_2	κ_3	am_Σ	Fit Range	$\chi^2/\text{d.o.f}$
0.13344	0.13344	0.13344	0.799 $^{+6}_{-3}$	6–23	43.7/30
0.13344	0.13344	0.13417	0.769 $^{+6}_{-4}$	6–23	46.3/30
0.13344	0.13344	0.13455	0.754 $^{+6}_{-4}$	6–23	42.5/30
0.13344	0.13417	0.13417	0.737 $^{+6}_{-5}$	6–23	43.0/30
0.13344	0.13417	0.13455	0.725 $^{+7}_{-6}$	6–23	39.2/30
0.13344	0.13455	0.13455	0.709 $^{+7}_{-7}$	6–23	32.6/30
0.13417	0.13344	0.13344	0.762 $^{+7}_{-4}$	6–23	35.9/30
0.13417	0.13344	0.13417	0.732 $^{+7}_{-4}$	6–23	45.6/30
0.13417	0.13344	0.13455	0.718 $^{+7}_{-6}$	6–23	39.3/30
0.13417	0.13417	0.13417	0.702 $^{+7}_{-5}$	6–23	40.6/30
0.13417	0.13417	0.13455	0.689 $^{+8}_{-7}$	6–23	37.3/30
0.13417	0.13455	0.13455	0.674 $^{+9}_{-9}$	6–23	32.3/30
0.13455	0.13344	0.13344	0.743 $^{+8}_{-4}$	6–23	38.5/30
0.13455	0.13344	0.13417	0.713 $^{+8}_{-5}$	6–23	36.7/30
0.13455	0.13344	0.13455	0.700 $^{+9}_{-6}$	6–23	41.8/30
0.13455	0.13417	0.13417	0.684 $^{+9}_{-7}$	6–23	35.6/30
0.13455	0.13417	0.13455	0.671 $^{+11}_{-8}$	6–23	44.6/30
0.13455	0.13455	0.13455	0.659 $^{+9}_{-13}$	6–23	30.1/30

Table A.24: ‘ Σ -like’ ($\kappa_1\{\kappa_2\kappa_3\}$) masses on the 16×48 lattice at $\beta = 6.0$, with C=NP, obtained from a double exponential fit to the (LLL,LLL) and (FFL,LLL) correlators.

κ_1	κ_2	κ_3	am_Λ	Fit Range	$\chi^2/\text{d.o.f}$
0.13344	0.13344	0.13344	0.798 $^{+6}_{-4}$	6–23	18.3/30
0.13344	0.13344	0.13417	0.763 $^{+7}_{-4}$	6–23	22.2/30
0.13344	0.13344	0.13455	0.744 $^{+8}_{-5}$	6–23	23.3/30
0.13344	0.13417	0.13417	0.728 $^{+8}_{-5}$	6–23	20.1/30
0.13344	0.13417	0.13455	0.708 $^{+9}_{-6}$	6–23	24.2/30
0.13344	0.13455	0.13455	0.690 $^{+10}_{-7}$	6–23	22.2/30
0.13417	0.13344	0.13344	0.767 $^{+7}_{-4}$	6–23	36.3/30
0.13417	0.13344	0.13417	0.735 $^{+8}_{-5}$	6–23	19.5/30
0.13417	0.13344	0.13455	0.715 $^{+9}_{-5}$	6–23	19.9/30
0.13417	0.13417	0.13417	0.699 $^{+9}_{-6}$	6–23	19.3/30
0.13417	0.13417	0.13455	0.679 $^{+11}_{-6}$	6–23	22.1/30
0.13417	0.13455	0.13455	0.662 $^{+12}_{-8}$	6–23	25.5/30
0.13455	0.13344	0.13344	0.752 $^{+8}_{-5}$	6–23	37.0/30
0.13455	0.13344	0.13417	0.718 $^{+9}_{-6}$	6–23	33.4/30
0.13455	0.13344	0.13455	0.700 $^{+10}_{-8}$	6–23	34.0/30
0.13455	0.13417	0.13417	0.683 $^{+10}_{-8}$	6–23	30.8/30
0.13455	0.13417	0.13455	0.666 $^{+11}_{-11}$	6–23	30.7/30
0.13455	0.13455	0.13455	0.647 $^{+13}_{-9}$	6–23	27.7/30

Table A.25: ‘ Λ -like’ ($\kappa_1[\kappa_2\kappa_3]$) masses on the 16×48 lattice at $\beta = 6.0$, with $C=NP$, obtained from a double exponential fit to the (LLL,LLL) and (FFL,LLL) correlators.

κ_1	κ_2	am_{PS}	Fit Range	$\chi^2/\text{d.o.f}$
0.13344	0.13344	0.3963 $^{+21}_{-15}$	9–19	17.3/9
0.13417	0.13344	0.3529 $^{+22}_{-17}$	9–19	17.7/9
0.13455	0.13344	0.3283 $^{+24}_{-18}$	9–19	17.2/9
0.13417	0.13417	0.3044 $^{+25}_{-18}$	9–19	17.8/9
0.13455	0.13417	0.2759 $^{+28}_{-18}$	9–19	17.0/9
0.13455	0.13455	0.2443 $^{+30}_{-16}$	9–19	16.6/9

Table A.26: Pion masses on the 32×64 at $\beta = 6.0$, with C=NP, obtained from a single exponential fit to the (SS,LL) correlator

κ_1	κ_2	am_V	Fit Range	$\chi^2/\text{d.o.f}$
0.13344	0.13344	0.5399 $^{+41}_{-41}$	10–15	5.0/4
0.13417	0.13344	0.5138 $^{+47}_{-50}$	10–15	4.5/4
0.13455	0.13344	0.5016 $^{+51}_{-56}$	10–15	4.6/4
0.13417	0.13417	0.4876 $^{+57}_{-60}$	10–15	3.7/4
0.13455	0.13417	0.4753 $^{+67}_{-68}$	10–15	3.6/4
0.13455	0.13455	0.4634 $^{+87}_{-83}$	10–15	3.1/4

Table A.27: Rho masses on the 32×64 at $\beta = 6.0$, with C=NP, obtained from a single exponential fit to the channel $\sum_{i=1}^3 \bar{\psi}^a \gamma_i \psi^a$ with the (SS,LL) correlator.

κ_1	κ_2	κ_3	am_Δ	Fit Range	$\chi^2/\text{d.o.f}$
0.13344	0.13344	0.13344	0.884 $^{+10}_{-9}$	2–16	12.8/12
0.13344	0.13344	0.13417	0.857 $^{+11}_{-10}$	2–16	13.0/12
0.13344	0.13344	0.13455	0.844 $^{+11}_{-10}$	2–16	13.0/12
0.13344	0.13417	0.13417	0.830 $^{+12}_{-10}$	2–16	13.3/12
0.13344	0.13417	0.13455	0.818 $^{+12}_{-11}$	2–16	13.4/12
0.13344	0.13455	0.13455	0.805 $^{+13}_{-10}$	2–16	13.9/12
0.13417	0.13417	0.13417	0.804 $^{+12}_{-10}$	2–16	13.8/12
0.13417	0.13417	0.13455	0.791 $^{+13}_{-10}$	2–16	14.2/12
0.13417	0.13455	0.13455	0.778 $^{+14}_{-11}$	2–16	15.1/12
0.13455	0.13455	0.13455	0.766 $^{+14}_{-12}$	2–16	16.3/12

Table A.28: Delta ($\{\kappa_1\kappa_2\kappa_3\}$) masses on the 32×64 at $\beta = 6.0$, with C=NP, obtained from a double exponential fit to the (SSS,LLL) correlator

κ_1	κ_2	κ_3	am_Σ	Fit Range	$\chi^2/\text{d.o.f}$
0.13344	0.13344	0.13344	0.794 $^{+11}_{-5}$	2-18	62.0/28
0.13344	0.13344	0.13417	0.762 $^{+12}_{-6}$	2-18	62.8/28
0.13344	0.13344	0.13455	0.745 $^{+13}_{-6}$	2-18	60.5/28
0.13344	0.13417	0.13417	0.720 $^{+15}_{-6}$	2-18	61.4/28
0.13344	0.13417	0.13455	0.713 $^{+13}_{-7}$	2-18	54.9/28
0.13344	0.13455	0.13455	0.676 $^{+22}_{-4}$	2-18	55.0/28
0.13417	0.13344	0.13344	0.753 $^{+14}_{-6}$	2-18	61.7/28
0.13417	0.13344	0.13417	0.720 $^{+15}_{-6}$	2-18	61.4/28
0.13417	0.13344	0.13455	0.703 $^{+17}_{-7}$	2-18	58.5/28
0.13417	0.13417	0.13417	0.687 $^{+17}_{-7}$	2-18	57.0/28
0.13417	0.13417	0.13455	0.670 $^{+18}_{-8}$	2-18	51.1/28
0.13417	0.13455	0.13455	0.643 $^{+24}_{-6}$	2-18	48.2/28
0.13455	0.13344	0.13344	0.730 $^{+17}_{-5}$	2-18	59.6/28
0.13455	0.13344	0.13417	0.696 $^{+19}_{-5}$	2-18	58.6/28
0.13455	0.13344	0.13455	0.697 $^{+13}_{-8}$	2-18	47.9/28
0.13455	0.13417	0.13417	0.662 $^{+22}_{-5}$	2-18	53.8/28
0.13455	0.13417	0.13455	0.655 $^{+18}_{-9}$	2-18	44.4/28
0.13455	0.13455	0.13455	0.628 $^{+23}_{-8}$	2-18	42.2/28

Table A.29: ‘ Σ -like’ ($\kappa_1\{\kappa_2\kappa_3\}$) masses on the 32×64 at $\beta = 6.0$, with C=NP, obtained from a double exponential fit to the (SSS,LLL) and (SSS,SSS) correlators.

κ_1	κ_2	κ_3	am_Λ	Fit Range	$\chi^2/\text{d.o.f}$
0.13344	0.13344	0.13344	0.794 $^{+11}_{-5}$	2-18	62.0/28
0.13344	0.13344	0.13417	0.756 $^{+13}_{-6}$	2-18	62.1/28
0.13344	0.13344	0.13455	0.735 $^{+16}_{-5}$	2-18	60.0/28
0.13344	0.13417	0.13417	0.726 $^{+13}_{-6}$	2-18	60.8/28
0.13344	0.13417	0.13455	0.695 $^{+20}_{-5}$	2-18	59.0/28
0.13344	0.13455	0.13455	0.690 $^{+16}_{-7}$	2-18	51.2/28
0.13417	0.13344	0.13344	0.765 $^{+11}_{-6}$	2-18	63.1/28
0.13417	0.13344	0.13417	0.726 $^{+13}_{-6}$	2-18	60.8/28
0.13417	0.13344	0.13455	0.705 $^{+16}_{-6}$	2-18	56.8/28
0.13417	0.13417	0.13417	0.687 $^{+17}_{-7}$	2-18	57.0/28
0.13417	0.13417	0.13455	0.665 $^{+21}_{-6}$	2-18	53.1/28
0.13417	0.13455	0.13455	0.651 $^{+20}_{-8}$	2-18	46.0/28
0.13455	0.13344	0.13344	0.750 $^{+12}_{-6}$	2-18	60.4/28
0.13455	0.13344	0.13417	0.712 $^{+13}_{-8}$	2-18	55.9/28
0.13455	0.13344	0.13455	0.669 $^{+25}_{-3}$	2-18	54.7/28
0.13455	0.13417	0.13417	0.673 $^{+17}_{-8}$	2-18	50.0/28
0.13455	0.13417	0.13455	0.640 $^{+26}_{-5}$	2-18	48.8/28
0.13455	0.13455	0.13455	0.628 $^{+23}_{-8}$	2-18	42.2/28

Table A.30: ‘ Λ -like’ ($\kappa_1[\kappa_2\kappa_3]$) masses on the 32×64 at $\beta = 6.0$, with C=NP, obtained from a double exponential fit to the (SSS,LLL) and (SSS,SSS) correlators.

κ_1	κ_2	am_{PS}	Fit Range	$\chi^2/\text{d.o.f}$
0.13460	0.13460	0.2779 $^{+17}_{-15}$	8–23	32.4/26
0.13510	0.13460	0.2472 $^{+19}_{-18}$	8–23	27.8/26
0.13530	0.13460	0.2346 $^{+20}_{-21}$	8–23	26.7/26
0.13510	0.13510	0.2131 $^{+21}_{-20}$	8–23	25.0/26
0.13530	0.13510	0.1988 $^{+20}_{-25}$	8–23	25.5/26
0.13530	0.13530	0.1831 $^{+19}_{-29}$	8–23	26.2/26

Table A.31: Pion masses on the 24×48 lattice at $\beta = 6.2$ with C=NP, obtained from a double exponential fit to the (LL,LL) and (FL,LL) correlators.

κ_1	κ_2	am_V	Fit Range	$\chi^2/\text{d.o.f}$
0.13460	0.13460	0.3890 $^{+33}_{-32}$	8–23	33.5/26
0.13510	0.13460	0.3711 $^{+44}_{-41}$	8–23	28.9/26
0.13530	0.13460	0.3642 $^{+51}_{-48}$	8–23	26.5/26
0.13510	0.13510	0.3535 $^{+54}_{-57}$	8–23	29.5/26
0.13530	0.13510	0.3477 $^{+65}_{-72}$	8–23	27.9/26
0.13530	0.13530	0.3422 $^{+76}_{-99}$	8–23	30.9/26

Table A.32: Rho masses on the 24×48 lattice at $\beta = 6.2$ with C=NP, obtained from a double exponential fit to the channel $\sum_{i=1}^3 \bar{\psi}^a \gamma_i \psi^a$ with the (LL,LL) and (FL,LL) correlators.

κ_1	κ_2	κ_3	am_Δ	Fit Range	$\chi^2/\text{d.o.f}$
0.13460	0.13460	0.13460	0.644 $^{+9}_{-8}$	9–23	28.9/24
0.13460	0.13460	0.13510	0.625 $^{+10}_{-8}$	9–23	28.2/24
0.13460	0.13460	0.13530	0.618 $^{+11}_{-9}$	9–23	31.3/24
0.13460	0.13510	0.13510	0.606 $^{+12}_{-10}$	9–23	30.7/24
0.13460	0.13510	0.13530	0.599 $^{+13}_{-10}$	9–23	34.0/24
0.13460	0.13530	0.13530	0.590 $^{+15}_{-10}$	9–23	35.5/24
0.13510	0.13510	0.13510	0.585 $^{+14}_{-11}$	9–23	31.9/24
0.13510	0.13510	0.13530	0.578 $^{+16}_{-11}$	9–23	35.1/24
0.13510	0.13530	0.13530	0.569 $^{+17}_{-12}$	9–23	35.8/24
0.13530	0.13530	0.13530	0.561 $^{+19}_{-13}$	9–23	36.0/24

Table A.33: Delta ($\{\kappa_1\kappa_2\kappa_3\}$) on the 24×48 lattice at $\beta = 6.2$ with C=NP, obtained from a double exponential fit to the (LLL,LLL) and (FFL,LLL) correlators.

κ_1	κ_2	κ_3	am_Σ	Fit Range	$\chi^2/\text{d.o.f}$
0.13460	0.13460	0.13460	0.579 $^{+6}_{-5}$	8–23	43.1/26
0.13460	0.13460	0.13510	0.557 $^{+6}_{-5}$	8–23	40.0/26
0.13460	0.13460	0.13530	0.548 $^{+6}_{-6}$	8–23	38.1/26
0.13460	0.13510	0.13510	0.538 $^{+6}_{-7}$	8–23	37.3/26
0.13460	0.13510	0.13530	0.529 $^{+7}_{-8}$	8–23	36.6/26
0.13460	0.13530	0.13530	0.521 $^{+7}_{-9}$	8–23	29.5/26
0.13510	0.13460	0.13460	0.553 $^{+7}_{-4}$	8–23	48.1/26
0.13510	0.13460	0.13510	0.533 $^{+6}_{-7}$	8–23	35.2/26
0.13510	0.13460	0.13530	0.524 $^{+6}_{-7}$	8–23	32.3/26
0.13510	0.13510	0.13510	0.513 $^{+6}_{-10}$	8–23	35.6/26
0.13510	0.13510	0.13530	0.504 $^{+7}_{-10}$	8–23	32.8/26
0.13510	0.13530	0.13530	0.495 $^{+8}_{-12}$	8–23	30.1/26
0.13530	0.13460	0.13460	0.542 $^{+7}_{-5}$	8–23	43.4/26
0.13530	0.13460	0.13510	0.517 $^{+8}_{-6}$	8–23	43.0/26
0.13530	0.13460	0.13530	0.506 $^{+10}_{-7}$	8–23	44.8/26
0.13530	0.13510	0.13510	0.489 $^{+11}_{-7}$	8–23	43.6/26
0.13530	0.13510	0.13530	0.475 $^{+12}_{-8}$	8–23	42.2/26
0.13530	0.13530	0.13530	0.483 $^{+9}_{-14}$	8–23	29.7/26

Table A.34: ‘ Σ -like’ ($\kappa_1\{\kappa_2\kappa_3\}$) on the 24×48 lattice at $\beta = 6.2$ with C=NP, obtained from a double exponential fit to the (LLL,LLL) and (FFL,LLL) correlators.

κ_1	κ_2	κ_3	am_Λ	Fit Range	$\chi^2/\text{d.o.f}$
0.13460	0.13460	0.13460	0.580 ⁺⁶ ₋₄	8-23	52.7/26
0.13460	0.13460	0.13510	0.554 ⁺⁶ ₋₄	8-23	48.8/26
0.13460	0.13460	0.13530	0.544 ⁺⁶ ₋₅	8-23	43.7/26
0.13460	0.13510	0.13510	0.530 ⁺⁷ ₋₆	8-23	46.2/26
0.13460	0.13510	0.13530	0.518 ⁺⁷ ₋₆	8-23	38.9/26
0.13460	0.13530	0.13530	0.506 ⁺⁹ ₋₇	8-23	39.8/26
0.13510	0.13460	0.13460	0.558 ⁺⁶ ₋₆	8-23	34.4/26
0.13510	0.13460	0.13510	0.532 ⁺⁸ ₋₅	8-23	52.2/26
0.13510	0.13460	0.13530	0.522 ⁺⁸ ₋₆	8-23	45.8/26
0.13510	0.13510	0.13510	0.506 ⁺⁹ ₋₇	8-23	49.0/26
0.13510	0.13510	0.13530	0.493 ⁺⁹ ₋₈	8-23	42.2/26
0.13510	0.13530	0.13530	0.480 ⁺¹¹ ₋₉	8-23	39.4/26
0.13530	0.13460	0.13460	0.550 ⁺⁷ ₋₇	8-23	33.0/26
0.13530	0.13460	0.13510	0.529 ⁺⁷ ₋₉	8-23	29.9/26
0.13530	0.13460	0.13530	0.520 ⁺⁶ ₋₁₀	8-23	22.4/26
0.13530	0.13510	0.13510	0.507 ⁺⁷ ₋₁₂	8-23	27.7/26
0.13530	0.13510	0.13530	0.497 ⁺⁷ ₋₁₄	8-23	24.4/26
0.13530	0.13530	0.13530	0.467 ⁺¹² ₋₁₀	8-23	36.9/26

Table A.35: ‘ Λ -like’ ($\kappa_1[\kappa_2\kappa_3]$) on the 24×48 lattice at $\beta = 6.2$ with C=NP, obtained from a double exponential fit to the (LLL,LLL) and (FFL,LLL) correlators.

Appendix B

Light Hadron Spectrum Results

Pion Chiral extrapolations

The pion masses for each data set tabulated in appendix A, are fitted to following ansätze.

- **Fit 1:** The three lightest pion masses are fitted to

$$m_{PS}^2 = C_1(m_1 + m_2). \quad (\text{B.1})$$

- **Fit 2:** All pion masses are fitted to

$$m_{PS}^2 = C_1(m_1 + m_2). \quad (\text{B.2})$$

- **Fit 3:** All pion masses are fitted to

$$m_{PS}^2 = C_1(m_1 + m_2) + C_2(m_1 + m_2)^2. \quad (\text{B.3})$$

- **Fit 4:** All pion masses are fitted to

$$m_{PS}^2 = C_1(m_1 + m_2) + C_3(m_1 + m_2)^3. \quad (\text{B.4})$$

- **Fit 5:** All pion masses are fitted to

$$m_{PS}^2 = C_1(m_1 + m_2) + C_2(m_1 + m_2)^2 + C_3(m_1 + m_2)^3. \quad (\text{B.5})$$

In these fits m_i , $i = 1, 2$, are parameterised as

$$m_x = \left(\frac{1}{2\kappa_i} - \frac{C_0}{2} \right), \quad (\text{B.6})$$

so that $\kappa_c = 1/C_0$.

Fit	κ_c	C_1	C_2	$\chi^2/\text{d.o.f}$
2	0.143388 $\begin{smallmatrix} +27 \\ -16 \end{smallmatrix}$	2.150 $\begin{smallmatrix} +8 \\ -10 \end{smallmatrix}$		2.1/1
3	0.143519 $\begin{smallmatrix} +104 \\ -93 \end{smallmatrix}$	2.007 $\begin{smallmatrix} +108 \\ -100 \end{smallmatrix}$	0.37 $\begin{smallmatrix} +24 \\ -29 \end{smallmatrix}$	

Table B.36: Chiral extrapolations for the pion calculated on the $12^3 \times 24$ lattice at $\beta = 5.7$ with C=TAD. In this case there are only three pion masses so not all fits could be performed. In Fit 3, as there are on degrees of freedom no minimisation on the parameters could be performed, and the quadratic equations are solved for the best fit and for each bootstrap clusters.

Fit	κ_c	C_1	C_2	$\chi^2/\text{d.o.f}$
2	0.143444 $\begin{smallmatrix} +28 \\ -23 \end{smallmatrix}$	2.145 $\begin{smallmatrix} +13 \\ -12 \end{smallmatrix}$		4.9/1
3	0.143543 $\begin{smallmatrix} +66 \\ -42 \end{smallmatrix}$	2.023 $\begin{smallmatrix} +50 \\ -66 \end{smallmatrix}$	0.31 $\begin{smallmatrix} +15 \\ -13 \end{smallmatrix}$	

Table B.37: Chiral extrapolations for the pion calculated on the $16^3 \times 24$ lattice at $\beta = 5.7$ with C=TAD. In this case there are only three pion masses so not all fits could be performed. In Fit 3, as there are on degrees of freedom no minimisation on the parameters could be performed, and the quadratic equations are solved for the best fit and for each bootstrap clusters.

Fit	κ_c	C_1	C_2	C_3	$\chi^2/\text{d.o.f}$
1	0.139267 $^{+21}_{-11}$	1.415 $^{+14}_{-21}$			0.2/1
2	0.139245 $^{+14}_{-9}$	1.463 $^{+7}_{-9}$			28.1/4
3	0.139305 $^{+22}_{-16}$	1.323 $^{+31}_{-35}$	0.77 $^{+16}_{-16}$		6.0/3
4	0.139288 $^{+19}_{-14}$	1.379 $^{+19}_{-21}$		3.14 $^{+58}_{-63}$	3.2/3
5	0.139262 $^{+32}_{-17}$	1.462 $^{+56}_{-87}$	-1.03 $^{+105}_{-69}$	7.24 $^{+277}_{-414}$	1.8/2

Table B.38: Chiral extrapolations for the pion calculated on the $16^3 \times 48$ lattice at $\beta = 6.0$ with C=TAD.

Fit	κ_c	C_1	C_2	C_3	$\chi^2/\text{d.o.f}$
1	0.137957 $^{+15}_{-31}$	1.06 $^{+4}_{-2}$			0.1/1
2	0.137910 $^{+14}_{-17}$	1.15 $^{+1}_{-2}$			10.1/4
3	0.137968 $^{+18}_{-39}$	0.99 $^{+8}_{-4}$	1.3 $^{+2}_{-7}$		2.6/3
4	0.137947 $^{+15}_{-30}$	1.07 $^{+5}_{-2}$		7.1 $^{+14}_{-35}$	3.0/3
5	0.137976 $^{+29}_{-55}$	0.97 $^{+16}_{-10}$	1.8 $^{+19}_{-27}$	-2.6 $^{+150}_{-117}$	2.6/2

Table B.39: Chiral extrapolations for the pion calculated on the $24^3 \times 48$ lattice at $\beta = 6.2$ with C=TAD.

Fit	κ_c	C_1	C_2	C_3	$\chi^2/\text{d.o.f}$
1	0.135310 $^{+16}_{-16}$	1.520 $^{+21}_{-17}$			4.0/1
2	0.135299 $^{+12}_{-9}$	1.557 $^{+8}_{-9}$			19.7/4
3	0.135335 $^{+20}_{-17}$	1.452 $^{+38}_{-40}$	0.64 $^{+22}_{-23}$		11.5/3
4	0.135324 $^{+17}_{-13}$	1.491 $^{+21}_{-23}$		3.10 $^{+85}_{-87}$	8.7/3
5	0.135262 $^{+28}_{-23}$	1.707 $^{+87}_{-95}$	-2.95 $^{+126}_{-118}$	16.15 $^{+546}_{-557}$	2.9/2

Table B.40: Chiral extrapolations for the pion calculated on the $16^3 \times 48$ lattice at $\beta = 6.0$ with C=NP.

Fit	κ_c	C_1	C_2	C_3	$\chi^2/\text{d.o.f}$
1	0.135243 $^{+23}_{-11}$	1.571 $^{+22}_{-30}$			0.1/1
2	0.135259 $^{+17}_{-10}$	1.573 $^{+14}_{-12}$			11.9/4
3	0.135290 $^{+27}_{-12}$	1.448 $^{+36}_{-55}$	0.78 $^{+31}_{-18}$		4.9/3
4	0.135275 $^{+21}_{-10}$	1.507 $^{+22}_{-30}$		3.11 $^{+117}_{-65}$	4.5/3
5	0.135225 $^{+50}_{-24}$	1.667 $^{+116}_{-174}$	-1.96 $^{+216}_{-162}$	11.93 $^{+709}_{-894}$	0.03/2

Table B.41: Chiral extrapolations for the pion calculated on the $32^3 \times 64$ lattice at $\beta = 6.0$ with C=NP.

Fit	κ_c	C_1	C_2	C_3	$\chi^2/\text{d.o.f}$
1	0.135873 $^{+9}_{-40}$	1.078 $^{+56}_{-8}$			0.1/1
2	0.135823 $^{+15}_{-19}$	1.167 $^{+15}_{-14}$			7.9/4
3	0.135895 $^{+14}_{-55}$	0.969 $^{+129}_{-31}$	1.8 $^{+2}_{-11}$		1.6/3
4	0.135869 $^{+13}_{-39}$	1.061 $^{+70}_{-20}$		10.9 $^{+16}_{-65}$	1.7/3
5	0.135896 $^{+41}_{-86}$	0.966 $^{+295}_{-156}$	1.8 $^{+31}_{-56}$	-0.1 $^{+351}_{-217}$	1.6/2

Table B.42: Chiral extrapolations for the pion calculated on the $24^3 \times 48$ lattice at $\beta = 6.2$ with C=NP.

Quark masses and Lattice Hadron Masses

Action	β	$N_s^3 \times N_t$	κ_n	$\bar{m}(1/a)$
TAD	5.7	12×24	0.143366 $\begin{smallmatrix} +100 \\ -88 \end{smallmatrix}$	4.20 $\begin{smallmatrix} +19 \\ -19 \end{smallmatrix}$
TAD	5.7	16×32	0.143400 $\begin{smallmatrix} +64 \\ -40 \end{smallmatrix}$	4.04 $\begin{smallmatrix} +13 \\ -10 \end{smallmatrix}$
TAD	6.0	16×48	0.139231 $\begin{smallmatrix} +21 \\ -15 \end{smallmatrix}$	3.68 $\begin{smallmatrix} +10 \\ -9 \end{smallmatrix}$
TAD	6.2	24×48	0.137914 $\begin{smallmatrix} +16 \\ -37 \end{smallmatrix}$	3.67 $\begin{smallmatrix} +13 \\ -25 \end{smallmatrix}$
NP	6.0	16×48	0.135266 $\begin{smallmatrix} +20 \\ -16 \end{smallmatrix}$	3.50 $\begin{smallmatrix} +10 \\ -10 \end{smallmatrix}$
NP	6.0	32×64	0.135223 $\begin{smallmatrix} +25 \\ -11 \end{smallmatrix}$	3.47 $\begin{smallmatrix} +12 \\ -10 \end{smallmatrix}$
NP	6.2	24×48	0.135842 $\begin{smallmatrix} +13 \\ -52 \end{smallmatrix}$	3.75 $\begin{smallmatrix} +14 \\ -40 \end{smallmatrix}$

Table B.43: Estimates of the “normal” quark mass obtained by matching am_{PS}/am_V with the physical value of M_π/M_ρ . Results are given for (1) κ_n and (2) the lattice quark mass \bar{m} evaluated at $1/a$. The quark mass is given in MeV.

Qty	Action	β	$N_s^3 \times N_t$	κ_s	$m_s(1/a)$
M_K/M_ρ	TAD	5.7	12×24	0.13986 ⁺⁷ ₋₇	103 ⁺³ ₋₄
M_{K^*}/M_ρ	TAD	5.7	12×24	0.13929 ⁺¹⁷ ₋₁₈	119 ⁺³ ₋₃
M_ϕ/M_ρ	TAD	5.7	12×24	0.13914 ⁺¹⁷ ₋₁₈	124 ⁺³ ₋₃
M_K/M_ρ	TAD	5.7	16×32	0.14011 ⁺¹¹ ₋₁₂	100 ⁺³ ₋₂
M_{K^*}/M_ρ	TAD	5.7	16×32	0.13964 ⁺²² ₋₂₁	113 ⁺⁴ ₋₄
M_ϕ/M_ρ	TAD	5.7	16×32	0.13950 ⁺²² ₋₂₁	117 ⁺⁴ ₋₄
M_K/M_ρ	TAD	6.0	16×48	0.13754 ⁺⁶ ₋₆	90 ⁺² ₋₂
M_{K^*}/M_ρ	TAD	6.0	16×48	0.13739 ⁺⁹ ₋₁₁	98 ⁺⁴ ₋₃
M_ϕ/M_ρ	TAD	6.0	16×48	0.13732 ⁺⁹ ₋₁₁	102 ⁺⁴ ₋₄
M_K/M_ρ	TAD	6.2	24×48	0.13668 ⁺⁶ ₋₇	90 ⁺³ ₋₅
M_{K^*}/M_ρ	TAD	6.2	24×48	0.13662 ⁺⁸ ₋₁₅	94 ⁺⁶ ₋₅
M_ϕ/M_ρ	TAD	6.2	24×48	0.13657 ⁺⁸ ₋₁₅	97 ⁺⁶ ₋₅
M_K/M_ρ	NP	6.0	16×48	0.13365 ⁺⁶ ₋₅	88 ⁺² ₋₃
M_{K^*}/M_ρ	NP	6.0	16×48	0.13350 ⁺¹¹ ₋₁₂	95 ⁺⁴ ₋₅
M_ϕ/M_ρ	NP	6.0	16×48	0.13343 ⁺¹¹ ₋₁₂	99 ⁺⁴ ₋₅
M_K/M_ρ	NP	6.0	32×64	0.13369 ⁺⁶ ₋₆	84 ⁺³ ₋₂
M_{K^*}/M_ρ	NP	6.0	32×64	0.13360 ⁺¹⁰ ₋₇	89 ⁺³ ₋₄
M_ϕ/M_ρ	NP	6.0	32×64	0.13354 ⁺¹⁰ ₋₇	92 ⁺³ ₋₄
M_K/M_ρ	NP	6.2	24×48	0.13466 ⁺⁷ ₋₇	88 ⁺² ₋₇
M_{K^*}/M_ρ	NP	6.2	24×48	0.13461 ⁺⁹ ₋₂₁	92 ⁺⁹ ₋₇
M_ϕ/M_ρ	NP	6.2	24×48	0.13455 ⁺¹⁰ ₋₂₁	96 ⁺⁹ ₋₇

Table B.44: Estimates of the strange quark mass obtained by matching different quantities with their physical values. Results are given for (1) κ_s and (2) the lattice quark mass m_s evaluated at $1/a$. The quark mass is given in MeV.

Action	β	$N_s^3 \times N_t$	am_π	am_ρ	am_K from M_{K^*}/M_ρ	am_K from M_ϕ/M_ρ	am_{K^*} from M_K/M_ρ	am_{K^*} from M_ϕ/M_ρ	am_ϕ from M_K/M_ρ	am_ϕ from M_{K^*}/M_ρ
TAD	5.7	12×24	0.1225 ⁺¹⁵ ₋₁₅	0.6857 ⁺⁸¹ ₋₈₀	0.4736 ⁺¹²⁴ ₋₁₂₅	0.4820 ⁺¹²² ₋₁₂₃	0.7753 ⁺⁷⁴ ₋₇₁	0.7941 ⁺⁹⁷ ₋₉₆	0.8647 ⁺⁷⁶ ₋₆₄	0.8944 ⁺¹¹² ₋₁₁₀
TAD	5.7	16×32	0.1188 ⁺²¹ ₋₂₂	0.6649 ⁺¹¹⁶ ₋₁₁₉	0.4551 ⁺¹²⁶ ₋₁₄₃	0.4632 ⁺¹²⁴ ₋₁₄₄	0.7531 ⁺¹¹⁹ ₋₁₀₉	0.7697 ⁺¹³⁶ ₋₁₄₀	0.8413 ⁺¹²² ₋₁₀₇	0.8668 ⁺¹⁵⁵ ₋₁₆₂
TAD	6.0	16×48	0.0709 ⁺¹² ₋₁₁	0.3964 ⁺⁶⁹ ₋₅₈	0.2650 ⁺⁸³ ₋₆₃	0.2700 ⁺⁸³ ₋₆₃	0.4517 ⁺⁶⁸ ₋₆₂	0.4589 ⁺⁸⁰ ₋₆₇	0.5069 ⁺⁷⁰ ₋₆₆	0.5165 ⁺⁹¹ ₋₇₆
TAD	6.2	24×48	0.0530 ⁺¹⁶ ₋₁₁	0.2964 ⁺⁸⁹ ₋₆₀	0.1946 ⁺¹²⁹ ₋₆₈	0.1985 ⁺¹²⁸ ₋₆₉	0.3391 ⁺⁷⁹ ₋₆₂	0.3429 ⁺¹⁰⁵ ₋₇₁	0.3818 ⁺⁷³ ₋₆₆	0.3857 ⁺¹²⁰ ₋₈₀
NP	6.0	16×48	0.0739 ⁺¹³ ₋₁₄	0.4136 ⁺⁷² ₋₇₇	0.2769 ⁺⁹⁷ ₋₉₁	0.2821 ⁺⁹⁷ ₋₉₁	0.4711 ⁺⁶⁷ ₋₇₅	0.4788 ⁺⁸³ ₋₉₀	0.5286 ⁺⁷⁰ ₋₇₆	0.5390 ⁺⁹⁶ ₋₁₀₂
NP	6.0	32×64	0.0730 ⁺¹¹ ₋₁₆	0.4087 ⁺⁶³ ₋₈₈	0.2696 ⁺⁶⁰ ₋₉₆	0.2749 ⁺⁶² ₋₉₇	0.4680 ⁺⁷⁷ ₋₉₇	0.4739 ⁺⁷⁵ ₋₁₀₆	0.5263 ⁺⁹² ₋₁₀₆	0.5330 ⁺⁸³ ₋₁₂₀
NP	6.2	24×48	0.0531 ⁺²¹ ₋₁₃	0.2971 ⁺¹¹⁹ ₋₆₈	0.1952 ⁺¹⁸⁴ ₋₇₁	0.1994 ⁺¹⁸³ ₋₇₁	0.3398 ⁺⁹⁷ ₋₇₇	0.3438 ⁺¹³⁸ ₋₈₁	0.3824 ⁺⁸⁷ ₋₉₀	0.3865 ⁺¹⁶⁰ ₋₉₂

Extrapolated/interpolated values of meson masses in lattice units.

Action	β	$N_s^3 \times N_t$	am_N	am_Λ	am_Σ	am_Ξ	am_Δ	am_{Σ^*}	am_{Ξ^*}	am_Ω
TAD	5.7	12×24	0.913 ⁺¹⁹ ₋₁₈				1.155 ⁺²⁶ ₋₂₄	1.262 ⁺²² ₋₂₁	1.369 ⁺¹⁹ ₋₁₈	1.476 ⁺²⁰ ₋₁₈
TAD	5.7	16×32	0.928 ⁺³⁶ ₋₂₂				1.132 ⁺⁴⁴ ₋₄₇	1.232 ⁺³⁴ ₋₃₉	1.332 ⁺²⁸ ₋₃₁	1.432 ⁺²⁶ ₋₂₆
TAD	6.0	16×48	0.546 ⁺¹¹ ₋₁₁	0.612 ⁺¹⁰ ₋₁₀	0.627 ⁺¹⁰ ₋₁₀	0.696 ⁺¹² ₋₁₀	0.676 ⁺¹⁶ ₋₁₆	0.736 ⁺¹³ ₋₁₃	0.796 ⁺¹³ ₋₁₁	0.856 ⁺¹⁴ ₋₁₀
TAD	6.2	24×48	0.401 ⁺¹³ ₋₈	0.456 ⁺¹⁴ ₋₈	0.462 ⁺¹⁵ ₋₈	0.510 ⁺¹⁷ ₋₉	0.499 ⁺¹⁸ ₋₁₄	0.547 ⁺¹⁸ ₋₁₁	0.595 ⁺¹⁷ ₋₉	0.643 ⁺²⁰ ₋₁₀
NP	6.0	16×48	0.553 ⁺¹² ₋₁₁	0.622 ⁺¹¹ ₋₁₀	0.645 ⁺¹¹ ₋₁₁	0.721 ⁺¹⁵ ₋₁₄	0.689 ⁺²⁰ ₋₂₄	0.754 ⁺¹⁷ ₋₂₀	0.819 ⁺¹⁶ ₋₁₇	0.883 ⁺¹⁷ ₋₁₇
NP	6.0	32×64	0.551 ⁺¹⁸ ₋₁₄	0.625 ⁺¹⁷ ₋₁₃	0.625 ⁺¹⁶ ₋₁₁	0.699 ⁺¹⁵ ₋₁₁	0.690 ⁺¹⁷ ₋₁₄	0.749 ⁺¹⁶ ₋₁₄	0.808 ⁺¹⁵ ₋₁₅	0.867 ⁺¹⁵ ₋₁₇
NP	6.2	24×48	0.402 ⁺¹³ ₋₁₂	0.457 ⁺¹⁶ ₋₁₀	0.466 ⁺¹⁷ ₋₈	0.524 ⁺²³ ₋₁₀	0.505 ⁺²⁸ ₋₁₆	0.551 ⁺²⁵ ₋₁₂	0.598 ⁺²⁵ ₋₁₀	0.644 ⁺²⁷ ₋₁₂

Extrapolated/interpolated values of baryon masses in lattice units. In calculating the strange baryons, m_s was determined by fixing M_{K^*}/M_ρ .

References

- [1] D. Gross and F. Wilczek. *Phys. Rev. D*, **8**, 3688, (1973).
- [2] D. Gross and F. Wilczek. *Phys. Rev. Lett*, **30**, 1343, (1973).
- [3] H.D. Politzer. *Phys. Rev. Lett*, **30**, 1346, (1973).
- [4] G. t'Hooft. Unpublished remarks at the (1972) Marseille Conference on Yang-Mills Fields.
- [5] M. Creutz. Quarks, Gluons and Lattices. Cambridge University Press, Cambridge, 1983.
- [6] C. Rebbi. Lattice Gauge Theories and Monte Carlo Simulations. World Scientific, Singapore, 1983.
- [7] H.J. Rothe. Lattice Gauge Theories. World Scientific, Singapore, 1992.
- [8] I. Montvay and G. Münster. Quantum Fields on a Lattice. Cambridge University Press, Cambridge, 1994.
- [9] H. Hamber and G. Parisi. *Phys. Rev. Lett*, **47**, 1792, (1981).
- [10] I. Montvay and G. Münster. Quantum Fields on a Lattice. In [8], 1994. Given by *Dyson's formula*, see page 96.
- [11] T. Cheng and L. Li. Gauge theory of elementary particle physics. Oxford University Press, Oxford, 1984.
- [12] K.G. Wilson. *Phys. Rev. D*, **10**, 2445, (1974).
- [13] H.B. Nielsen and M. Ninomiya. *Nucl. Phys. B*, **185**, 20, (1981).
- [14] L. H. Karsten and J. Smit. *Nucl. Phys. B*, **183**, 103, (1981).

- [15] K.G. Wilson. in *New Phenomena in Subnuclear Physics*, 1975.
- [16] L. Susskind. *Phys. Rev. D*, **16**, 3031, (1977).
- [17] G.P. Lepage. in *From Action to Answers-Proceedings of the 1989 Theoretical Advanced Summer Institute in Particle Physics*, 1990.
- [18] N. Metropolis et al. *J. Chem. Phys.*, **21**, 1087, (1953).
- [19] S.Duane et al. *Phys. Lett. B*, **195**, 216, (1987).
- [20] G.P. Lepage. Redesigning lattice qcd. Lecture course at Computing Particle Properties School, March 1997. 36 Internationale Universitatwochen fur Kern und Teilchenphysik, Schladming, Austria.
- [21] D. Leinweber and T. Cohen. *Phys. Rev. D*, **3512**, 3512, (1994).
- [22] B Efron. The jackknife, the bootstrap and other resampling plans. *Society for Industrial and Applied Mathematics*, (1982).
- [23] P. Hasenfratz and F. Niedermayer. *Nucl. Phys. B*, **414**, 785, (1994).
- [24] K. Symanzik. *Mathematical problems in theoretical physics*, volume 153. Springer, New York, 1982.
- [25] K. Symanzik. *Nucl. Phys. B*, **226**, 187,205, (1983).
- [26] M. Lüscher and P. Weisz. *Comm. Math. Phys.*, **97**, 59, (1985).
- [27] M. Lüscher and P. Weisz. *Comm. Math. Phys.*, **98**, 433, (1985).
- [28] B. Sheikholeslami and R. Wohlert. *Nucl. Phys. B*, **259**, 572, (1985).
- [29] H.W. Hamber and C.M. Wu. *Phys. Lett. B*, **136**, 255, (1984).
- [30] G. Heatlie et al. *Nucl. Phys. B*, **352**, 266, (1991).
- [31] J. Mandula et al. *Nucl. Phys. B*, **228**, 8, (1983).
- [32] UKQCD Collaboration, C.R. Allton et al. *Phys. Lett. B*, **284**, 377, (1992).

- [33] P. Lepage and P. Mackenzie. *Phys. Rev. D*, **48**, 2250, (1993).
- [34] E. Gabrielli et al. *Nucl. Phys. B*, **362**, 475, (1991).
- [35] UKQCD Collaboration P.A. Rowland. *Nucl. Phys. B (Proc. Suppl.)*, **53**, 308, (1997).
- [36] K. Jansen et al. *Phys. Lett. B*, **372**, 275, (1996).
- [37] M. Lüscher et al. *Nucl. Phys. B*, **478**, 365, (1996).
- [38] M. Lüscher et al. *Nucl. Phys. B*, **491**, 323, (1997).
- [39] M. Lüscher et al. *Nucl. Phys. B (Proc. Suppl.)*, **53**, 905, (1997).
- [40] R Sommer. To appear in the proceedings of “Lattice QCD on Parallel Computers”, University of Tsukuba, March, 1997. hep-lat/9705026.
- [41] M. Lüscher and P. Weisz. *Nucl. Phys. B*, **479**, 365, (1996).
- [42] M. Lüscher et al. *Nucl. Phys. B*, **491**, 344, (1997).
- [43] S. Sint and P. Weisz. *hep-lat/9704001*.
- [44] K. Symanzik. *Nucl. Phys. B*, **190** [FS3], 187,1, (1981).
- [45] M. Lüscher. *Nucl. Phys. B*, **254**, 365, (1985).
- [46] M. Lüscher et al. *Nucl. Phys. B*, **384**, 168, (1992).
- [47] S. Sint. *Nucl. Phys. B*, **421**, 135, (1994).
- [48] S. Sint. *Nucl. Phys. B*, **451**, 416, (1995).
- [49] J.N. Labrenz and S.R. Sharpe. *Nucl. Phys. B (Proc. Suppl.)*, **34**, 335, (1994).
- [50] J.N. Labrenz and S.R. Sharpe. *Phys. Rev. D*, **54**, 4595, (1996).
- [51] T. Bhattacharya et al. *Phys. Rev. D*, **53**, 6486, (1996).

- [52] R.D. Kenway. in proceedings of XII International Conference on HEP, Leipzig, 1984. 51, eds. A. Meyer and E. Wieczore.
- [53] A. Billoire, E. Marinari, and G. Parisi. *Phys. Lett. B*, **154**, 160, (1985).
- [54] APE Collaboration, P. Bacilieri et al. *Phys. Lett. B*, **214**, 115, (1988).
- [55] APE Collaboration, P. Bacilieri et al. *Nucl. Phys. B*, **317**, 508, (1989).
- [56] G. Kilcup. *Nucl. Phys. B (Proc. Suppl.)*, **9**, 201, (1989).
- [57] V.N Gribov. *Nucl. Phys. B*, **139**, 1, (1978).
- [58] S. Gusken et al. *Nucl. Phys. B (Proc. Suppl.)*, **17**, 361, (1990).
- [59] E. Eichten G. Hockney and H. B. Thacker. *Nucl. Phys. B (Proc. Suppl.)*, **17**, 529, (1990).
- [60] R. Gupta et al. *Phys. Rev. D*, **48**, 3330, (1994).
- [61] P. Lacock et al. *Phys. Rev. D*, **51**, 6403, (1995).
- [62] C. Allton et al. *Phys. Rev. D*, **47**, 5128, (1993).
- [63] R.M. Baxter. New Approaches to Particle Spectra in Lattice QCD. PhD thesis, University of Edinburgh, 1993.
- [64] M. Teper. *Phys. Lett. B*, **183**, 345, (1987).
- [65] M. Albanese. *Phys. Lett. B*, **192**, 163, (1987).
- [66] S. Perantonis et al. *Nucl. Phys. B*, **326**, 544, (1989).
- [67] P.A. Boyle. Heavy Meson Phenomenology. PhD thesis, University of Edinburgh, in preparation.
- [68] K.B. Teo and J.W. Negele. *Nucl. Phys. B (Proc. Suppl.)*, **34**, 390, (1994).
- [69] G.S. Bali and K. Schilling. *Phys. Rev. D*, **47**, 661, (1993).
- [70] M. Creutz. *Phys. Rev. D*, **36**, 2394, (1987).

- [71] F.R. Brown and T.J. Woch. *Phys. Rev. Lett*, **58**, 163, (1987).
- [72] N. Cabibbo and E. Marinari. *Phys. Lett. B*, **119**, 387, (1982).
- [73] A.D. Simpson. Algorithms for QCD. PhD thesis, University of Edinburgh, 1991.
- [74] S.M. Pickles. Algorithms for Lattice QCD. PhD thesis, University of Edinburgh, in preparation.
- [75] D.A. Smith. PhD thesis, University of Edinburgh, in preparation.
- [76] W. Bardeen et al. *hep-lat/9705008*.
- [77] W. Bardeen et al. *hep-lat/9705002*.
- [78] UKQCD Collaboration, H.P. Shanahan et al. *Phys. Rev. D*, **55**, 1584, (1997).
- [79] UKQCD Collaboration, C.M. Michael and H.P. Shanahan. *Nucl. Phys. B (Proc. Suppl.)*, **47**, 337, (1996).
- [80] UKQCD Collaboration, R.D Kenway. *Nucl. Phys. B (Proc. Suppl.)*, **53**, 206, (1997).
- [81] S.M. Ryan. Light Hadron Spectroscopy and Soft Covariant Gauges in Lattice QCD. PhD thesis, University of Edinburgh, 1996.
- [82] JLQCD Collaboration, S. Aoki et al. *Nucl. Phys. B (Proc. Suppl.)*, **47**, 355, (1996).
- [83] UKQCD Collaboration, C.R. Allton et al. *Phys. Rev. D*, **49**, 474, (1994).
- [84] QCDPAX Collaboration, Y. Iwasaki et al. *Phys. Rev. D*, **53**, 6443, (1996).
- [85] C.R. Allton et al. *Nucl. Phys. B*, **489**, 427, (1997).
- [86] F. Butler et al. *Nucl. Phys. B*, **430**, 179, (1994).
- [87] C. Davies et al. *Phys. Rev. D*, **50**, 6936, (1994).

- [88] A. Duncan et al. *Phys. Rev. D*, **51**, 5101, (1995).
- [89] W.H. Press et al. *Numerical Recipes in C*. Cambridge University Press, New York, 2nd edition, 1992.
- [90] D.W. Marquardt. *Society for Industrial and Applied Mathematics*, **11**, 431, (1963).
- [91] R. Fletcher. *Practical Methods of Optimization*. John Wiley & Sons, New York, 2nd edition, 1981.
- [92] M. Lüscher. *Comm. Math. Phys.*, **104**, 177, (1986).
- [93] D. Hochberg and H.B. Thacker. *Nucl. Phys. B*, **257**, 729, (1985).
- [94] M. Fukugita et al. *Phys. Lett. B*, **294**, 380, (1992).
- [95] S.R. Sharpe. *Phys. Rev. D*, **41**, 3233, (1990).
- [96] S.R. Sharpe. *Phys. Rev. D*, **46**, 3146, (1992).
- [97] C. Bernard and M. Golterman. *Phys. Rev. D*, **46**, 853, (1992).
- [98] E. Jenkins et al. *Phys. Rev. Lett*, **75**, 2272, (1995).
- [99] M. Booth et al. *Phys. Rev. D*, **55**, 3092, (1997).
- [100] S. Collins et al. *Nucl. Phys. B (Proc. Suppl.)*, **47**, 378, (1996).
- [101] S. Gottlieb. *Nucl. Phys. B (Proc. Suppl.)*, **53**, 155, (1997).
- [102] MILC Collaboration S. Gottlieb et al. To appear in the proceedings of “Lattice QCD on Parallel Computers”, University of Tsukuba, March, 1997. hep-lat/9707014.
- [103] K.C. Bowler et al. *Phys. Lett. B*, **162**, 354, (1985).
- [104] S. Ono. *Phys. Rev. D*, **17**, 888, (1978).

- [105] R.M. Barnett et al. Review of Particle Properties. *Phys. Rev. D*, **54**, 1, (1996).
- [106] J.F Donoghue et al. Dynamics of the Standard Model. Cambridge University Press, Cambridge, 1992.
- [107] E. Eichten and K. Gottfried. *Phys. Lett. B*, **66**, 286, (1977).
- [108] C. Quigg and J.L. Rosner. *Phys. Rept. C*, **56**, 167, (1979).
- [109] K. Gottfried et al E. Eichten. *Phys. Rev. D*, **21**, 203, (1980).
- [110] UKQCD Collaboration, P. Lacock and C. Michael. *Phys. Rev. D*, **52**, 5213, (1995).
- [111] S. Collins et al. *Nucl. Phys. B (Proc. Suppl.)*, **53**, 881, (1997).
- [112] M. Göckeler et al. *Phys. Lett. B*, **391**, 388, (1997).
- [113] M. Göckeler et al. *hep-lat/9707021*.
- [114] H. Wittig. Verification of $O(a)$ -improvement. To appear in the proceedings of "Lattice 97".
- [115] CP-PACS Collaboration T. Yoshie et al. CP-PACS results with the Wilson action. To appear in the proceedings of "Lattice QCD on Parallel Computers", University of Tsukuba, March, 1997.
- [116] T. Yoshie. Review of Light Hadron Spectroscopy. To appear in the proceedings of "Lattice 97".
- [117] CP-PACS Collaboration S. Aoki al. To appear in the proceedings of "Lattice 97", *hep-lat/9709139*.